ELECTRICAL, THERMAL AND SPECTROSCOPIC STUDIES ON DISORDERED SUPERIONIC CONDUCTORS

A THESIS
SUBMITTED FOR THE DEGREE OF
DOCTOR OF PHILOSOPHY

By
P. BALAYA

SCHOOL OF PHYSICS
UNIVERSITY OF HYDERABAD
HYDERABAD - 500 134.
INDIA

AUGUST 1992

TO

MY PARENTS

INVOCATION

As ranked in every alphabet the first

The self-same vowel stands, so in all worlds

Th' eternal GOD is chief

Thiruvalluvar

CERTIFICATE

This is to certify that the work contained in this thesis entitled, '**ELECTRICAL, THERMAL AND SPECTROSCOPIC STUDIES ON DISORDERED SUPERIONIC CONDUCTORS**' has been carried out by **Mr P. Balaya** under my supervision and the same has not been submitted elsewhere for any degree to the best of my knowledge.

C S SUNANDANA
(SUPERVISOR)

Hyderabad
August, 1992

DEAN
SCHOOL OF PHYSICS

DEAN
SCHOOL OF PHYSICS
University of Hyderabad
P.O. Central University
Hyderabad-500 134 (INDIA)

DECLARATION

I hereby declare that the matter embodied in this **thesis** is original and is the result of investigations carried out by me under the supervision of **Dr.C S Sunandana**, School of Physics, University of Hyderabad, Hyderabad. I further declare that this work has not formed the basis for the award of any degree either here or elsewhere.

(P BALAYA)

Date

School of Physics
University of Hyderabad
Hyderabad - 500 134

ACKNOWLEDGEMENTS

It is with high regard, I express my deep sense of gratitude to **Dr. C.S. Sunandana**, who has been a constant source of inspiration encouragement and guidance to me throughout my research. He has been remarkably patient and understanding of all my modes, habits and tendencies. Working in his laboratory has been a pleasant and memorable experience.

I express my sincere thanks to **Prof. G.S. Agarwal**, **Prof. A.K. Bhatnagar**, **Prof. V. Srinivasan** and **Prof. S.R. Shenoy** the former Deans and **Prof. A.P. Pathak**, the present Dean, School of Physics for providing me with necessary facilities.

I gratefully thank **all the faculty members** for their help, constructive suggestions and criticisms throughout the course of my work.

Grateful thanks are due to **Prof. R. Jagannathan**, **Dr. M.V. Rajasekharan**. School of Chemistry for many helpful discussions and suggestions.

I take this opportunity to express my thanks to my lab-mates: M/s. Y. Srinivasa Rao, J. Sucharita, N.R.K. Murthy, Meraj Fathima Athiya, S. Rama Rao, M. Vidyullatha and V. SriRama Swaminathan for their kind cooperation.

I am deeply indebted to all my dear friends and colleagues - too numerous to mention - whose cooperation, encouragement and suggestions made my stay in the University very happy and memorable.

With heartfelt indebtedness I recall M/s. C. Balachander and K. Devaraj, G. Swarajyam, B. Viswanathan, A. Sivalingam and V. Balaji for their encouragement.

I thank Dr K V Reddy, Principal Scientific Officer, M/s S Manjunath, K Sathya Bhaskar, Nirmalananda and T S Pramod Kumar of the Central Instrumental Laboratory and Mr V Bhaskar Rao of School of Chemistry for their cooperation.

I thank Mr P Prasada Rao for his assistance in the fabrication of AC Conductivity Meter.

I thank Mr R Nagarajan for typing the thesis with the utmost care and patience.

I also extend my thanks to Mr A Anantha Rao for his neat draughtsmanship.

I thank all the non-teaching staff, both technical and office, of the School of Physics for their constant cooperation.

I gratefully acknowledge the financial assistance from the Dept. of Science & Technology (SP/G2/Mo2/85 dated 23.9.1985) and Council of Scientific & Industrial Research in the form of Junior and Senior Research Fellowship.

Finally I owe my deep debt of gratitude to my parents for their encouragement and moral support throughout my academic career.

P. BALAYA

PREFACE

The present thesis reports the results of our investigations on a few disordered superionic conductors (SICs), taken up as a part of a basic research programme in the field of Solid State Ionics at the University of Hyderabad. Studies on SICs have become very important for scientific understanding of ion motion as well as for technological applications. The rapid progress made in this field is evident in the steadily increasing number of contributed papers in several journals including Solid State Ionics and the Journal of Non-Crystalline Solids and at the series of biennial International Conferences on Solid State Ionics, the eighth of which was held in Lake Louise, Canada during October 1991 and also at the biennial conferences of the Asian Society for Solid State Ionics, the third of which is due to be held at Varanasi, India during November 1992.

Ion-conducting systems selected for investigations, to be presented in this thesis include (1) quenched Li_2SO_4 - a disordered crystalline system, (2) Li_2O-TeO_2 and Li_2O-Na_2O-TeO_2 glasses and (3) AgI-based borate and tellurite glasses.

Chapter 1 - General Introduction

The first chapter begins with a general introduction to superionic conductors - the microscopic theory of ionic transport is presented along with a brief focus on "classic", crystalline SICs, from the point of view of structure and its relation to superionic conduction. The latter part of this chapter concerns glassy electrolytes. This part starts with a general discussion about basic aspects of amorphous

systems, such as glass formation and various factors which can facilitate the glass formation. Special experimental tools that focus on the basic structure of ionic glasses with special reference to silicate, borate and tellurite glasses are outlined in perspective. Possible mechanisms of ion transport in glassy electrolytes are presented with particular reference to the systems investigated by us.

Chapter 2 - Experimental Techniques

This chapter includes a brief description of the different major experimental probes employed in our work - powder X-ray diffraction (XRD), differential scanning calorimetry (DSC), ionic conductivity measurement using lock-in amplifier, followed by the design of sample holder used and electron spin resonance (ESR).

Chapter 3 - AC Conductivity Meter

This chapter starts with a brief account of the importance of AC measurement in the field of SICs. An electronic system designed and constructed for AC measurement (complex impedance/admittance, total AC conductivity) on superionic conductors at several frequencies upto 60 KHz is described in detail. This system consists of a quadrature oscillator, a current-to-voltage converter and a phase sensitive detector. The performance of the system is convincingly demonstrated using two test samples and other measurement possibilities are discussed.

Chapter 4 - Quenched Lithium Sulphate

In this Chapter we shall discuss the results obtained on melt-quenched Li_2SO_4 through AC conductivity and DSC measurements from the point of view of Li^+ conduction. Melt-quenching of Li_2SO_4, aided by

impurities such as Li_2CO_3 is found to stabilize FCC/microcrystalline structures (as evidenced from XRD results), and to produce ~ 5-6 orders enhancement in conductivity (relative to monoclinic phase) at 100°C with activation energy of 0.4 eV. IR and ESR results on quenched Li_2SO_4 melts highlight the role of SO_4^{2-} and CO_3^{2-} molecular motions and structural disorder in leading to ambient superionic conduction.

Chapter 5 - Alkali-Tellurite Glasses

The first part of this chapter highlights the significance of tellurite glasses vis-a-vis borate glasses in terms of their structure and physical properties. The second part deals with the thermal stability and the resultant structure of 30 Li_2O-70 TeO_2 glass - a eutectic composition, through DSC and XRD measurements. The electrical conductivity of this lithium tellurite composition in its crystalline and non-crystalline forms are also discussed. The last part presents a brief account of the mixed alkali effect (MAE) observed through various physical properties in silicate and borate glass systems. A brief account of the various theories of MAE, based on cation-cation interaction, cation-network interactions, with special reference to changes in bond strength among different species is followed by our own observation of MAE in the Li_2O-Na_2O-TeO_2 glass system and its discussion in the light of above theories.

Chapter 6 - Silver Ion Conducting Glasses

In this chapter we present a comprehensive study of Ag_2O-B_2O_3/TeO_2 and AgI-Ag_2O-B_2O_3/TeO_2 glass systems through AC conductivity, DSC and ESR spectroscopy, from the points of view of (1) optimization of Ag^+ conduction, (2) thermal stability and (3) mobile cation environment and its interaction with network formers. The results are discussed on the

basis of structural models suggested by Minami et al & Seshasayee et al

Chapter 7 - Summary and Suggestions for Further Work

The principal conclusions from the results reported in chapters 3-6 are summarized in this chapter followed by suggestions for further work.

To the best of our knowledge the results reported here (except for the conductivity and glass transition temperature data on silver ionic glasses) are completely new and the thesis represents our first efforts to understand them

CONTENTS

CHAPTER 1

GENERAL INTRODUCTION

1.1 INTRODUCTION TO SUPERIONIC CONDUCTORS

1.1.1 Short History

1.1.2 Classification of Ionic Conductors

1.1.3 Phase Transitions

1.1.4 Theory of Ionic Conduction - General Approach

1.2 NATURE OF SUPERIONIC CONDUCTING PHASES

1.2.1 AgI Compounds

1.2.2 β-Alumina

1.2.3 Fluorite Structured Compounds

1.3 GLASS FORMATION

1.4 FACTORS THAT INFLUENCE GLASS FORMATION

1.4.1 Electronegativity and Bond Type

1.4.2 Viscosity

1.4.3 Structural Considerations

1.4.4 Eutectic Composition

1.5 CRYSTALLIZATION IN SUPERCOOLED LIQUIDS

1.5.1 Mechanism of Nucleation (Homogeneous)

1.5.2 The Kinetics of Crystal Growth

1.6 EXPERIMENTAL PROBES FOR STRUCTURAL STUDIES

1.6.1 X-ray and Neutron Diffraction

1.6.2 EXAFS

1. GENERAL INTRODUCTION

1.1 INTRODUCTION TO SUPERIONIC CONDUCTORS

1.1.1 Short History

Superionic conductors (SICs) are a class of materials which achieve ionic conductivities comparable with those of molten salts ($\sigma > 10^{-1}$ S cm^{-1}) while still in the solid phase. Superionic conductors are sometimes called fast ion conductors or solid electrolytes (since the conductivities are comparable to those of liquid electrolytes). The fast ion-conduction was indeed realized in the nineteenth century itself. The first observation dates back to 1839 when Faraday[1] reported a drastic increase in the ionic conduction of PbF_2 as its temperature was increased above 177°C. Later, in 1899 Nernst[2] found high oxygen ion conductivity at elevated temperature in Y_2O_3 stabilized ZrO_2 (YSZ) which is a non-stoichiometric material with high extrinsic vacancy concentrations. The early 1900's saw one of the few important superionic conductors viz. α-AgI (body centered cubic) above the first-order phase transition at 146°C[3] from the β-phase at ambient. Another classic example is the high temperature lithium ion conducting α-phase (face centered cubic) of Li_2SO_4[4] which is stable between 572-830°C. In the middle of 1960's, sodium β-alumina[5] was proposed as a high conducting sodium ion conductor which is a stoichiometric compound possessing a high intrinsic sodium ion vacancy concentration. This work on β-alumina, had initiated an increased activity in the field of SICs, and has revealed many new materials with high values of conductivity, mainly with H^+, Li^+, Na^+, Ag^+, Cu^+, F^- and O^{2-} as mobile ions.

1 1 2 Classification of Ionic Conductors

O Keeffe[6,7] has divided the solid ion conductors into three classes Class I contains normal ion conductors that attain high ionic conduction only on melting, with low conductivity and large activation energy (~ 1 eV) in the solid state These materials are <u>not</u> fast ion conductors The alkali halides are examples of class I materials Class II contains systems which <u>acquire</u> fast ion conduction via a first-order phase transition with change in the crystallographic symmetry Actually O'Keeffe divides Class II into two subclasses Class IIa, contains materials showing a large discontinuous change in ionic conductivity and a major change in the lattice symmetry of both mobile and immobile sub lattices, such as the α-β transition in AgI, while class IIb contains those crystals, where the changes in the crystal symmetry for the immobile sub lattice are <u>minor</u> Class III contains materials where ionic conduction is obtained via a <u>diffuse</u> transition with no change in the symmetry of the non-conducting lattice, often called the Faraday transition Examples for this group are the fluorides PbF_2, CaF_2 and BaF_2 Pardee and Mahan[8] have chosen a slightly different classification scheme that relates directly to the nature of the phase transitions They do not distinguish between class IIa and IIb but add a new class of materials that enter the fast ion conducting phase via a second-order phase transition with a lambda anomaly in the specific heat, characterized by a smooth change in ionic conductivity (but with a discontinuous temperature derivative) An important example of this class is $RbAg_4I_5$ which shows superionic conduction at room temperature Class III remains a separate, less well understood category

Very recently Ratner and Nitzan [9] have divided SICs into (i)

framework crystalline materials with rigid skeletons and mobile ions and (ii) highly disordered materials

They further subdivided the framework crystalline materials into (a) soft crystals and (b) hard crystals. Soft framework crystals like AgI, CuI, Ag_2HgI_4 have (i) predominantly ionic binding (ii) readily polarizable heavy ions (iii) low Debye temperatures and (iv) sharp order to disorder phase transitions between low and high conducting phases accompanied by a large increase of enthalpy. Hard framework crystals (e.g., β-Alumina, $LiAlSiO_4$) possess (i) covalent binding and thus high frequency for local vibrations (ii) high Debye temperatures (iii) low polarizability for mobile ions and (iv) no crystallographic phase transitions.

The highly disordered materials such as glasses and polymers are characterized by lack of long range order and hence they possess complicated structural characteristics. Therefore these materials are less understood than the crystalline electrolytes.

1.1.3 Phase Transitions

The basic origin of superionic conduction is the disorder and the low activation energy associated with correlated motions of the ions. Therefore the superionic conducting phases are found in systems that may transform crystallographically or are thermally disordered without too much gain in enthalpy. The phase stability is ensured by a simultaneous gain in entropy on disordering. The entropies of fusion of the alkali halides are all very similar, with a mean value of 24.2 kJ $mole^{-1}$ for the 20 salts from LiCl to CsI. But in many superionic conductors, the

observed entropy change at the solid state phase transition ΔS_t is of order 10 kJ mole^{-1} which points to the fact that sublattice melting is indeed taking place[10]

In order to establish many equivalent sites for disordering, it is clear that fast ion conducting phases should have a high crystallographic symmetry This general trend is assured for systems obeying the first Landau rule[11] of phase transition, which in this context requires that the space group of the superionic conducting phase is a supergroup of the ordered one Second-order phase transitions and those of first order corresponding to O'Keeffe's subclass IIb are Landau transitions However, for the SICs belonging to the class IIa, the superionic conducting phases almost always possess highly symmetric cubic or hexagonal space groups

1.1.4 Theory of Ionic Conduction - General Approach

The conduction characteristics in ionic crystals have been considered extensively in a number of papers[12a,12b,13] We shall therefore discuss briefly the ionic conductivity with respect to the mobility and the concentration of the conducting species

The transport of ions through an ionic crystal depends on the presence of defects At temperatures above absolute zero, even nominally pure ionic crystals contain vacancy lattice sites and interstitial ions There are two ways in which these vacant sites (vacancies) and interstitial ions can arise An ion on a normal lattice site is thermally activated to an interstitial position leaving a vacancy in the normal lattice site The interstitial ion and the ionic vacancy together

constitute a Frenkel defect Vacancies of anion and cation are introduced in pairs - called Schottky defect pairs - into the lattice from surface sites, dislocations and grain boundaries The mechanisms of ionic transport process may be summarized as follows

(a) The vacancy mechanism exchange of a vacancy with a neighbouring ion in a normal lattice site (Fig 1 1a)

(b) The interstitial mechanism transport of an interstitial ion to a neighbouring equivalent interstitial site (Fig 1 1b)

(c) The interstitialcy mechanism displacement of an ion in a normal lattice site to an interstitial site by a neighbouring interstitial ion (Fig 1 1c)

In a single-phase material, assuming that conduction occurs predominantly for a single ionic species, the electrical conductivity is given by

$$\sigma = n(Ze)\mu \qquad (1)$$

The basic understanding of ionic conduction is based on a model of diffusion by isolated jumps with random walk of the mobile species For diffusion through interstitial sites, the potential of the mobile species is assumed to be as shown in Fig 1 2 If the hopping through the interstitial sites occur in single uncorrelated steps, then random walk theory leads to the diffusion coefficient D

$$D = \alpha\, d^2\, \nu \qquad (2)$$

where α - is a geometrical factor, d the ion jump distance and ν the

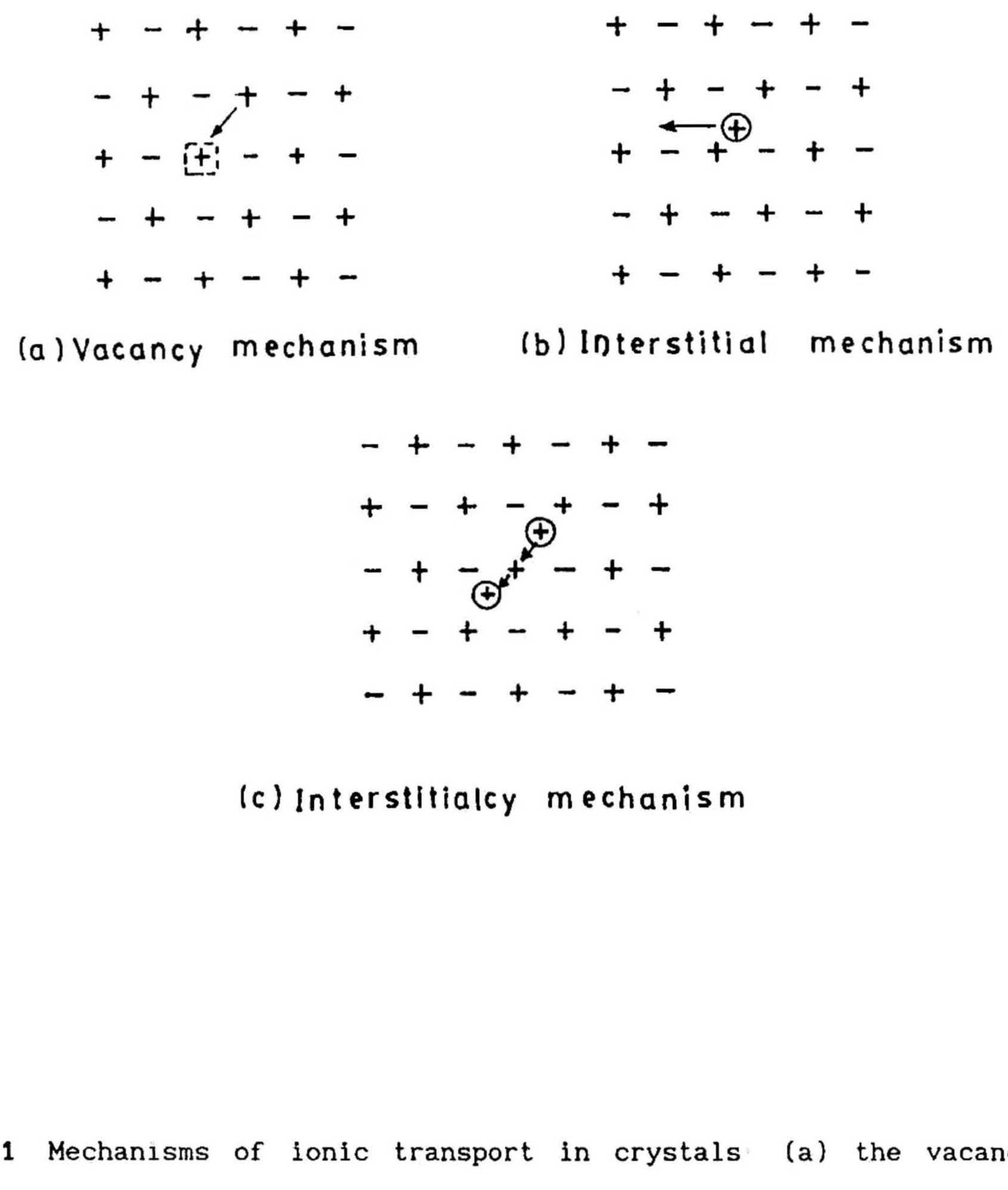

(a) Vacancy mechanism

(b) Interstitial mechanism

(c) Interstitialcy mechanism

Fig. 1.1 Mechanisms of ionic transport in crystals (a) the vacancy mechanism, (b) the interstitial mechanism, (c) the interstitialcy mechanism. Small circles represent cations, large circles represent anions.

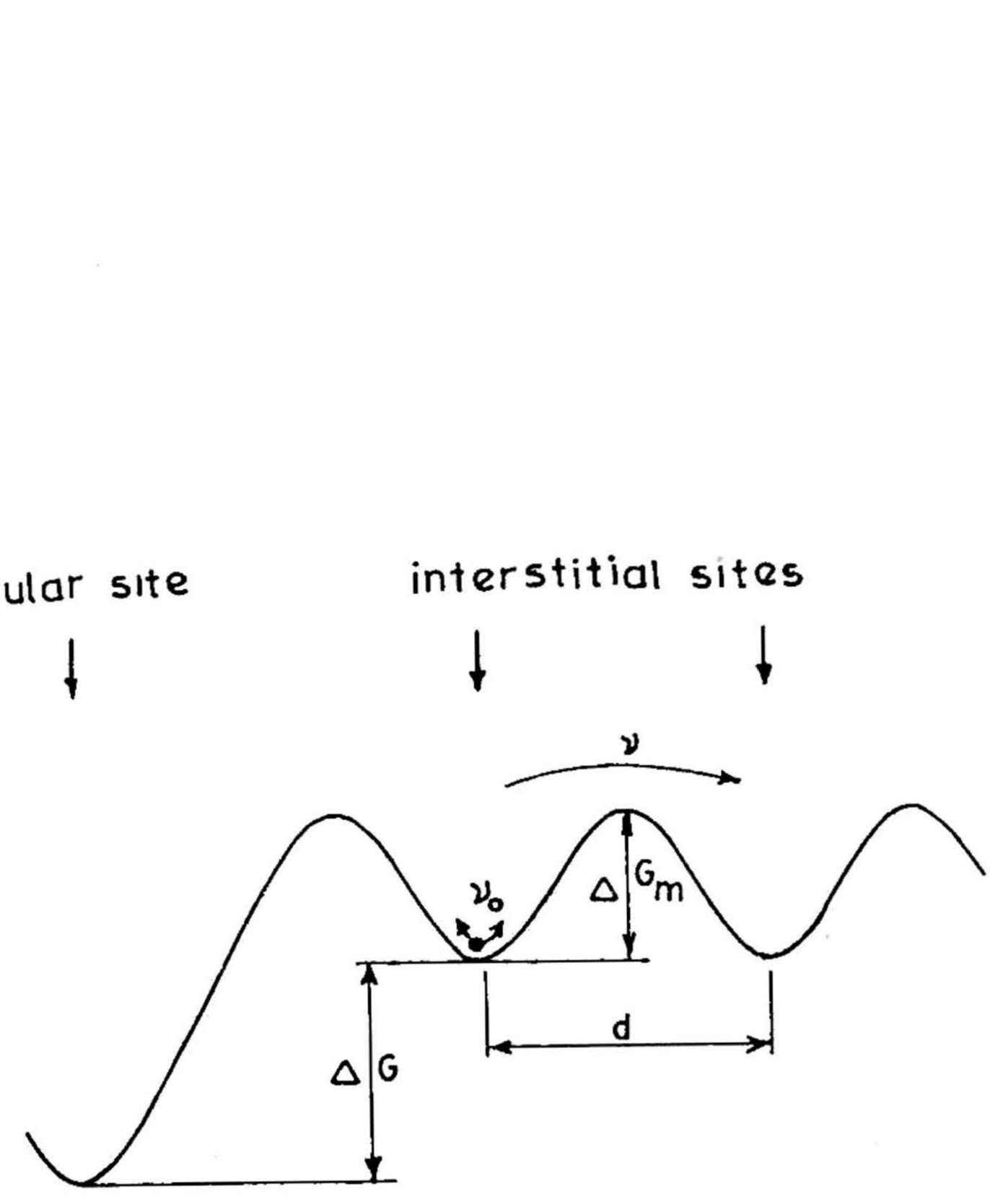

Fig. 1.2 Single particle potential assumed in the classical theory of diffusion ΔG_m is the enthalpy of motion for the interstitial to interstitial migration of particles

average jump frequency The latter depends on the energy barrier for migration E_m- presented by its neighbours and on the attempt frequency ν_o of the particle in its local potential well Thus if ν_o is a characteristic atomic vibrational frequency the probability for jump per second ν is expressed as

$$\nu = \nu_o \exp(-E_m/kT) \qquad (3)$$

where k is the Boltzmann's constant and T is the absolute temperature Thus the atom makes ν_o passes at the barrier with a probability $\exp(-E_m/kT)$ on each trial of surmounting it by thermal energy

The diffusion coefficient then becomes

$$D = \alpha\, d^2\, \nu_o \exp(-E_m/kT) \qquad (4)$$

The Nernst-Einstein equation, $\mu kT = ZeD$ which relates the mobility μ to the diffusion coefficient, may be used to obtain the conductivity

$$\sigma = \frac{n(Ze)^2\, \alpha\, d^2\, \nu_o}{kT} \exp(-E_m/kT) \qquad (5)$$

In normal ionic materials the concentration of charge carriers (Frenkel or Schottky defects) is only that generated by thermal excitations Thus the defect concentration in either case is given by

$$n = n_o \exp\,(-E_f/kT) \qquad (6)$$

where E_f is half the defect-pair formation energy The conductivity then becomes

$$\sigma = \alpha\, n_o (Ze)^2\, \nu_o d^2 (kT)^{-1} \exp -\left(\frac{E_m + E_f}{kT} \right) \qquad (7)$$

$$\sigma = \frac{\alpha\, n_o\, (Ze)^2\, \nu\, d^2}{kT} \exp -(E_a/kT) \qquad (8)$$

where $E_a = E_m + E_f$

At low temperatures, the defects are primarily induced by impurities Therefore we obtain

$$\sigma = \alpha\, n_o (Ze)^2\, \nu_o\, d^2 (kT)^{-1} \exp\,(-E_m/kT) \qquad (9)$$

Eqn (7) represents the ionic conduction behavior in the so-called 'intrinsic region' An Arrhenius plot of log (σT) versus 1/T would be a straight line Then E_a, which is the sum of both - the energy for defect formation (E_m) and the energy for defect migration (E_f) may be computed from the slope of the straight line On the other hand, Eqn (8) represents the ionic conduction behavior in the "extrinsic region' The slope (E_a) of the Arrhenius plot of log (σT) versus 1/T would yield the activation energy of mobility E_m

In superionic conductors, the high ionic conductivities are due to the unusual crystal structures of these ionic solids In the crystal lattice, the anions form an arrangement that provides for a large number of interstitial sites on which the cations/anions are distributed in a disordered fashion In other words, these crystals have an 'open structure' containing "built in defects' The migration of these defects is less restricted than the thermally activated conduction process Therefore, it is important to note that within the temperature range where the unusual crystal structures are stable, the ionic conductivity of these crystals is relatively insensitive to both impurities and temperatures

Thus the unique character of SICs arises from the value "n" of the concentration of the charge carriers with respect to n_o, the total

number of ions The 'n' represents an important fraction (β) of potentially mobile ions because of the presence of structurally inherent vacant positions

$$n = \beta\, n_o \tag{10}$$

and
$$\sigma = \frac{\alpha\, \beta\, n_o\, (Ze)^2\, \nu_o\, d^2}{kT} \exp\,(-E_a/kT) \tag{11}$$

$$\sigma = \frac{\sigma_o}{T} \exp\,(-E_a/kT) \tag{12}$$

where σ_o is the pre-exponential factor

Thus in contrast to conventional ionic conductors, the slope of the plot log (σT) versus 1/T for a SIC will represent only the energy for migration of defects as in the case of extrinsic conduction

This simple model assumes harmonic vibration of an isolated particle in a rigid potential well and ignores anharmonicity, polarization effects, and correlation between moving species which are influential factors in fast-ion conduction

SIC materials have conductivities comparable to those of liquid electrolytes with low activation energies (0 1-0 3 eV) and the concentration of mobile ions involved in charge transport is so high that their interactions play an essential role and thus the correlation effects between carriers must be considered Also, the cooperative motion of ions can lead to higher conductivities than if isolated jumps alone are considered[14] To understand the conduction process in SICs, one must establish as to how large numbers of correlated interstitial ions and/or vacancies are created and how they move in the lattice

Detailed structural studies (by diffraction and light scattering experiments) might help obtain information about possible sites in the lattice, partial occupancies, correlations between ions and vacancies and ion dynamics

1.2 NATURE OF SUPERIONIC CONDUCTING PHASES

1.2.1 AgI compounds

α-AgI was one of the first solid electrolytes to be found to exhibit a very high ionic conductivity as shown in the Fig 1.3 ranging between 1.2 and 2.6 S cm^{-1}. In 1914, Tubandt and Lorenz [3] observed that the highly conducting α-phase is stable above 146°C. Below 146°C, AgI crystallizes in a hexagonal (Wurtzite) structure[15] and its ionic conductivity[16,17] (exclusively carried by Ag^+ ions) is about 10^{-4} S cm^{-1}. The first attempt to explain this fast ion conductivity of α-AgI was made by Strock[18] who found that α-AgI belongs to space group Im3m (O_h^9) the cubic unit cell, (a = 5.044 Å) and contains two Ag^+ ions with iodide ions at the corners and body centre (Fig. 1.4). These two Ag^+ ions per elementary cell seem to be distributed over 42 space group sites with different coordinations 6(b), 12(d) and 24(h). The 6(b) sites appear to be octahedrally coordinated, and are high energy sites, and thus it is unlikely that Ag^+ ions would reside there long, if they move through such sites at all. The 12(d) sites are at the centers of tetrahedra which share faces and provide a network of pathways through which the Ag^+ ions can move. The 24(h) sites are at the centers of the shared faces, and the Ag^+ ions are expected to move rapidly through them. In α-AgI, the conduction passage ways for Ag^+ ions are formed by the face-sharing tetrahedra. X-ray diffraction studies[18] failed to detect any significant preference for a particular type of site, **i.e.**,

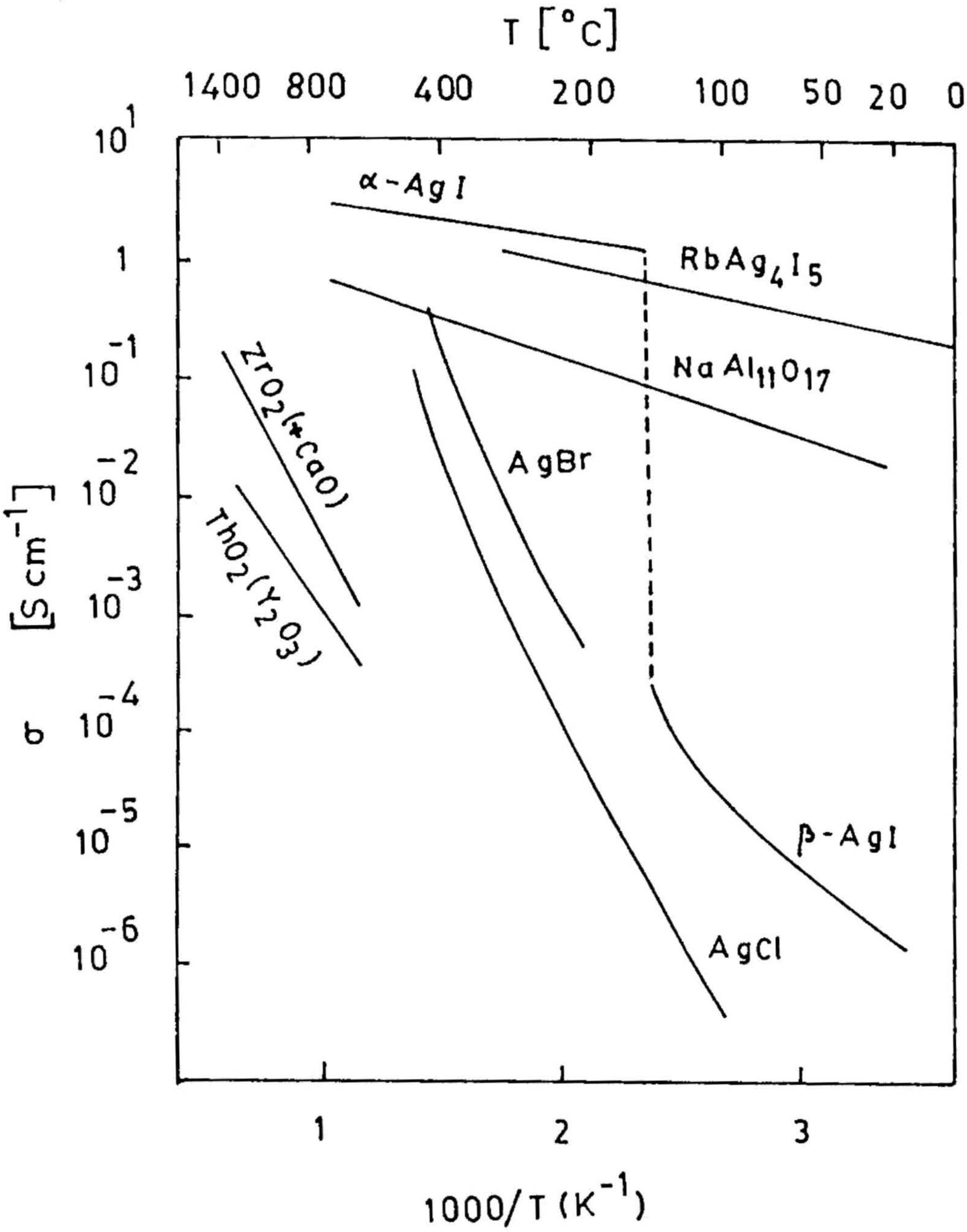

Fig. 1.3 The ionic conductivity of selected superionic conductors

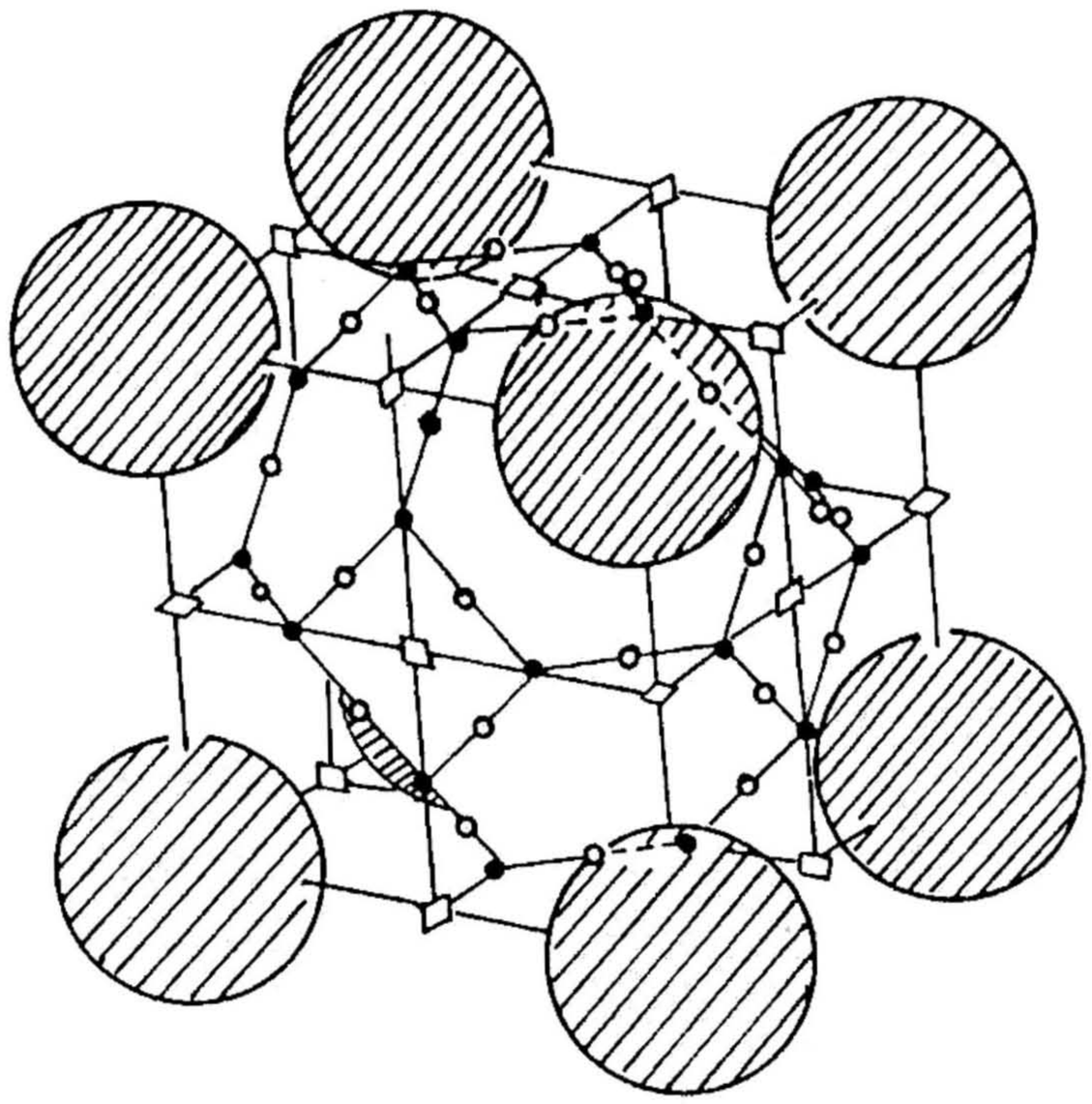

Fig 1.4 Structure of α-AgI, showing interstitial cation sites, large hatched circles, iodine ions, squares, octrahedral 6 b sites, solid circles, tetrahedral 12 d sites; open circles, 24 h sites.

the three site energies are very nearly equal Thus no meaningful distinction can be made between "regular" and 'interstitial silver sites, the number of almost equivalent sites being much larger than the number of Ag^+ ions Therefore it was concluded that the Ag^+ sublattice is in a molten state In an α-AgI crystal with the so-called molten sublattice, during diffusion, the mobile Ag^+ ions have to move through the periodic potential generated by the I^- ions forming the ordered lattice, and in doing so, there are always plenty of empty sites in the neighbourhood and the mobility is primarily determined by the detailed structure of the single ion potential along the pathways and also by the nature of the cationic short-range order induced by the ion-ion interaction

In this connection, it is interesting to have a look at the crystal structure of β-AgI[19] shown in Fig 1 5 In β-AgI which has low ionic conductivity the I^- sublattice forms tetrahedral and octanedral voids The Ag^+ ions occupy only tetrahedral sites in an ordered manner The unoccupied octahedra are connected with each other and with the tetrahedra by common faces The octahedra form rows parallel to the c-axis This seems to be the ideal arrangement for an ionic conductor, if only the geometrical features are considered Thus an Ag^+ ion may jump from a tetrahedral site into an octahedron and may move now through the crystal within a row of octahedra (Fig 1 5) However, at 140°C only about 1% of the Ag^+ ions occupy the octahedra This result suggests that ionic conduction involving interstitial sites (Frenkel disorder) does not allow high ionic conduction Only ion movement between regular sites generates high conductivity In a more general way, jumps of ions

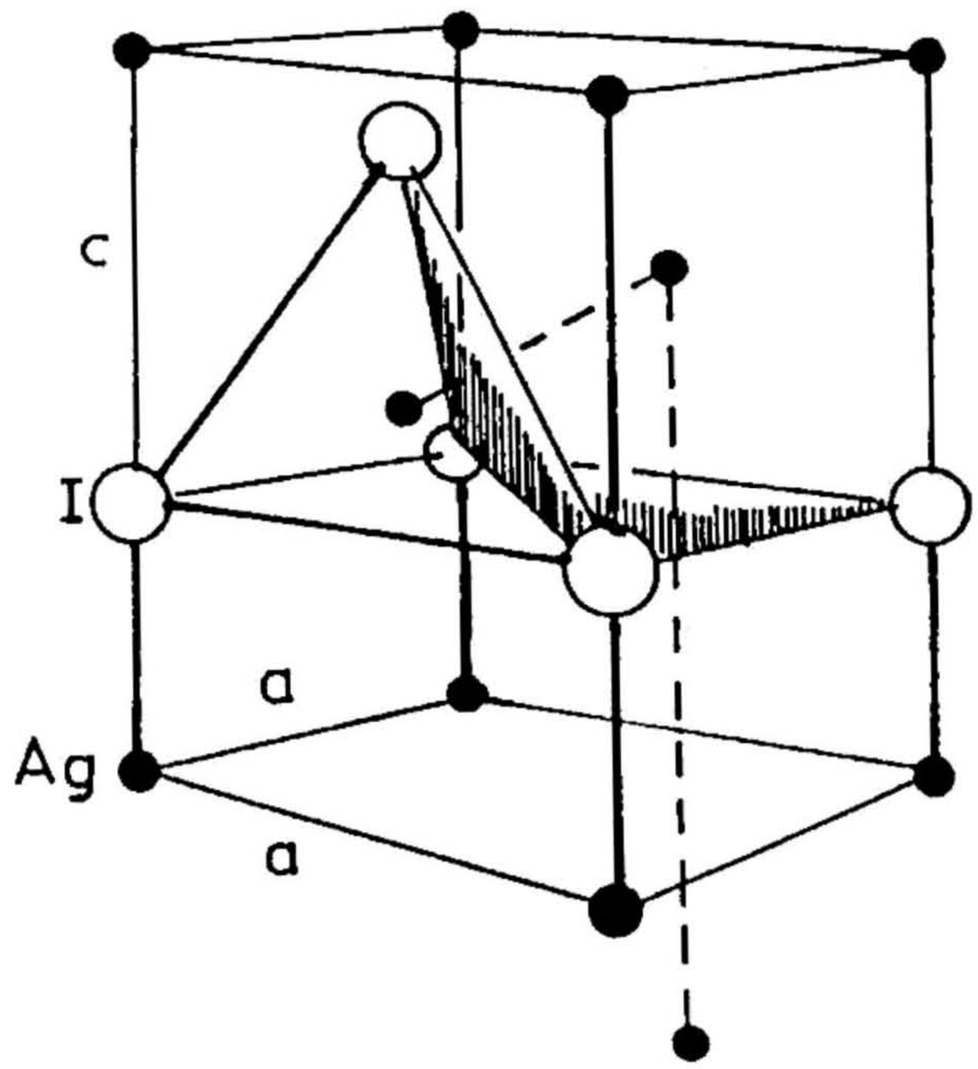

Fig 1.5 Crystal structure of β-AgI. β-AgI crystallizes in the wurtzite type structure. The Fig. shows a possible Ag^+-migration path. A silver ion jumps from a tetrahedral void into an unoccupied octahedra (first hatched position) and then moves parallel to the c-axis through the chain of unoccupied octahedra (second hatched position)

between sites with similar site energies are required and such jumps require an occupational disorder as found in α-AgI

Similar high conducting silver electrolytes are α-Ag_3SI, α-Ag_2HgI_4, and α-$RbAg_4I_5$

In α-Ag_3SI (BCC anion structure) unit cell, three silver ions are distributed over 42 available sites[20] Even in the low temperature modification, β-Ag_3SI, the anion arrangement provides 12 sites for the three silver ions in a unit cell As a result, the conductivity of β-Ag_3SI is as high as 10^{-2} S cm^{-1} even at room temperature[21] A face centered cubic arrangement can also provide excess sites for the cations as shown by α-Ag_2HgI_4 (stable at 50°C and above) Ketelaar[22] suggested that in the α-Ag_2HgI_4 unit cell, three cations are randomly distributed over four available sites

A cubic but more complicated structure is also observed in α-$RbAg_4I_5$[23], the solid electrolyte with the highest ionic conductivity at room temperature, discovered by Bradley and Greene[24], and, Owens and Argue[25] The unit cell of this compound contains four formula units The Rb^+ ions and the I^- ions are in fixed lattice positions while the 16 Ag^+ ions in the unit cell are distributed over 56 possible lattice sites The structural disorder of the silver ions is the reason for the high conductivity of such electrolytes[26,27]

1 2 2 β-Alumina

Among the solid electrolytes, the compounds with β-alumina structure exhibit unusually high, purely ionic conduction, and have been

extensively studied

In 1967 Yao and Kummer[5] discovered sodium β-alumina with the nominal composition $NaAl_{11}O_{17}$ ($Na_2O\ 11Al_2O_3$) which contains four layers of oxygen ions in cubic close-packing with the aluminum ions occupying octahedral and tetrahedral interstitial sites (see Figs 1 6 and 1 7) These form spinel-like blocks along the direction of c-axis in the unit cell, which are held by a loosely packed reflection plane perpendicular to c-axis containing Al-O-Al bridging groups and sodium ions The Al_2O_3 blocks are completely impenetrable for the sodium ions, and their motion is restricted to the pathways along the two-dimensional honeycomb net in the interlayer making single crystal β-alumina a highly anisotropic superionic conductor

Thus the sodium ions have a high mobility in the mirror plane and conductivity values of about 10^{-2} S cm^{-1} at 25°C and 10^{-1} S cm^{-1} at 300°C have been reported [28] The relatively weak binding across the reflection plane accounts for the excellent cleavage parallel to the basal planes and the fact that single crystals invariably grow as thin flat platelets with large faces perpendicular to the c-axis

There exist at least two β-alumina phases[29-31] in the Na_2O-Al_2O_3 phase diagram the β-Al_2O_3 phase with a Na_2O/Al_2O_3 ratio between 1/9 and 1/11 and the β -Al_2O_3 phase with a ratio between 1/5 and 1/8 β -Al_2O_3 has a higher ionic conductivity than the β-phase It can be stabilized by small amounts of MgO[29]

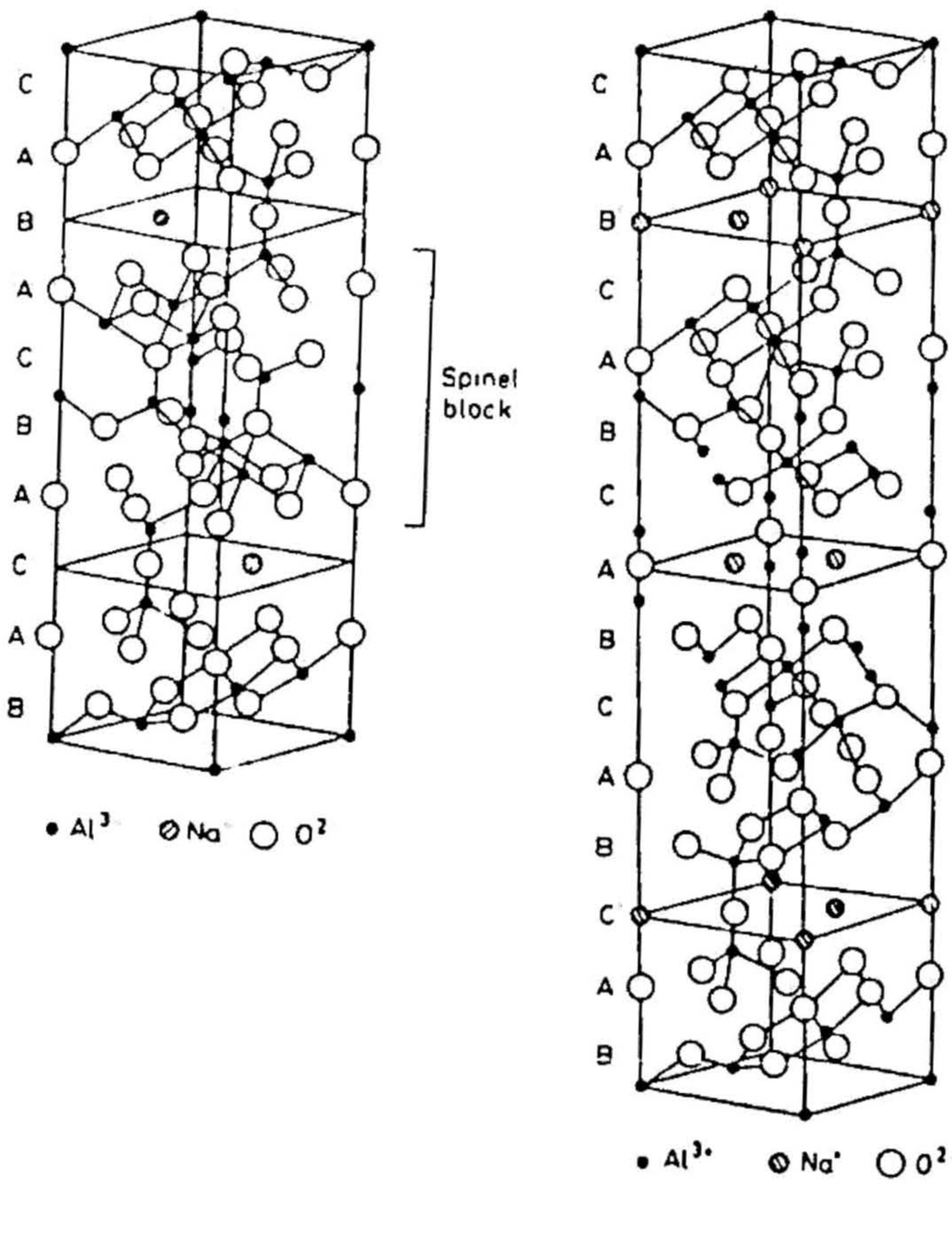

Fig 1 6 Structure of β-alumina (left) and β"-alumina (right)

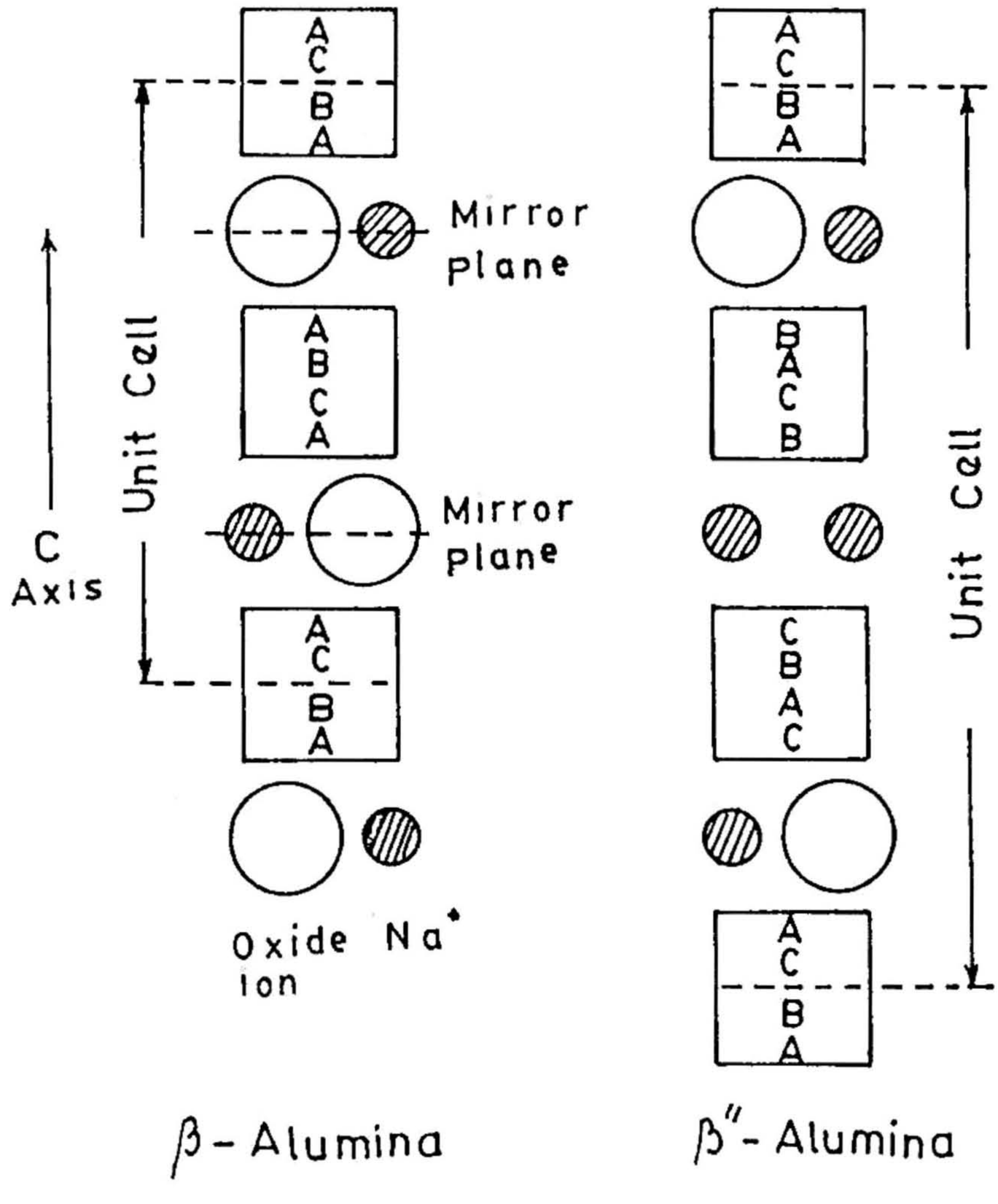

Fig 1 7 Oxide ion packing arrangement in β-alumina and β"-alumina

Note letters refer to stacking arrangements where ABC represent face-centered cubic packing while ABAB would represent hexagonal packing

The β-Al_2O_3 structure generally refers to the atomic arrangement which characterizes a large family of isomorphs with the nominal composition $AM_{11}O_{17}$ where A = Na, Li, Rb, Ag, Tl and M = Al, Ga, Fe Substitution of the A ion can be accomplished by ion exchange in an appropriate molten salt, the properties of electrolytes containing varying proportions of two A ions have been examined The mobility of an ion in the reflection plane will be a function of its radius and for a particular isomorph there will be an optimum size The mobility of sodium ions, for example, in sodium β-alumina is greater than that of the lithium ion because the small size of the latter allows it to approach the oxygen ions more closely The resultant electrostatic potential well formed by the three nearest neighbour oxygen ions is lower than would be the case for the larger sodium ion which is subject to greater repulsive forces A correspondingly large activation energy is thus necessary to enable the lithium ion to jump into a neighbouring vacant site The activation energies of Na^+ ion (or) and Li^+ ion conduction shown in Fig 1 8 are in accordance with this explanation

1 2 3 **Fluorite Structured Compounds**

Several halides that have the fluorite (CaF_2) structure reveal high halide ion conductivity One of the best examples is PbF_2 in which $\sigma \approx 5$ S cm^{-1} at $500^{o}C$ At room temperature PbF_2 have a very low conductivity and as such is a typical ionic solid Other materials that behave like PbF_2 are $SrCl_2$, which has a very high conductivity between ~ $700^{o}C$ and the melting point $873^{o}C$ and CaF_2, which arrives in the highly conducting condition just as the melting point, $1418^{o}C$ is approached

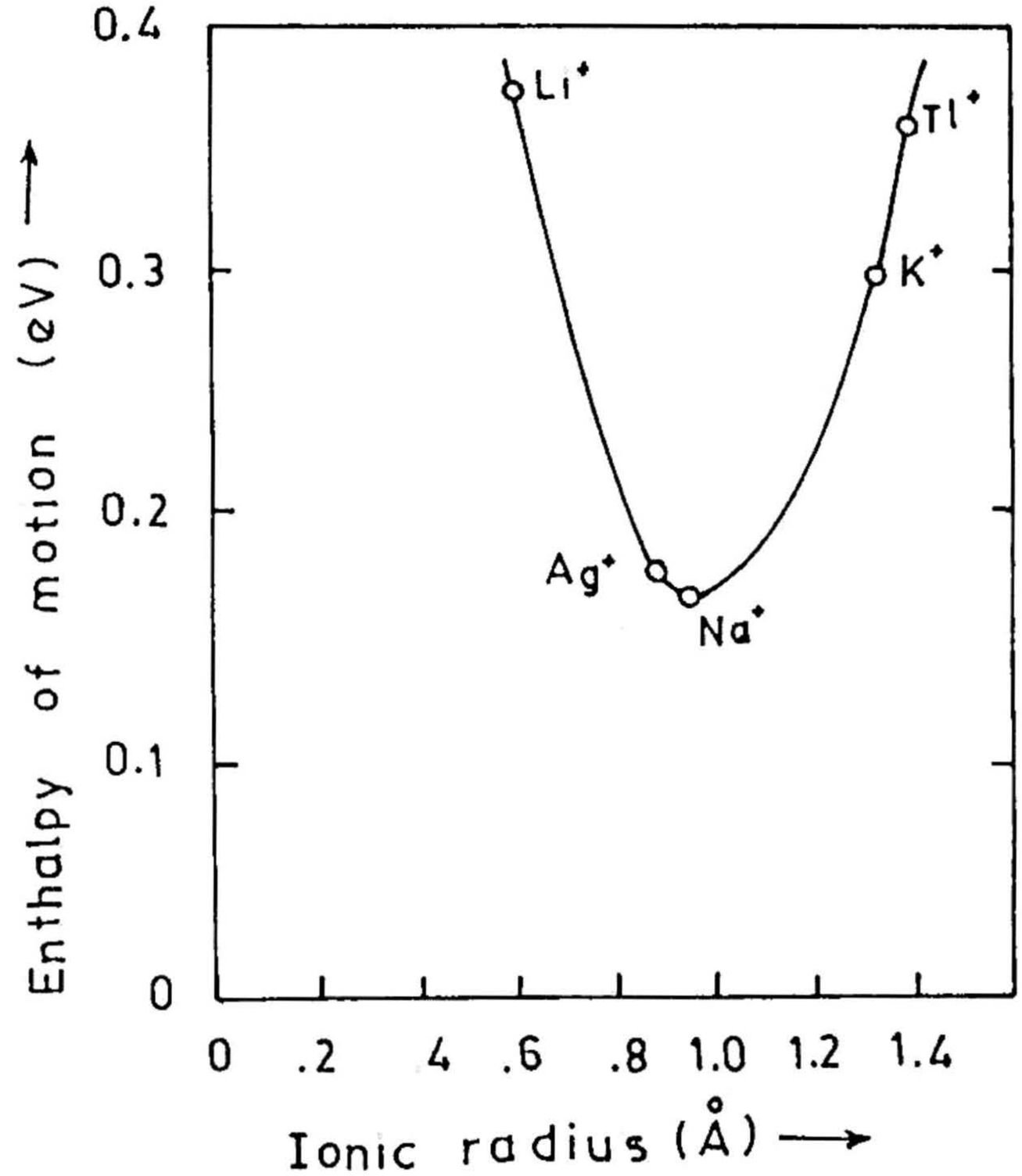

Fig. 1.8 The dependence of enthalpy of motion on the ionic radius for various ions in β-alumina

A common way of describing the fluorite structure is as a primitive cubic array of anions (F^-) in which the eight-coordinate sites at the cubic body centres or alternately empty and occupied by a cation for example in CaF_2 the primitive cubes of F^- ions are formed with Ca^{2+} ions at the body centres of alternate cubes (see Fig 1.9) The sites available for interstitial F^- are then at the centres of the set of empty alternate cubes; these sites are normally coordinated by six calciums in an octahedral arrangement and eight fluorines at the cube corners In creating an interstitial F^- ion, one of the corner F^- ions must move off its corner site and into the body of the cube

The best known and most thoroughly investigated oxygen ion conductors are those based upon stabilized-zirconia Pure ZrO_2 is monoclinic at ambient temperature (a = 5.12 Å, b = 5.17 Å, c = 5.29 Å $\beta = 99^{\circ}11'$) and transforms reversibly to a tetragonal structure above $1150^{\circ}C$ For the fluorite structure to be stable in any compound the ratio of cation to anion radius must be greater than 0.732, whereas for ZrO_2 this ratio is only 0.724[32] The high-temperature, superionic cubic fluorite structure of ZrO_2 may be stabilized (even at much lower temperatures) by forming solid solutions (with Y_2O_3, CaO or MgO) or by introducing non-stoichiometry Doping of ZrO_2 with CaO results in the generation of oxygen ion vacancies, and these disorder sites found to be responsible for the ionic conductivity of zirconium oxide In the case of ZrO_2-CaO, the range of stability of the fluorite phase is approximately 12-20 mole% of CaO, corresponding to 6-10 % oxygen vacancies Table I summarizes the conductivity results of a few oxygen ion conductors for the temperature range shown

(a)

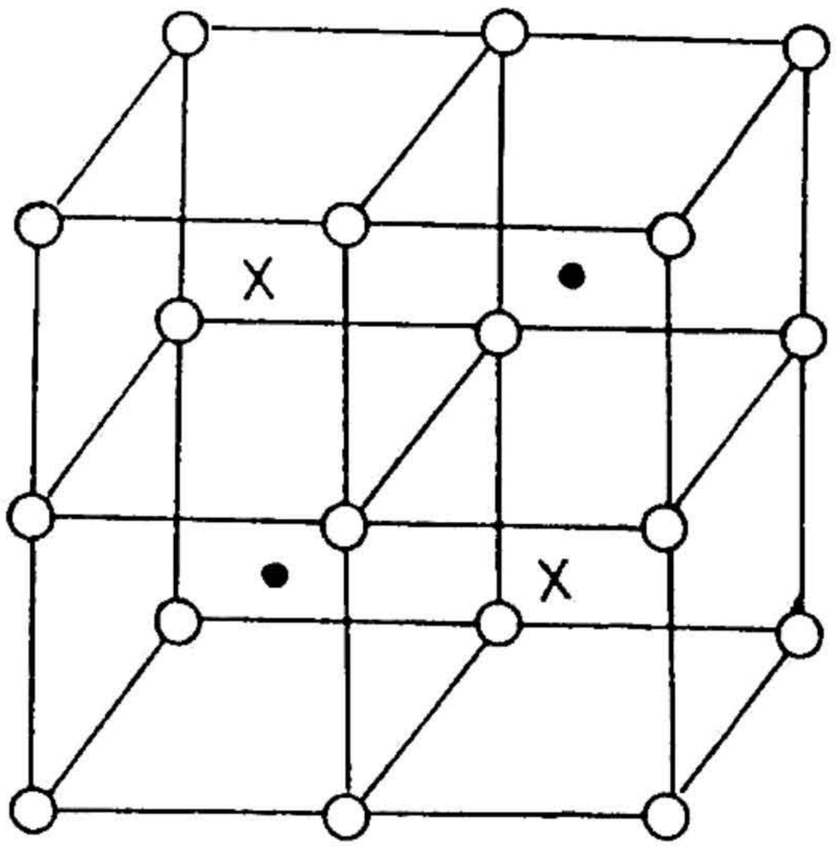

● = Ca^{2+}

○ = F^{-}

X = interstitial site

(b)

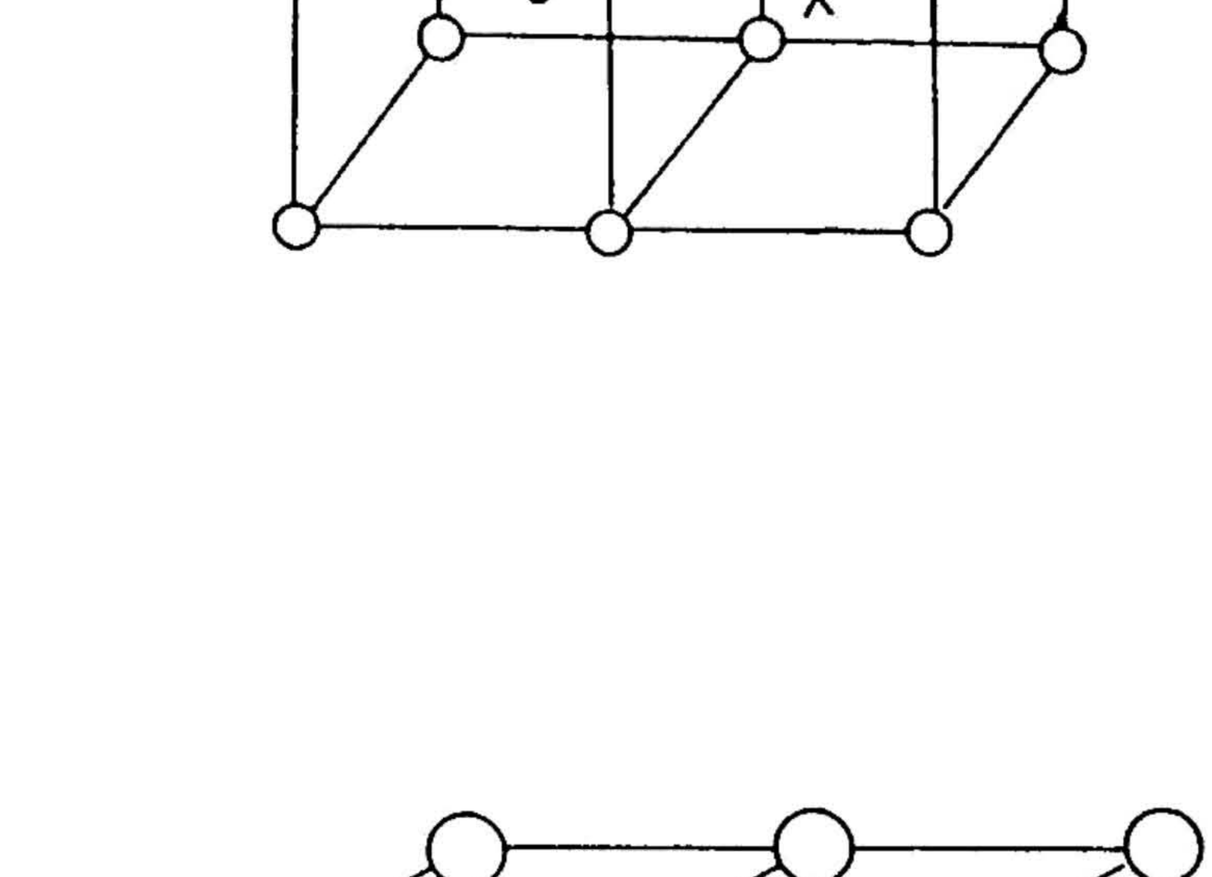

○ O^{2-}

○ Li^{+}

□ Li vacancy

Fig 1 9 The crystal structure of (a) CaF_2 (Fluorite) (b) Li_2O (anti-fluorite)

TABLE I

Conductivity results of a few oxygen ion conductors

Compound	Temperature(^{o}C)	$\sigma \times 10^{-2}$ (S cm^{-1})	Ref
ZrO_2 (10 mole% Sc_2O_3)	600 - 1400	2 - 100	33
ZrO_2 (10 mole% Y_2O_3)	600 - 1400	3 - 50	33
ZrO_2 (13 mole% CaO)	640 - 1000	0.2 - 30	34

Thus the fluorite structure appears to be particularly suitable for high ionic conductivity

The antifluorite structure also favours superionic conduction For instance Li_2O which exhibits thermally induced Frenkel disorder and fast-ion conduction at high temperature[35,36] crystallizes in the cubic antifluorite structure i e , it has the same structure as CaF_2 with anions and cations interchanged (the tetrahedrally coordinated Li^+ ions form a simple cubic array and the eight-coordinate O^{2-} ions occupy alternate cube centres, see Fig 1 9)

Certain other compounds adopting the antifluorite structure are Na_2O, K_2O, Rb_2O, Na_2S and K_2S Na_2S at high temperature appears to undergo a phase transition to a superionic state with Na^+ sublattice disordering Conductivity and neutron diffraction studies on these compounds should be of interest

From the results of various investigations on these crystalline SICs, the following points emerge[23]

(1) Conductivity appears to be associated with the nature of passage ways, the simpler the latter are, the higher will be the conductivity

(2) 3-D networks generally lead to higher average conductivity than 2-D networks

(3) Larger volumes of crystal space occupied by the conduction

passage ways lead to higher conductivity This is related to the points (1) and (2)

(4) The ratio of available sites to current carriers should always be greater than 3 Even a factor of 2 may not give a solid electrolyte because it is probable that at least half the sites will be too close to the other half

Thus it is well understood that the ions may move easily and rapidly in crystals, with a high degree of potential disorder if their ionic radii match the cross section of the conducting paths and if these paths connect regular lattice sites with each other In all the electrolytes discussed above structural defects or lack of rigidity in one of the sublattices gives rise to enhanced ionic conduction In such a case, the non-crystalline solids possessing a large degree of disorder could be better choice than crystalline systems in revealing a significant and selective ionic conduction

The remaining part of this chapter is concerned with the structure and ionic properties of amorphous electrolytes Before we discuss these aspects of ionic glasses we make an attempt to answer the following questions

(1) how do glasses form?

(2) Why do glasses form? In particular, why are some materials so much better glass formers than others?

1.3 GLASS FORMATION

Glass is generally obtained by supercooling a liquid in such a manner that it does not crystallize. It may also be prepared through variety of other techniques[37] provided crystallization is suppressed. Most compounds when melted have a viscosity about the same as that of water (10^{-2} Poise, P). On cooling the melt it very rapidly crystallizes at, or a little below the melting temperature T_m (see Fig. 1.10). There are however, a few materials which form melts, which are considerably more viscous. The high viscosity indicates that the atoms or molecules in the melt are not so easily moved relative to one another by applied stresses. On cooling below the melting point, crystallization does occur but at a significantly lower rate than in the materials of first group. The process of crystallization involves structural changes, i.e., the rearrangement of atoms relative to one another.

If the crystallization rate is low enough, it is possible to go on cooling the melt, below the melting point avoiding the occurrence of crystallization. As the melt cools, its viscosity continues to increase. This viscous liquid below the melting point is a supercooled liquid (region b-e in Fig. 1.10). It is incorrect to refer to it as a glass. On further cooling, the viscosity reaches a high value (~ 10^{13}-10^{14}P) that the material acquires the rigidity of a crystalline solid but without regular 3-D periodicity of a crystal structure. This change in properties or behaviour from an undercooled liquid to a glass, takes place at a temperature or over a range of temperatures called the glass transition temperature (T_g). The T_g depends on the rate of cooling of the undercooled liquid. It is found that the slower the rate of cooling, the larger is the region over which the liquid may be supercooled and

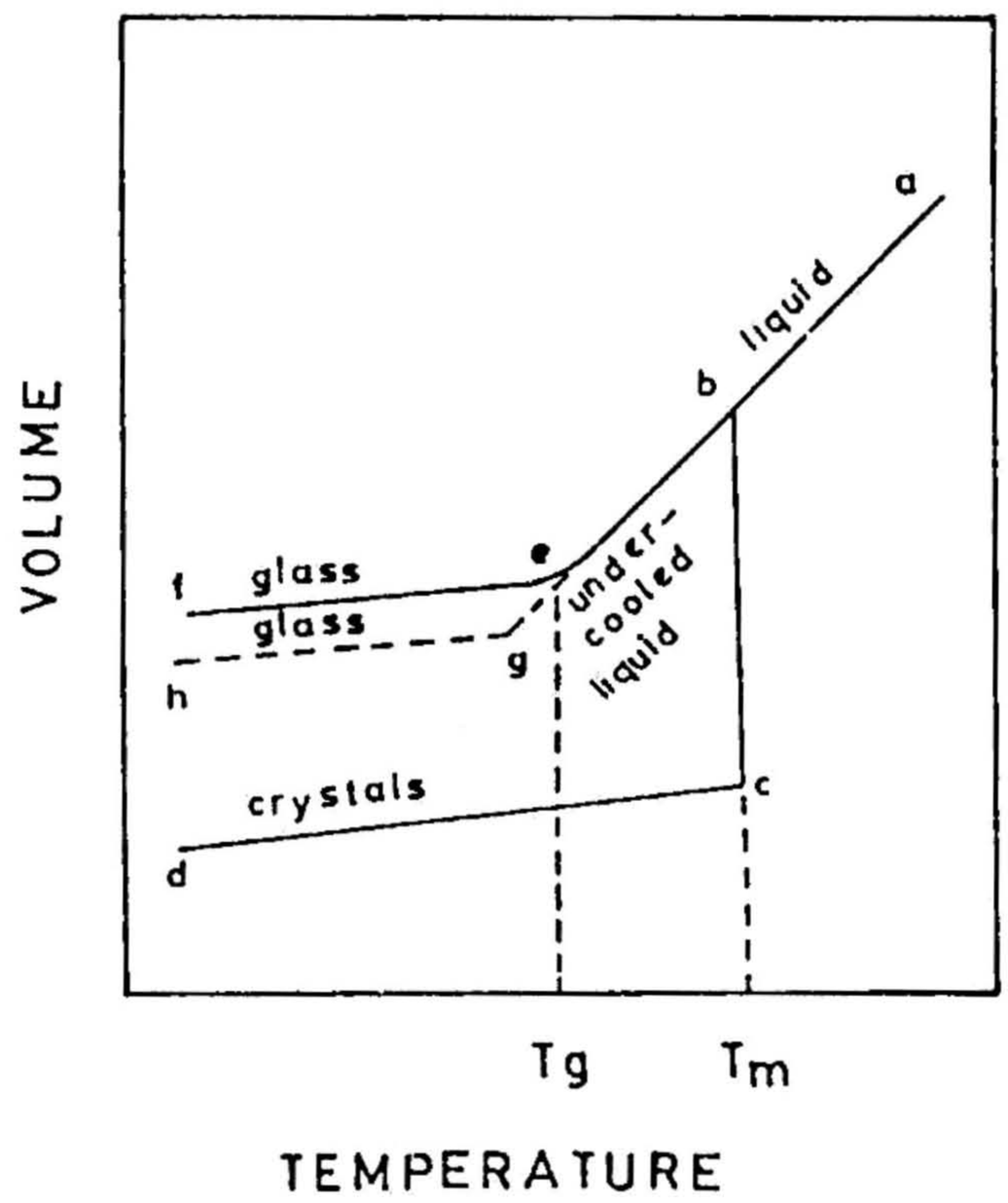

Fig. 1.10 Volume-temperature characteristics (schematic) for crystal, liquid and glass

hence lower is the glass transition temperature (compare points e and g in Fig 1.10)

1.4 FACTORS THAT INFLUENCE GLASS FORMATION

The question why do certain materials readily form glasses on cooling a melt? or why do certain chemical compositions of materials have a greater glass-forming tendency than others? - is one of considerable scientific and technological importance Several factors do play a significant role in determining the case of glass formation[38-40]

1.4.1 Electronegativity and Bond Type

The main glass forming oxides are SiO_2, B_2O_3, GeO_2 and P_2O_5 They are all oxides of elements with intermediate electronegativity, these elements are not sufficiently electropositive to form ionic structures, such as MgO, NaCl, but also are not sufficiently electronegative either to form covalently bonded, small molecular structures, such as CO_2 Instead, the bonding is usually partly ionic and partly covalent and the structures are best regarded as 3-D polymeric structures Oxides of other elements around this group in the periodic table also show a tendency to glass formation Some, such as As_2O_3 and Sb_2O_3 form glasses if cooled very rapidly Others, such as Al_2O_3, Ga_2O_3, Bi_2O_3, SeO_2 and TeO_2 are known to be conditional glass-formers, i e , they do not form glasses individually, but may do so in the presence of certain other non-glass forming oxides For instance, a range of liquid compositions in the $CaO-Al_2O_3$ system forms glasses although CaO and Al_2O_3 do not, by themselves, form glasses **The** glass-forming oxides, SiO_2, B_2O_3, etc , can form glasses either alone or when mixed with considerable quantities

of non-glass forming oxides For instance, glasses may be readily formed from SiO_2 or B_2O_3 to which upto 20 to 40 mole % of an alkali oxide has been added.

1.4.2 Viscosity

A factor that is undoubtedly important in glass formation is the viscosity of liquids above their melting points The glass-forming oxides B_2O_3, GeO_2 and P_2O_5 all form very viscous liquids, e.g., the viscosity of silica just above its melting point, 1715°C is 10^7 P By contrast, most inorganic substances, which do not form glasses readily are fluid in the liquid state, e.g., the viscosity of liquid H_2O at 0°C or molten LiCl at 613°C is ~ 2×10^{-2} P Viscosity is related to the structure and bonding that is present Thus, molten silica may be regarded as an amorphous, polymeric structure with strong Si-O bonds and this is the reason for its high viscosity In order for such a liquid to crystallize, many strong bonds must break and reform and considerable atomic reorganization is necessary Clearly these processes take place with more difficulty in viscous, polymeric liquids than they do in fluid, ionic or molecular liquids There are exceptions to this general relation between melt viscosity and glass-forming ability, however Two examples of liquids that are fluid but readily yield glasses on cooling are (a) aqueous solutions of $ZnCl_2$ and (b) molten mixtures of $LiNO_3$ and $Ca(NO_3)_2$

1.4.3 Structural Considerations

Goldschmidt[41] made one of the earliest attempts to discover characteristics common to glass-forming oxides and suggested that the ability of an oxide to form a glass might be related to the way in which

the oxygen ions are arranged around the cation to form the unit cell of the crystal structure. In stable crystal structures the number of anions immediately surrounding a cation (coordination number) is determined by the relative sizes of the anion and cation. It can be shown from geometrical considerations that for an oxide M_xO_y the coordination number of M cations will be four if the radius ratio R_M/R_O lies between 0.225 and 0.414. In this case the oxygens are arranged at the corners of a tetrahedron with the cation occupying a central position. Goldschmidt pointed out that for a number of glass-forming oxides including SiO_2, GeO_2 and P_2O_5 a tetrahedral arrangement occurred in the crystalline state and suggested that this might be a criterion of glass-forming ability.

Zachariasen[42] pointed out that the ability of an oxide to form a tetrahedral configuration could not be an absolute criterion of glass-forming ability since the radius ratio for BeO for e.g. will permit oxygen ions to form tetrahedral groupings around the beryllium ion and yet this oxide cannot be obtained in the glassy state. This led him to examine more closely the characteristics of glass-forming oxides and to develop the random network theory of glass structure.

Starting from the basis that the interatomic forces in glasses and crystals must be essentially similar and that the atoms in glass oscillate about definite equilibrium positions, Zachariasen deduced that the atoms must be linked in the form of a three-dimensional network in glass as in crystals. The network in a glass could not be a periodic one since glasses, unlike crystals, do not give sharp X-ray diffraction peaks. Zachariasen also proposed that the energy content of a substance

in the glassy state must not be greatly different from that of the corresponding crystal network. Thus for a glass-forming oxide the coordination number of the cation must be closely similar in the glass to that observed in the crystal. This means that the units of structure in the glass and in the crystal will be practically identical. In the crystal these structural units are built up to give a regular lattice but in the glass there is sufficient distortion of bond angles to permit the structural units to be arranged in a non-periodic fashion giving a random network. Fig 1 11 shows the differences between the regular crystalline lattice and the random network for an oxide having the formula M_2O_3. In both cases the structural unit is the MO_3 triangle. Thus glasses possess short-range order since the oxygens are arranged in fairly regular polyhedra but long-range order is absent. This view of glass structure is entirely consistent with the liquid-like nature of glass.

It should be pointed out, however, that the structure depicted in Fig. 1 11b represents a rather large departure from the crystal lattice in Fig. 1 11a. Smaller deviations in bond angles would probably be sufficient to generate a non-periodic network giving a structure sufficiently lacking in long-range order to account for X-ray and neutron scattering results. For e g , in vitreous silica the variation in Si-O-Si bond angle is probably only about ± 10%.

Having postulated the random network structure for glass, Zachariasen proposed certain conditions for glass formation. For an oxide M_xO_y to form a glass it was proposed that

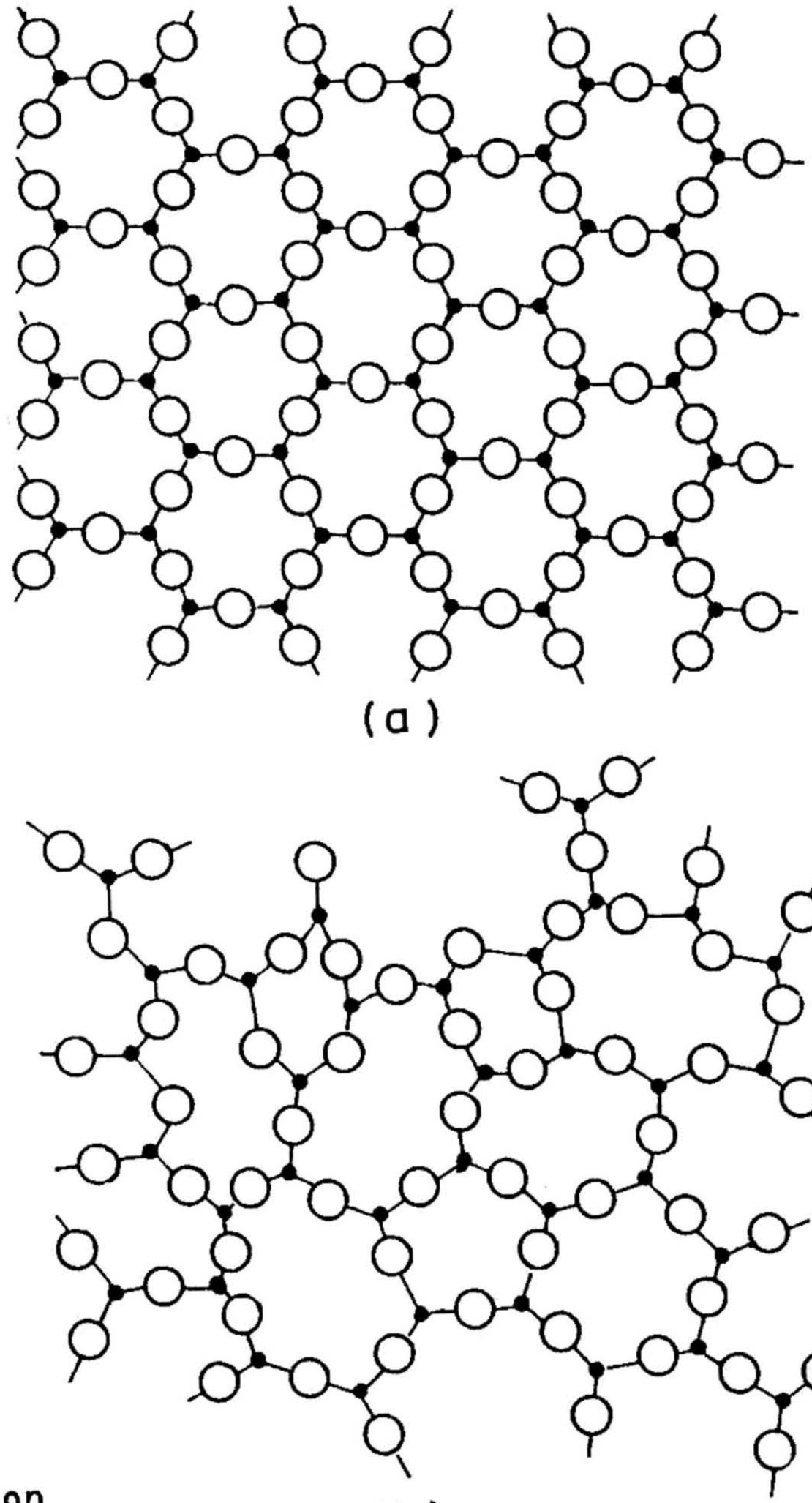

Fig 1.11 Two-dimensional representation of an oxide M_2O_3 in (a) crystalline form and (b) glass form

(a) an oxygen atom must not be linked to more than two M atoms;

(b) the number of oxygen atoms surrounding M must be small;

(c) the oxygen polyhedra must share corners only and not edges or faces.

A fourth, less important condition proposed by Zachariasen, namely that at least three corners in each oxygen polyhedron must be shared, is not strictly applicable since glasses are known in which this condition would not be fulfilled.

The oxides M_2O and MO cannot meet the conditions proposed by Zachariasen. The oxides M_2O_3 can do so if the oxygens form triangles around each M atom and the oxides MO_2 and M_2O_5 can do so if the oxygen form tetrahedra around each M atom.

Vitreous boric oxide (B_2O_3) is a good example of a glass whose structure is built up of triangular units. These units are found in many crystalline borates. Vitreous silica (SiO_2), germania (GeO_2), phosphorus pentoxide (P_2O_5), and arsenic oxide (As_2O_5), are examples of glasses built up of tetrahedral units, the tetrahedra SiO_4, GeO_4, PO_4, AsO_4 are also found in the crystalline state.

1.4.4 Eutectic Composition

The glass-forming tendency is found to be greater for a binary material (say a silicon-gold alloy) than for an elemental one (say, pure Si). This has to do with the relation between T_g and T_m. Fig. 1.12 shows the phase diagram for the binary system $Au_{(1-x)}Si_x$. For the alloy ($o < x < 1$), the liquid is stabilized and thus the melting point T_m is lowered.

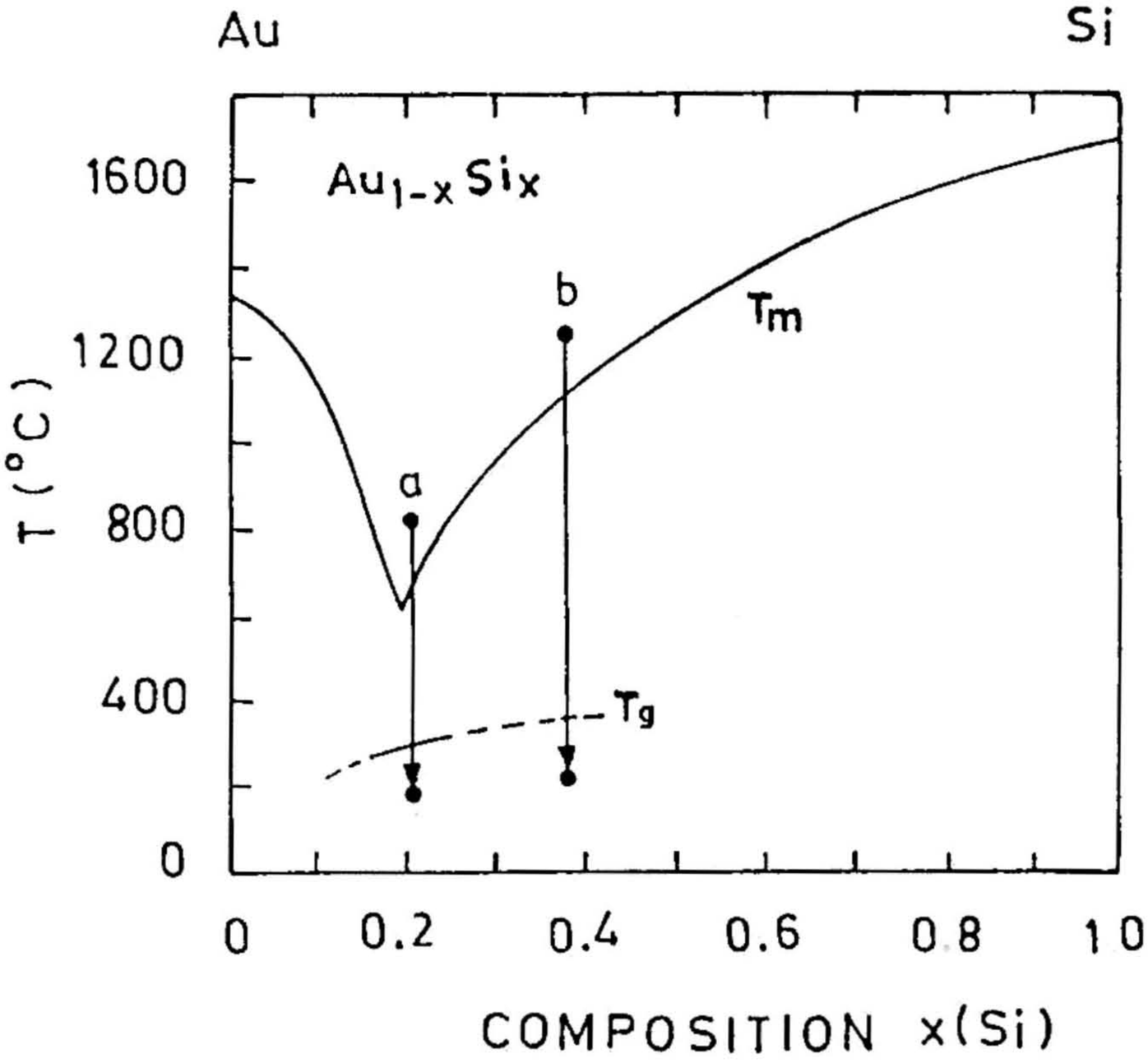

Fig. 1.12 Glass formation in the gold-silicon system. Two quenches from the liquid state at two compositions are indicated. Glasses can be prepared much more readily in quench **a** than in quench **b** (after Zallen[44])

relative to that of end components (x = 0 or 1), by the entropy of mixing and the attractive interaction between the two components There is a deep eutectic at composition x = 0 2, at which the melting point is minimized This composition range where a deep eutectic occurs is claimed to be more favourable for glass formation[43,44] i e , near the eutectic composition, as at 'a' in the Fig 1 12, a liquid is much more readily quenched to the glass than a liquid at a distant composition such as 'b" The 'treacherous territory' between T_m and T_g within which the melt is both thermodynamically ($T < T_m$) and kinetically ($T > T_g$) capable of crystallizing is much broader and more forbidding at 'b' than at 'a' Thus the eutectic composition is favoured for glass formation, a conclusion consistent with the observation that $Au_{0\ 8}Si_{0\ 2}$ can be splat-quenched to glassy state but not Si and Au

1 5 CRYSTALLIZATION IN SUPERCOOLED LIQUIDS

Crystallization is the process by which the regular lattice of the crystal is generated from the less well-ordered liquid structure Two parts of the crystallization process are to be distinguished nucleation and crystal growth Nucleation may be homogeneous or heterogeneous and it is important to distinguish between the two types In homogeneous nucleation, the first tiny seeds are of the same constitution as the crystals which grow upon them in the absence of any heterogeneous nuclei such as foreign particles In heterogeneous nucleation the nuclei can be quite different chemically, from the crystals which are disposed A form of heterogeneous nucleation which is frequently observed when a piece of glass is heated in air beyond T_g, is one in which the crystals grow from nuclei, such as dust particles or scratches on the glass surface

1 5 1 Mechanism of Nucleation (Homogeneous)

There are two contributions to the change of free energy that occurs on nucleation First, the formation of a boundary or surface between the embryo and the mother phase results in a gain of free energy due to the interfacial energy Secondly, since the arrangement of the atoms within the embryo will be less disordered than that in the surrounding phase, there will be a reduction in free energy of the system There are thus two opposing factors which govern the actual free energy change and these can be approximated in the following fashion to give ΔF, the free energy change for a spherical inclusion of radius r

$$\Delta F = - \frac{4}{3} \pi r^3 \Delta f_v + 4\pi r^2 \Delta f_s \qquad (10)$$

where Δf_v is the change of free energy per unit volume resulting from transformation from one phase to the other and Δf_s can be equated with the interfacial tension Under certain circumstances it would be necessary to include a term on the right-hand side of the expression for the energy increase due to the strain energy resulting from the change in atomic arrangement within the embryo as compared with the surrounding phase In the case of a supercooled melt, however, this effect would normally be negligible Examination of Eqn 10 shows that when r is small the interfacial energy term predominates, but with increase of radius of the embryo the interfacial energy becomes a smaller fraction of the total energy change Once some critical radius is reached, the volume free energy term will predominate and further growth will lead to a lower free energy and therefore to a more stable system Regions smaller than the critical radius (embryos) require an increase in free energy to form and they will continually form and redissolve with the total number in the system remaining constant Some embryos will attain the critical radius and will continue to grow with a decrease of free energy and

hence will constitute stable nuclei. At the critical radius the free energy change will attain its maximum value and by differentiation of Eqn 10 the critical radius r^* may be derived:

$$r^* = 2\,\Delta f_s/\Delta f_v \tag{11}$$

This corresponds to a maximum free energy change ΔF^* as given by

$$\Delta F^* = 16\pi(\Delta f_s)^3/3(\Delta f_v)^2 \tag{12}$$

Becker and Doering[45] and Frenkel[46] have employed statistical mechanics to derive expressions for I, the rate of homogeneous nucleation. These have the form

$$I = A \exp(-\Delta F^*/kT) \tag{13}$$

where A is a constant and ΔF^* is maximum free energy of activation for formation of a stable nucleus as given above

This expression neglects the effects of diffusion rate but in a viscous liquid the activation energy for diffusion of molecules across the phase boundary may well constitute a major barrier to nucleation. Therefore, a general equation for the rate of homogeneous nucleation in condensed systems gives a better approach. This expression is

$$I = A \exp\left[\frac{-(\Delta F^* + Q)}{kT}\right] \tag{14}$$

where Q is the activation energy for diffusion of molecules across the phase boundary. A plot of I against T has the shape shown in Fig 1.13. This theory is approximate only, but it does at least serve to provide a qualitative explanation of experimental observations. For small degrees of supercooling, ΔF^* is large since the value of the volume free energy change Δf_v is very small and consequently the nucleation rate is low. With further supercooling Δf_v increases markedly until ΔF^* becomes

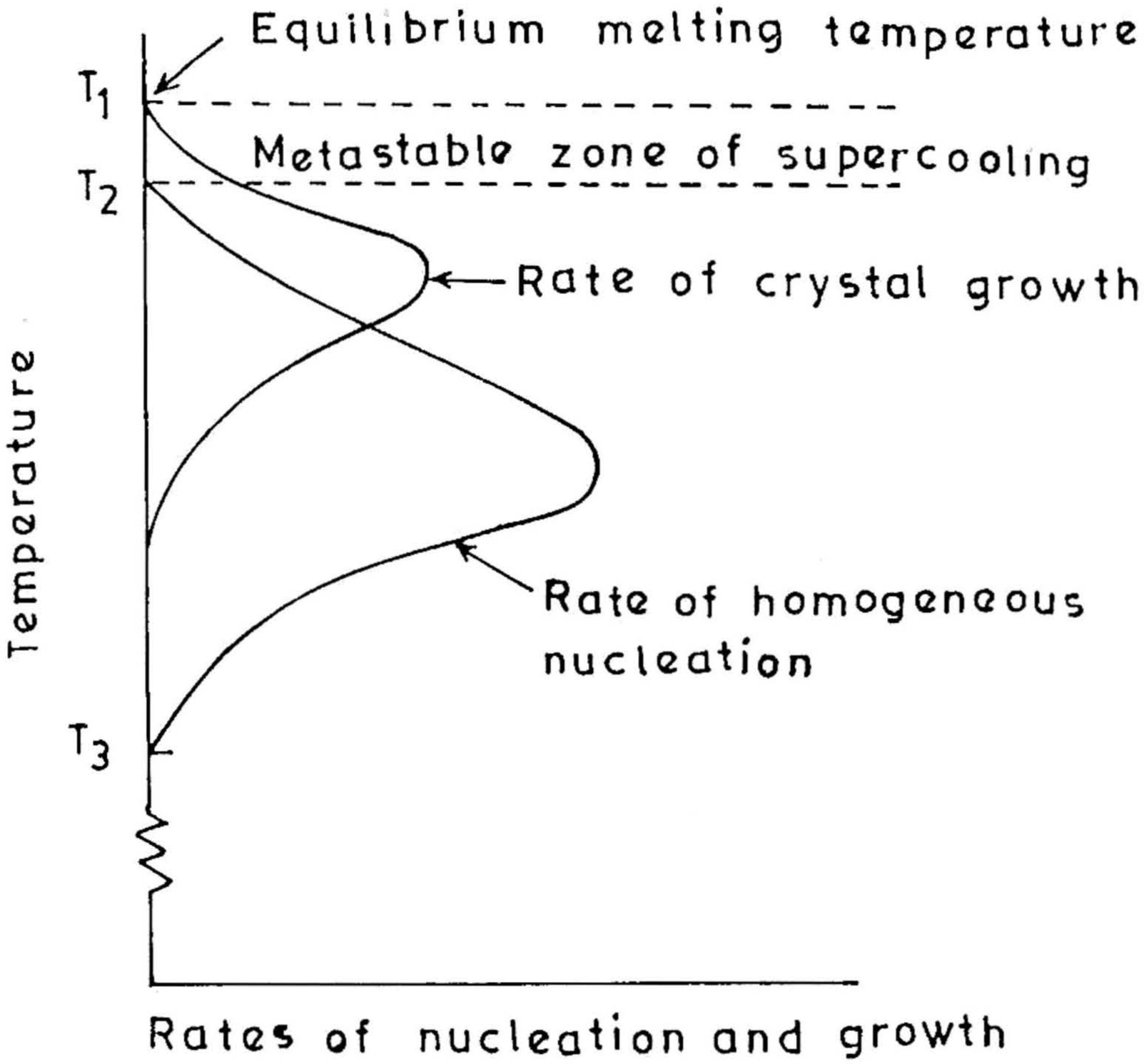

Fig 1.13 Rate of homogeneous nucleation and crystal growth in a viscous liquid

comparable in magnitude with Q, under these conditions the maximum nucleation rate is achieved The nucleation rate diminishes with further supercooling when ΔF^* becomes negligible in comparison to Q

1 5 2 **The Kinetics of Crystal Growth**

Once a nucleus has been formed by the mechanism of homogeneous nucleation or if the melt contains nuclei of a foreign material, crystals of easily measurable size can grow A simple theoretical analysis of the mechanism of crystal growth, due to Turnbull and Cohen[47], leads to the following equation for the growth rate

$$u = a_o \nu \exp(- E/RT) [1-\exp(\Delta G/RT)] \quad (15)$$

where ΔG is the decrease in free energy per mole when the liquid crystallizes and is expected to have the same value for macroscopic crystals as for submicroscopic embryos (an expectation which may not be fulfilled in practice) E is the activation energy, or kinetic energy barrier, which must be overcome for an atom, molecule, or some other structural unit to detach itself from the liquid structure and attach to the surface of the growing crystal, a_o is a distance of the order of the interatomic distance and ν is the frequency of thermal vibrations in the material The general form of the variation of u with T is also shown in Fig 1 13 Experimental results always show this type of variation Again it is difficult to make comparisons between theoretical and experimental values of u, largely because of the difficulty in identifying the structural changes involved in the process of crystal growth This is particularly so if one is interested in the practically important glasses which contain many components The structural mechanisms involved in forming a critical nucleus may be quite different from those which determine macroscopic crystal growth

In Fig 1.13, below the equilibrium melting temperature, there exist a temperature interval, referred to as the metastable zone in which the nuclei do not form at a detectable rate. In this zone however crystals can grow if nuclei are provided, i.e. if the melt is 'seeded'.

1.6 EXPERIMENTAL PROBES FOR STRUCTURAL STUDIES

The outstanding structural questions to be resolved in the field of solid state ionics may be classed as follows: short range order where we seek to understand local coordination, characteristics and in particular, whether or not distinct environments for mobile and immobile cations can be distinguished, intermediate range order where information on second and third nearest neighbour relationships is sought. To answer these questions techniques such X-ray and neutron diffraction, vibrational spectroscopy, nuclear magnetic resonance and FXAFS are being applied[48,49].

1.6.1 X-ray and Neutron Diffraction

The most valuable information obtained from X-ray diffraction (XRD) is the radial distribution function (RDF). The importance of the RDF lies principally in the fact that the area under a given peak gives the effective coordination number for that particular shell of atoms. The first peak is generally sharp. The position of the first peak in the RDF gives a value for the average nearest-neighbour bond length r_1, and similarly the position of the second peak gives the next-nearest neighbour distance r_2; a knowledge of both immediately yield a value for the bond angle θ given by

$$\theta = 2 \sin^{-1} \left(\frac{r_2}{r_1} \right) \qquad (16)$$

Neutron diffraction studies of crystals[50,51] and disordered systems[52] provide structural information which complements X-ray results since for non-magnetic materials, neutron scatter predominantly from nuclei The strength of this scattering varies quite strongly from one isotope to isotope, in an almost random manner, so contrast studies using isotopic substitution are widely used and particularly with hydrogeneous materials

In a neutron scattering process see Fig 1 14 - there is energy transfer

$$\Delta E = \hbar w \qquad (17)$$

and momentum transfer

$$\Delta P = \hbar Q \qquad (18)$$

from the neutron to the scattering system Typically a neutron scattering experiment yields the probability of the occurrence of scattering processes with transfer of energy and momentum within small intervals about $\hbar w$ and $\hbar Q$ respectively This probability is proportional to the so-called total scattering function S(Q,W) The right hand side of Fig 1 14 is a schematic plot of this function versus energy transfer, while Q is held constant

The different kinds of contributions to the spectrum may be observed as

(i) The elastic scattering, which reflects the static properties of the sample

(ii) The inelastic scattering, due to the periodic motion of the atoms or ions in the sample

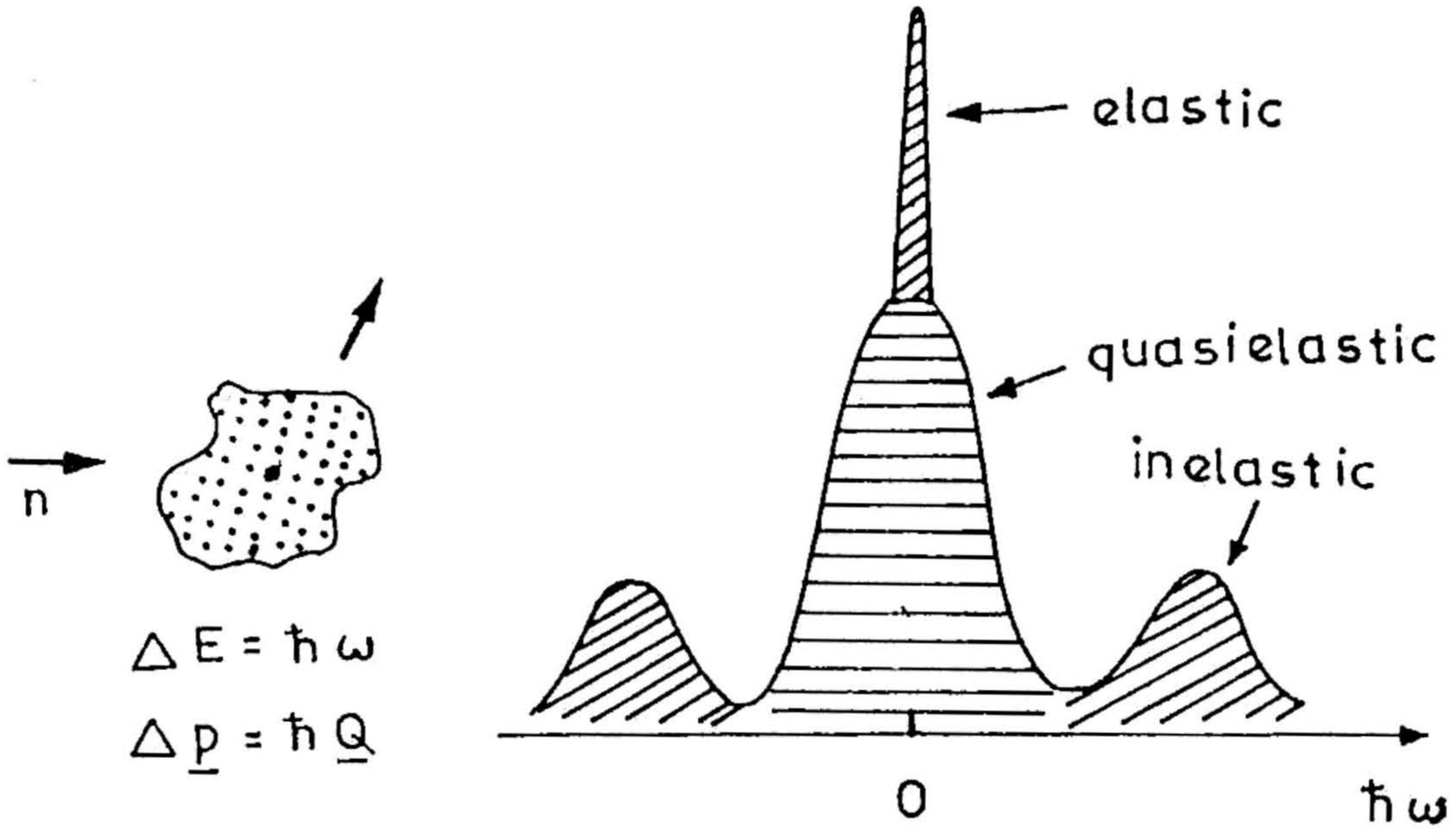

Fig 1 14 Schematic plot of total neutron scattering as a function of energy transfer

(iii) The quasielastic scattering, which is caused by any kind of non-periodic motion.

1 6 2 **EXAFS**

The diffraction techniques and their variants (anomalous scattering, isomorphous and isotopic substitution) are only suitable for binary compounds which are directed by three partial pair-correlation functions (and hence need three separable diffraction experiments to determine them). For systems containing more than two components, only EXAFS is really suitable as a direct structural probe. It has the virtue of being chemically specific, so the average local order around the atomic species which absorbs the X-ray photon is determined.

EXAFS (extended X-ray absorption fine structure) is the result of two fundamental processes. (a) K (or L) - absorption of an X-ray photon which is the photoelectric effect and (b) an effective diffraction of the electron so emitted. In the case of an isolated absorbing atom (absorber) one sees only the characteristic rise in absorption coefficient (absorbance) μ [= ln (I_o/I)], I_o - intensity of incident and I-the reflected beams], at the energy corresponding to the edge and exponential decrease thereafter. When the absorber is surrounded by other atoms, μ exhibits undulations. Thus EXAFS consists of the oscillations, as a function of photon energy in the absorption cross section for the photo excitation of an electron from a deep core state to a continuum state. These oscillations are a final state electron effect, arising from the interference between the outgoing wave function and that small fraction of itself which is scattered back from the near-neighbour atoms. This interference reflects directly the net phase

shift of the backscattered electron, which is predominantly proportional to the product of the momentum of the electron $\vec{k}$ and the distance travelled. The atomic identity of both the excited and backscattering atoms has a more subtle but nonetheless significant effect on the interference. As a consequence, analysis of the EXAFS can yield not only the distance but also the type and number of the nearest neighbors of the excited atoms.

Since EXAFS arises from scattering by the near neighbors of the excited atom species only, a given measurement involves a subset of those pair-correlation functions which are probed in a single diffraction measurement. This is a substantial simplification. In X-ray and neutron diffraction studies of superionic conductors, the complicated diffraction pattern contains both Bragg peaks (or Debye lines) from long-range order and a liquid-like diffuse scattering pattern from short-range correlations. These two contributions are often dominated by the stationary lattice and the mobile-ion/mobile ion correlations, respectively. EXAFS, on the other hand, measures primarily the pair-correlation function of the mobile species with respect to the immobile ions. Thus, the EXAFS technique is especially well suited to determining the path taken by the mobile ions in high conducting phase of SICs.

1.6.3 Light Scattering, Raman, Brillouin and Rayleigh Processes

Light scattering has been used in numerous ways to study both acoustic and optical phonons in solids. The information obtained in superionic conductors by light scattering spectroscopy and an attempt to correlate these results with the data gained by different techniques

have been reviewed by Delaney and Ushioda[53] and Hayes[54] When a beam of monochromatic light, say from a laser, of wavelength ~ 500 nm, strikes a sample most of the incident beam is transmitted as for X-rays About one photon in 10^{14} is inelastically or quasi-elastically scattered and detected The scattering arises from fluctuations in polarizability, caused by local change in the relative permittivity (dielectric constant) of the medium For liquids one can probe density fluctuations and atomic collision processes (because the electron distribution is distorted in the colliding particles) In ordered solids, lattice vibrational i e , phonon modes can be characterized Superionic conductors are more complicated because of the disordered nature of the mobile ion conductors (crystalline) and random network structure (glasses) The scattering processes incorporate some of the features of both liquids and solids which complicates the interpretation Specialized theories are being designed to account for the anharmonic and disordered nature of solid electrolytes

Traditionally Raman scattering refers to the inelastic light scattering from optical phonons and Brillouin scattering, to scattering from acoustic phonons However, in the modern context the distinction is made more on the basis of the magnitude of the accompanying frequency shift of the light and the experimental techniques used in measuring the frequency shift in the scattering process In a Raman scattering experiment one usually measures a frequency shift of 1 cm^{-1} (1 meV = 8 cm^{-1}) or greater by using a grating spectrometer, while in Brillouin scattering the typical range of frequency shift is 10^{-3} cm^{-1} (30 MHz) to 1 cm^{-1} (30 GHz) and a Fabry-Perot interferometer is employed Quasi-elastic light scattering with a frequency shift less than a few

tens of MHz is referred to as Rayleigh scattering, and here the standard method of spectrum analysis is a photon beating technique

From light scattering experiments one determines the energy, momentum, lifetime, and symmetry of an elementary excitation The energy ($\hbar\omega$) and momentum ($\hbar k$) are obtained from the difference ($\omega = \omega_i - \omega_s$) between the frequency of the incident light (ω_i) and the scattered light (ω_s) and the difference in the wave vector ($\vec{k} = \vec{k}_i - \vec{k}_s$) The lifetime τ is the inverse of the spectral linewidth Γ The symmetry of an elementary excitation is found from the polarization selection rules of the scattering process, that is, the scattering intensity is finite only for certain combinations of the polarization of the incident light ($\vec{e}_i$) and the scattered light ($\vec{e}_s$) The coupling constant of the elementary excitation to the incident photons, which determines the scattering intensity, is an important parameter in light scattering experiments

1.6.4 Nuclear Magnetic Resonance

NMR is sensitive to the nature of chemical binding and symmetry NMR studies are of use principally in the field of ionic glasses through the quadrupolar interactions The solid state (high resolution) NMR studies, in which resolution comparable with liquid state NMR is achieved by 'magic-angle' spinning, will be critical in resolving the controversies concerning chemical environment and mobile ion fractions

NMR absorption occurs when the energy of the applied magnetic field matches that of an allowed transition between energy levels of the nuclear magnetic moment Quadrupolar effects arise in those nuclei with spin values greater than 1/2 The interaction of this dipole moment with

any electric field gradient existing at the nuclear site alters the spacing of the magnetic energy levels The electric field gradients in turn are sensitive to charge distributions around the nuclei; this distribution is a sensitive function of the local structure and bonding[55] Not only does NMR technique clearly distinguish between the various chemical environments such as tetrahedral and octahedral coordinations of probed nucleus, but tetrahedral sites with different second nearest neighbours may also be revealed in the right conditions Furthermore, the presence of a microscopic crystalline fraction can be detected in partly devitrified samples by the line shape analysis due to the narrow band characteristic of the ordered phase

1 7 STRUCTURE OF GLASSES

A thorough understanding of the microscopic structure of glasses is a prerequisite for explaining their physico-chemical properties including their mechanical and thermal stability, ionic diffusion and conductivity and their temperature and concentration dependences. According to Ingram et al.,[56] 'ignorance of conduction mechanism in glass stems largely from an ignorance of glass structure'. Indeed, the various proposed models of ionic conduction in glass invariably invoke some structural model or the other in order to describe the gross environment in which the ion transport occurs. Thus it is appropriate to discuss briefly the structure of important glass-forming oxides

1 7 1 Vitreous Silica

The random network proposed by Zachariasen[42] still probably the best description for the structure of fused SiO_2 is supported by the X-ray diffraction results. The structure is built up of corner-sharing

SiO_4 tetrahedra which link up to form an infinite three-dimensional network that lacks symmetry or long range order In order to maintain electro-neutrality, each corner oxygen is shared between only two tetrahedra and consequently the structure is rather open

The X-ray powder diffraction pattern of a glass is very diffuse, consisting of broad humps rather than sharp peaks, compare the X-ray powder diffraction patterns of vitreous and crystalline cristobalite (Fig 1 15) A radial distribution curve for vitreous SiO_2 is given in Fig 1 15c in which the probability of finding a second atom is represented on the ordinate by a pair distribution function The straight line gives the results expected for a hypothetical material that consists of a random array of non-interacting point atoms The large peak in the SiO_2 curve at 1 62 Å and the second, smaller peak at 2 65 Å correspond to silicon-oxygen and oxygen-oxygen distances in SiO_4 tetrahedra These values are similar to those found in crystalline SiO_2 and in silicates These first two peaks are reasonably narrow in Fig 1 15, because the corresponding distances are approximately constant in both glasses and in crystals, i e the SiO_4 tetrahedra are not distorted The other peaks, however, are increasingly broadened since a spread of corresponding distances is present in the glass The third peak at ~ 3 12 Å represents the nearest silicon-silicon distance, i e , the distance between the centers of two SiO_4 tetrahedra Since the Si-O-Si angle varies somewhat as the tetrahedra are twisted or rotated in various ways relative to each other, there is a spread in values of the silicon-silicon distances Other peaks are assigned as follows ~4 15 Å -silicon to second oxygen ~ 5 1 Å-combined peak for oxygen to second oxygen and silicon to second silicon No clear peaks are observed

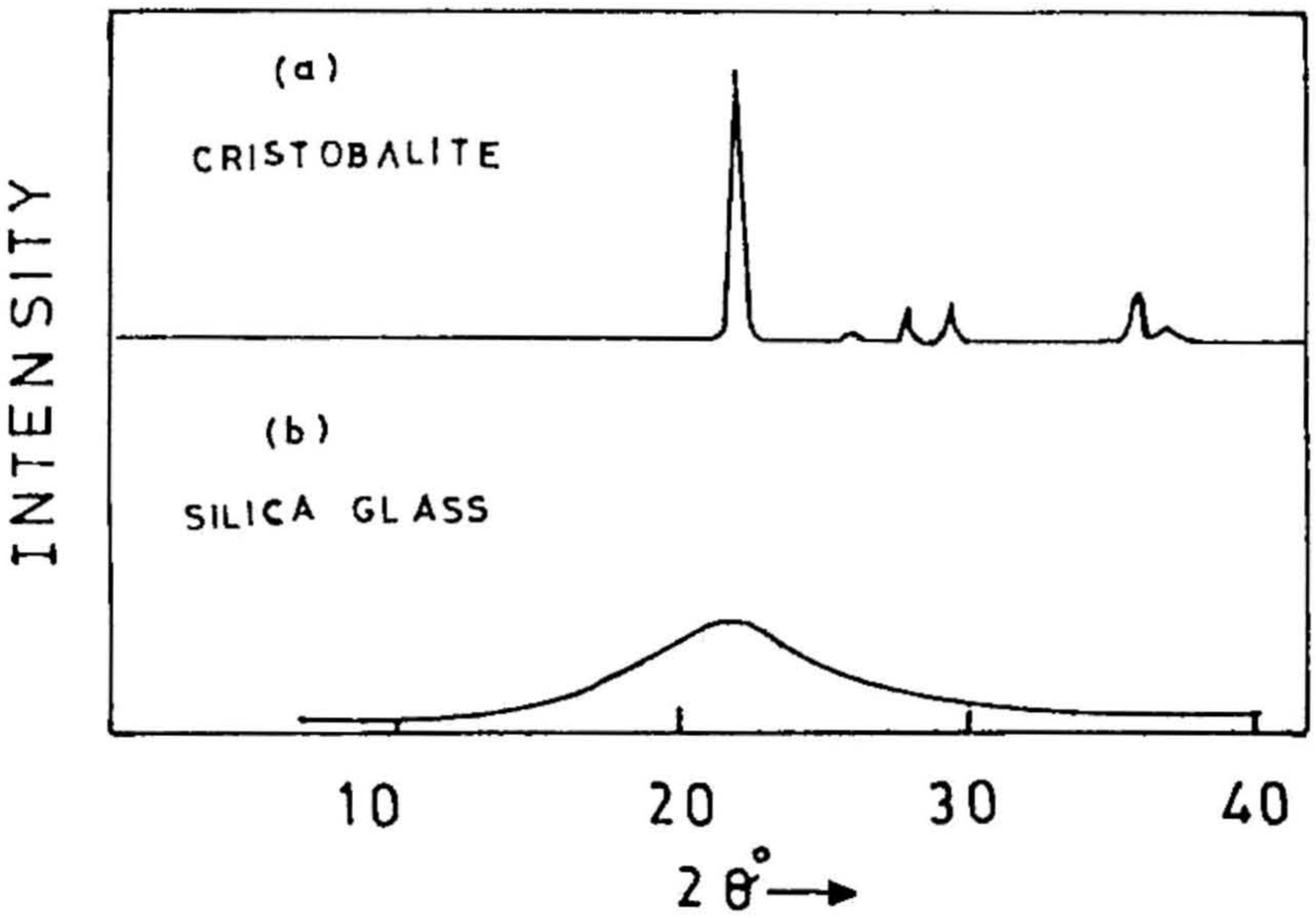

Fig 1.15 X-ray powder diffraction pattern of (a) cristobalite and (b) glassy SiO_2

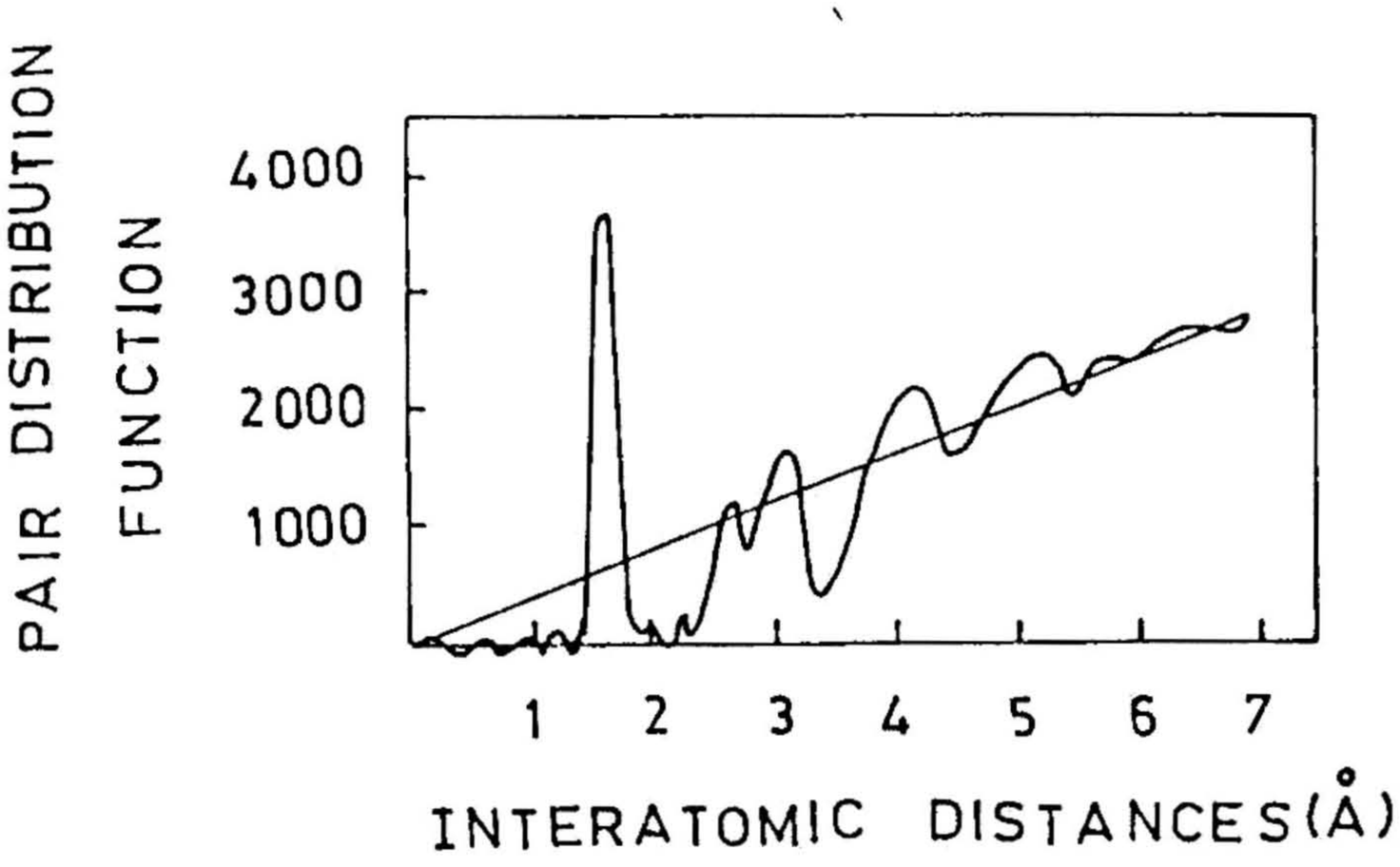

(c) X-ray diffraction results for SiO_2 glass (From Mozzi and Warren[57])

beyond 6 to 7 Å and this is consistent with a random network model for the structure of vitreous SiO_2

1 7 2 Silicate Glasses

The structure and properties of binary silicate glasses depend very much on the nature of the second oxide With network modifying oxides such as alkali and alkaline earth oxides, the silica network is gradually broken up as more of the second oxide is added Viscosity decreases with increasing modifier and thermal expansion increases As extra oxide ions are added to SiO_2, Si-O-Si bridging linkages are cleared to give non-bridging oxide ions (Fig 1 16) The oxygen linked to two silicons are called bridging oxygen while those attached to only one are non-bridging

By the time that the ratio (second oxide to silica) has increased to 1 2 (e g , as in $Na_2O\ 2SiO_2$ or $Na_2Si_2O_5$), the silicon to oxygen ratio has decreased to 1 2 5 For every SiO_4 tetrahedron, this means that, on average, one of the four corner oxygens must be a non-bridging oxygen In crystalline silicates of this formula, e g $Na_2Si_2O_5$, the silicate anions are usually infinite two-dimensional sheets in the glass, small pieces of sheet anion may also be present but it is more likely that an open three-dimensional framework structure exists and the cations, Na^+, etc , occupy relatively large holes in the framework

The distribution of the cations such as Na^+ is not entirely random as there is some evidence from X-ray diffraction studies that the cations may cluster together The significance of this is not well understood It could be simply that the arrangements of available holes

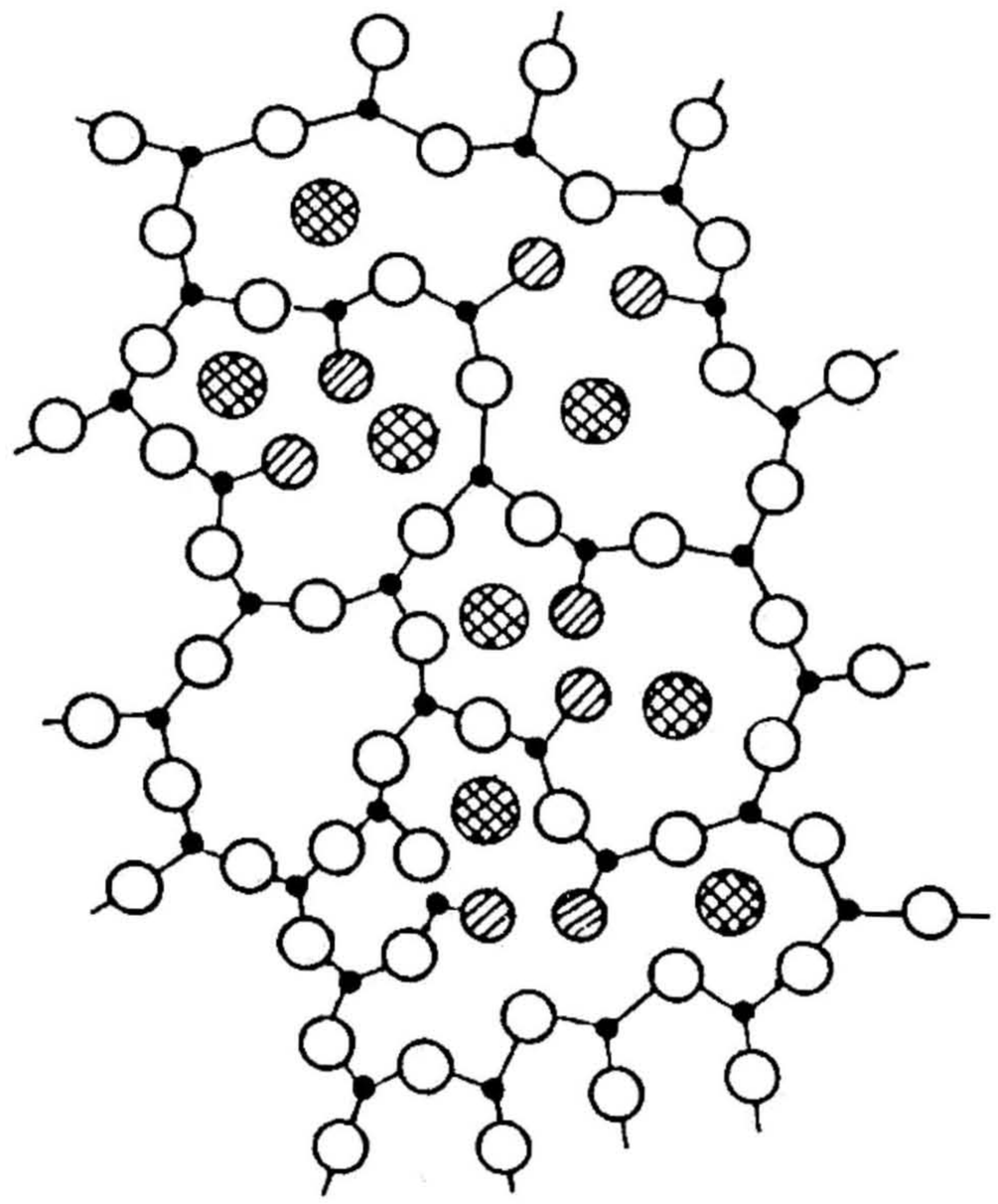

● Silicon ion

Sodium ion

○ Bridging oxygen ion

Non-bridging oxygen ion

Fig 1 16 Two-dimensional representation of the structure of soda-silica glass (The structure is shown in a simplified form since only three of the four oxygen ions surrounding each silicon ion are depicted)

in the glass network is not random, an alternative possibility is that there is some kind of attractive cation-cation interaction, presumably also involving oxide ions, which leads to clustering

As the amount of second oxide is increased further, the silica network breaks up even more, the melts become more fluid and the tendency to devitrify on cooling increases. Usually by the time the ratio (second oxide silica) is 1 1, it is difficult, if not impossible, to retain the liquids as glasses on cooling

1.7.3 Vitreous B_2O_3 and Borate Glasses

Initially a random network of planar BO_3 triangles was proposed for B_2O_3 glass, with oxygen situated at the corners of the triangle. These units were joined randomly as the corners and ring structures of variable members were generated. But the model was unable to explain many physical properties, particularly the great difference in viscosity from that of fused silica

At present the interpretation offered by Krogh-Moe[58a,58b] is consistent with the available structural information. Boroxyl groups-(Fig. 1.17(A)) alternating boron and oxygen atoms on a planar six-membered ring-are linked randomly to give a three-dimensional network. The three-fold coordination of boron agrees with NMR results[59a,59b]. From the X-ray diffraction measurements, the radial distribution curves of B_2O_3 glass give peaks at 1.37 and 2.40 Å, these correspond to B-B and O-O distances of BO_3 triangles, (these distances differ from those in crystalline borates that contain BO_4 tetrahedra and in which, for instance, the B-O distances are larger, 1.48 Å). The most

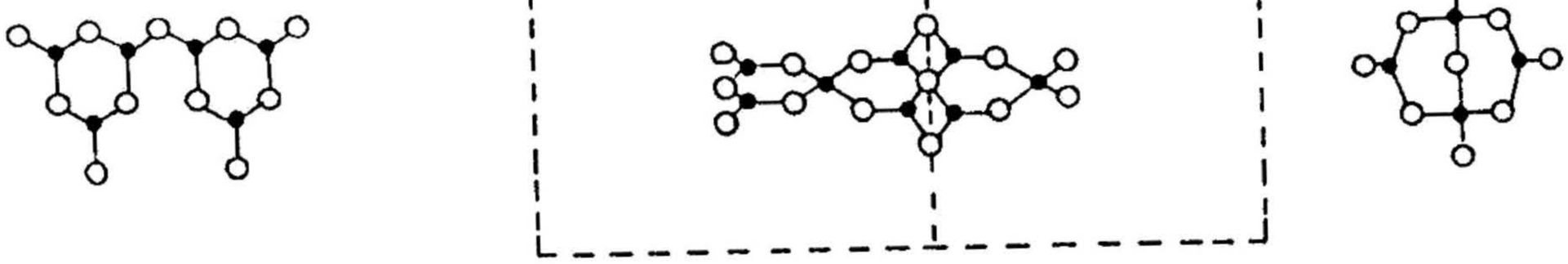

Fig 1.17 A Structural units in borate glasses (a) boroxol group (b) pentaborate, (c) triborate, (d) diborate (from Krogh-Moe[58a])

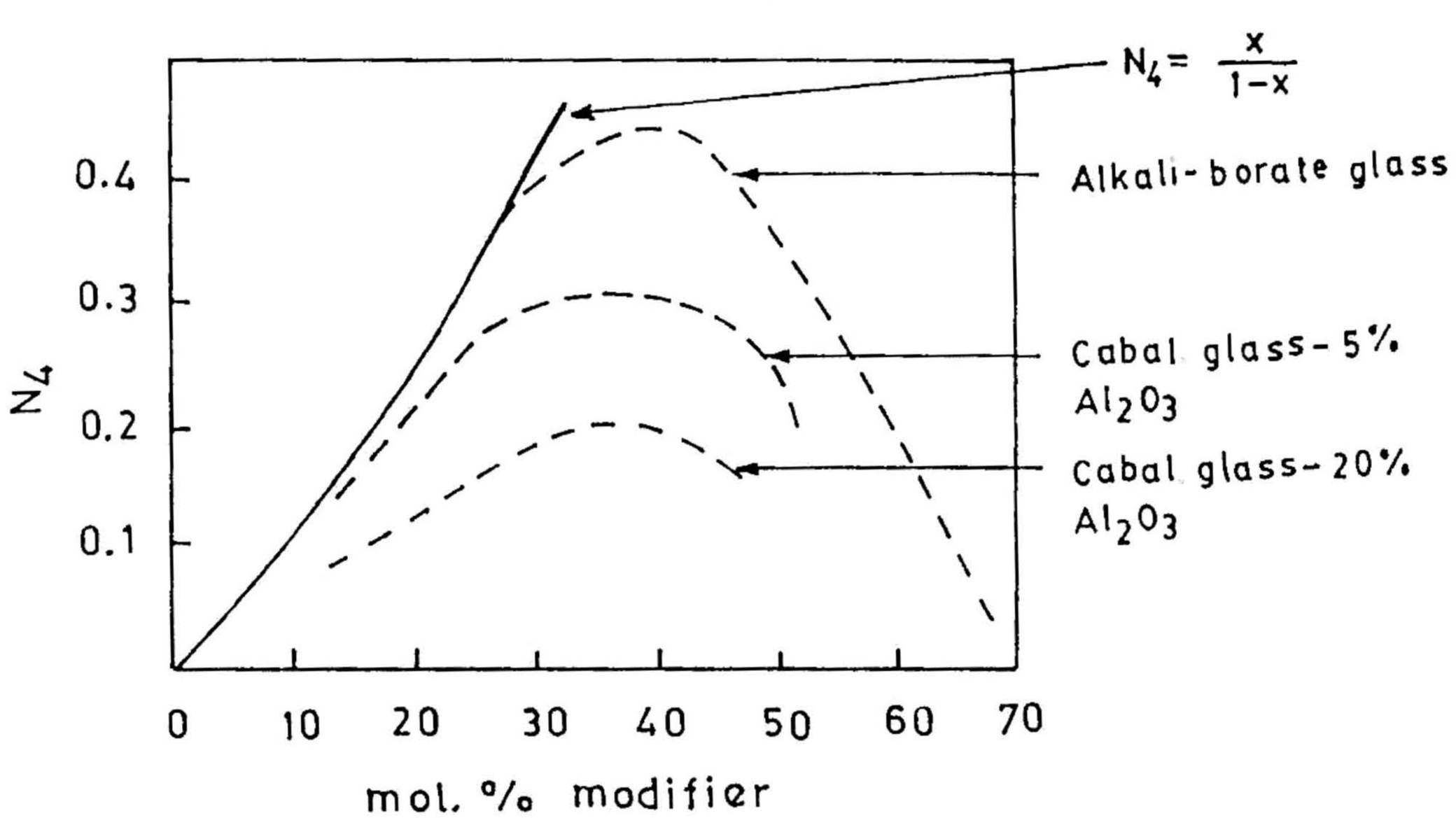

B Number of four-coordinate borons in alkali-borate and calcium alumino-borate glasses

recent X-ray and neutron diffraction studies further substantiate the model that about 0 75 of the B atoms are members of boroxyl group and the rest are in BO_3 triangles attached randomly to the group[60] As temperature increases the number of boroxyl rings decreases and the structure approaches a random network of BO_3 triangles Most properties including viscosity, are attributable to this model

Addition of alkali oxide to vitreous B_2O_3 gives rather different results to those obtained in the corresponding alkali silicates and an effect known as the boron oxide anomaly is observed In the system Na_2O-B_2O_3 for example, the viscosity of the melt increases with increasing soda content and passes through a maximum at ~ 16 mole% Na_2O The coefficient of thermal expansion of the glasses decreases with increasing Na_2O content and passes through a minimum at 16 mole% Na_2O Other properties also show either maxima or minima around this composition By contrast, the alkali silicates become more fluid their coefficient of thermal expansion increases steadily with increasing alkali content and no maxima or minima in properties are observed

Bray[59b] has shown, using B^{11} NMR spectroscopy that a gradual change in the coordination number of boron from three to four occurs as the alkali oxide is added The number of four coordinated borons (N_4) is given by

$$N_4 = \frac{x}{1-x}$$

where x is the mole fraction of alkali oxide N_4 increases more slowly until reaching a maximum of ca 45% for 35% < x <45% depending on the alkali oxide after which N_4 starts decreasing, and BO_3 starts forming

with non-bridging oxygens At yet higher concentrations N_4 decreases sharply and approaches zero at 70 mole%

IR spectra have been interpreted by Krogh-Moe in terms of structural units present in the glass (Figs 1 17 b-d) The alkali additions initially form triborate and pentaborate groups Near x = 20 mole%, diborate groups begin to form and increase in number (at the expense of triborate and pentaborate units) with increasing alkali content At 33% alkali the structure consists mainly of interpenetrating diborate networks This model explains the monotonic increase of N_4 upto 33% alkali as well as the IR spectra Two types of BO_3 groups are observed[59a] in the NMR spectra for 10% <x< 30% This model suggests that these could arise from the pentaborate and triborate units

The MD calculations[61] of Ag_2O-B_2O_3 glasses have established that the $BO_3 \longrightarrow BO_4$ conversion follows the relation x/1-x where x is the molar fraction of Ag_2O, and, these two groups are connected by the bridging oxygens At Ag_2O contents ≥ 20 mole% BO_4 showed a tendency to decrease and BO_3 with non-bridging oxygens appeared However these calculations found no evidence for the diborate, triborate, and pentaborate groups in the glassy network As a consequence it was argued that the BO_3 and BO_4 units are linked in rings, or arrangements involving more than six units

The effect of aluminum on the structure of 'cabal' glass (calcium boroaluminate) is shown in Fig 1 17(B) which plots N_4 as the ordinate The aluminum is four coordinated and deprives the boron of its oxygen so

that the number of BO_4 decreases, as a result the number of BO_3 groups increases with NBOs, with increase in aluminum content

1 7 4 **Tellurite Glasses**

Recent neutron scattering experiments[62] have established that the structural unit making up the TeO_2 glass is a (TeO_{3+1})-distorted tetrahedron in which three oxygen atoms are bound to a central tellurium atom with the bond length of r = 1 95 Å, and the remaining oxygen atom is located at the position of r = 2 18 Å, far from the tellurium atom Upon the addition of a modifier oxide such as Li_2O Na_2O, BaO etc , the average coordination number of oxygen atoms surrounding of a tellurium atom has been found[52] to decrease monotonically from four to three This behaviour is remarkably different from those for B_2O_3, SiO_2 and GeO_2 glasses as may be observed from Figs 1 18 a and b A broken line in Fig 1 18 b means that one unit of (TeO_{3+1}) tetrahedron is modified into one unit of (TeO_3)-trigonal pyramid with the formation of one non-bridging oxygen atom as one unit of BaO/Na_2O is added into the glass

1 8 IONIC TRANSPORT IN GLASSES

The ionic character of the conductivity in oxide glasses was established in 1884, when Warburg[63] demonstrated the transport of sodium between two amalgams separated by a thuringer glass, by the application of a DC voltage across the glass envelope Glasses that are found to be superionic conductors, acquire this property through the alkali cations Li^+, Na^+, K^+ or Ag^+, $Cu^+$and have a simple composition with a network-forming oxide (SiO_2 B_2O_3, P_2O_5 etc) and a network-modifying oxide (Li_2O, Na_2O, K_2O, Ag_2O, Cu_2O) Glasses offer a

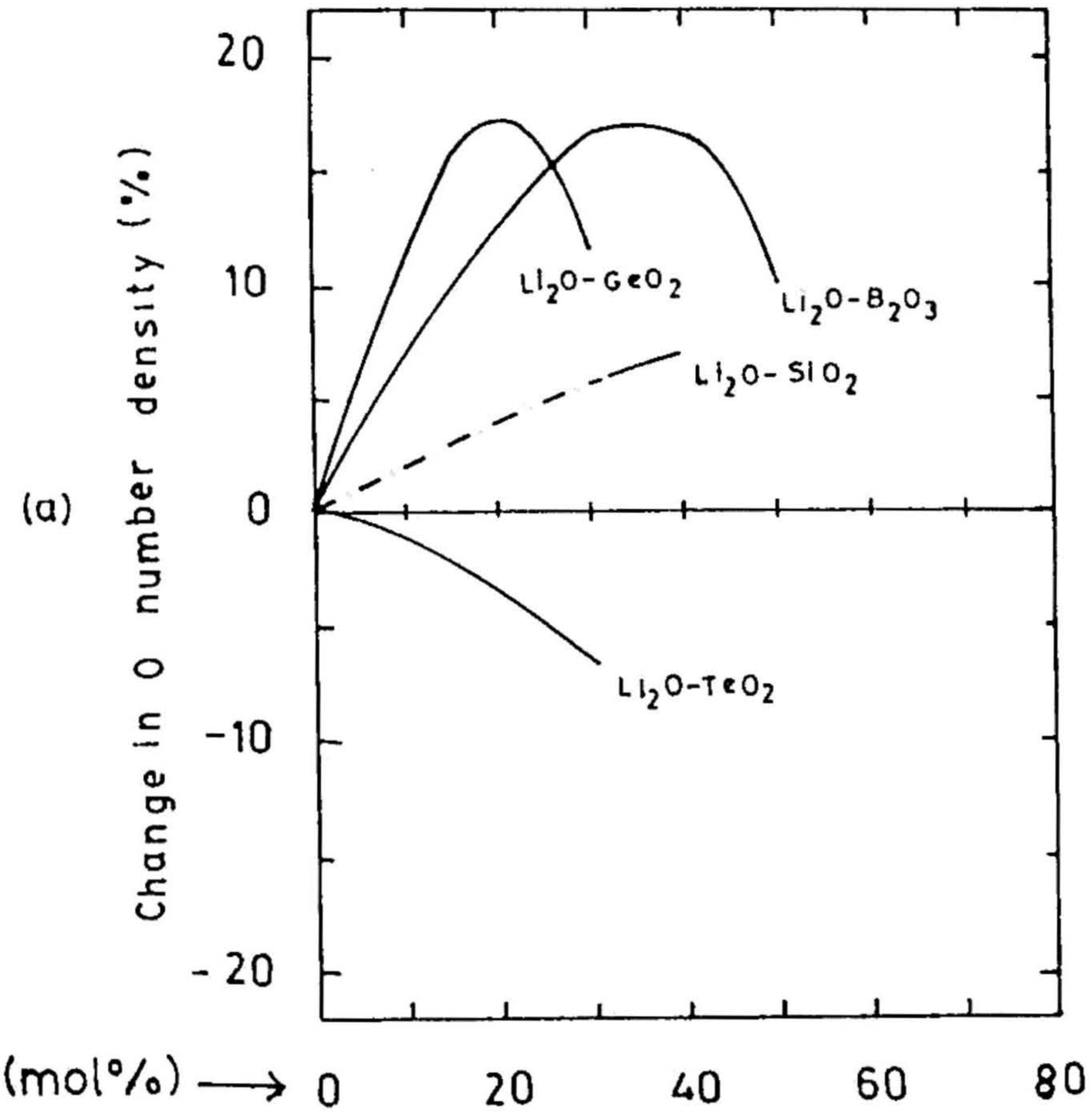

Fig 1 18(a) Number densities of O atoms in Li_2O-SiO_2, $Li_2O-B_2O_3$, Li_2O-GeO_2 and Li_2O-TeO_2 glasses A dotted line for Li_2O-SiO_2 glass means the region of phase-separation

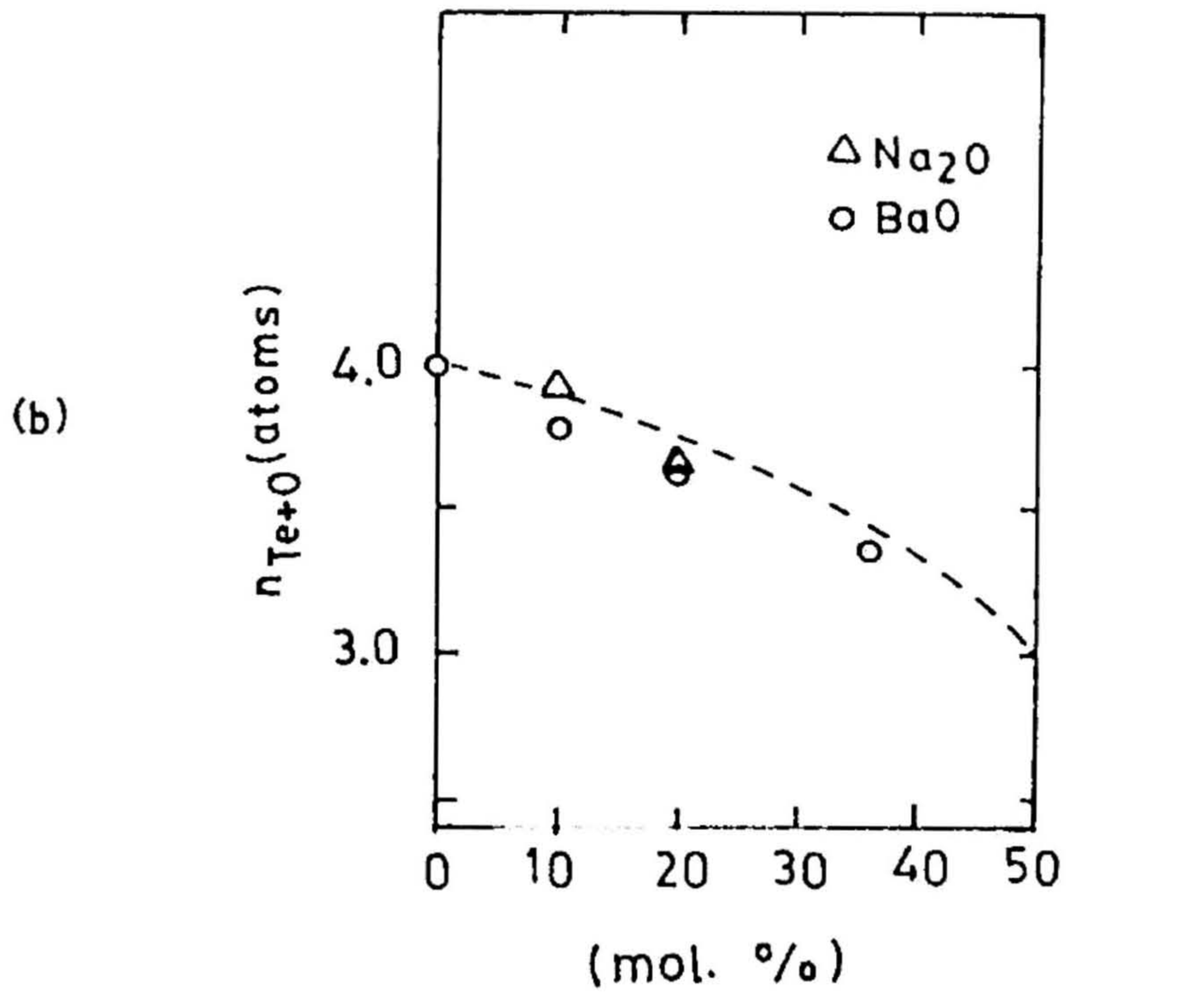

(b) Coordination number of O atoms bound to a Te atom in Na_2O-TeO_2 and $BaO-TeO_2$ glasses (from Suzuki[62])

larger number of advantages over crystalline electrolytes including physical isotropy absence of grain boundaries, continuously variable composition, ease of thin film formation for device application and good stability

1 8 1 Glass Exhibiting Fast Ion Conduction

(a) Silver Conductors

Highly conducting Ag^+ glasses have been prepared in two ways (1) from pseudobinary systems such as $AgI-Ag_2MoO_4$, $AgI-Ag_2CrO_4$ and $AgI-Ag_3AsO_4$ where the silver oxy-salts are not themselves glass formers, (2) by adding AgI to mixtures of Ag_2O and traditional glass formers such as B_2O_3, V_2O_5, GeO_2 and P_2O_5 (or to mixtures of Ag_2S with P_2S_5 As_2S_3, GeS_2 etc)

Minami et al [64-66] reported greatly enhanced conduction in silver borate glasses when Ag_2O modifier was replaced by AgX (X = I, Br, Cl) It is worth noting that in glasses containing AgBr and AgCl instead of AgI their conductivities are very high, in spite of the low conductivity of constituents (compare the conductivity values in Fig 1 for crystalline AgCl and AgBr)

Minami explained the enhanced conductivity by postulating the existence of two distinct populations of Ag^+ ions mobile ions associated with the AgI and BO_4 networks, and immobile ions linked with the non-bridging oxygens of BO_3 groups due to the strong partial covalency existing in them

Fig 1 19 shows the composition dependence of the conductivity at 25°C in selected oxide - and sulphide - based glasses as a function of AgI content[67] In each case the conductivity rises steeply with addition of AgI Even though the base glasses are so different it is remarkable that the limiting conductivities are nearly the same (about 10^{-2} S cm^{-1}) In these optimized conductors Ag^+ ion migration is thought to proceed along diffusion paths between loosely packed I ions much as in α-AgI Broadly speaking the incorporation of oxyanions interrupts the path and decreases the mobility of Ag^+ ions[68]

On the other hand neutron diffraction in combination with other experimental techniques (Raman scattering, NMR, mechanical relaxation) strongly indicate a fractal percolating network within the host glass which serves as a conducting pathway for the Ag^+ ions [69-71] Thus there is an on-going debate concerning the details of the ion transport mechanisms the clustering of AgI microdomains versus the existence of mobile and immobile Ag^+ cations This aspect is discussed further in Chapter 7

(b) **Alkali Glasses**

Tuller and Coworkers extensively summarized the transport properties of superionic conducting 'alkali' glasses in a few review articles[72 73] In alkali borate glasses they established that the observed ionic conductivity decreases in the order $\sigma_K < \sigma_{Na} < \sigma_{Li}$ Also as a general rule the conductivity of alkali oxide glasses (borate silicate etc) increases considerably with an increase in the content of the network modifier such as Li_2O, Na_2O and K_2O However the molar ratio of modifier to former oxides cannot be increased indefinitely **In**

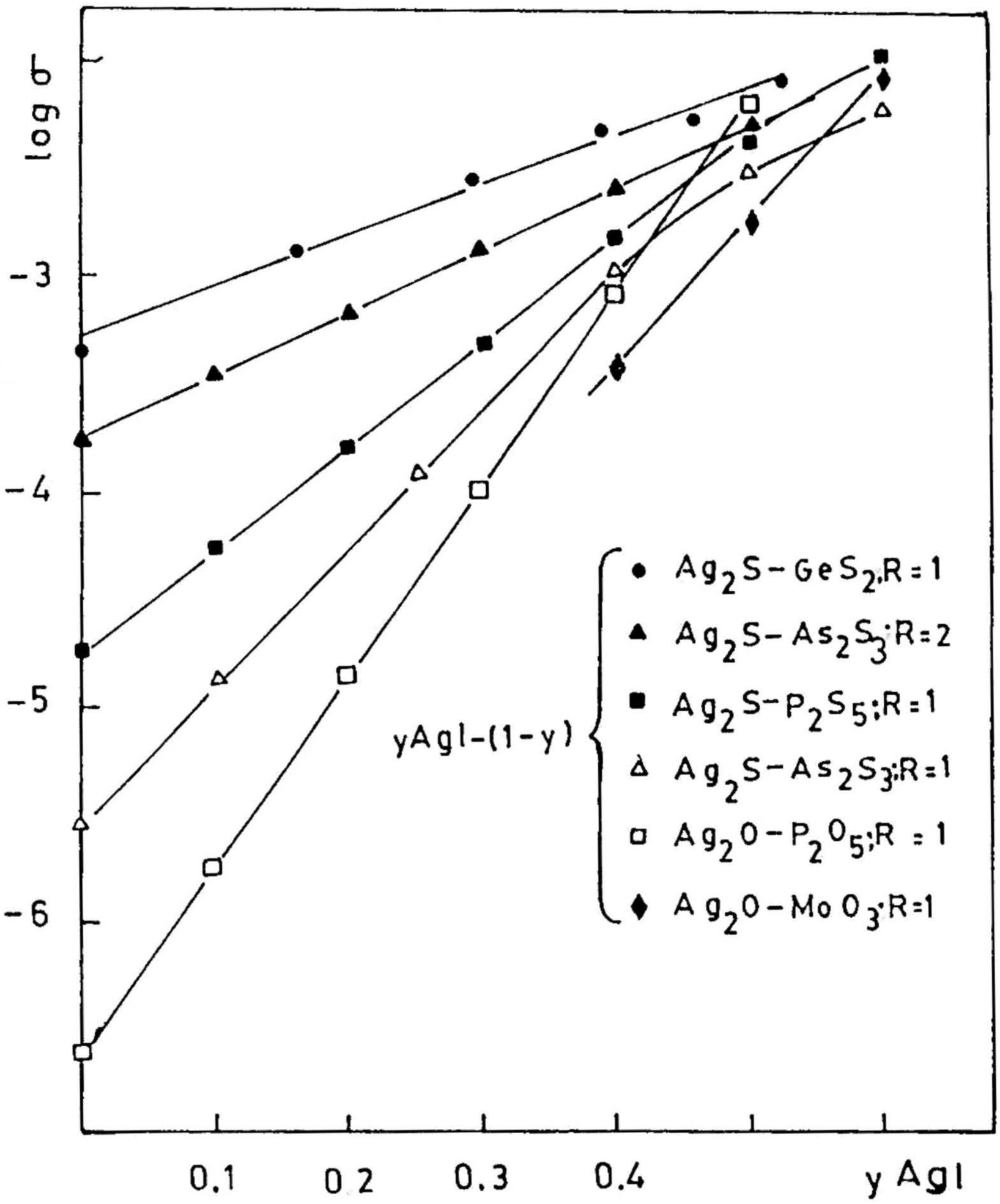

Fig 1.19 Electrical conductivity in various oxide and sulphide based glasses as a function of AgI content

fact, the mean length of macromolecular chains in these glasses formed by structural units such as SiO_4, BO_4, BO_3 etc , diminishes rapidly with the above ratio and it becomes increasingly difficult to obtain a glass under normal quenching conditions Dissolving alkali halides (LiCl, NaCl) by partial replacement of alkali oxide (Li_2O, Na_2O etc ,) can avoid this difficulty and will increase the concentration of alkali cations Lithium halo borate glasses containing F, Cl, Br and I were synthesized and characterized by Levasseur and coworkers[74,75] They found that conductivity increased with total Li^+ content (see Fig 1 20a) and observed the largest conductivity enhancement upon addition of LiI to form B_2O_3-0 56 Li_2O-Y LiI glasses, although the utility of LiI addition was limited by the low solubility of LiI in the vitreous matrix Fig 1 20a also illustrates the role played by the diffusion path Clearly the conductivity of B_2O_3-0 56 Li_2O- Y LiX glasses (X = halogen) increases with increasing size of X, which enlarges the diffusion paths[76]

The alkali ion conductivity increases (and the activation energy decreases) with the covalent character of the matrix Fig 1 20b established by Levasseur et al ,[77] shows that the conductivity of the B_2X_3-0 50 Li_2X-0 10 LiI glass increases when the B-O bonds give place to B-S bonds in the glass network The corresponding activation energy decreases Li^+ conductivity despite stronger binding to the matrix trespasses that of Na^+ due to the smaller size of the mobile ion, which makes easier the diffusion process through the glass (conductivity at RT exceeds 10^{-3} S cm^{-1}) Thus covalency and steric hindrance are in competition in amorphous materials Certain other optimum Li^+

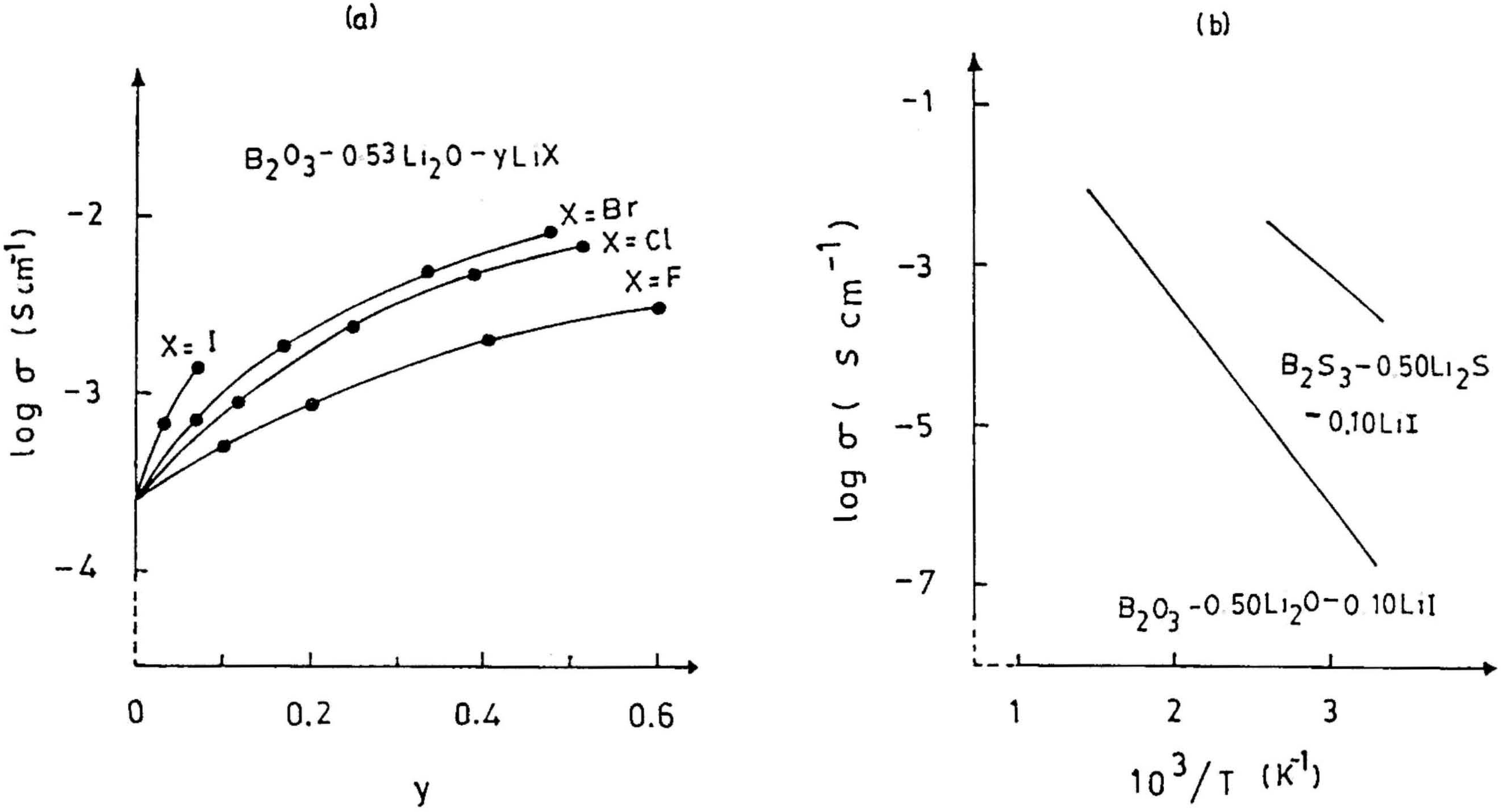

Fig 1.20a Variation of conductivity at 300°C versus LiX content in B_2O_3-0.53 Li_2O-y LiX (X=F, Cl, Br, I)

1.20b Comparison of log σ versus $10^3/T$ curves for two homologous oxide and sulphide glasses

conductors are lithium silicate doped with Li_2SO_4 [78,79] and complex Li_2O-LiF-$Al(PO_3)_3$ [80] and Li_2O-LiF-Li_2SO_4-B_2O_3 [81] mixtures

1.8.2 Microscopic Models

The microscopic description of the conduction mechanism expressed by Eqn 8 cannot account for the large variation observed for glass conductivities with composition. A number of models have been proposed to account for various aspects of ionic conduction in glasses, in particular, the behaviour of DC conductivity activation energy E_a. Extensive reviews of these have been given by Ingram[82] and Tuller[73]. Three of these models are briefly discussed below.

(a) Anderson and Stuart Model

Anderson and Stuart[83] considered the activation energy (E_a) for DC conductivity (or the diffusion coefficient) as the sum of two terms (1) the electrostatic binding energy E_b required to remove a cation from the host network and (2) the strain energy E_s associated with the long-range mobility (gate passing). Thus

$$E_a = E_b + E_s \tag{19}$$

Here polarization effects are presumed small in the case of alkali mobile cations and are thus neglected.

The electrostatic term E_b has the form

$$E_b = -(1-1/m)\ A\ Z\ Z_j\ e^2 \left(\frac{1}{r+r_j} - \frac{1}{\lambda/2}\right) \tag{20}$$

where the factor (1-1/m) comes from the inverse $(r + r_j)^m$ dependence of the repulsive energy as calculated from ionic crystals. A is the Madelung constant, and Z and Z_j are the charges on the two interacting ions. Physically, this energy term represents the difference in energy

of an alkali carrier ion of radius r in its equilibrium position neighboring a non-bridging oxygen of radius r_j and its energy at the 'saddle point" between equipotential sites (sites also coordinated by non-bridging oxygens) separated by the two jump distances However use of Eqn 20 yields values for E_b nearly an order of magnitude too large Anderson and Stuart reasoned that addition of large concentrations of network modifying cations to the glass network distorts the oxygen charge clouds reducing the binding energies considerably They then scaled E_b by a covalency parameter 'γ' whose value they found experimentally to be equal to the measured dielectric constant ε of the glass The modified form of E_b thus obtained is

$$\Delta E_b = \frac{Z Z_j e^2}{\varepsilon} \left[\frac{1}{(r + r_j)} - \frac{1}{\lambda/2} \right] \qquad (21)$$

The strain energy component to the total activation energy, E_s is given explicitly by

$$E_S = 8\pi/2 \; G \; r_D \; (r - r_D)^2 \qquad (22)$$

G = shear modulus

It is assumed that E_s is the strain energy created when a mobile ion of radius r enlarges a 'doorway" or opening between equipotential sites or interstices in the glass network originally of radius r_D so that it can accommodate passage of the mobile ion Anderson and Stuart approximate this energy by the elastic energy needed to dilate a spherical cavity from radius r_D to r and use the formalism developed by Frenkel for a close packed liquid reducing it by a factor of 1/2 to provide better agreement with diffusion data for the more open glass network They found that E_s is fairly insensitive to changes in r_D

except for very large or very small ions and predicted the activation energy for diffusion of inert gases in a number of silicate glasses quite accurately using $r_D = 0.6$ Å

Hakim and Uhlmann[84] introduced a slight modification and modelled the conductivity dependence on alkali modifier content for a series of alkali silicate glasses using the expression for E_a

$$E_a = E_b + E_s$$

$$E_a = \frac{Z Z_j e^2}{\varepsilon} \left[\frac{1}{r + r_j} - \frac{1}{\lambda/2} \right] + 8\pi r_D (r - r_D)^2 f(c/a) \qquad (23)$$

They considered the glass doorway cavities to be more accurately modelled as ellipsoids than as spheres so Eqn 23 includes the factor f(c/a) which depends on the ratio of the minor c, to the major a axis of the ellipsoid. Hakim and Uhlmann recognized that while the cavity shape is not a function of alkali content, molar volume and therefore doorway radius r_D depend on alkali modifier content. They expressed this dependence as $\Delta r_d / r_d = 1/3\ (\Delta V / V_o)$ where V_o is the molar volume of the alkali free glass. Using this formalism, Hakim and Uhlmann found that the strain energy contribution to the total activation energy increased with increasing alkali ion radius with contributions of 80%, 50% and 20% for the Cs, K, and Na silicates respectively.

(b) **The Weak Electrolyte Model**

The ionic conductivity of electrolytes are often expressed by using the relation

$$\sigma = n Z e \mu$$

where n is the number of mobile ions per unit volume, μ the mobility of

ions of charge Ze If all the alkali ions (or silver ions) are equally mobile, then the situation is analogous to the complete dissociation of strong electrolytes in aqueous solution If the number of mobile ion is less than the stoichiometric concentration, then such glasses can be regarded as weak electrolytes

Weak electrolytes theory introduced by Ravaine and Souquet[85,86] considered the conductive glasses as solid solutions in which the network former components behave as weakly dissociated electrolytes obeying the following dissociation equilibria

$$M_2O = M^+ + OM^- \tag{24}$$

implying

$$[M^+] = K^{1/2}\, a_{M_2O}^{1/2} \tag{25}$$

where (M^+) is the concentration of dissociated ions, K-the dissociation constant (independent of concentration) and a_{M_2O} the thermodynamic activities of the corresponding glass components Although this approach does not provide any description of the physical state of these species, M^+ may be regarded as dissociated 'free' alkali (or silver) ions, M_2O as hopped entities and OM^- as vacancies in the vicinity of non-bridging oxygens Since only M^+ are able to move under an applied electric field, it is tempting experimentally to correlate the conductivity variations to those of thermodynamic quantities This has been done on different silica glasses where the ratios of the thermodynamic activities of two different glass compositions have been obtained from concentration cell EMF measurements Fig 1.21 shows a plot of these ratio versus the corresponding ratios of the electrical conductivities for various pairs of glasses On logarithmic scale, they fit a linear relationship according to

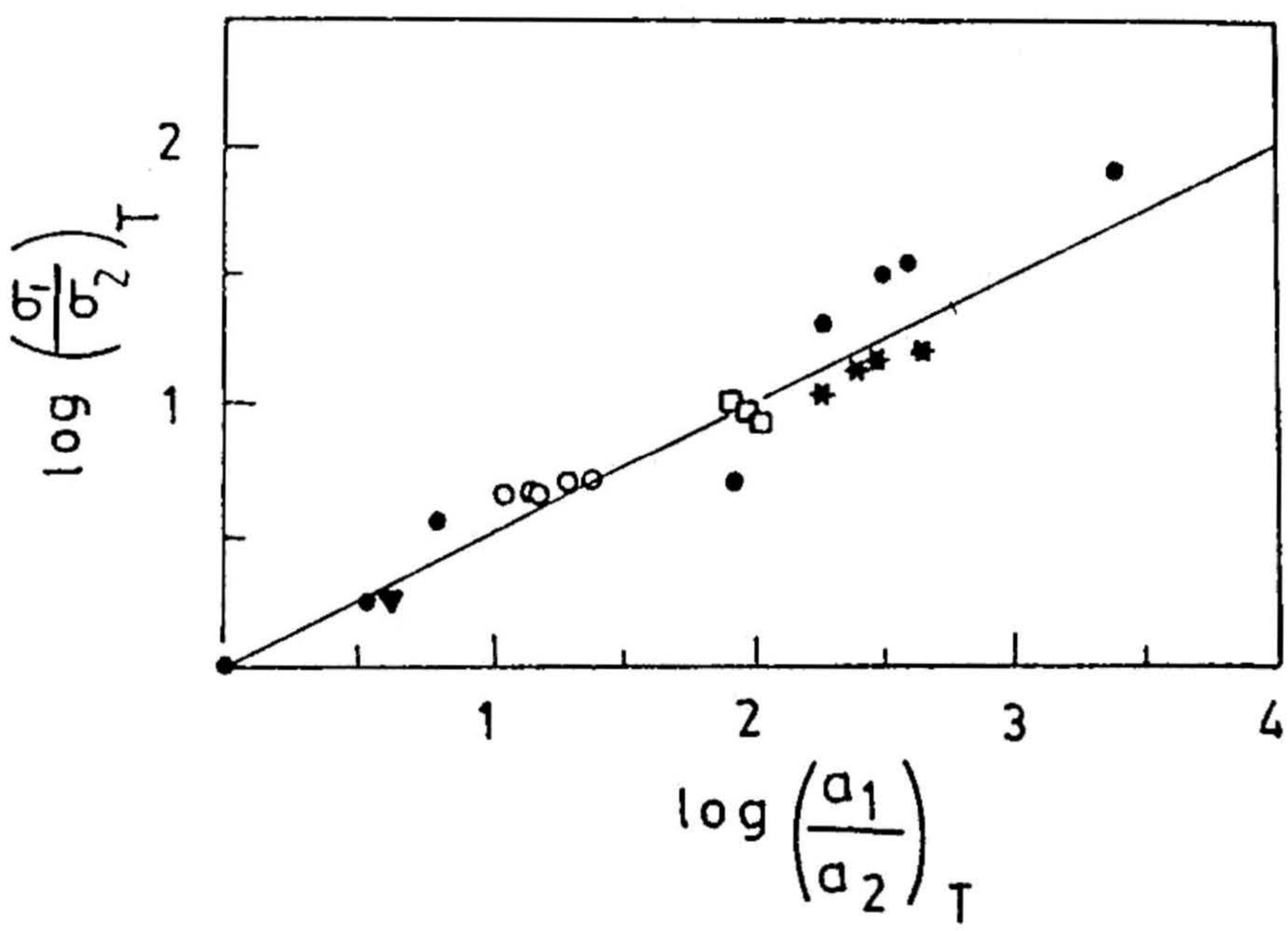

Fig 1.21 Conductivity ratio versus activity ratio for various pairs of glasses[86]

$$\sigma_1/\sigma_2 = \left[a^{(1)}_{M_2O} / a^{(2)}_{M_2O} \right] \qquad (26)$$

As a consequence of Eqns (24) and (25), relation (26) suggest that the mobility of the free ion is independent of glass composition and hence structure The change in conductivity with composition is thus controlled by the charge in the carrier concentration

(c) **Random Site Model**

In the random site model[87] all alkali (or silver) ions are treated as potentially mobile carriers and no distinction is made between mobile and immobile species Instead, there exists a wide Gaussian distribution of alkali ion sites of differing free energy Such a Gaussian distribution of activation energies was found by Wapenaar and Schoonman[88] for disordered fluoride ion charge carriers in fluorite structured solid solutions with a width ρ ($\rho = \rho_o (x)^{1/2}$) where x-is the excess fluoride ion concentration Thus the mobility varies with the distribution of activation energies and thereby with the glass composition In general the variation of carrier concentration is relatively small and thus the change in conductivity with composition is mainly controlled by the change in the mobility

1.8.3 Structural Models

(a) **Minami's Structural Model**

A structural model (see Fig 1.22) for the $AgX-Ag_2O-B_2O_3$ glasses was proposed by Minami et al.,[64] based on the functional dependence of σ_{RT} on the concentration of the total Ag^+ or of AgX. According to them there are three types of Ag^+ ions type I ions are bonded to the non bridging oxygens of the BO_3 group with strong partial covalency,

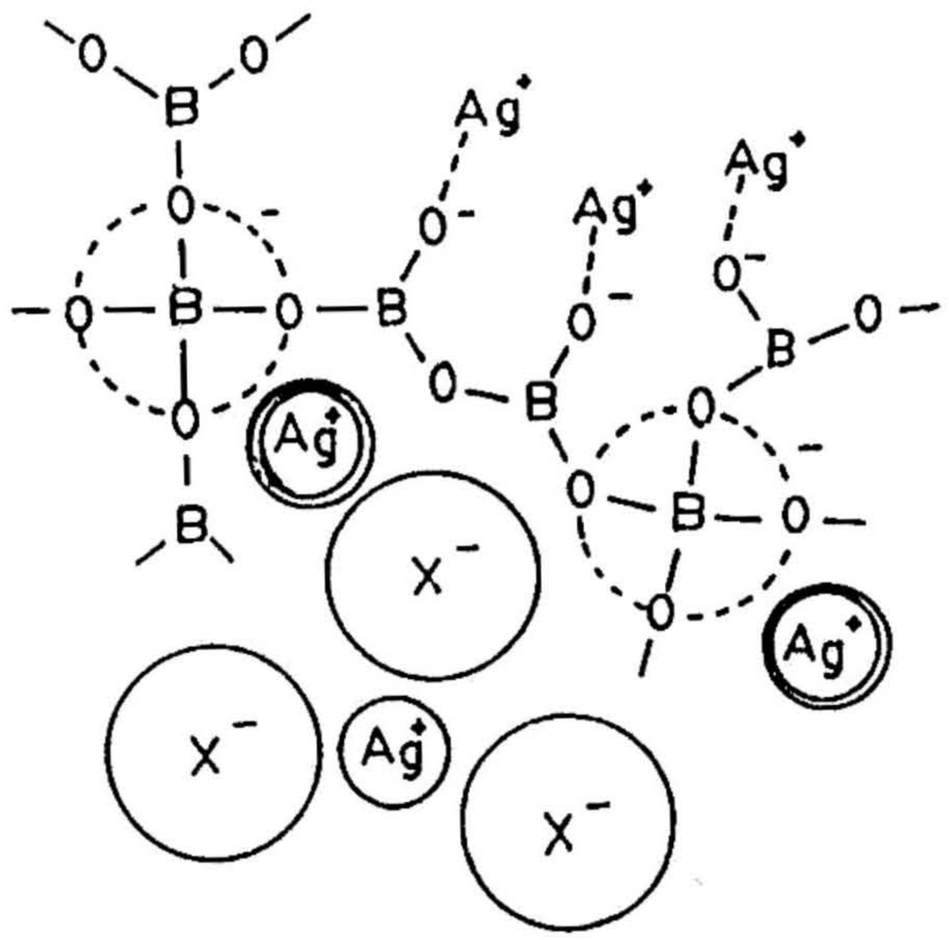

Fig 1.22 Two-dimensional representation of glass structure in the systems $AgX-Ag_2O-B_2O_3$ where X = I, Br (from Minami et al [64])

type II ions interact weakly with the oxygens of BO_4 group and type III ions are surrounded by I^- ions From their conductivity data it was suggested that the latter two types (II and III) of Ag^+ ions contribute to the conductivity and thus it was established that mobile Ag^+ ions responsible for superionic conduction in these glasses come from both AgI and Ag_2O constituents

(b) **Modified Random Network Model**

A pictorial representation of the structure of glass might look- in the light of modern knowledge - like the 'modified random network' model of Greaves[89] (Fig 1 23) This is described by islands of network which separate narrow conduction channels providing the pathways along which ion migration occurs The transport path for mobile ions in the ionic glasses is defined by the location of the non-bridging (negatively charged) anion sites Furthermore as the concentration of mobile cations is increased, the glassy matrix in general undergoes a progressive depolymerization of the network as bridging anions are converted into non-bridging sites Well defined channels appear which are bordered by non-bridging anion sites, at a certain composition of mobile ions, fractal percolation paths involving such channels becomes established throughout the structure, thereby facilitating steady-state diffusive (DC) transport

(c) **Chemical Approach**

Very recently, a chemical approach has been made by Rao and coworkers[90a,90b] to investigate the origin of superionic conduction in a number of AgI based glasses, with the general formula $AgI-Ag_2O-M_xO_y$ (M_xO_y = MoO_3, SeO_3, WO_3, V_2O_5, P_2O_5, GeO_2, B_2O_3, As_2O_3 CrO_3) An index

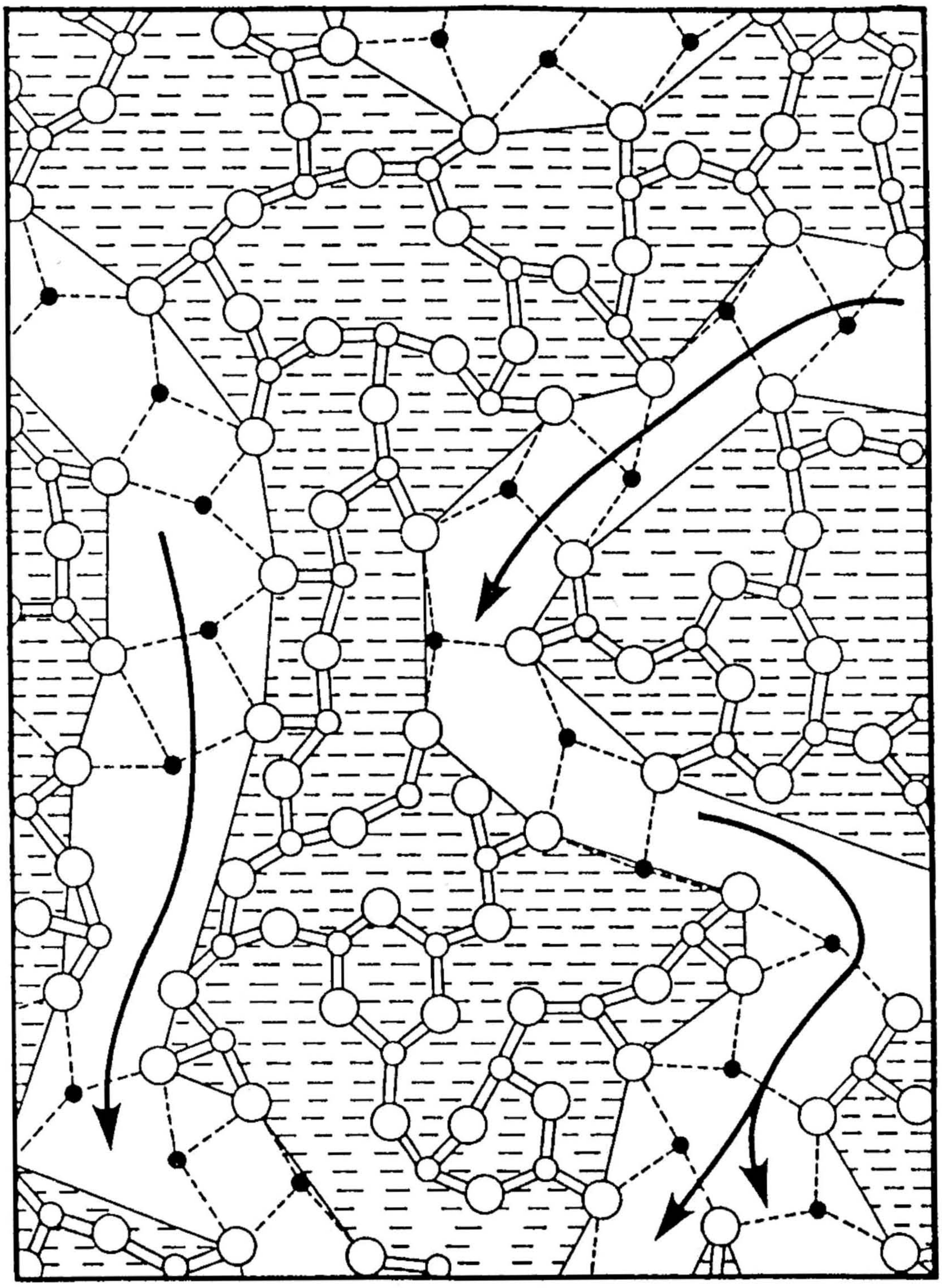

Fig. 1.23 Two-dimensional representation of the modified random network model (after Greaves[89]). The arrow indicates the location of percolation channel which are the presumed pathways for ion migration.

known as "structural unpinning number", SUN (S), has been defined for this purpose based on the unscreened nuclear charge of silver ions and the equilibrium electronegativities of the halide-oxyanion matrix in these glasses. The variation of the glass transition temperature (T_g), conductivity (σ) and the activation energy (E_a), with the concentration of AgI have been discussed in the light of the SUN. Conductivities increase uniformly in any given glass series as a smooth function of S, and level off at high values. The entire range of conductivity appears to vary as $\ln \sigma_o/[1-\exp(-aS)]$, where $\ln \sigma_o$ corresponds roughly to the conductivity of the hypothetical AgI glass and 'a' is a constant which could be obtained as the slope in the graph of $\ln E_a$ versus S. While SUN provides insight to the chemical origin of conductivity in glasses, it is still not able to explain why a large jump in conductivity occurs at the $\beta \longrightarrow \alpha$ transition of AgI.

1.9 GLASS TRANSITION AND STRUCTURAL RELAXATION

When an equilibrium liquid is quenched rapidly enough to prevent crystallization, it becomes a glass. Since the glass is in the non-equilibrium state relaxing towards equilibrium, its physical properties are often found to be time-dependent even in the absence of external forces. Such relaxation phenomena, known as "structural relaxation", considerably affect ionic transport properties of glasses especially near the glass transition temperature T_g. Fig. 1.24 shows the DC conductivity of $(AgI)_{0.70}-(Ag_2MoO_4)_{0.30}$ in the liquid state and in the glassy state. In the glassy state the temperature dependence of conductivity has been usually summarized in terms of the Arrhenius law, although slight deviations were observed near the glass transition temperature[91]. On the other hand, in the liquid state the experimental

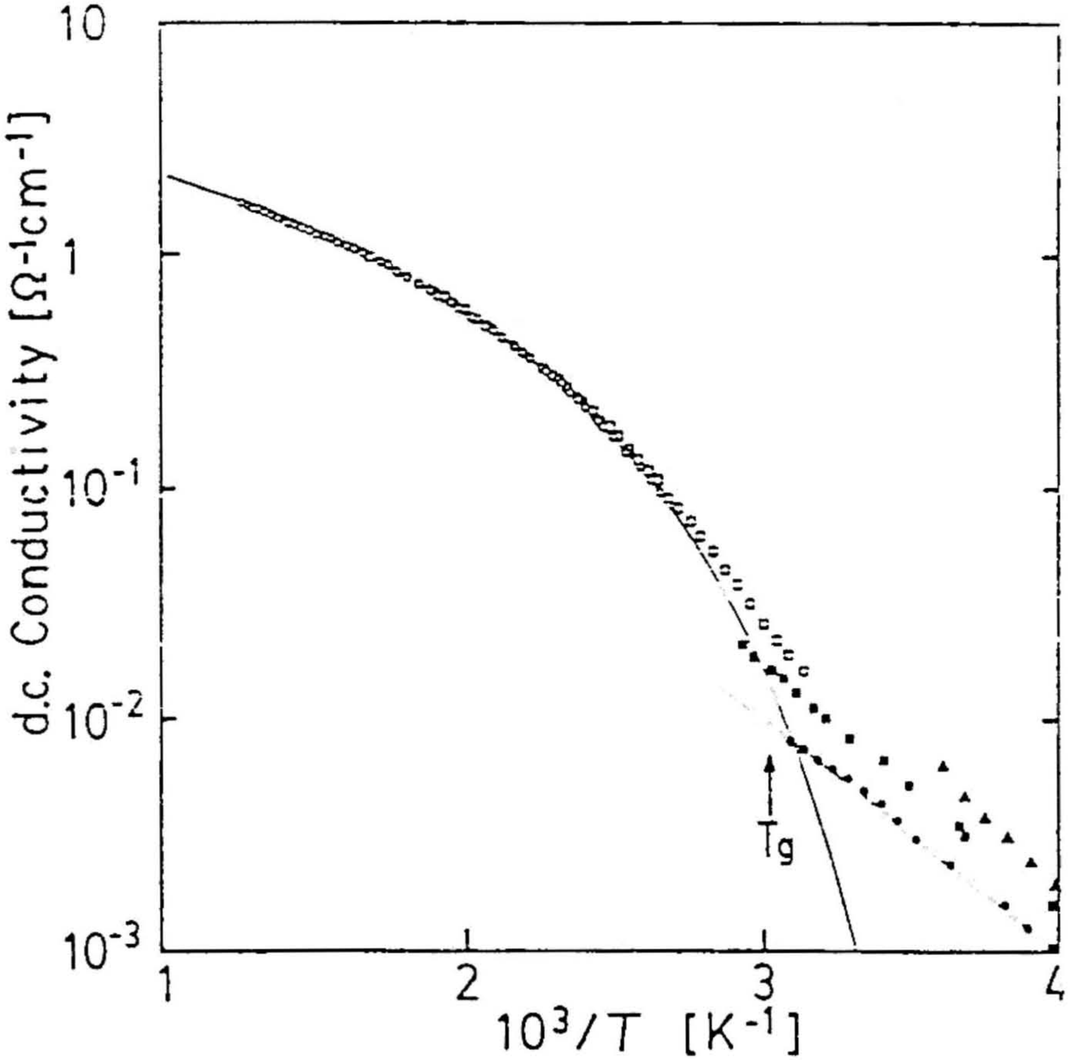

Fig 1.24 The DC conductivity of $(AgI)_{0.70}$-$(Ag_2MoO_4)_{0.30}$ in the liquid state and in the glassy state

conductivity obeys the Vogel-Tammann-Fulcher law well

$$\sigma = \sigma_o \exp\left(\frac{-B}{T-T_o}\right) \tag{27}$$

where σ_o, T_o and B are empirical parameters independent of temperature

It should be noted that the structural relaxation can also be studied by differential scanning calorimetry (DSC) and AC response technique by obtaining τ_s (structural relaxation time) and τ_σ (conductivity relaxation time) respectively

Angell[92], evaluated τ_s from the data of the viscosity and DSC experiments, and the τ_σ from AC measurements, and introduced the decoupling index

$$R_\tau = \frac{\tau_s}{\tau_\sigma} \tag{28}$$

The values of R_τ of Ag^+ conducting glasses are $R_\tau \geq 10^{12}$ at the glass transition temperature, this means that the motion of the mobile silver cation is extremely decoupled from the frame-work ions and is thus a measure of the ease of cation migration compared to other atomic processes involved in structural rearrangements at T_g

1.10 APPLICATIONS

The most promising application of SICs is in solid state batteries Two kinds of batteries may be distinguished (i) small primary cells where long life time and no self-discharge are essential requirements, and (ii) rechargeable secondary batteries, when high energy density is the main criterion A battery of the first type used as a cardiac pacemaker is based on lithium iodide solid electrolyte Here, the requirement is low power and continuous operation for long periods (~15

years) A typical pacemaker cell consists of a lithium anode, lithium iodide electrolyte and poly-2-vinylpyridine-I_2 complex as cathode High energy density batteries are important from the point of view of alternative energy sources being useful for vehicular transport and load-levelling in power stations An important landmark in the development of high energy density batteries is the Na/S battery, which employs Na-β alumina as the solid electrolyte and molten sodium and sulphur as electrodes The cell voltage of 2 08 V is derived from the chemical reaction between sodium and sulphur to produce sodium polysulphide The theoretical energy density of the Na/S battery is quite high (~ 750 W h Kg^{-1}) as compared with the energy density of 170 W h Kg^{-1} of an ordinary lead-acid battery The main disadvantage is the use of molten sodium and sulphur Thus the critical element in this battery application is that the electrolyte must be a relatively good conductor for ionic species and at the same time must allow passage of electrons or holes If the electrolyte were to allow both ionic and electronic species to move through it, the electrodes would be effectively shorted out and the externally measurable electric potential difference drastically reduced

Very recently, scientists of the Matsushita electric company of Japan have come up with a solid state rechargeable battery using a paper thin copper conductive solid electrolyte $Rb_4Cu_{16}I_7Cl_{13}$ and $Cu_2Mo_6S_{7.8}$ electrode[93] This very compact cell delivers 0 55 V with a current density of 10 mA/cm^2 and has an extended charge-discharge cycle life of more than 1000 !

SICs have been made use for developing electrochromic displays WO_3 is a pale yellow solid that becomes deep blue when a small amount of Na is incorporated, owing to the formation of Na_xWO_3 one of the so-called 'tungsten bronzes" Since the change occurs reversibly and very fast, the material has been used in displays Recently Kuwano[94] has designed a novel recording technique based on electron beam irradiation of 0 58 AgI-0 19 Ag_2O-0 23 WO_3 glass which offers several advantages such as fine focus, fast scan rate and high resolution power

Other applications include various gas monitoring cells, such as oxygen sensors for traditional combustion control, electrochemical cells for direct determination of thermodynamic functions involved in chemical reactions, and electrolytes in electrical condensers

1 11 SCOPE OF THE PRESENT WORK

A critical examination of the extensive literature on ionic conduction revealed that the high ionic conductivity in crystalline compounds is due to defects - either inherent in their structure (e g , β-alumina fluorite/antifluorite structures) or a result of disorder in one of the sublattices (e g , Ag^+ in α-AgI) Thus highly disordered crystalline solids and non-crystalline solids would support a high conducting metastable phase at ambient

Physical studies on SICs in the form of single crystals are known to lead to mechanical fracture by way of cracks in the sample when passing through the elastic-plastic phase transitions twice and much information about high temperature phase is lost in the process Polycrystalline compacts - on the other hand - have grain boundaries and

non-uniform grain-sites that considerably impede ion movement which render them non-optimal conductors In this context therefore stabilization/modification of high-temperature plastic phase Li_2SO_4 at ambient and AgI based glasses assumes both scientific and technical importance Motivated by these ideas we have focused on selected physical studies of disordered superionic conductors

The present thesis deals with a systematic investigation of the conductivity dependence on preparative conditions and hence on the degree of disorder The conductivity is found to increase as we increase the quenching temperature of Li_2SO_4 melt The Li_2O-TeO_2 glasses exhibit higher conductivity than its corresponding crystallized products The conductivity increases in a linear fashion by the addition of AgI to Ag_2O-B_2O_3 and to Ag_2O-TeO_2 glass systems, whereas the conductivity changes in a nonlinear manner, when one alkali ion is gradually replaced by another in the Li_2O-Na_2O-TeO_2 glass system

REFERENCES

1 M Faraday *Experimental Researches in Electricity* Vol 1 (Taylor and Francis London 1839) p 426

2 W Nernst, Z *Elektrochem* **6** (1899) 41

3 C Tubandt and E Lorenz, Z *Phys Chem* **87** (1914) 513

4 A Benrath and K Drekopf, Z *Phys Chem* **99** (1921) 57

5 Y F Y Yao and J T Kummer *J Inorg Nucl Chem* **29** (1967) 2453

6 M O Keeffe and B G Hyde, *Phil Mag* **33** (1976) 219

7 M O' Keeffe in *Superionic Conductors* ed by G D Mahan and W L Roth (Plenum, New York, 1976) p 101

8 W J Pardee and G D Mahan, *J Solid State Chem* **15** (1975) 310

9 M A Ratner and A Nitzan, *Solid State Ionics* **28-30** (1988) 3

10 J B Boyce and B A Huberman *Phys Rep* **51** (1979) 189

11 M B Salaman in *Physics of Superionic Conductors* ed by M B Salaman Top App Phys , Vol 15 (Springer-Verlag, Berlin 1979) p 175

12 a A B Lidiard in *Handbuck der Physik*, Vol 20 ed by S Flugge (Springer-Verlag, Berlin, 1957) p 246

b L W Barr and A B Lidiard, in *Physical Chemistry*, Vol 10 ed by W Jost (Academic Press, New York, 1970) p 151

13 C C Liang in *Applied Solid State Science*, Vol 4 ed by R Wolfe (Academic Press, New York, 1974) p 95

14 H Sato, in *Solid Electrolytes*, ed by S Geller, Top App Phys , Vol 21 (Springer-Verlag, Berlin, 1977) p 3

15 G Burley, *J Chem Phys* **38** (1968) 2807

16 G Cochrane and N H Fletcher, *J Phys Chem Solids* **32** (1971) 2557

17 H Hoshino and M Shimoji, *J Phys Chem Solids* **35** (1974) 321

18 W L Strock, Z *Phys Chem* **B25** (1934) 411, **B31** (1936) 132

19 H Schulz in *The Physics of Superionic Conductors and Electrode Materials*, ed by J W Perram (Plenum Press, New York, 1983) p 5

20 B Reuter and K Hardel, Z *Anorg Allgem Chem* **340** (1965) 168

21 T Takahashi and O Yamamoto, *Electrochim Acta* **11** (1966) 779

22 J A A Ketelar, Z *Kristallogr Abt* **A87** (1934) 436

23 S Geller, in *Solid Electrolytes*, ed by S Geller, (Springer-Verlag, Berlin, 1977) p 41

24 J N Bradley and P D Greene, *Trans Faraday Soc* **63** (1967) 424

25 B B Owens and G R Argue, *Science* **157** (1967) 308

26 S Chandra in *Superionic Solids - Principles and Applications* (North-Holland, Amsterdam, 1981) p 56

27 K Shahi, *Phys Stat Sol* **A41** (1977) 11

28 M S Whittingham and R A Huggins, *J Chem Phys* **54** (1971) 414

29 J T Kummer, *Progr Solid State Chem* **7** (1972) 141

30 B C H Steele, in *Solid State Chemistry* Vol 10 ed by L E J Roberts (Butterworths, London 1972) P 117

31 B C H Steele and G J Dudley, Inorganic Chemistry Ser 2 *Solid State Chemistry* Vol 10 ed by L E J Roberts (Butterworths, London, 1975) P 181

32 R M Dell and A Hooper, in *Solid Electrolytes General Principles, Characterization, Materials, Applications,* ed by P Hagenmuller and W Van Gool (Academic Press, New York, 1978) P 291

33 T H Etsell and S N Flengas, *Chem Rev* **70** (1970) 339

34 J M Wimmer, L R Bidwell and N M Tallan, *J Am Ceram Soc* **50** (1967) 198

35 J M Baker, A A Jenkins and R C C Ward, *J Phys Condens Matter* **3** (1991) 8467

36 R A Huggins, *Electrochim Acta* **22** (1977) 773

37 S R Elliott *Physics of Amorphous Materials* (Longman London 1984) p 1

38 P W McMillan, *Glass Ceramics* (Academic Press, London 1979) p 7

39 S R Elliott *Physics of Amorphous Materials* (Longman London 1984) p 23

40 A R West *Solid State Chemistry and its Applications* (John Wiley & Sons, Chichester, 1984) p 594

41 V M Goldschmidt in *Geochemische Verteilungsgesetze der Elements* Viii Vid Akad (1926)

42 W H Zachariason, *J Am Chem Soc* **54** (1932) 3841

43 J W Allen, A C Wright and G A N Connell *J Non-Cryst Solids* **42** (1980) 509

44 R Zallen, *The Physics of Amorphous Solids* (John Wiley & Sons, New York, 1983) p 11

45 R Becker and W Doering, *Ann Phys* **24** (1935) 719

46 J Frenkel *Kinetic Theory of Liquids* (Clarendon Press, Oxford, 1946)

47 D Turnbull and M H Cohan, *J Chem Phys* **29** (1958) 1049

48 R G Linford and S Hackwood, *Chem Rev* **81** (1981) 327

49 S R Elliott *Physics of Amorphous Materials* (Longman London, 1984) p 53

50 S M Sharipo and F Reidringer, in *Physics of Superionic Conductors,* ed by M B Salaman, Top App Phys Vol 15 (Springer-Verlag, Berlin & New York, 1977) p 45

51 N H Andersen, K N Clausen and J K Kjems, in *Neutron Scattering* ed by D L Price and K Skold, Methods in Exp Phys , Vol 23 Part B (Academic Press New York, 1987) p 187

52 K Suzuki, *Neutron Scattering*, ed by D L Price and K Skold, Methods in Exp Phys , Vol 23 Part B (Academic Press, New York, 1987) p 243

53 M J Dalaney and S Ushioda, in *Physics of Superionic Conductors*, ed by M B Salaman Top App Phys , Vol 15, (Springer-Verlag, Berlin & New York 1977) p 111

54 W Hayes, in *Light Scattering in Solids IV Recent Results*, ed by M Cardona & G Gilntherodt, (Springer-Verlag, Berlin & New York, 1982) p 93

55 P E Stallworth and P J Bray in *Advances in Structural Analysis*, ed by D R Uhlmann and N J Kreidl Glass Science and Technology, Vol 4B (Academic Press, New York, 1990) p 77

56 M D Ingram, M A Mackenzie, W Müller and M Torge *Solid State Ionics* **40 & 41** (1990) 671

57 R L Mozzi and B E Warren, *J Appl Cryst* **2** (1969) 164

58a J Krogh-Moe, *J Non-Cryst Solids* **1** (1969) 269

b D L Griscom, in *Borate Glasses Structure, Properties, Applications* ed by L D Pye, V D Frechette and N J Kreidl, Mat Sci Res , Vol 12 (Plenum Press, New York, 1978) p 11

59a P J Bray and J G Ó Keefe, *Phys Chem Glasses* **4** (1963) 37

b S G Bishop and P J Bray, *Phys Chem Glasses* **7** (1966) 73

60 P A V Johnson, A C Wright and R N Sinclair, *J Non-Cryst Solids*, **50** (1982) 281

61 M C Abramo, G Carini and G Pizzimenti, J Non-Cryst Solids **21** (1988) 527

62 M Ueno and K Suzuki, *Kakuriken Kenkyu Hokoku* (Tohoku Univ) **16** (1983) 49

63 G Warburg, *Ann Phys* **21** (1884) 622

64 T Minami, Y Ikeda and M Tanaka, *J Non-Cryst Solids* **52** (1982) 159

65 T Minami, Y Ikeda and M Tanaka *Solid State Ionics* **9 & 10** (1982) 577

66 T Minami, *J Non-Cryst Solids* **56** (1983) 15

67 E Robinel, B Carette and M Ribes *J Non-Cryst Solids* **57** (1983) 49

68 A Schiraldi *Electrochim Acta* **23** (1978) 1039

69 L Borjesson, L M Torell and W S Howells, *Phil Mag* **B59** (1989) 105

70 M Mangion and G P Johari, *Phys Rev* **B36** (1987) 8845

71 M Tachez R Mercier, J P Malugani and A J Dianoux, *Solid State Ionics* **18 & 19** (1986) 372

72 H L Tuller, D P Button and D R Uhlmann, *J Non-Cryst Solids* **40** (1980) 93

73 F A Fusco and H L Tuller, in *Superionic Solids and Solid Electrolytes* ed by A L Laskar and S Chandra (Academic Press, New York, 1989) p 43

74 A Levasseur, J-C Brethous, J M Reau and P Hagenmuller and M Couzi, *Solid State Ionics* **1** (1980) 177

75 A Levasseur, J -C Brethous, M Kbala and P Hagenmuller, *Solid State Ionics* **5** (1981) 651

76 A Levasseur, J -C Brethous, J -M Reau and P Hagenmuller, *Mat Res Bull* **14** (1979) 921

77 A Levasseur, R Olazeuaga, M Kbala and P Hagenmuller, *C R Acad, Sci* **293** (1981) 563

78 A Kone, B Barrou, J L Souquet and M Ribes, *Mat Res Bull* **14** (1979) 393

79 A Kone, M Ribes and J L Souquet, *Phys Chem Glasses* **23** (1982) 18

80 M Jagla and J O Isard, *Mat Res Bull* **15** (1980) 1327

81 S I Smedley and C A Angell, *Solid State Commun* **27** (1978) 21

82 M D Ingram, *Phys Chem Glasses* **28** (1987) 215

83 O L Anderson and D A Stuart, *J Am Ceram Soc* **37** (1954) 573

84 R M Hakim and D R Uhlmann, *Phys Chem Glasses* **12** (1971) 132

85 D Ravaine and J L Souquet, *Phys Chem Glasses* **18** (1977) 27

86 D Ravaine, *J Non-Cryst Solids* **73** (1985) 287

87 A M Glass and K Nassau, *J Appl Phys* **51** (1980) 3756

88 K E D Wapenaar and J Schoonman, J Electrochem Soc **126** (1979) 667

89 G N Greaves, *J Non-Cryst Solids* **71** (1985) 203

90a M C R Sastry and K J Rao, *Solid State Ionics* **37** (1989) 17

b M C R Sastry and K J Rao, *Proc Indian Acad Sci (Chem Sci)* **102** (1990) 541

91 J Kawamura and M Shimoji, *J Non-Cryst Solids* **88** (1986) 281

92 C A Angell, *Solid State Ionics,* **18 & 19** (1986) 72

93 T Sotomura, S Kondo and T Iwaki, in *Recent Advances in Fast Ion Conducting Materials and Devices*, ed by B V R Chowdari, Q G Liu and L Q Chen (World Scientific, Singapore, 1990) p 325

94 J Kuwano, *Solid State Ionics* **40 & 41** (1990) 696

CHAPTER 2

EXPERIMENTAL TECHNIQUES

2 EXPERIMENTAL TECHNIQUES

The major experimental probes employed in the present investigations are briefly described in this chapter

2.1 X-RAY DIFFRACTION

W.L. Bragg showed that the X-rays reflected from a lattice plane and the effect associated with it could be derived by the equation

$$n\lambda = 2d\sin\theta \quad \text{(Bragg's law)} \tag{1}$$

in which n is an integer (the 'order'), λ the wavelength of the X-rays, d the interplanar spacing, and θ the angle of incidence of the X-ray beam on the lattice plane

In a crystalline powder, the tiny crystals are oriented at random If such a powder is struck by an X-ray beam, many planes will be so oriented, that Bragg's law is simultaneously satisfied and an X-ray diffraction pattern is obtained To be certain that all possible planes are exposed to the X-ray beam, the specimen is usually rotated by an angle θ on its own axis during exposure Most of the X-ray beam will pass directly through the sample and the diffracted beams are collected by a detector (scintillation counter) which is rotated by 2θ the output of which is processed and ther fed into an automatic recorder The result is a chart which gives a record of counts per second (proportional to diffracted beam intensity) versus diffraction angle 2θ The block diagram of the Seifert X-ray powder diffractometer used in the present study is shown in Fig 2.1

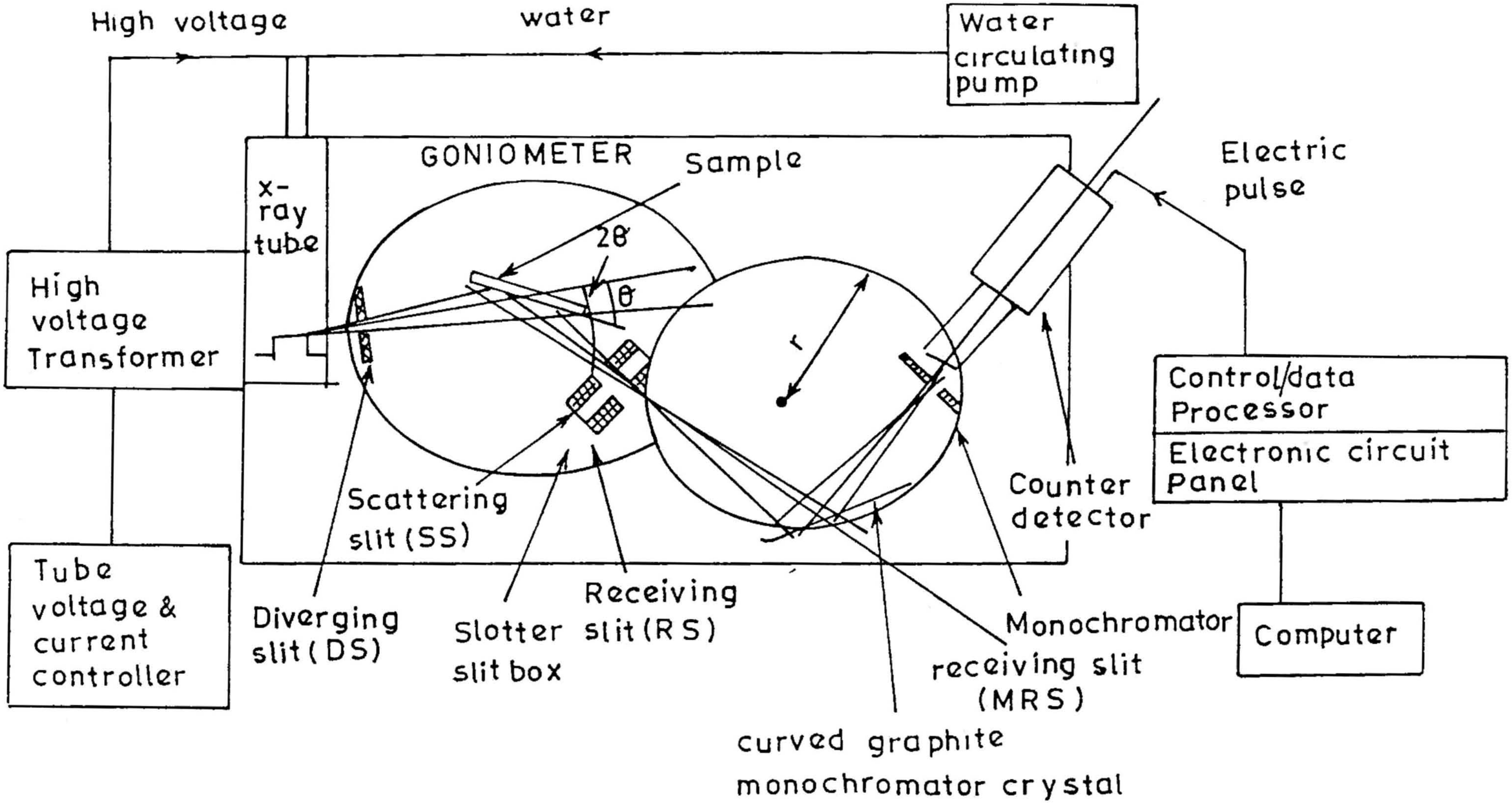

Fig. 2.1 Schematic diagram of Seifert X-ray diffractometer system

Powder specimens are best prepared for XRD study by placing the finely ground powder in a recess in plastic or teflon plate compacting it under just sufficient pressure to cause cohesion without use of a binder and smoothing off the surface. Sometimes vacuum grease was also used as a binder. Occasionally, quenched ingot was also used 'as-such' for recording the XRD pattern.

In principle the following information can be obtained from the diffraction peak characteristics:

1. Position. The position of the peak measured as the angle θ yields size (i.e., lattice parameter and d-values), shape (i.e., cubic, tetragonal etc.,) and orientation (hence it can be used for crystal orientation and preferred orientation determinations) of the unit cell.

2. Intensity. The relative intensity of the peaks measured either as the peak height or, more correctly as the area under its profile (integrated intensity), provides the data for determining the position of the atoms in the unit cell. The intensity I_{hkl} of a Bragg reflection with Miller indices hkl is given by[1]

$$I_{hkl} = I_o\left(\frac{e^2}{mc^2}\right) p\, L\, \frac{\Omega\, \lambda^3 p_{hkl}}{\omega}\, A\, \frac{S}{v^2}\, F^2_{hkl}\, \frac{1}{\rho_1} \qquad (2)$$

where

I_o is the incident beam intensity,

e, m, and c are the fundamental constants,

p_{hkl} is the multiplicity factor,

L is the Lorentz factor,

Ω is the unit cell volume,

λ is the wave length of X-rays,

ω is the angular velocity of the rotation of the specimen,

$A \approx 1/2\mu$ is the transmission factor for a flat specimen,

S is the cross section of the primary beam,

F_{hkl} is the structure factor, and

ρ is the density of the specimen

3. Shape : The shape of the peak of which its breadth is a useful guide, provides information regarding crystallite size and lattice imperfections, including strains

In the present study, the powder XRD was recorded at RT on a Seifert X-ray powder diffractometer and was extensively used for the phase identification and the determination of unit cell parameters

The Cu Kα radiation (λ=1.5418 Å) was used along with Ni filter as monochromatic radiation. The X-ray machine was operated with 40 kV voltage and 30 mA current. The X-irradiation of the polycrystalline samples was also performed in the same setting.

For phase identification, our powder patterns were compared with standard patterns given in Powder Diffraction File (the JCPDS file[2]). Accurate cell parameters were obtained from the d-spacing of the powder pattern, and proper assignments of Miller indices hkl to various lines. Using a least square minimization program 'POWD' developed by Wu[3], unit cell parameters accurate to three figures were calculated. The errors involved in the cell parameter calculations are mainly due to the uncertainty in reading the 'angular' positions of the peaks, which are accurate to $\pm 0.2^{o}$

2 2 DIFFERENTIAL THERMAL ANALYSIS AND DIFFERENTIAL SCANNING CALORIMETRY

Differential thermal analysis (DTA)is a technique in which the temperature of the sample (T_S) is compared with that of an inert reference material (T_R) during a programmed change of temperature Alumina is usually used as the reference material The sample and reference temperatures are normally the same until some thermal event such as melting, decomposition or change in crystal structure occurs in the sample, in which case the sample temperature either lags behind (if the change is endothermic) or leads (if the change is exothermic) the reference temperature, the difference in temperature (ΔT) between them are recorded as a function of temperature of the whole system A horizontal baseline corresponding to $\Delta T = 0$ occurs and superimposed on this is a sharp peak due to a thermal event in the sample The peak area or peak heights are only qualitatively related to the magnitude of the enthalpy changes occurring It is possible to calibrate DTA equipment so that quantitative enthalpy values can be obtained, from the peak areas but the calibration is usually tedious If calorimetric data are required then it is usually better and easier to use differential scanning calorimetry (DSC)

In the DSC cell, the difference in temperature between the sample and reference is measured, as in DTA, but by careful attention to cell design so that the response of the cell is calorimetric A schematic diagram of the DuPont 9900 model DSC instrument is shown in Fig 2 2 The cross-sectional view of DSC cell shown in Fig 2 3 employs a constantan disc as the primary means of transferring heat to the sample and reference positions, and as one of the elements of the temperature measuring thermoelectric junctions The sample of interest and a

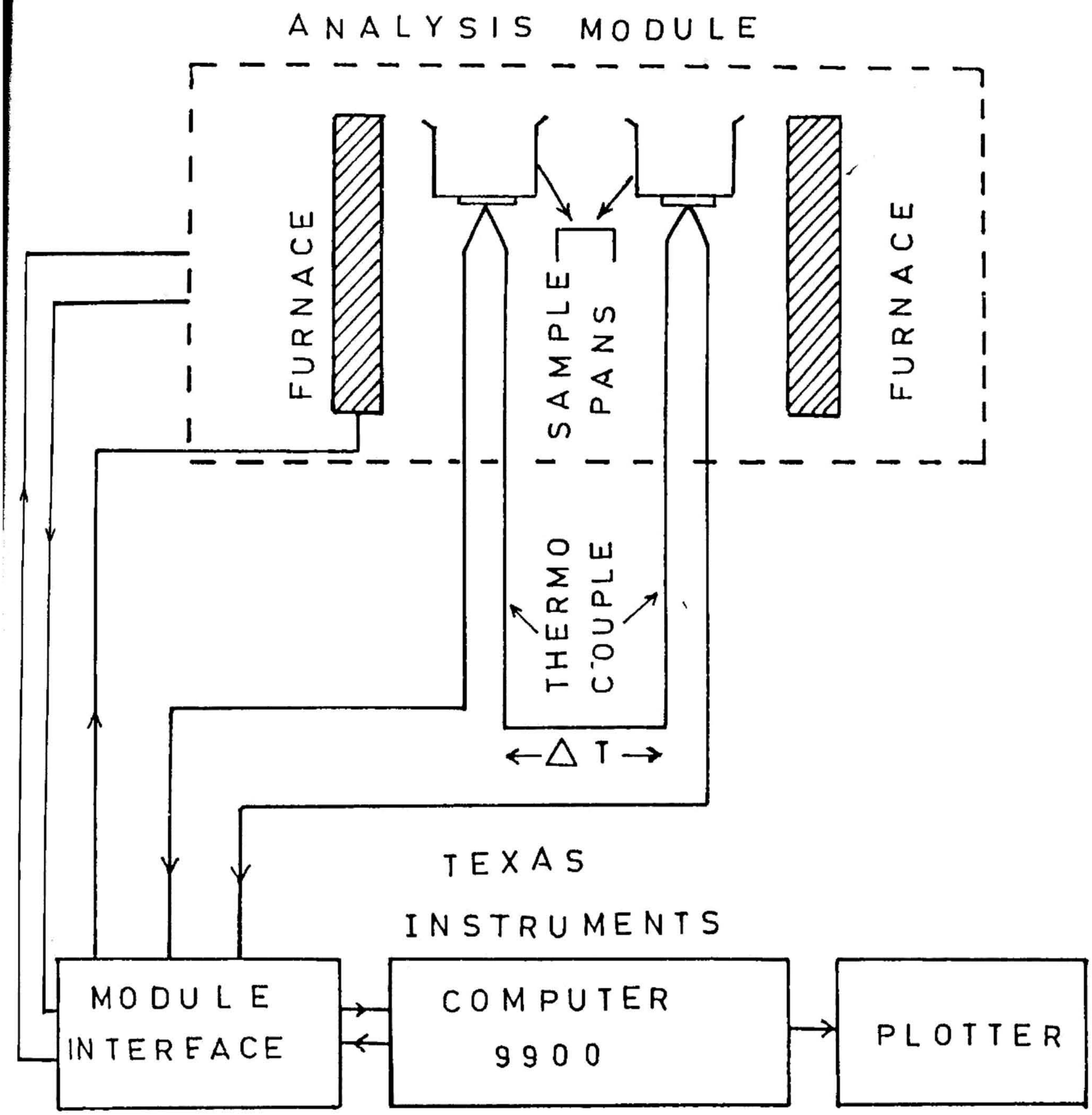

Fig 2.2 Schematic diagram of the differential scanning calorimetry system

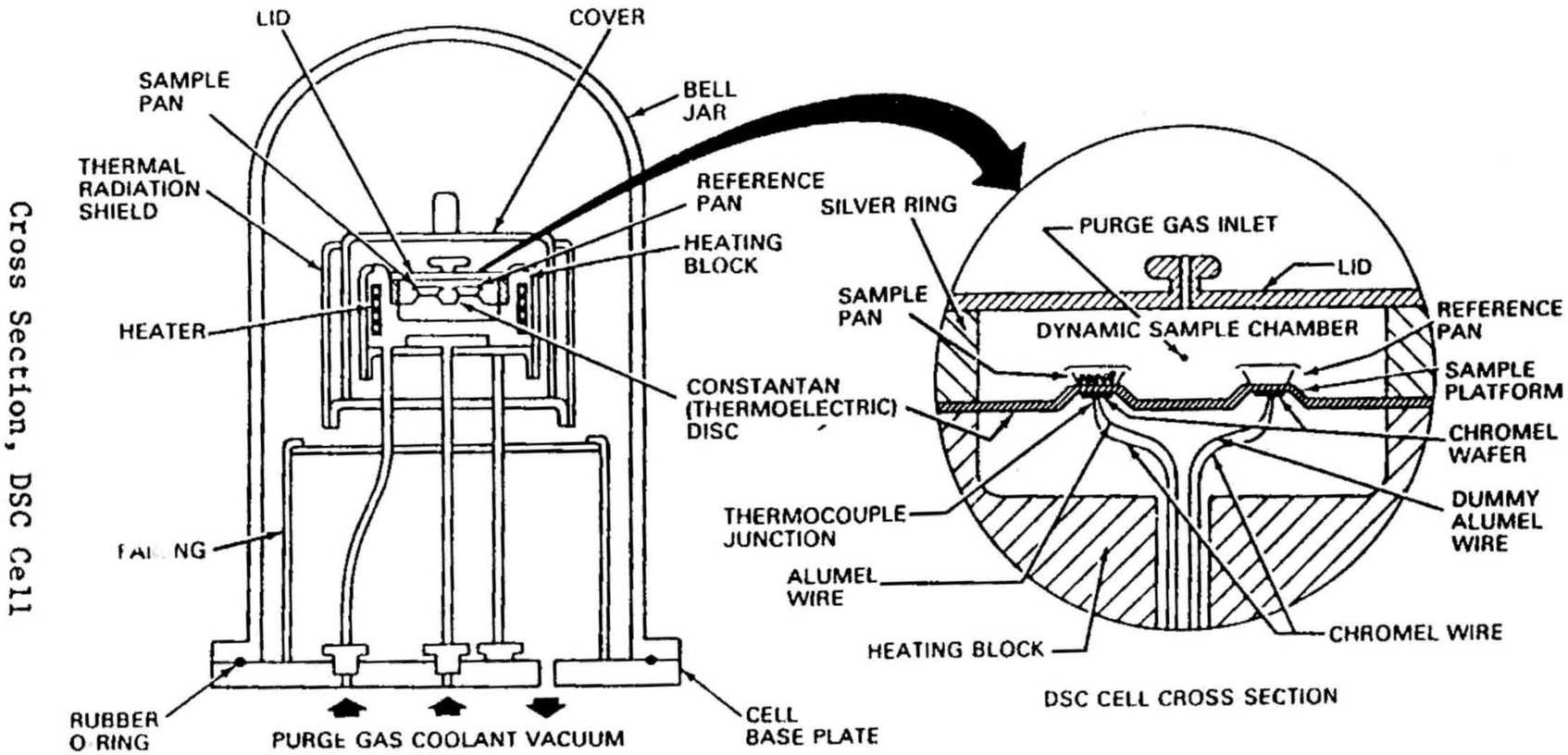

Fig. 2.3 DSC cell and its cross-section

reference are placed in pans which sit on raised platforms on the constantan disc Heat is transferred through the disc into the sample and reference The differential heat flow to the sample and reference is monitored by chromel/constantan area thermocouples formed by the junction of the constantan disc and the chromel wafer which centers the downside of each platform Chromel and alumel wires are connected to the underside of the chromel wafers, and the resultant chromel/alumel thermocouple is used to directly monitor the sample and reference temperatures Constant calorimetric sensitivity is maintained by electronic linearization of the cell-calibration coefficient

The difference ΔT between T_S and T_R is given by

$$\Delta T = T_S - T_R = R\,(C_S - L_R)\,\frac{dT_p}{dt} \qquad (3)$$

where C is the total heat capacity of sample (or reference) plus crucible, R is the thermal resistance, and (dT_p/dt) the rate at which the programmed temperature changes The apparatus constant relating the area under the peak to enthalpy can be obtained by using a reference material with known transition enthalpy

The thermal analysis was performed on mixtures of Li_2CO_3 and TeO_2 using DTA set up to construct the phase diagram of this binary system, whereas, the thermal behaviour of the sample was investigated using DSC The DSC measurements were performed with selected heating rates (2 5 5 10 20 and 40^{o}C/min) under argon atmosphere on both crystalline and glassy samples of mass ~ 20 mg, encapsulated ('crimped) between aluminum pans with empty aluminum pans reference The temperature and the cell constant of the instrument were calibrated for each heating rate on the basis of onset temperature of the endothermal peak and the

enthalpy recorded during the melting of high pure (5N) indium The glass transition temperature onset and peak temperatures of the crystallization are obtained using the software standard data analysis [4]

2 3 MEASUREMENT OF IONIC CONDUCTIVITY

The DC conductivity is defined as the steady-state current which flows in the sample subjected to unit electric (DC) field The measured quantity is usually the conductance (G) which is the ratio of steady-state current to applied voltage The conductivity is obtained from the conductance and ratio of length to cross-sectional area (l/A) of a rectangular sample according to

$$\sigma = G\ l/A \tag{4}$$

A cell for measuring the conductance of an electrolyte sample must (a) transform the electronic current from the external circuit into an ionic current in the sample and (b) transmit the potential difference across the sample to the voltage-measuring device without introducing any additional potential

The transformation of current occurs at the electrode/electrolyte interface where either a Faradaic or a displacement current flows A Faradaic current occurs when an ion present in the electrolyte can be placed onto (or removed from) the electrode surface in response to the electronic current, e g when a lithium-based electrolyte is placed in between two lithium-metal electrodes

The standard method of conductivity measurement has a displacement current at the interface where ionic charge accumulates at one side to exactly balance the accumulation or depletion of electrons The charge accumulation creates an interfacial potential which would rise rapidly on application of a DC voltage Therefore an alternating signal must be applied This creates a constant interfacial potential which is determined by interfacial capacitance, current and frequency

$$V_{int} = I/(2\pi\omega\ C_{int}) \qquad (5)$$

The interfacial potential can be minimized by increasing the frequency of the applied signal For most cases a frequency of 1 kHz, or higher, ensures that any interfacial potentials are negligible

At high frequencies, however, the current is not the steady-state value Internal displacement, or capacitive currents due to ions vibrating in potential wells without jumping the barriers are added to the current due to true conductivity The displacement current is out of phase with the potential, whereas the conductive current is in phase, and therefore a distinction can be made by examining the complex impedance/admittance

$$Z^* = V^*/I^* \text{ or } Y^* = I^*/V^* \qquad (6)$$

where the out of phase components are represented by imaginary parts

The complex admittance of the sample between inert electrodes is measured using either the AC conductivity meter over a frequency 100 Hz - 60 KHz (described in Chapter 3) or the instrumental set up (shown in the Fig 2 4) which provides the measurement possibilities upto 120 KHz In the latter method, an alternating voltage (V_{in}) of nearly 150 mV r m s is applied across the sample and a standard decade capacitor (HP

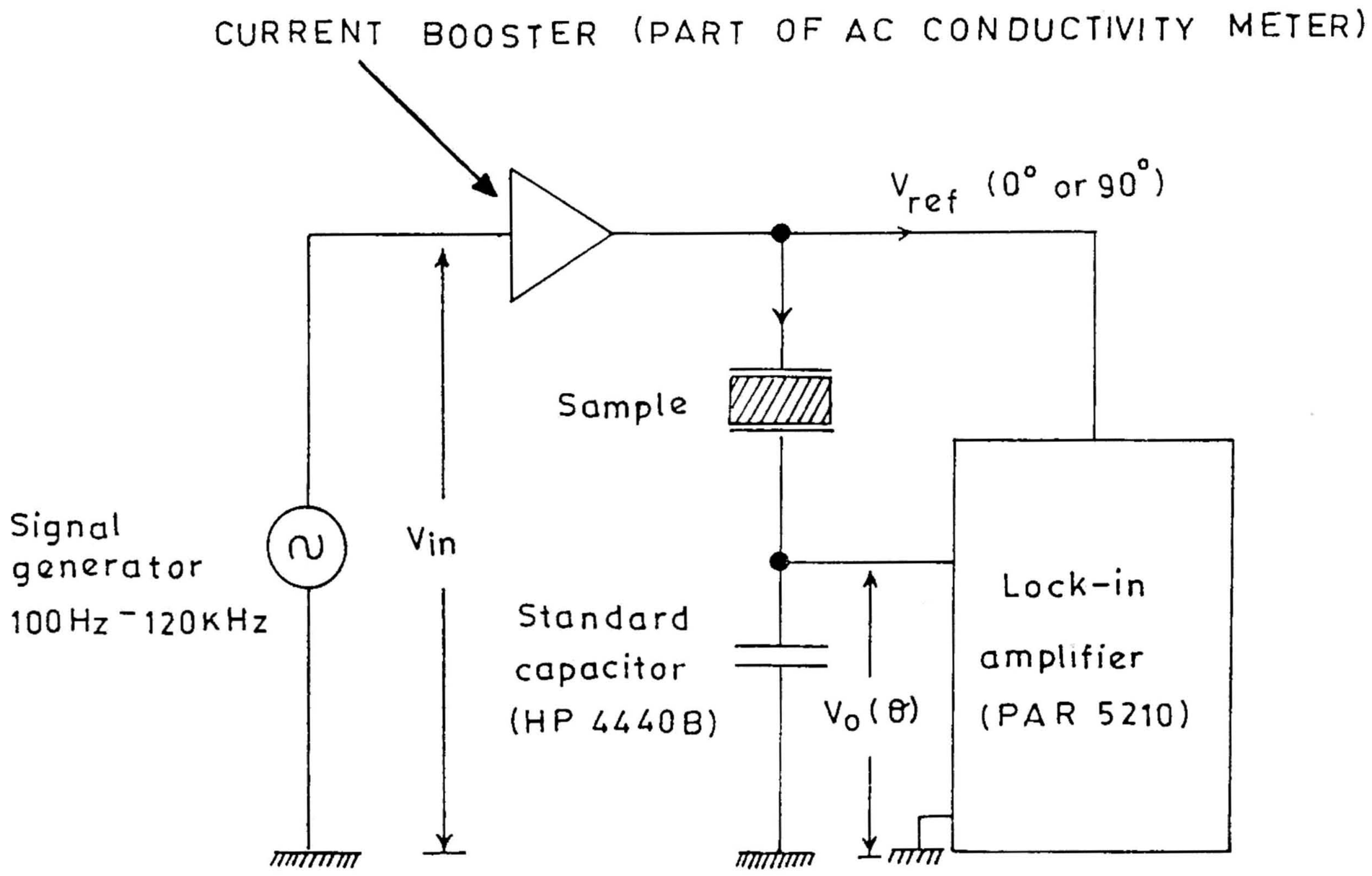

Fig. 2.4 Bloc diagram of the instrumental set up used for AC conductivity measurement

Model 4440 B) which are connected in series. The current through the sample is determined by measuring the voltage (V_o) across the reference capacitor (C_o) using a two phase lock-in amplifier (PAR Model 5210). The output of the lock-in-amplifier V_o (θ), was measured for specified θ where θ-is the phase difference set between reference signal and voltage across C_o. The output voltages V_o (0^o) and V_o (90^o), for $\theta = 0^o$ and 90^o are used to calculate the real (ε'), and the imaginary (ε'') parts of the complex permittivity (ε^*) as follows

$$\varepsilon' = \frac{1}{\varepsilon_o}\left[\frac{V_o(0^o)\, C_o}{V_{in}-V_o(0^o)}\right] \tag{7}$$

and

$$\varepsilon'' = \frac{1}{\varepsilon_o}\left[\frac{V_o(90^o)\, C_o}{V_{in} - V_o(90^o)}\right] \tag{8}$$

where ε_o is the permittivity of free space (8.854×10^{-14} F cm^{-1})

The complex admittance Y^* is related with the complex dielectric permittivity ε^* through

$$Y^* = Y' + jY'' = j\omega\varepsilon^* = j\omega(\varepsilon' - j\varepsilon'') \tag{9}$$

These results are usually presented in two-dimensional plots, either as Bode (real or imaginary parts versus log [frequency]) or as Nyquist or Cole-Cole plots (real versus imaginary parts). Results over a wide frequency range are often conveniently summarized in terms of an equivalent circuit[5,6,7], which is an electrical circuit that has identical admittance to the real physical system over the measured frequency range.

The design of the conductivity sample holder used in our measurement to achieve a reliable result is shown in Fig. 2.5. A good

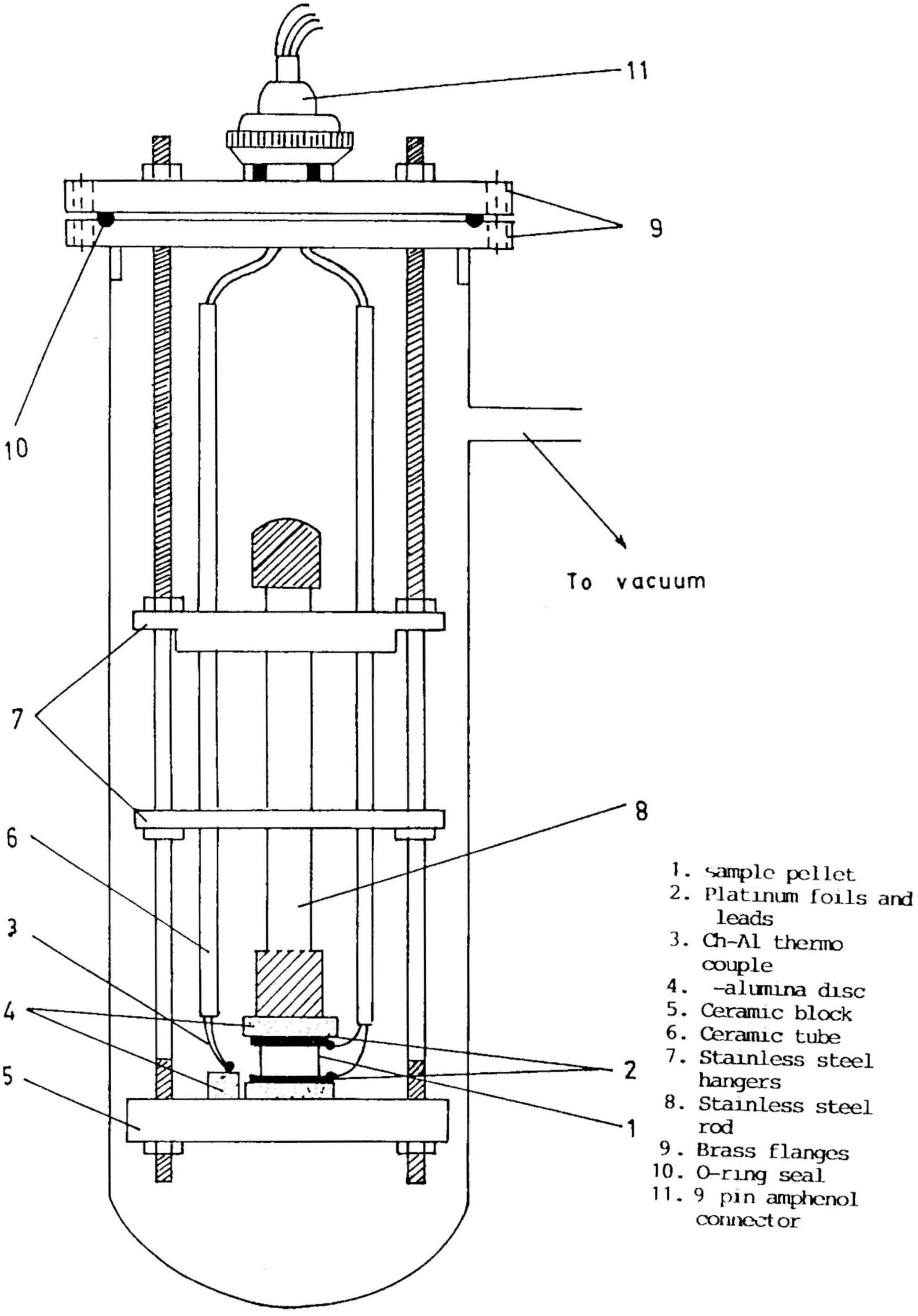

Fig 2.5 Schematic diagram of the apparatus used for conductivity measurement

electrical contact is found to be essential This is ensured by the use of thick platinum foils spot-welded with platinum wires serving as blocking electrodes These electrodes are attached to the opposite faces of the samples using organo-silver or gold paste (Eltecks Corporation Bangalore, No 0070) Gradual heating upto 150°C (depending upon T_g values in the case of glasses) decomposes the resin and hardened metallic residue adheres strongly to the sample The whole assembly is introduced into the vertical stainless steel conductivity jig, with high-pure Al_2O_3 pellets serving as isolating spacers Mild pressure on the electrode assembly was achieved with the help of the screw arrangement as shown in Fig 2 5 The temperature was measured with a chromel/alumel thermocouple the tip of which is maintained in close proximity to the cell for maximum accuracy The jig is lowered into a glass envelope thus permitting measurements to be made under a vacuum, of ~ 10^{-2} torr In addition dry silica gel is introduced into the cell to absorb the moisture present if any The entire assembly is clamped centrally inside a vertical muffle furnace attached to an ON-OFF temperature controller The thermal stability of the sample is achieved by allowing sufficient time and measured to an accuracy of ± 1°C Perfect shielding is mandatory to avoid the AC pick ups from the furnace particularly at high temperatures We employed a furnace giving very low inductive noise to overcome this difficulty to a considerable extent In addition, a thick stainless steel sheet (connected to main ground) was inserted in between the conductivity set up and the furnace The furnace body, input and output terminals of the sample are also shielded perfectly

The bulk DC conductivity derived from complex admittance analysis is then plotted either as a log σT versus $10^3/T$ plot or as a log σ versus $10^3/T$ plot. The slope of this generally linear plot is the activation energy E_a for ionic conduction. The error involved in the conductivity measurement is mainly due to the accuracies in the measurement of sample conductance, thickness and cross-sectional area. Sufficient time is allowed to stabilize the thermal status of the sample and all the equipments involved in the measurement to achieve a stable and reliable output of the circuit shown in Fig. 2.4. Sufficient care was taken to accurately measure the sample thickness and its area.

The activation energy for ionic conduction was determined by least squares fitting of the conductivity versus temperature relation, the calculated values of the probable errors are in the range ± 0.01 to 0.03 eV in all our measurements.

2.4 ELECTRON SPIN RESONANCE

In an ESR experiment, a highly uniform and reasonably stable static magnetic field H, is applied to a paramagnetic material placed in a microwave resonant cavity. The microwave magnetic field component perpendicular to the direction of the static field causes magnetic dipole transitions when the microwave energy quantum, $h\nu$ (where ν-is the frequency and h-is Planck's constant) is equal to the Zeeman energy splitting $g\beta H$, of the two spin states (M = 1/2 and - 1/2) of the paramagnet i.e., $h\nu = g\beta H$. The parameter g-is the spectroscopic splitting factor representing the nature of unpaired electrons and β-is the basic unit of electronic magnetic moment called the Bohr magneton ($\beta = e\hbar/(2m_e) = 9.274 \times 10^{-24}$ J/T).

Resonance transitions are observed in ESR by sweeping the magnetic field intensity, rather than by sweeping the microwave frequency which is technically impracticable. Each type of unpaired electrons is identified not by the microwave frequency, but by the g-factor obtained from the resonance condition as

$$g = (h/\beta)\ (\nu/H) \qquad (10)$$

The nature of the electron spins (s-, p-, d- type) and their microscopic environments can be derived from ESR parameters.

A typical X-band ESR spectrometer is blocked out in Fig. 2.6, according to the function of groups of components. The region labelled 'source' contains the Gunn oscillator (as in the JEOL instrument) or a reflux Klystron (as in a Varian instrument) and those components which control or measure the frequency and the intensity of the microwave beam. The 'cavity system' includes the components which hold the sample and which direct and control the microwave beam to and from the sample. The 'detection' and 'modulation systems' - monitor, amplify and record the signal. Finally, the 'magnet system' provides a stable, linearly variable and homogeneous magnetic field, typically upto 0.5 tesla.

The ESR spectra of metastable crystalline solids subjected to X-irradiation, as well as of glassy samples reported in this thesis were recorded on a JEOL (FE-3X) X-band ESR spectrometer under optimized conditions of modulation amplitude, receiver gain, time constant and scan time. Temperature and microwave power were used as variable parameters to investigate changes in the spectra even as the species or the matrix underwent changes such as tumbling motion or glass transition.

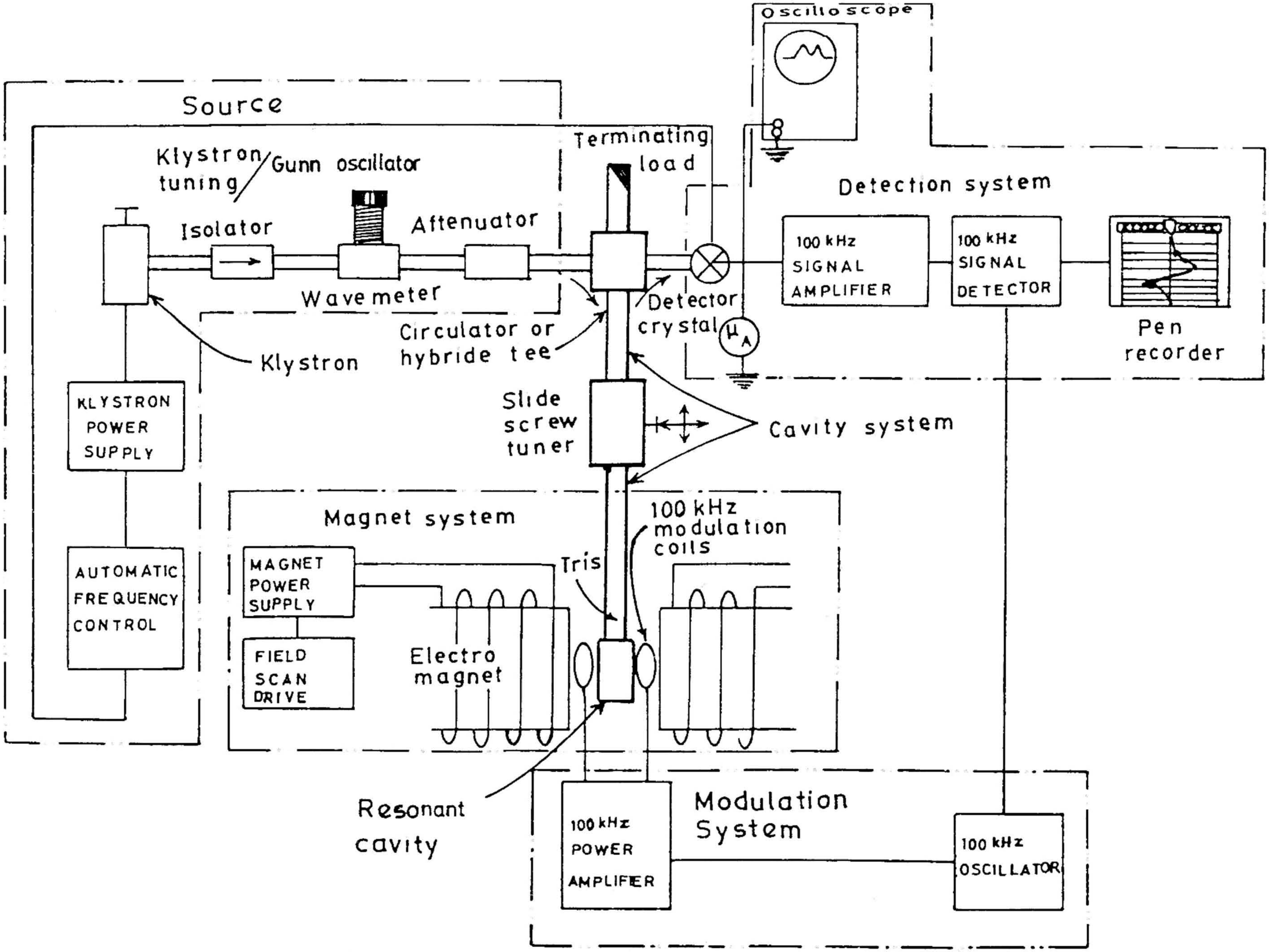

Fig 2.6 Block diagram of an ESR X-band spectrometer

Variable temperature accessory supplied with the instrument (Model NM 7700) was used for recording spectra at selected temperatures range RT to 200^{o}C. The input microwave power as monitored at the side arm of the directional coupler was varied from 1 to 50 mW while performing power saturation experiments.

REFERENCES

1 B K Vainshtein, in *Modern Crystallography* Springer Ser in Solid State Sci , ed by M Cardona, P Fulde and H J Queisser (Springer Verlag, Berlin, 19 8) P 306

2 Publication DBNBS-(-26 Published by *JCPDS Associateship*, National Bureau of Standard

3 Wu, Flinders University of South Australia, Australia

4 *DSC Standard Data Analysis-Version 2 0,* (c) 1986 by E I du Pont Nemours & Co (Inc), Wilmington, DE 19898

5 J E Bauerle, *J Phys Chem Solids* **30** (1969) 2657

6 J R McDonald, in *Superionic Conductors*, ed by G D Mahan and W L Roth (Plenum New York, 1976) p 81

7 I R Raistrick, in *Annual Review of Materials Science* Vol 16 (1986) 343

CHAPTER 3

AC CONDUCTIVITY METER

3. AC CONDUCTIVITY METER

3.1 **INTRODUCTION**

The electrolytic conduction in ionic/superionic solids is mainly due to the movement of charged ions under the influence of an applied electric field. When a constant DC potential is applied to an electrolyte sandwiched between two different electrodes as shown below

-	nonblocking electrode	$A^+ B^-$	blocking electrode	+

the cation starts moving towards the negative electrode. As a result, the right end of the electrolyte suffers a depletion of cations as no more ions are supplied at the positive electrode. As soon as the circuit is switched on the instantaneous current and voltage give a measure of total conductivity (ionic plus electronic). The current decays slowly with the lapse of time yielding a stabilized final value. This is a measure of the electronic conductivity.

These polarization effects[1] are troublesome in a DC measurement unless non-polarizing electrodes capable of supplying mobile ions at the anode/electrolyte interface are used. Then the electrode configuration becomes

-	nonblocking electrode	$A^+ B^-$	nonblocking electrode	+

where the electrode materials are the same as those of the mobile species. This avoids the problem of polarization, but the utility of such electrodes is limited by the following circumstances.[2]

(a) the extent of electronic conductivity cannot be evaluated for the transport number measurement, (b) the type of mobile ions has to be known before hand. Further, if more than one type of charge carriers is present, it is difficult to find a material which can act as a reversible electrode for various types of mobile ions. (c) it is not always easy to handle the mobile species electrodes. For example in fluoride ion conductors like PbF_2, having a fluorine electrode is tricky.

The problems associated with the choice and use of an appropriate non-blocking electrode can be overcome by employing blocking electrodes and measuring as a function of frequency.

Apart from the undesirable polarization effects, when the DC measurements are performed on ionic conductors, over a wide range of temperatures, another unavoidable difficulty arises from the presence of interfering voltages due to the Thomson and Seebeck effects. These interfering voltages make measurement more difficult because of their random variations with changes of room temperature. To avoid these heating effects and the difficulty due to polarization, an AC method employing synchronous rectification is devised for the measurement of electrical conductivity.

AC measurements are also significant because in addition to bulk conductivity, many other electrochemical parameters are also sampled as a function of applied frequency. The resultant alternating current is out of phase with the applied AC voltage and perturbs various processes within the measuring cell (such as surface, interfacial, grain boundary

ionic transport and double-layer formation at electrode/electrolyte interface) in different ways

In superionic conductors, particularly in sintered polycrystalline and ill-quenched glassy forms the grain boundary contribution becomes significant. The extraction of intrinsic conductivity must therefore involve a measurement technique such as an impedance/admittance technique which would enable a clear separation of the observed response into intrinsic and grain boundary contributions. In such cases a simple DC measurement would be vitiated by the presence of significant polarization and grain boundary effects, thus making an AC measurement mandatory.

Our design of this electronic instrument is a considerably modified version of Nelson who used a full-wave rectifier[3] for detection instead of the phase sensitive detection (PSD) employed in the present case. One of the main advantages of PSD over precision rectifier is the total rejection of discrete frequency noise such as AC mains pick up and unwanted signals due to DC offset, 1/f noise and various thermal effects.

3.2 DESCRIPTION OF THE CIRCUIT

The instrumental set up is shown Fig. 3.1.

3.2.1 Quadrature oscillator and buffer

Fig. 3.2 shows the quadrature oscillator[4]. This is a low-distortion (≤ 0.1%) two-phase sine-wave oscillator, which provides three stable outputs at 0^{o} (sine), 90^{o} (cosine) and 180^{o} (-sine) phases

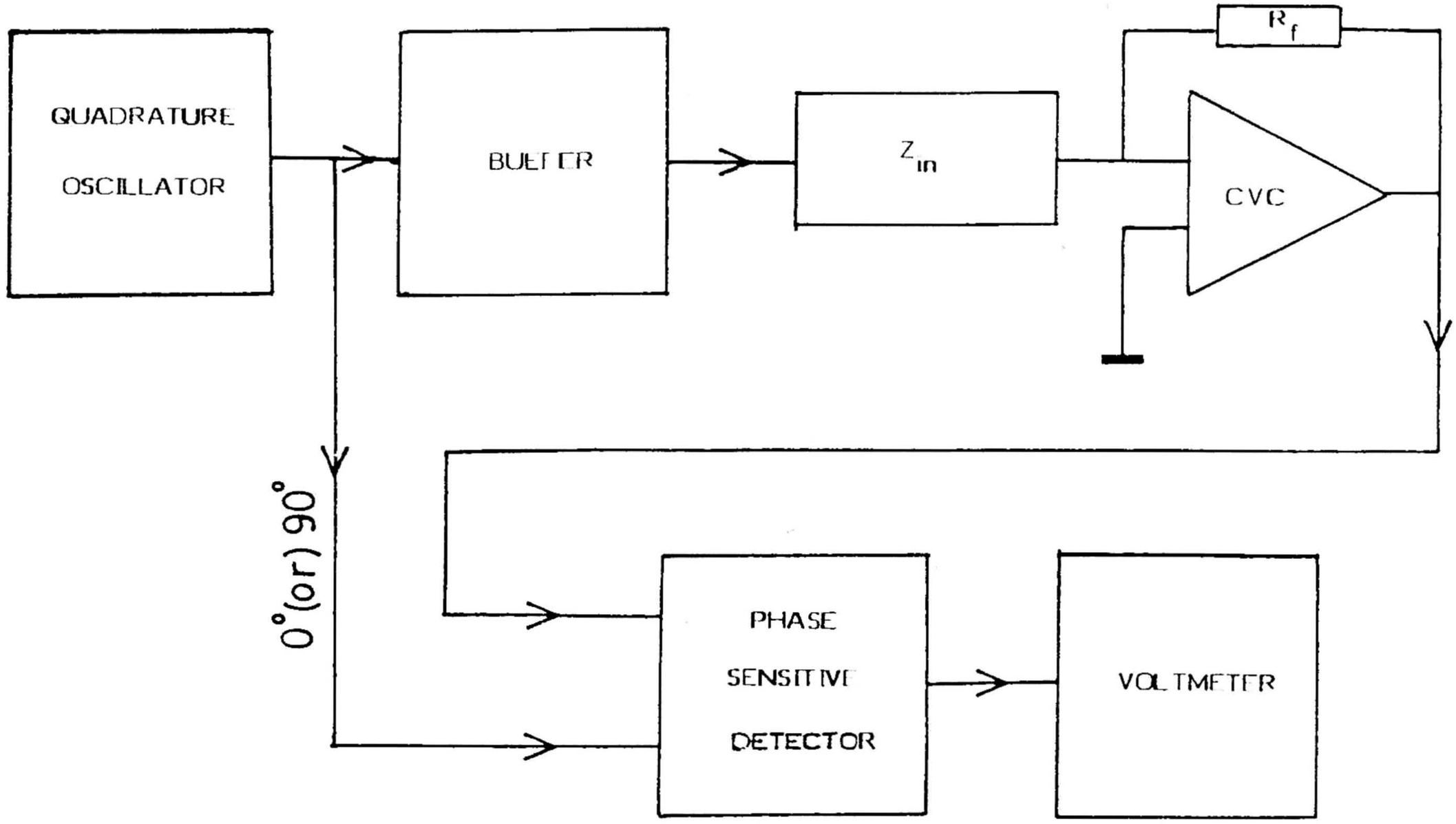

Fig 3.1 Block diagram of the electronic system showing various modules (CVC = current-to-voltage converter)

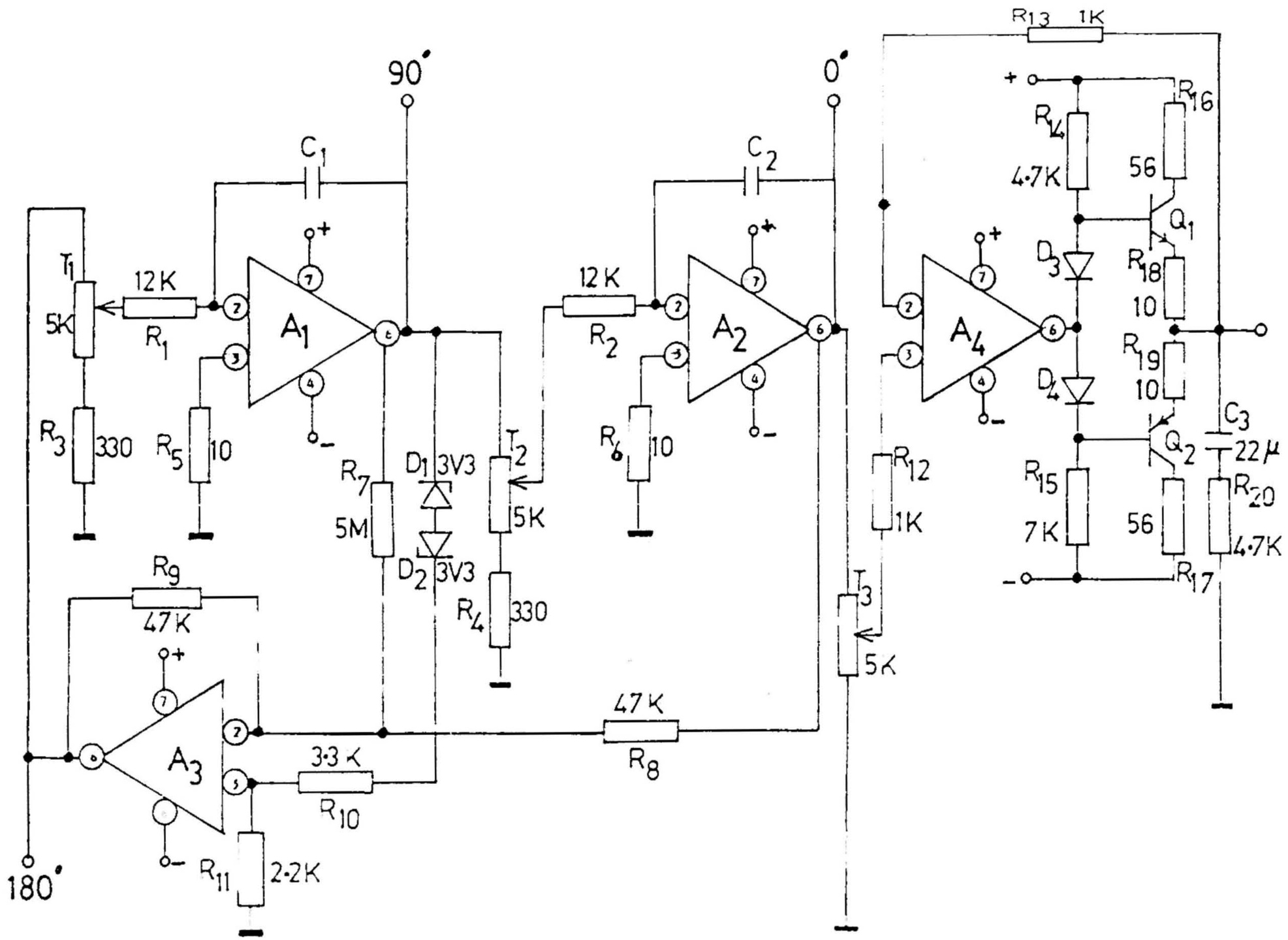

Fig 3.2 Quadrature oscillator and buffer amplifier (A_1 to A_4) are 741 type Transistors Q_1 = SL 100 and Q_2 = SK 100

Basically it has two integrators connected with feedback via a unity gain inverter Oscillations will occur at a frequency where each integrator has unity gain i e , when $1/\omega RC = 1$ (where $R_1 = R_2 = R$ and $C_1 = C_2 = C$) For different frequency ranges different matched pairs of capacitors can be selected using band switch arrangement The resistor R_7 applies a small amount of 'negative damping' to ensure that the oscillator starts as soon as the circuit is switched on The amplitude is limited by using zener diodes D_1 and D_2 The module consisting of operational amplifiers A_1, A_2 and A_3 now develops a total phase shift of 360° and constitutes a positive feedback loop with unity gain which will stimulate and sustain stable oscillations

Measurements on superionic conductors have shown that the sample resistance often becomes a few ohms at temperatures $T \geq T_t$, where T_t is the insulator-to-electrolyte transition temperature As the operational amplifiers are limited by their maximum output currents the oscillator output has to be boosted before it is allowed to excite the sample This may however be accomplished by adding power transistors Q_1 and Q_2 which provide sufficient current to drive the sample The use of such a pair of NPN and PNP transistors in the output stage is also referred to as complementary symmetry The input stage of the buffer also includes a trimpot for adjusting the voltage level required to excite the sample

3 2 2 Current-to-voltage converter

Fig 3 3 shows the current-to-voltage converter (CVC) This operates on the principle that the current through the input impedance (Z_x) and the feedback resistors (R_f) will always be equal in order to maintain zero voltage difference between the two inputs The unknown

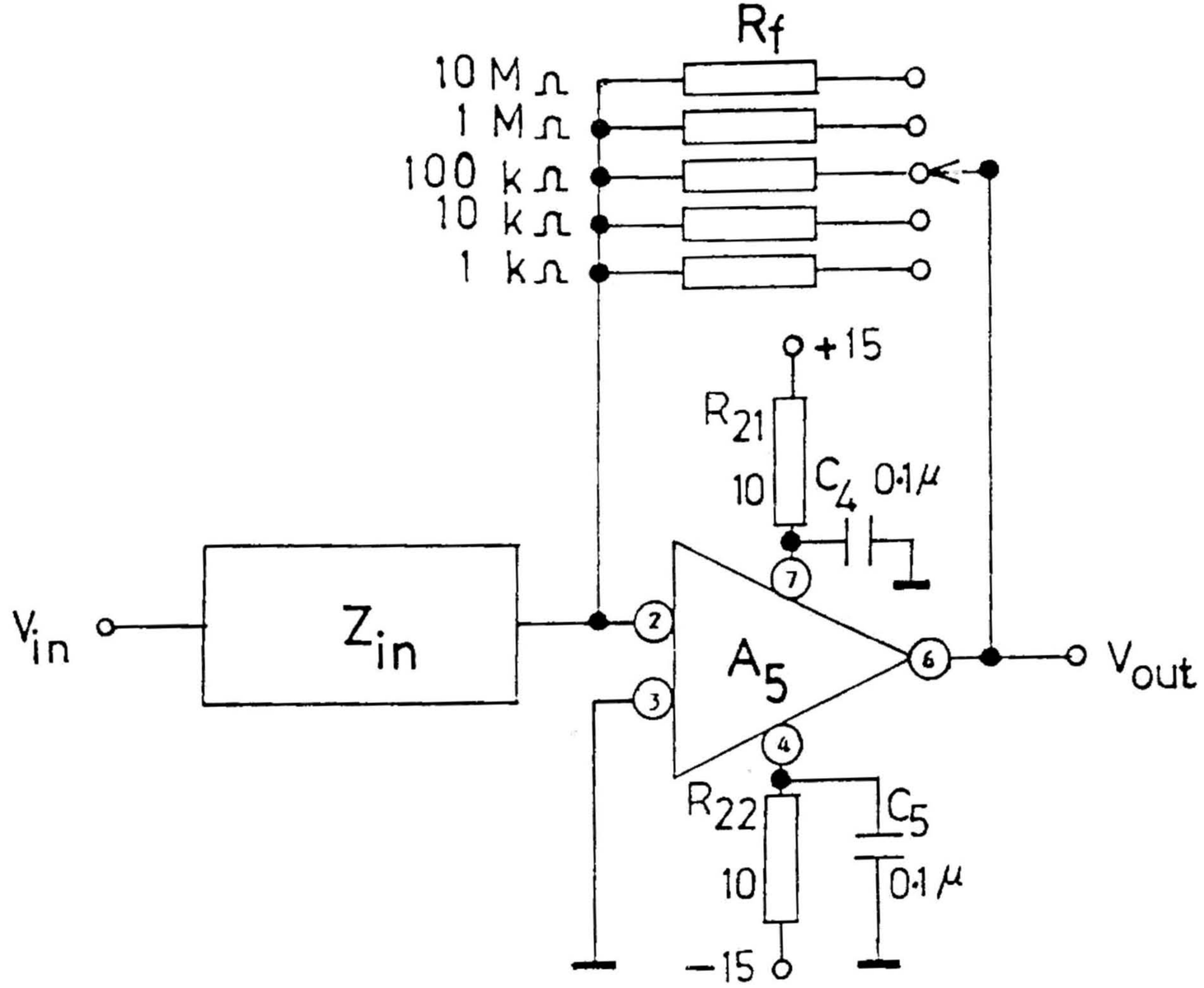

Fig. 3.3 Current-to-voltage converter A_5 = NF 357 The feedback resistors are 0 1% tolerance metal film resistors with virtually zero stray reactance

impedance (Z_x) may then be calculated using the Kirchoff's law as

$$Z_x = (v_i R_f)/v_z \qquad (1)$$

If Z_x is a purely resistive element, then there will only be a change in the amplitude of the exciting signal (v_i) with no change in the phase But if Z_x is purely capacitive, then there will not only be a phase difference between the output and input signals but also a change in their amplitudes Generally if Z_x is a complex impedance which involves both resistive and capacitive reactances in parallel or in series, the output signal undergoes both amplitude and phase modulations

The real and imaginary parts of Z_x are derived using lock-in technique with the help of phase sensitive detector and represented as $Z\cos\theta$ versus $Z\sin\theta$ along the x-axis and y-axis of a complex-Z plane, in the so called impedance plot (One could also present these results in the form of an admittance plot or modulus plot) The various forms of impedance/admittance spectra provide detailed and separate information about all possible combinations of R_x and C_x This is done by comparing these experimental plots with those that could be generated by equivalent circuit models[5,6]

As mentioned by Nelson, selection of the operational amplifier for use as a CVC is a crucial aspect of its design, one should select an operational amplifier with a high input impedance and a wide unity gain-bandwidth product NF 357 having an input impedance of 10^{13} ohms in parallel with less than 3 pf and 20 MHz unity gain bandwidth product is used as a CVC in our instrument

Another important aspect of design is the selection of reference resistors One should use perfectly non-reactive resistors as standards For this purpose one could prefer either 0 1% metal film resistors or 0 1% wire wound resistors whose reactive components are nullified by symmetrical opposite windings These non-reactive resistors are checked thoroughly before their use as standard resistors 0 1% metal oxide resistors were found unsuitable as references, as they exhibit considerable reactive components

3 2 3 Phase Sensitive Detector

During conductivity measurements the signals of interest are always accompanied by high levels of noise and interference due to 1/f noise, AC pick ups and thermoelectric voltages The main purpose of using phase sensitive detectors (PSD) is to reject totally all these unwanted signals[7] This is achieved by limiting the bandwidth of detection to that just necessary to include the range of frequencies occurring in the signal Signals at other frequencies are averaged to zero and thus a greatly improved signal-to-noise ratio is achieved

Several phase sensitive detectors have been described in the literature with electronic switching for rectification,[8,9,10] with different circuit configurations We opted for a different technique for the demodulation Two square waves 180^{o} out of phase to each other are used to control two pairs of switches The outputs from this switching network pass through a low-pass filter and a differential amplifier Because of its high input impedance the differential amplifier isolates the output circuit from the PSD circuit and provides a low output impedance suitable for connecting it to even an ordinary multimeter

If $v_1[V_1 \sin \omega t]$, $v_z[V_z \sin(\omega t + \phi)]$ and $v_r[V_r \sin(\omega t + \theta)]$ are the excitation, CVC output and reference signals respectively with ϕ-the phase difference introduced by the reactive component of Z_x and θ-the angle of reference signal set with respect to excitation signal, then the multiplier output is

$$v_z v_r = 1/2\ V_z V_r [\sin(\omega t + \phi)\ \sin(\omega t + \theta)] \quad (2)$$

$$= 1/2\ V_z V_r [\cos(\theta - \phi) - \cos(2\omega t + \theta - \phi)] \quad (3)$$

the second component of which is completely rejected by the low-pass filter. The alternate positive and negative DC components corresponding to the alternate half cycles of modulated AC signal (V_z) are added using a differential amplifier whose output is given by

$$V_o = 1/2\ V_z V_r \cos(\theta - \phi) \quad (4)$$

If the chosen impedance is purely resistive (i.e., $\phi = 0^\circ$) then the output of the detector is

$$V_o = 1/2\ V_z V_r \cos\theta$$

whose real and imaginary parts can be separated by properly choosing the in-phase ($\theta = 0^\circ$) and quadrature phase ($\theta = 90^\circ$) signals as reference The corresponding output of the detector will be

$$V_o \text{ (with } \theta = 0^\circ) = 1/2\ V_z V_r,$$

$$V_o \text{ (with } \theta = 90^\circ) = 0$$

If the chosen impedance also includes some reactive components the quadrature output will always be non-zero Correspondingly the inphase output will be less than the maximum output $1/2\ V_z V_r$

In the present design the PSD consists of a phase shifter, a zero-crossing detector, an inverter, a switching network, a low-pass filter and a differential amplifier

The reference signals (0^{o} and 90^{o} phases) are derived from the same quadrature oscillator. These signals are sent through the phase shifter to adjust the phase accurately, so that the reference (v_r) can be precisely set in-phase or 90^{o} out of phase with the excitation signal (v_i) applied to the sample. Part (a) of Fig. 3.4 shows the phase shifter. This has a gain of unity and enables continuous phase adjustment from 0^{o} to 180^{o}.

The reference signal from the phase shifter is sent to the zero-crossing detector (ZCD) which is a high speed voltage comparator (response time ~ 200 ns). Basically this ZCD-acts as a high gain amplifier which can change its state each time the input signal changes direction. Thus the circuit part (b) of Fig. 3.4, squares the input signals into a series of rectangular output pulses with rising and falling slopes corresponding to the input zero-crossing.

Two square waves differing in phase by 180^{o} are generated using the CMOS 4049[11] inverting buffers and are used as control signals for the switching action which is the heart of PSD.

The switching is done by CMOS FET 4066[12] which possesses four independent bilateral analog switches. Two switches are controlled by one square wave (reference 1) and the other two by the other inverted square wave (reference 2). Only those input signals that are in synchronization with the carrier frequency are extracted. The switching action may be clearly understood by looking at Fig. 3.5.

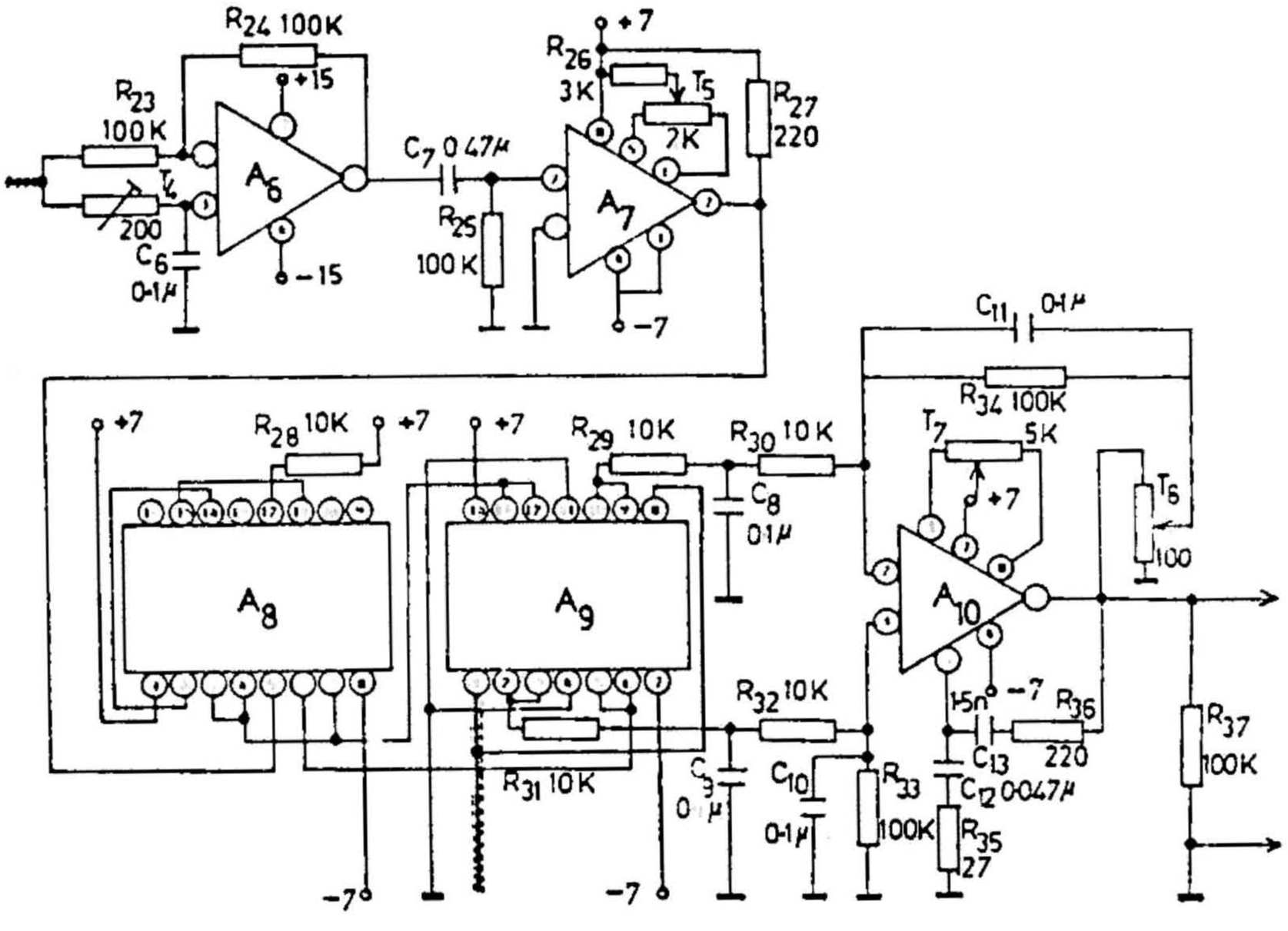

Fig 3.4 Phase sensitive detector A_6 = NF 356, A_7= LM 311, A_8= CMOS 4049, A_9 = CMOS 4066, A_{10} = 725 The frequency compensation for A_{10} is done externally as shown

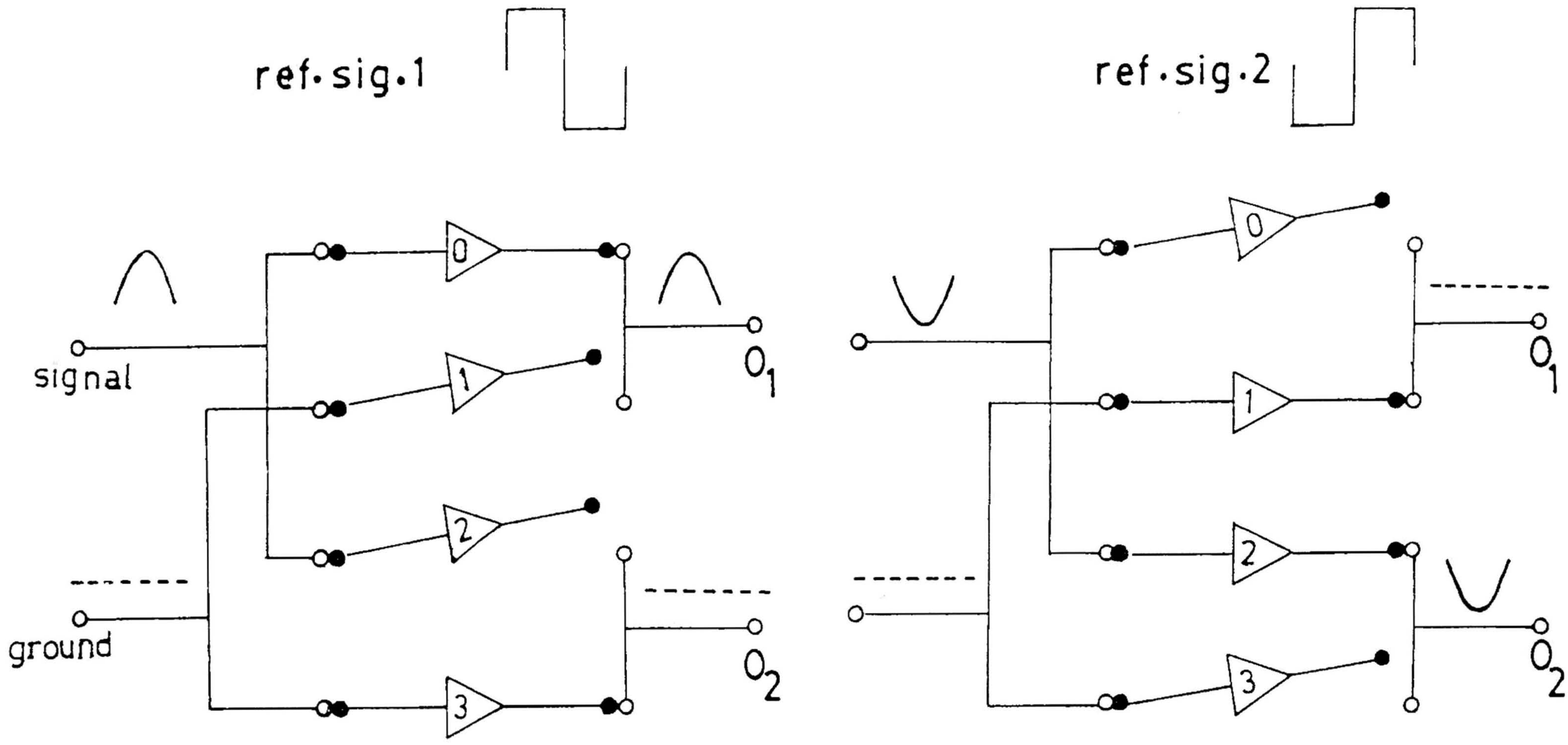

Fig 3.5 Switching action of A_9 (of Fig 3.4) FETs 0 and 3 are controlled by reference signal 1 while 1 and 2 are controlled by reference signal 2 Outputs O_1 and O_2 are sent to the non-inverting and inverting inputs of differential amplifier

The outputs of the switches are then applied to the low-pass filter which is an RC network in our case This smooths out the ripple components of the signals coming from FET switches and supplies positive DC voltage and ground to the non-inverting and inverting inputs of differential amplifier, during positive half cycles of reference 1 During the negative half cycles of reference 1, the switching occurs such that the low-pass filter delivers negative DC voltage and ground to the inverting and non-inverting inputs Being a differential amplifier this last stage simply adds the inputs and delivers a positive DC voltage Proper care was taken using an offset trimpot and appropriate resistors to eliminate the offset voltages due to FET switches and differential amplifier

3.3 EXPERIMENTAL PROCEDURE

The Au/electrolyte/Au configuration mounted in an electrically shielded conductivity cell (see Chapter 2) is connected to the inverting input of the CVC The input and output terminals of the sample are shielded perfectly

The 0^{o} phase output of the oscillator is boosted using the buffer stage and its output is adjusted to ~ 100 mV peak to peak As the voltage levels at different frequencies seem to show slight variations, the constancy of the input signal to the sample is checked at several selected frequencies using the detecting stage The output of the synchronous detector is made zero by adjusting the signal (v_i) and the reference (v_r) into quadrature at the multiplier using the phase shifter The detector output with reference (v_r) and exciting signal (v_i) in-phase at the multiplier now measures the voltage level to be

used as input This signal is allowed to excite the sample at the input of CVC, and appears as the measurand signal (both amplitude and phase modulated) at the output of CVC This measurand signal (v_z) is ther sent to the detecting part for further analysis with 0^o and 90^o phases as reference signals to extract the corresponding real and imaginary parts of the impedance Z_x

3 4 PERFORMANCE ACHIEVED

The working of the instrument has been tested by performing complex admittance/impedance and AC conductivity measurements on (a) sintered polycrystalline pellet of 40% Li_4SiO_4-60% Li_3VO_4 in the temperature range 100-350^{o}C and (b) 30% Li_2O-70% TeO_2 glass in the temperature range 70-200^{o}C at various frequencies upto 60 kHz using two probe configuration The CVC also allows us to choose the three-probe measurement

The data collected in the test cases are analyzed in the form of admittance/impedance plots A typical admittance plot is shown in Fig 3 6 for 40% Li_4SiO_4-60% Li_3VO_4 sintered pellet The plot consists of a depressed semicircle at low frequencies and a spike at high frequencies corresponding to the grain boundary (σ_{gb}) and bulk conductance (σ_b) respectively It is often observed[15] that at low temperature there is a clear separation of bulk and grain boundary contributions, the grains being more conductive than the grain boundaries As the temperature increases, the separation becomes less, corresponding to a decrease in the grain boundary contribution At room temperature the total electrolyte conductance is dominated by the grain boundary term, but above 200^{o}C this term becomes negligible The present data on the 40%

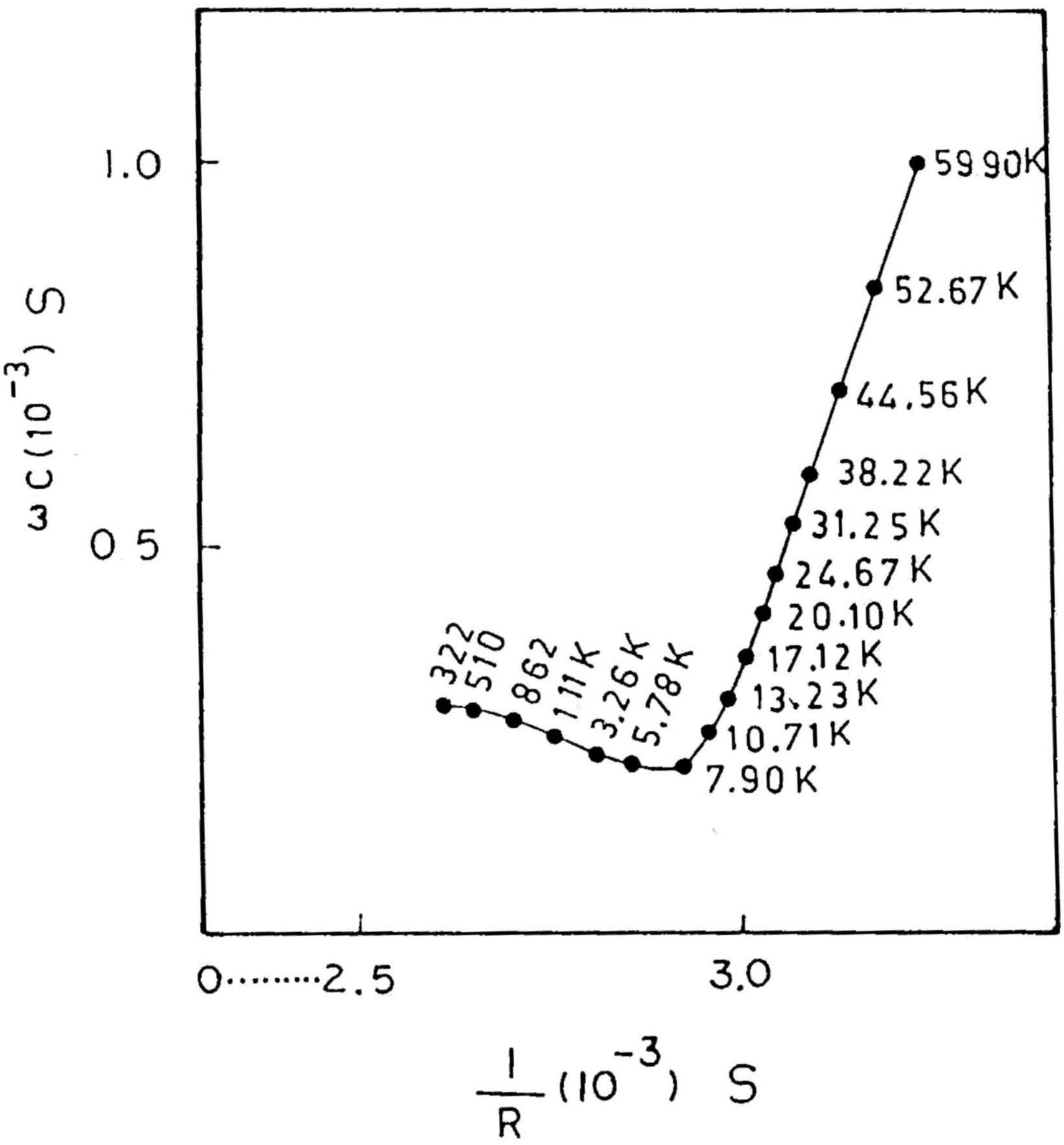

Fig 3.6 A typical complex-admittance plot of the 40% Li_4SiO_4- 60% Li_3VO_4 sintered pellet at 195°C The numbers along the plot refer to measurement frequencies

Li_4SiO_4-60% Li_3VO_4 sintered polycrystalline pellet with a very small grain size indicate that, as expected, the grain boundary term is significant to higher temperatures. This profile very closely resembles one of the theoretical admittance plot of Bauerle[6] for a model circuit comprising a resistance and a series capacitance in parallel with another capacitance. The abrupt rise in the admittance suggests that the sample is becoming increasingly capacitive. The bulk DC conductivity of polycrystalline lithium silicate-lithium vanadate and glassy lithium oxide-tellurium oxide systems are separated from the grain boundary contributions by the analysis of all admittance/impedance plots and presented as a log σ versus $10^3/T$ plot as shown in Fig. 3.7. The activation energies deduced from these DC plots are 0.49 eV and 0.79 eV for the polycrystalline and the glassy systems respectively.

After applying the exciting signal (v_1) at a particular frequency to the sample, the in-phase reference is carefully adjusted using the phase shifter to give a maximum voltage at the output. This voltage is used in the calculation of total AC conductivity at that frequency. Fig. 3.8 shows log (total AC conductivity) versus frequencies at 195°C of 40% Li_4SiO_4-60% Li_3VO_4.

3.5 OTHER POSSIBLE APPLICATIONS

The real (ε') and imaginary (ε'') components of the complex dielectric constant ε^* of ionic and electronic materials may also be determined from the same results obtained with non-reactive resistors as feedback elements using the relations

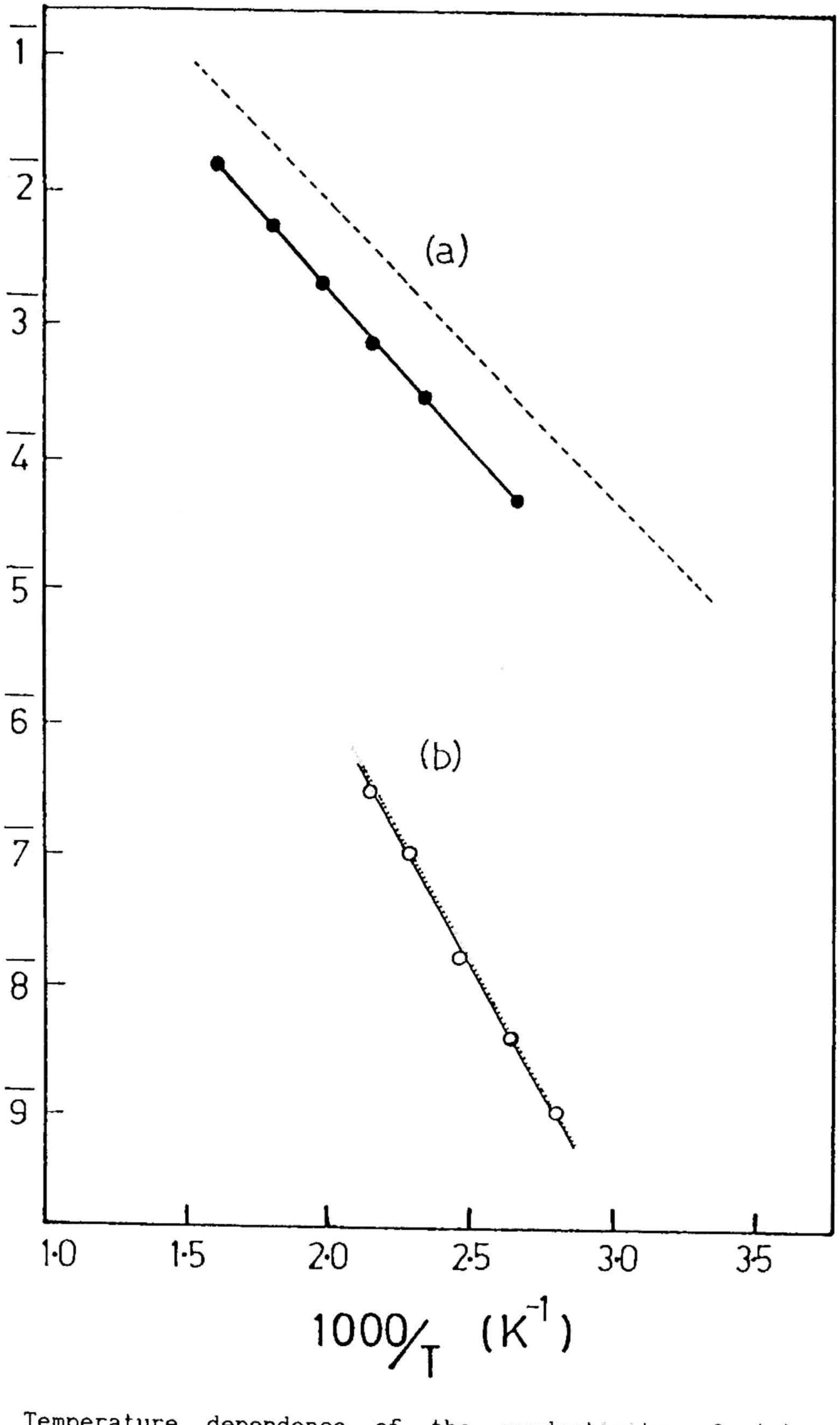

Fig. 3 7 Temperature dependence of the conductivity of (a) polycrystalline 40% Li_4SiO_4-60% Li_3VO_4 and (b) 30% Li_2O-70% TeO_2 glass, extracted from admittance/impedance plots at different temperatures, shown as Arrhenius (log σ versus $10^3/T$) plot. Dashed line: data of Khorassani and West[13]. The difference is due to the ageing effect on polycrystalline sample stored for about 3 years. Dotted line: data of Tanaka et al.[14]

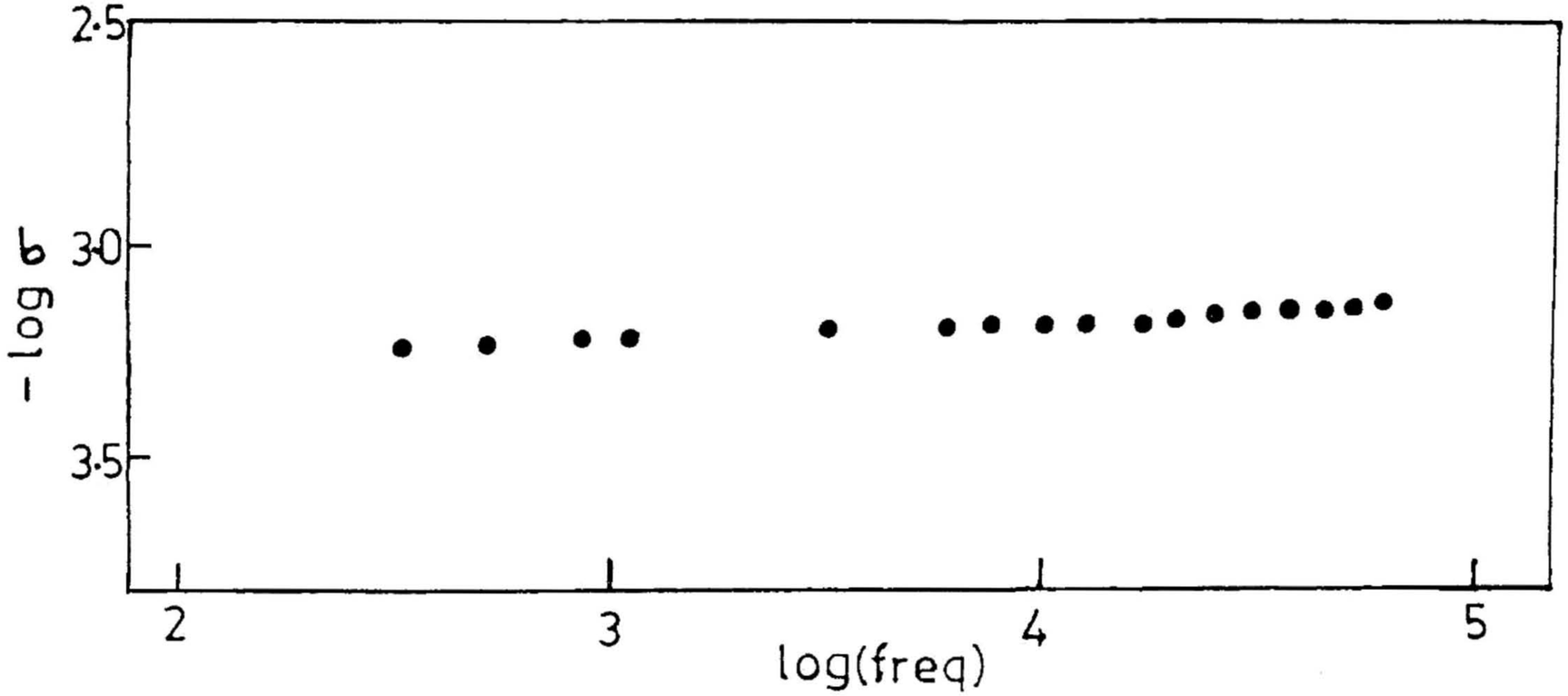

Fig 3 8 Frequency dependence of total AC conductivity of 40% Li_4SiO_4-60% Li_3VO_4 at 195°C shown as log σ versus log f plot

$$\varepsilon' = (\sigma''(\omega)/\omega\ \varepsilon_o \quad (5)$$

and

$$\varepsilon'' = (\sigma'(\omega))/\omega\ \varepsilon_o \quad (6)$$

One drawback of this direct calculation from conductivity results is that the measurement sensitivity falls with decreasing frequency. One could possibly solve this problem by using standard capacitors (such as HP Model 4040B) with negligible stray conductance as feedback elements instead of resistors. The results obtained with 0^o and 90^o phases as reference signals can now be directly used for the calculation of ε' and ε'' along the x and y-axes of the complex plane. The use of capacitors as feedback element (instead of resistors) is more advantageous because, suitable capacitors with virtually zero stray conductance (normally C_f = 10-100 pf) are more easily obtained than resistors of 10^1-10^7 Ω with negligible stray reactances.

3.6 CONCLUSIONS

An electronic system was specially designed and fabricated for the measurement of total AC conductivity and complex admittance/impedance. This system gives reliable and accurate data at various frequencies upto 60 kHz. Though the CVC technique was used by Nelson for the total AC conductivity measurement, the separation of real and imaginary parts of complex admittance/impedance from the distorted signal coming out of CVC, by a phase sensitive detector is new as far as our knowledge goes. The CVC technique for the AC conductivity measurement is also not well known in the field of superionic conductors. As these materials are very well known to have resistances (of the order of 10^6-10^8 Ω), at ambient temperatures, the conventional technique of connecting a standard resistor in series with the sample and measuring the AC voltage drop

across the sample, using the lock-in amplifier or the frequency response analyzer always introduces an impedance mismatch, whereas CVC which does not introduce any such thing would conveniently measure upto 200 MΩ (with R_f = 10 MΩ) at the lowest frequency possible. Application of this technique to a Li_2O-TeO_2 glass composition and Li_4SiO_4-Li_3VO_4 sintered polycrystalline pellet has helped isolate the grain boundary contribution to conductivity and deduce activation energies for Li^+ ion conduction. The PSD described here has definite advantages in terms of effective noise rejection, simplicity and low cost. These features permit construction of this instrument very easily even in small research laboratories.

REFERENCES

1 J B Wagner, in *Electrode Processes in Solid State Ionics*, ed by M Kleitz and J Dupuy (Holland, Reidel, 1976) p 185

2 S Chandra, in *Superionic Solids - Principles and Applications* (North-Holland Amsterdam, 1981) p 145

3 R N Nelson *J Phys* **E** *Sci Inst* **13** (1980) 376

4 H M Jones, in *A Practical Introduction to Electronic Circuits* (Cambridge, New York, 1985) p 186

5 J R McDonald in *Superionic Conductors*, ed by G D Mahan and W L Roth (Plenum, New York, 1976) p 81

6 J E Bauerle, *J Phys Chem Solids* **30** (1969) 2657

7 M L Meade in *Lock-in Amplifiers Principles and Applications* (Peter Peregrinus, London, 1983)

8 T Williams, *J Phys* **E** *Sci Inst* **3** (1970) 441

9 D P Blair and T H Sydenham, *J Phys* **E** *Sci Inst* **8** (1975) 621

10 Sthanapati, A K Ghoshal, A K Dey , A K Pal and S N Bhattacharya *J Phys* **E** *Sci Int* **10** (1977) 26

11 Fairchild, in *CMOS Data Book* (Schlumberger, California, 1977) Vol 7, p 102

12 Fairchild, in *CMOS Data Book* (Schlumberger, California, 1977) Vol 7,p 114

13 A Khorassani and A R West, *J Solid State Chem* **53** (1984) 369

14 K Tanaka, T Yoko, H Yamada and K Kamiya, *J. Non-Cryst Solids* **103** (1988) 250

15 A. Hooper, *J. Phys.* **D:** *App. Phys.* **10** (1977) 1487

CHAPTER 4

QUENCHED LITHIUM SULPHATE

4. QUENCHED LITHIUM SULPHATE

4.1 INTRODUCTION

Lithium Sulphate (LS) is a uniquely interesting compound among alkali-metal sulphates from the point view of structure and physical properties. It belongs to the monoclinic crystal class (β-phase) at ambient, (a = 8.239, b = 4 954, c = 8 474, $\beta = 107^{o}98'$) but undergoes a first-order reconstructive phase transition to an FCC (α-phase) at $575^{o}C$. Fig. 4 1 shows the partial X-ray pattern of Li_2SO_4, depicting the drastic changes in Bragg angles and intensities of diffraction peaks during the transition $\alpha \longrightarrow \beta$ Li_2SO_4[1]. Cubic LS has very high ionic conductivity ~ 3 S cm^{-1} close to its melting point $860^{o}C$ ascribable to the high mobility of lithium ions[2], whereas the monoclinic phase[3] has a much lower conductivity ($\sigma T \sim 10^{-10}$ S cm^{-1} at $100^{o}C$, obtained by linear extrapolation as shown in Fig 4 2). While the Li^{+} ions are highly mobile in the FCC phase, the sulphate ions form a translationally fixed lattice. Both the volume change (4 5%)[4] and the latent heat are much larger at the phase transition than at the melting point ($\Delta H_t \approx 4\ \Delta H_f$)[5] signalling a considerable orientational disorder of sulphate groups in the cubic phase. The heat capacity measurement around the temperature of fusion of Li_2SO_4[6] suggested the existence of premelting phenomena[7], which evidenced the plastic phase before its fusion. Thus, while the ambient phase is elastic, insulating and crystallographically ordered, the high-temperature FCC phase is plastic, superionic and disordered with respect to Li^{+} positions and SO_4^{2-} motions implying that the sulphate tetrahedra in the α-phase are matrix isolated unlike the germanate in $Li_{4-3x}Al_xGeO_4$ solid solutions where the framework is an interconnected, three-dimensional polymer[8].

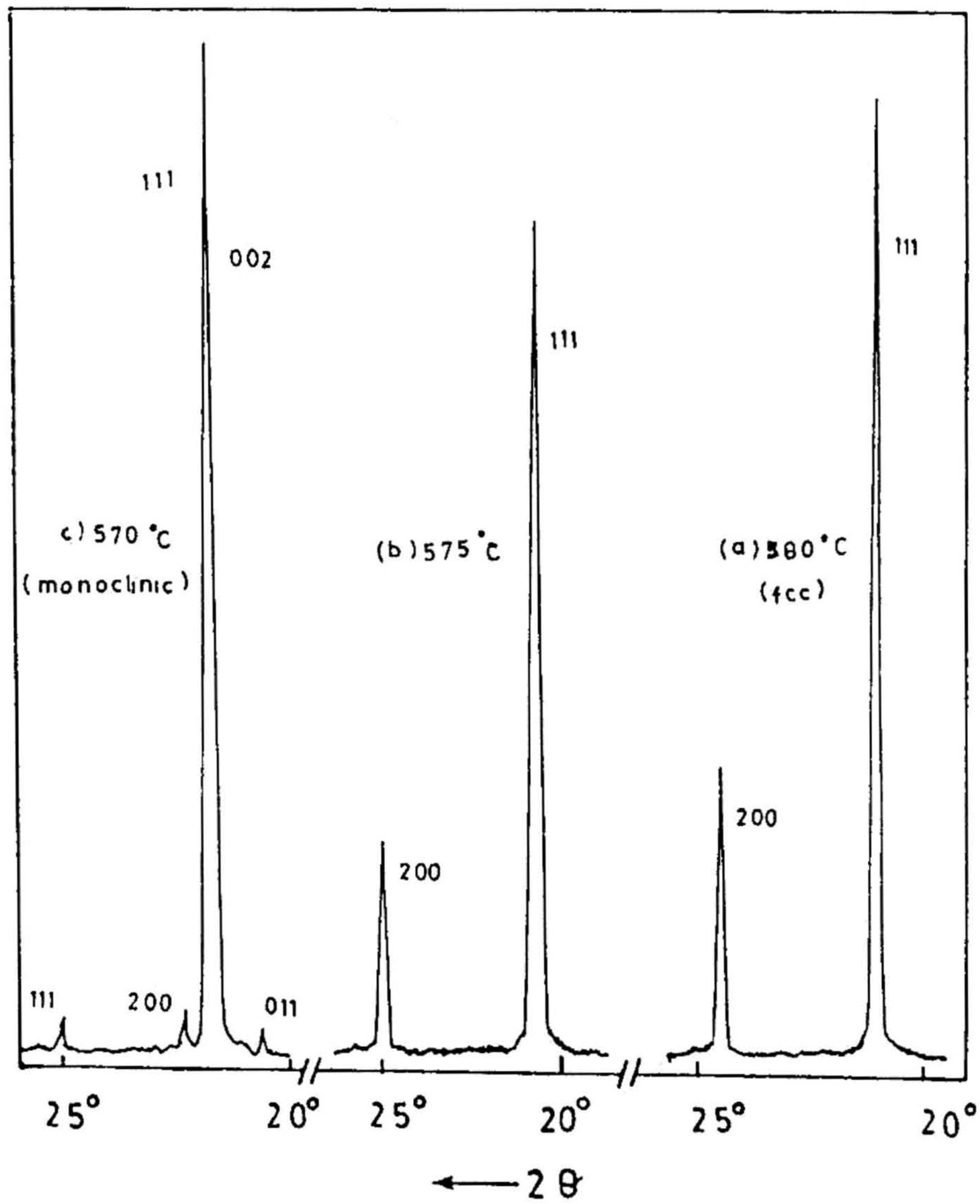

Fig 4.1 X-ray powder patterns showing transition $\alpha \longrightarrow \beta$ Li_2SO_4

(a) 580°C, Only the 111 and 200 peaks representing the pure FCC phase are seen

(b) 575°C, The 111 peak is disturbed by a new peak at $2\theta = 21.7^{\circ}$ This shows that a pert of the sample has transformed into a low temperature modification

(c) 570°C The pattern now represents a monoclinic phase

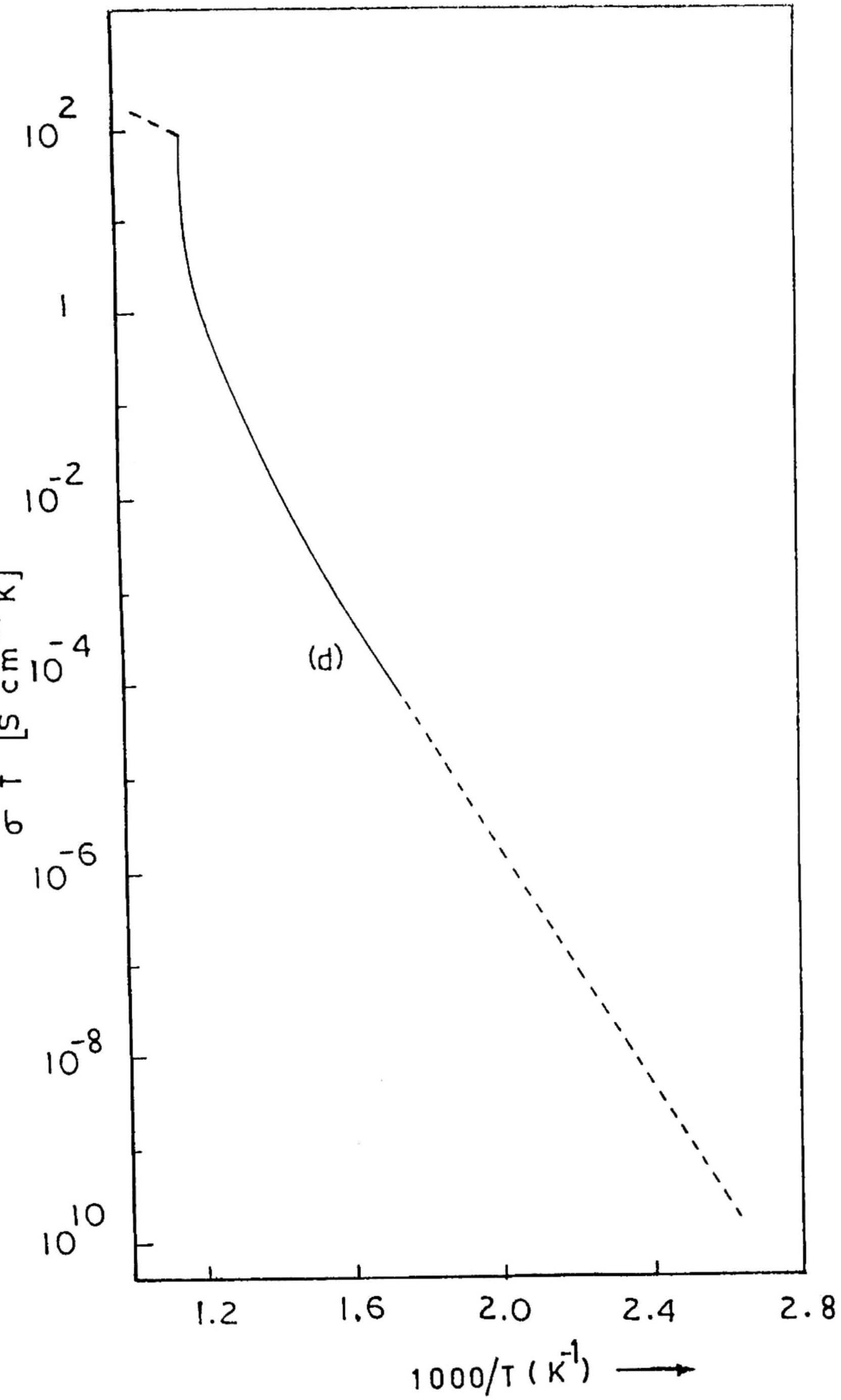

Fig 4.2 Temperature dependence of the conductivity for the polycrystalline Li_2SO_4 The dotted line represent the extrapolation of the conductivity to low temperature region

The feature common to most solid electrolytes as we discussed in Section 1 2 is a large value for the ratio of available lattice sites to the number of charge carrying ions It has been suggested (see Chapter 1) that an appropriate value for this ratio, should not be less than 3, and a solid electrolyte with a ratio of 2 is unlikely However, the high- temperature modification of Li_2SO_4 constitutes a notable exception with a lattice site to Li^+ ion ratio of 1 5, and yet having a very high Li^+ conductivity

The high ionic conductivity is closely related to the structure of the compounds Also, it is characteristic for superionic conducting phases that ions of the 'right' size are much more mobile than other ions Thus, in β-alumina Na^+ ions are more mobile than the larger K^+ or the smaller Li^+ ions (see Chapter 1) In contrast to this observation all mono and divalent cations (e g , Ag^+, Na^+, Mn^{2+}, Zn^{2+} etc ,) have a high mobility in the FCC Li_2SO_4 phase Thus, in α-phase the diffusion coefficients are of the order of 10^{-5} S^{-1} cm^2 for monovalent and 10^{-6} S^{-1} cm^2 for divalent cations[9] This clear advantage increases the choice of anode materials, in power source applications

4 1 1 Structure of α-Li_2SO_4: X-ray Diffraction Studies

Forland and Krogh-Moe[10] proposed the first structural basis of the high-temperature Li_2SO_4 The X-ray pattern showed a very small number of sharp lines They found the high-temperature structure to be FCC with a = 7 07 Å and from space-group consideration, suggested the following two models

Model A

S = (0, 0, 0)

O = (x, x, x), (x, $\bar{x}$, $\bar{x}$), ($\bar{x}$, x, $\bar{x}$), ($\bar{x}$, $\bar{x}$, x)

Li = two of the three sets of coordinates

(1/4, 1/4, 1/4), (3/4, 3/4, 3/4), (1/2, 1/2, 1/2)

The S-O distance of 1.50 Å would result in a x-value of 0.12 Å. A lithium ion at (1/4, 1/4, 1/4) or (3/4, 3/4, 3/4) would be tetrahedrally coordinated by SO_4^{2-} ions while at (1/2, 1/2, 1/2) it would be octahedrally coordinated (see Fig. 4.3). This cell assumes ordered sulphate ion orientations with non-centrosymmetric space group $F\bar{4}3m$.

Model B

S = (0, 0, 0)

O = (√2x, √2x, x), (-√2x, -√2x, x), (-√2x, √2x, -x), (√2x, -√2x, -x)

Li = (1/4, 1/4, 1/4), (3/4, 3/4, 3/4)

This leads to Li-O distances of 2.06 Å, with all lithium ions now tetrahedrally coordinated by oxygen and O-O distances for different sulphate group of 3.18 Å, such a structure is purely FCC only when there is disorder among orientations of SO_4^{2-} groups.

4.1.2 Structure of α-Li_2SO_4. Neutron Diffraction Studies

Nilsson et al.,[11] used powder neutron diffraction (PND) to determine the structural characteristic of high-temperature phase and in particular the spatial distribution of the Li^+ ions and possible orientational preference of sulphate ions with the aim of establishing the ionic conduction mechanism in the α-phase. The PND pattern showed

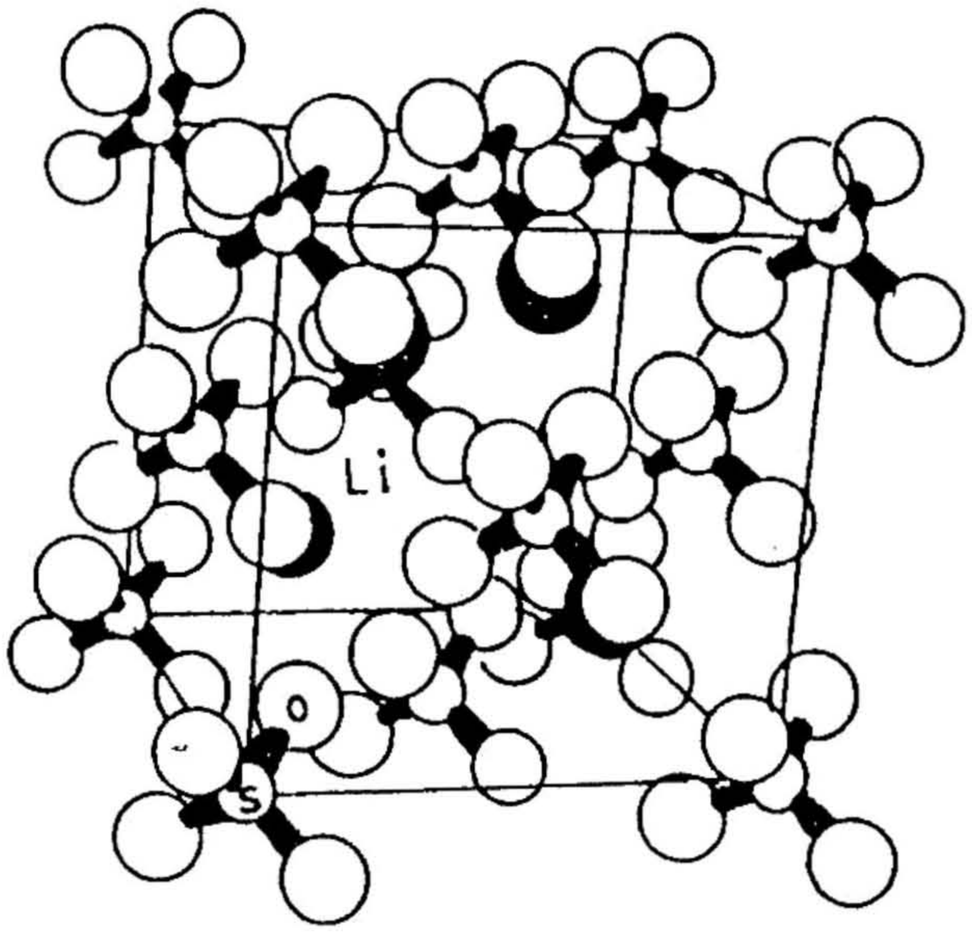

Fig 4.3 A schematic illustration of the ordered model $F\bar{4}3m$ of FCC Li_2SO_4

Bragg peaks superimposed on broad 'liquid-like' background, consisting of atleast three wide humps as shown in Fig 4 4, and was suggested that the oxygen atoms are the main source of the background

The PND study established the α-phase structure as a FCC (a = 7 07 Å) with SO_4^{2-} ion situated at the origin and the oxygen atoms rotationally disordered about the sulphur atom The neutron data additionally demonstrated the location of Li^+ ion around (1/4, 1/4, 1/4) tetrahedral rather than (1/2, 1/2, 1/2) octahedral site showing that the high-temperature LS has a structure very closely related to the antifluorite structure It is to be noted that the antifluorite structure-just as the fluorite structure-also favours fast-ion conduction (see Chapter 1)

Several series of refinements of neutron diffraction data were made based on disordered models, involving rotational disorder of sulphate groups with centrosymmetric space group Fm3m Neutron data very strongly support the model of highly orientationally disordered sulphate groups, which is illustrated in Fig 4 5

The neutron diffraction experiment also revealed that Li^+ ions occupy the ± (1/4, 1/4, 1/4) positions in the unit cell, while the (1/2, 1/2, 1/2) position is unoccupied by Li^+ The (1/2, 1/2, 1/2) position merely lies on the transit path of the diffusing Li^+ ion, and the latter moves in the vicinity of this position for a period which is short compared to time spent in the ± (1/4, 1/4, 1/4) positions

4 1 3 Structure of Molten Li_2SO_4

Ohno[12] examined the structure of molten Li_2SO_4 by considering the

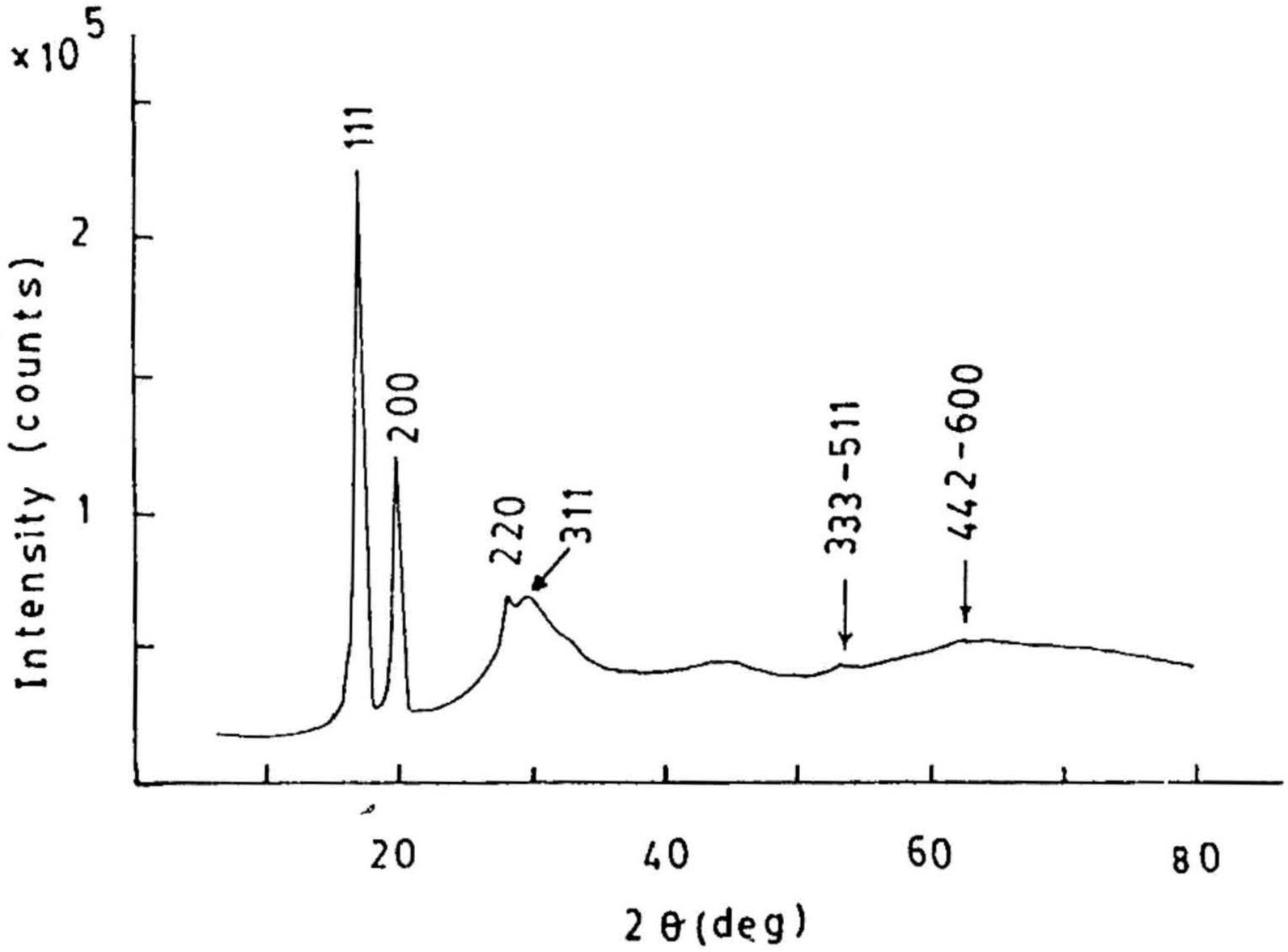

Fig. 4.4 Neutron diffraction profile of FCC Li_2SO_4 at 635°C The profile consist of a liquid-like background upon which the Bragg reflections are superimposed

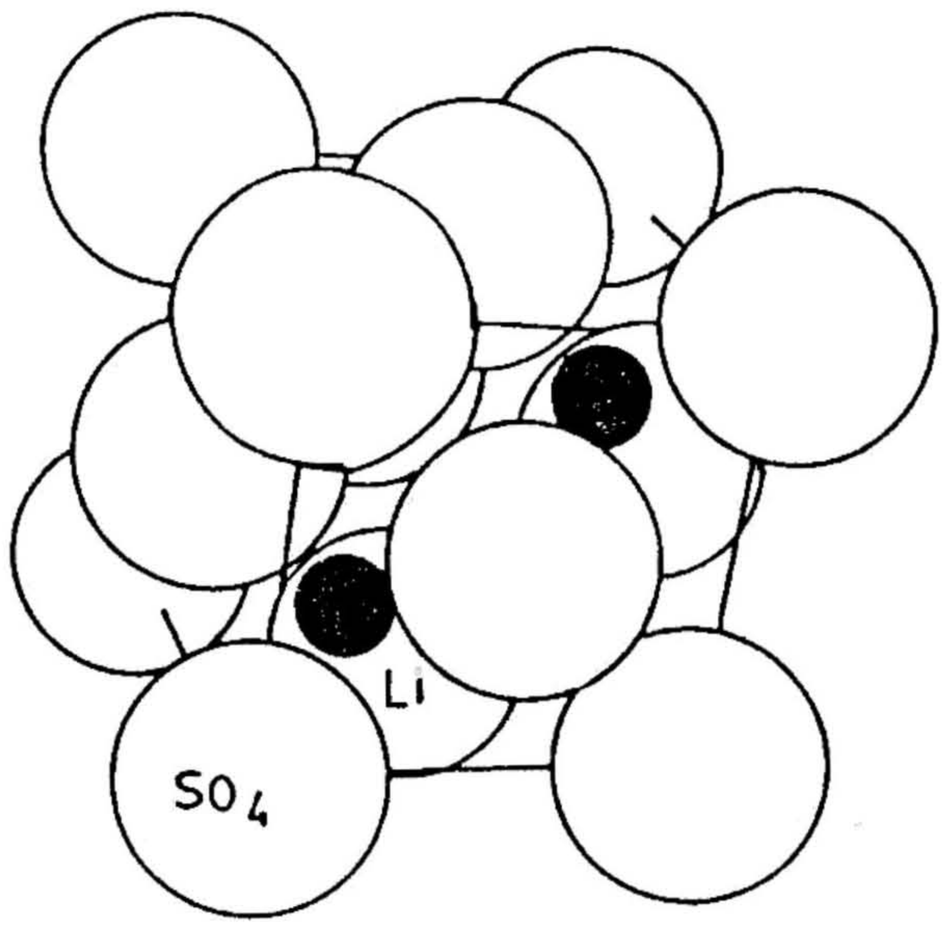

Fig 4.5 A stereoscopic illustration of the disordered model Fm 3m for the structure of α-Li_2SO_4 at 635°C

radial distribution function from X-ray diffraction and the molar volume The existence of tetrahedral SO_4^{2-} ions was demonstrated by the analysis of the first peak in the radial distribution function S-O and O-O distances for the sulphate ion in the molten state are 1 50 Å and 2 45 Å respectively

4 1 4 Ion Transport Mechanisms in α-Li_2SO_4

Two possibilities have been suggested for the conduction of Li^+ ions in FCC-Li_2SO_4 The paddle-wheel mechanism of Lunden[13,14] and percolation-type mechanism of Secco[15,16] Lunden suggests that the strongly coupled rotation of SO_4^{2-} ions to the Li^+ ions, the cogwheel' or 'paddle-wheel' mechanism is mainly responsible for higher cation mobility and thus very high conductivity

Brillouin scattering studies reveal[17] plastic behaviour and low transverse sound velocities, attributed to possible rotational-translational coupling, i e , interaction between transverse model oscillations and reorientations of sulphate ions thus supporting the paddle-wheel concept

The dynamics of Li^+ ions and sulphate ions in the superionic phase of Li_2SO_4 have been investigated by analyzing spectral line shapes using Raman spectroscopy[18] The component due to sulphate ion reorientation is separable by comparison of polarized and depolarized spectral bandwidths for the symmetric (A_i) internal mode of sulphate group The reorientation time derived thereby, for FCC Li_2SO_4 corresponds well with the value 2 ps reported on the basis of molecular dynamics simulation[19] The Arrhenius activation energy 0 40 eV obtained from

the temperature dependence of reorientation time is sufficiently close to activation energy for cation diffusion 0 34 eV, thus supporting the 'paddle-wheel' mechanism

The solid solution of α-Li_2SO_4 with 2 5 mole% Li_2CO_3 yielded diminished Li^+ conductivity This has been attributed to the replacement tetrahedral SO_4^{2-} ions with planar CO_3^{2-} groups, thereby reducing the effect of reorientational disorder of the SO_4^{2-} group on the Li^+ mobility[20] We would like to comment here that only an experiment which looks at the Li^+ and SO_4^{2-} motions simultaneously could reveal the actual mechanism for Li^+ conduction

The second model of Secco, invokes "free volume' or 'excluded volume' availability in the structure and easy conduction paths created thereby for Li^+ motion, based on results of electrical conductivity and differential scanning calorimetry (DSC) measurements on Li_2SO_4 incorporating WO_4^{2-} as guest ion in SO_4^{2-} sublattice A 'gate' concept was recently introduced[16] in which the rotating sulfate anions in Li_2SO_4 may contribute to the conductivity with Li^+ cation but indirectly by increasing the probability of a successful translational jump, when favourable instantaneous orientations of the SO_4 oxygens occur at the transport 'bottleneck" acting as a gate That is, the gate action of the percolation mechanism assigns a passive role for SO_4 reorientation in simply allowing passage of the cation with no transfer of momentum

Recently the structural and dynamical aspects of α-Li_2SO_4 have been calculated[21] on a model employing orientationally averaged sulphate-sulphate interaction potential The calculated mobility of Li^+

and the structure agrees, well with the experimental data indicating that the paddling effect of the sulphate tetrahedra on Li^+ ion mobility is less important and that the ion transport process is mainly through the percolation mechanism

FCC Li_2SO_4 appears to have the best lithium ionic conductivity above 575°C However, this temperature is still too high for its practical application as a solid electrolyte in lithium batteries While α-AgI has been stabilized at room temperature in a Ag_2O-B_2O_3 glass matrix[22] it is worth mentioning that no such ambient temperature modification of Li_2SO_4 is available that could impart a high enough Li^+ conductivity

Stabilization of the plastic, α-phase of Li_2SO_4 at ambient is thus an alluring prospect from the following points of view

(1) It would offer the possibility of conveniently characterizing the cubic structure by powder X-ray/neutron diffraction at room temperature

(2) It would enable development of an optimally conducting superionic phase at ambient, usable as a battery system

(3) Most importantly, the dynamical aspects of the high-temperature phase such as SO_4^{2-} reorientational motion, could be conveniently investigated in the frozen α - phase, and

(4) A detailed study of FCC phase stabilized at room temperature might help resolve the existing controversy about the mechanism of Li^+ conduction in the superionic phase

Only a few reports exist on the stabilization of high-temperature phases of ionic conductors at ambient temperature. Hooper et al [23] succeeded in stabilizing the high temperature cubic ν-Na_3PO_4 phase at room temperature (as characterized by XRD), upon addition of $AlPO_4$ into tetragonal α-Na_3PO_4 to form $Na_{3(1-x)}Al_xPO_4$, with $x \geq 0.1$. However, enhancement of conductivity was not achieved.

Sigaryov and Vasiulev[24] achieved an enhanced Na^+ conduction in $Na_3In_2(PO_4)_3$ by quenching it from 1277°C, (a temperature close to its melting point), compared to the slowly cooled $Na_3In_2(PO_4)_3$. Powder XRD yielded a larger cell volume with no difference in their structure, thus confirming a more disordered state of the quenched $Na_3In_2(PO_4)_3$. The infra-red (IR) spectral investigation suggested that the static disorder[25,26] of PO_4 tetrahedra is frozen upon quenching from high temperature.

In this chapter we report the results of our investigations on the melt-quenched Li_2SO_4 H_2O, through XRD, DSC, electrical conductivity, IR and electron spin resonance (ESR) spectroscopy in order to obtain information about the structural and dynamical aspects of the metastable phase(s) induced by quenched-in disorder through the combined effects of temperature and internal pressure. Following upon our initial effort[27], the present study focuses on (i) the optimization of the cubic phase, (ii) the thermodynamic characterization of the cubic phase, (iii) the molecular disorder as they relate to enhanced Li^+ conductivity obtained by quenching and (iv) the role of ionic/molecular impurities in cubic-phase stabilization.

4.2 EXPERIMENTAL

The quenched samples were obtained by supercooling the melt of Li_2SO_4 H_2O 'Loba' (LSL), (laboratory reagent with 98% purity) on a stainless steel slab kept at various temperatures (T_q). These quenched bulk samples are immediately transferred to an annealing furnace maintained at a temperature (T_a) mentioned below and were isothermally annealed for about 4 hours under a reduced pressure of 10^{-2} torr.

The samples are designated as follows:

QL_{100} ($T_{quenching} = 100^{\circ}C$, $T_{annealing} = 100^{\circ}C$)

QL_{200} ($T_q = 200^{\circ}C$, $T_a = 200^{\circ}C$)

and QL_{300} ($T_q = 300^{\circ}C$, $T_a = 300^{\circ}C$)

In order to check the reproducibility of the results of 'Loba' samples attempts were also made to quench the melt of the 'Alfa' Li_2SO_4 H_2O (LSA) mixed with 2 mole% of Li_2CO_3 (Alfa) which also belongs to the monoclinic class. The melt quench (at $200^{\circ}C$) of this sample, annealed at $200^{\circ}C$, for 4 hours under vacuum is denoted as QAC_{200} (2% Li_2SO_4)

Quenching experiments were also carried out on pure 'LSA" from both melt and high temperature solid state where the sample was isothermally hold at $650^{\circ}C$ for 10 hours.

The different crystalline phases that are stabilized in these quenched samples were characterized by powder X-ray diffraction recorded at room temperature with a Seifert X-ray powder diffractometer using Ni-filtered Cu-Kα radiation at 1.2°/min in the range 5°-80°. Data analysis was done using the "POWD" software.

The thermal behaviour of samples was investigated using Du Pont 9900 differential scanning calorimeter Measurements were performed under argon atmosphere on both bulk and powdered forms of quenched samples of mass 20 mg encapsulated between aluminum pans The temperature was calibrated and cell constant of the instrument determined for a heating rate of 20^{o}C/min as mentioned in the Chapter 2

Two-terminal AC electrical conductivity measurements were performed on monolithic parallelopipeds obtained by quenching The bulk DC conductivity of these samples were derived from the complex admittance analysis of the data collected using the instrumental set up, (Fig 2 4) over the frequency range 100 Hz - 120 KHz The conductivity measurements were performed in the temperature range 30-300^{o}C, under a vacuum of 10^{-2} torr with silica gel serving as moisture absorber

The IR spectra were recorded with a Perkin-Elmer double beam spectrophotometer (Model No 297)using the standard KBr disc technique in the frequency range 4000-200 cm^{-1} First derivative ESR spectra on X-irradiated quenched bulk ingot were recorded on a X-band JEOL ESR spectrometer (Model FX-3X) at -196^{o}C, room temperature and at selected high temperatures

4 3 RESULTS AND DISCUSSION

4 3 1 X-ray Diffraction

Melts of LSA and QAC_{200} (2% of Li_2CO_3) quench to a milk coloured product of poor mechanical strength, while melts of LSL yield strong smooth yellowish bars on quenching Fig 4 6 compares the powder XRD pattern of QL_{200} bulk ingot with that of LSL powder (with monoclinic structure) recorded at RT The pattern of QL_{200} consists of a very

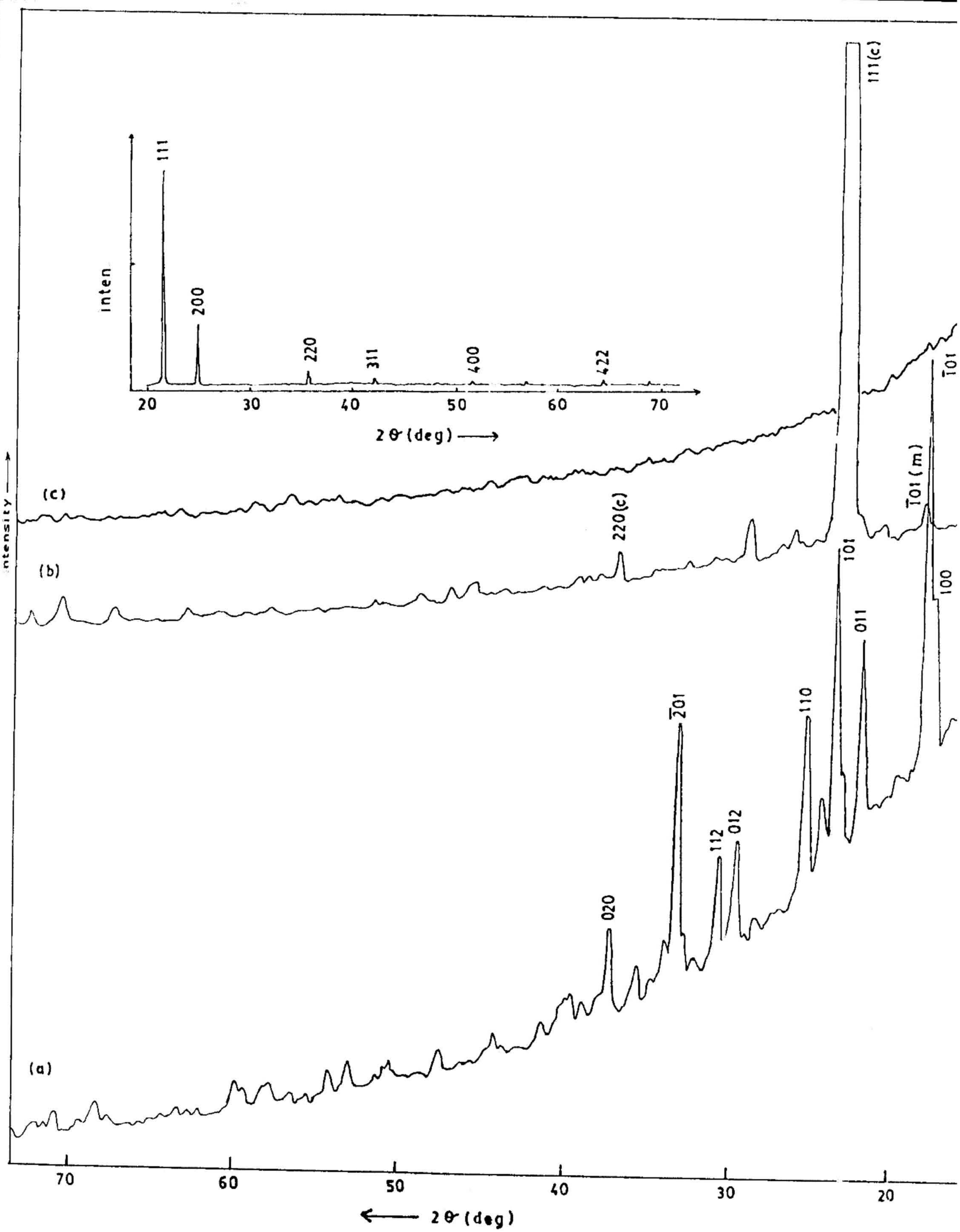

Fig. 4.6 X-ray powder diffraction patterns of (a) LSL (monoclinic), (b) QL_{200} (predominantly FCC) and (c) QL_{300} (diffuse structure characteristic of non-crystalline or micro-crystalline nature). The insert is the diffraction profile of FCC Li SO

intense (111) reflection and other very weak reflections characteristic of the FCC (plastic) phase, in excellent agreement with the pattern obtained at 610°C for FCC Li_2SO_4 [28] A few very weak lines are also seen, indicating a few percent of a second phase - most probably the monoclinic phase On the basis of a careful comparison of the intensity of reflections of FCC phase with those of the weak reflections due to the presence of monoclinic phase, we conclude that the major phase which is stabilized by quenching is an orientationally disordered cubic structure Fig 4 6c presents the pattern recorded for QL_{300} - a diffuse background with no reflections suggesting that QL_{300} is poorly crystalline and is most probably representative of a micro-crystalline structure

Fig 4 7 presents the XRD patterns of (a) LSA quenched from high temperature solid state (sintered at ~ 650°C), (b) QL_{200} ground into powder, and (c) QAC_{200} (2% of Li_2CO_3) While quenching from the high-temperature solid state of "LSA gives a mixture of very short lived (~ a few days) minor cubic phase with major monoclinic phase as shown in Fig 4 7a, quenching from its melt produces a thin glassy layer deposited on a polycrystalline crust (which as before contains a minor fraction of the cubic phase) The glassy layer - however, is not thick enough to permit us for further characterization Although QL_{200} quenched bulk ingot is predominantly cubic, the powdering of this specimen, however gives a complex diffraction pattern as seen from Fig 4 7b Table I shows the indexing of the observed lines, corresponding to the cubic phase The unit cell parameter determined for the cubic phase using least square fitting program is 6 98 Å a value slightly lower than 7 07 Å, reported for the FCC phase at 610°C The monoclinic phase (M),

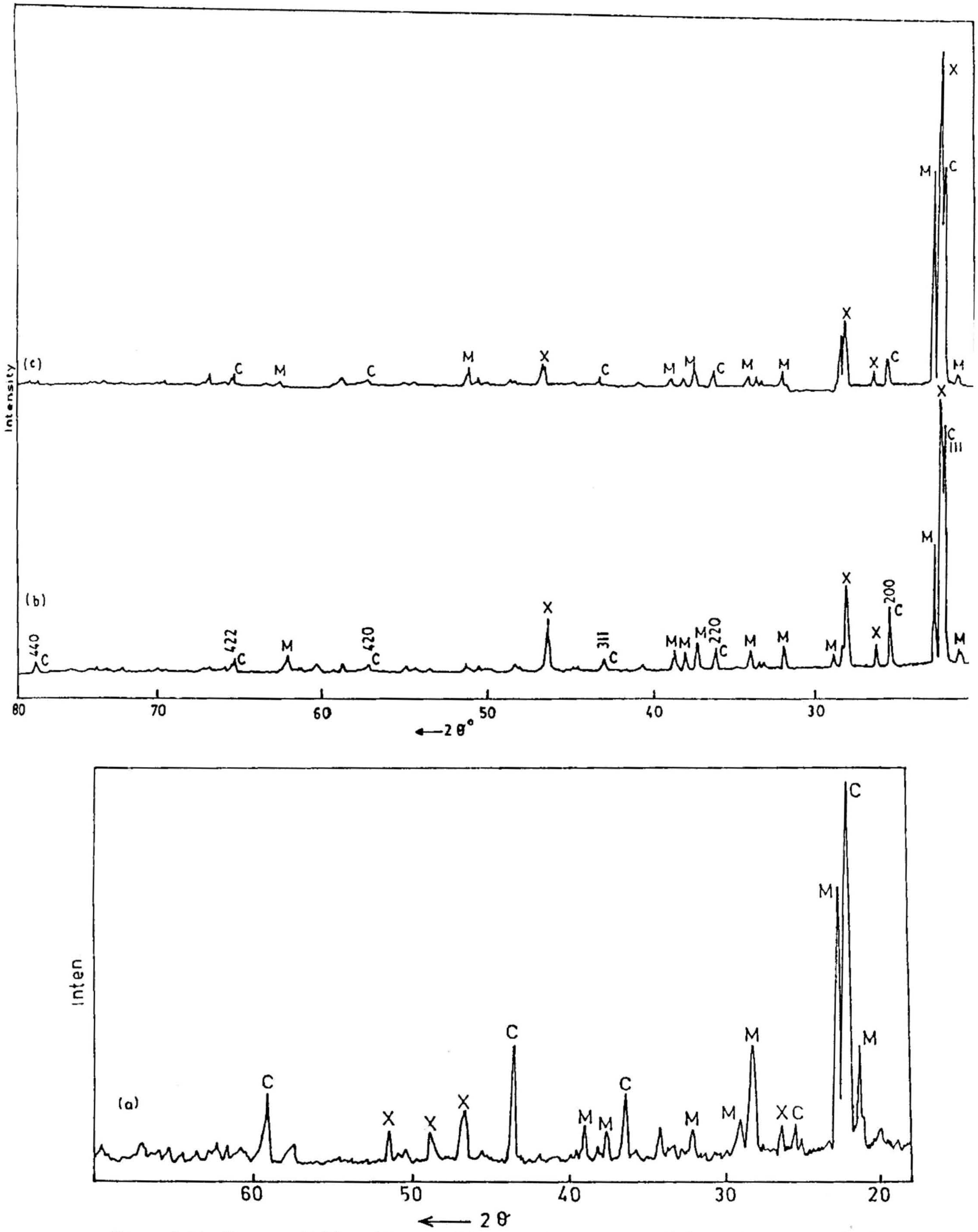

Fig 4.7 X-ray diffraction patterns of samples (a) LSA quenched from high-temperature solid state (~ 650°C), (b) QL_{200} ground into powder and (c) QAC_{200} (2% of Li_2CO_3)

TABLE I

Powder X-ray data of FCC phase (a = 6 98 Å) stabilized in quenched

$Li_2SO_4\ H_2O$ (QL_{200} - pulverized)

d_{obs}	d_{cal}	hkl	Δd
4 0311	4 0311	111	0 000
3 4930	3 4910	200	0 002
2 4781	2 4685	220	0 009
2 0918	2 1051	311	0 013
1 5703	1 5612	331,420	0 009
1 4256	1 4252	422	0 000
1 2319	1 234	440	0 002

appears along with cubic phase on pulverization There also remain a number of unidentified lines which indicated the presence of another additional phase (X) Attempts to fit these lines to the known patterns of pure reagents ($Li_2SO_4 H_2O$, Li_2SO_4 and Li_2CO_3) failed, indicating that this phase is indeed a by-product of quenching and pulverization Fig 4 7c shows the diffraction pattern of QAC_{200} (2% of Li_2CO_3) Significantly this pattern is exactly similar to that of QL_{200} ground into powder

These observations suggest that it is impossible to stabilize the cubic phase of Li_2SO_4 by quenching pure starting material (e g , "LSA") either from the high temperature solid-state or from the melt The predominantly cubic phase stabilization could be achieved only by super cooling the melt of 'LSL', where Li_2CO_3 which is present as a congenital impurity acts as the sulphate network modifier,increases the viscosity of the melt considerably, and thus arrests the cubic phase at ambient during quenching We could not succeed in stabilizing a predominantly cubic structure, by deliberately introducing CO_3^{2-} into LSA, eventhough its powder XRD pattern agreed well with that of powdered QL_{200}

4 3 2 Differential Scanning Calorimetry

The DSC curve of nominally pure LSL (Fig 4 8a) revealed the phase transition as an endothermic doublet peaking at 552 and 570°C But if LSL was either ground very well or slowly cooled from melt, we could not notice these double transitions for the phase transformation, and hence, we suspect that these two endotherms could be due to the inhomogeneous mixing of LSL at its preparation stage

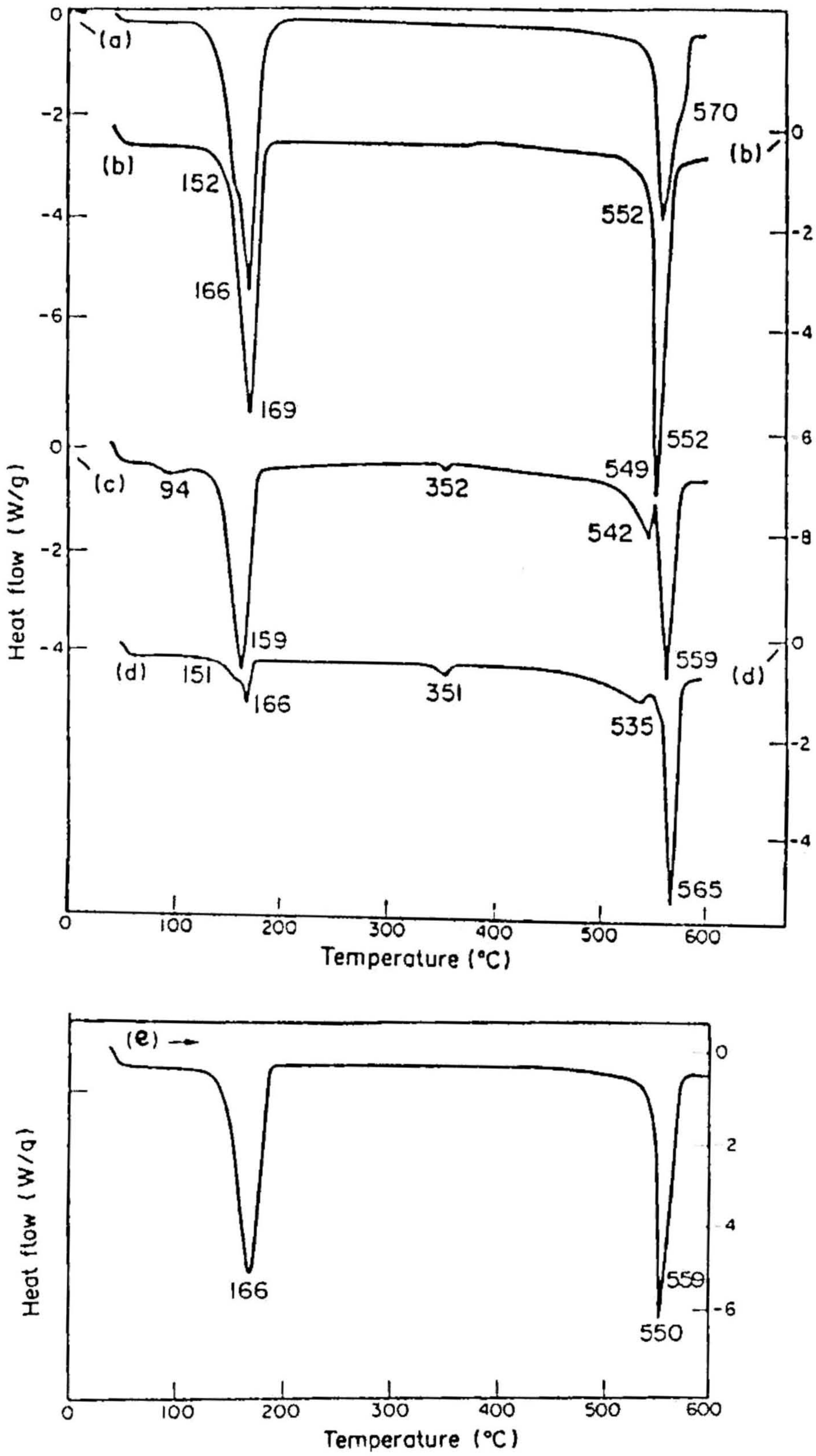

Fig 4.8 DSC scans for $Li_2SO_4 H_2O$ and quenched melts in the temperature range 30-600°C (a) LSL, (b) QL_{100}, (c) QL_{200}, (d) QL_{300} and (e) aged QL_{300} powder. Note the absence of intermediate temperature peak in (e) and the growth of dehydration peak around 166°C.

Fig 4.8(b,c,d) shows the thermal behaviour during the DSC scans on bulk pieces of QL_{100}, QL_{200} and QL_{300}. The quenching and annealing of QL_{300} at 300°C, favoured an almost complete dehydration compared to QL_{100} and QL_{200}. Also the second phase transition observed in LSL, has disappeared, and the first endotherm due to the phase transition at 552°C, has shifted to higher temperatures upon increase of quenching temperature. It is to be noticed that additional endotherms have now appeared: one at 350°C and another in the temperature range 530-550°C. While the hump just before the phase transition in QL_{100} has almost merged with the transition at 552°C, they are clearly seen as broad humps in the case of QL_{200} and QL_{300}. The areas under both of these new endothermic features increase upon increasing the quenching temperature. The DSC scan of QL_{300} powder stored at ambient for a few days (whose XRD pattern resembles well that of monoclinic structure), exhibits considerably altered events as shown in Fig 4.7e. The dehydration peak of this stored QL_{300} powder becomes very intense and the intermediate endotherms at 351 and 535°C of QL_{300}, have now disappeared completely. These changes are attributed to the inherent instability, due to pulverization of the phase stabilized upon quenching. Release of internal pressure probably destabilizes the cubic phase, while increase of surface area results in moisture absorption.

Recently Di and Bakker[29] have reported that on grinding upto 60 hours at ambient of the A-15 intermetallic compound Nb_3Au in a high-energy ball mill transformed to the high temperature BCC phase (identified by XRD studies). DSC of this sample revealed an exothermic peak around 730°C, corresponding to a phase transition from the metastable BCC to the A15 structure. Such an exothermic event characterizing the transition from cubic to monoclinic phase was not

observed in the present case during thermal treatment However, the FCC phase stabilized at ambient (by quenching) is a thermodynamically metastable state and hence, it always tends to change to a stable one upon heating through certain molecular relaxational processes[30a,30b] When QL_{200} was gradually heated upto 650°C and cooled slowly the intensity of (111) reflection of FCC phase decreased on the other hand the intensity of reflections belonging to the monoclinic phase correspondingly increased These changes in intensity during the heating process along with the observation, of the disappearance of the intermediate endotherms at 351°C and 535°C in the DSC scan of QL_{300} powder aged at ambient for a few days suggest that the endotherms at 351°C, and around 530-550°C are likely to be associated with the atomic migration triggered by structure Thus these endotherms represent a two step destabilization of the cubic phase, and provides unequivocal thermodynamic characterization of the stabilized α-phase

4.3.3 Electrical Conductivity

Fig 4.8 presents the plot of log σT versus $10^3/T$ of QL_{100} and QL_{200} These results refer to measurements made on samples after three months of their preparation QL_{100} and QL_{200} showed a very high conductivity (σT) ~ 5 to 6 orders of magnitude higher compared to that of polycrystalline 'LS' at 100°C The activation energy of QL_{10} and QL_{200} are calculated to be 0.42 eV, and 0.40 eV respectively These values are very close to the earlier published values of 0.43 eV[31,32] for polycrystalline α-Li_2SO_4 but much lower compared to 1.2 eV[33] and 1.4 eV[3] for the monoclinic phase Since Li_2CO_3 is soluble upto 10 mole% in the cubic phase of Li_2SO_4[34] it is important to note that the high conductivity achieved by quenching is not due to the two phase

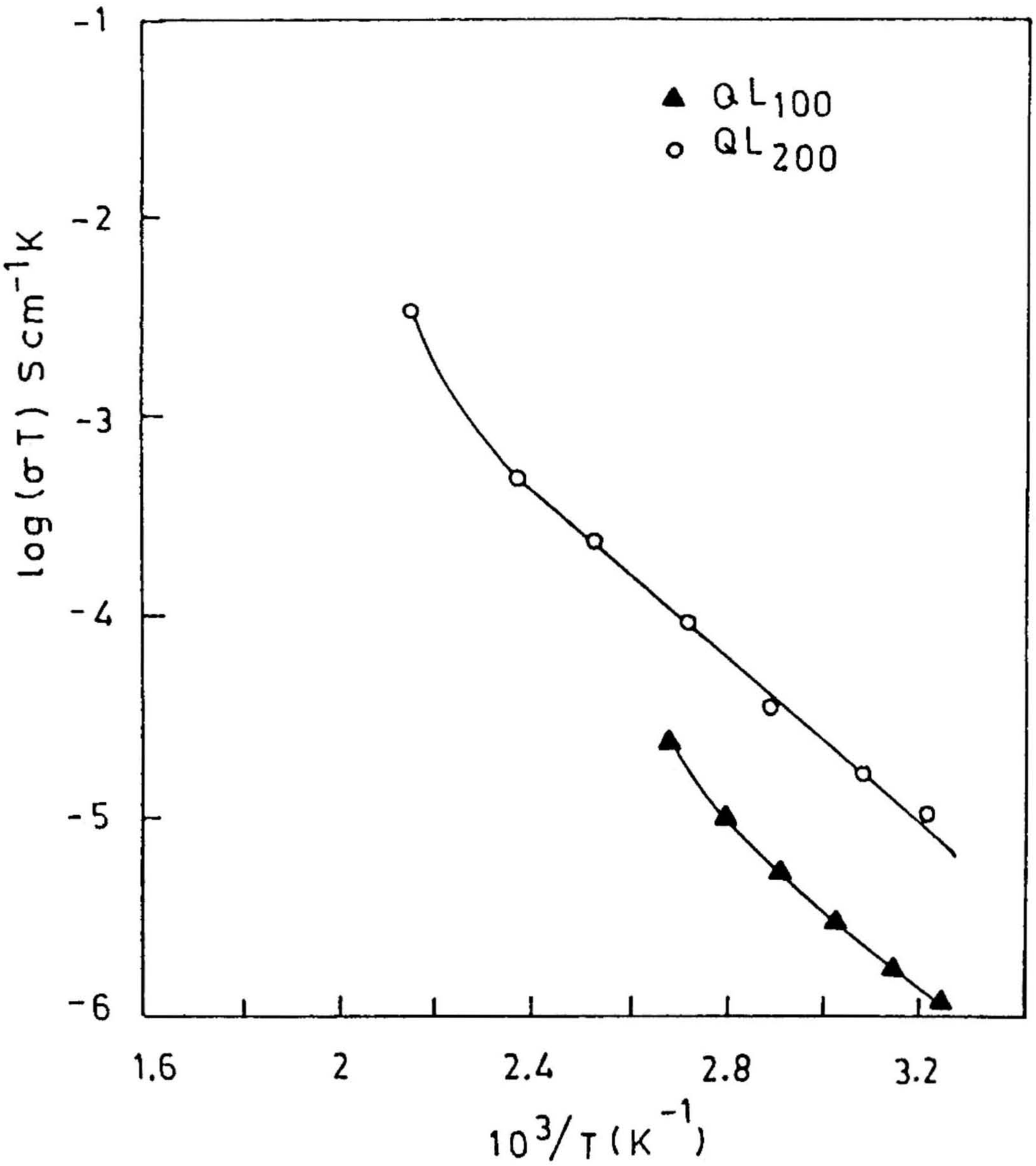

Fig. 4.9 Temperature dependence of the conductivity of quenched Li_2SO_4 samples QL_{200} has yielded the maximum conductivity The upper limit for temperature was set by the quenching temperature T_q

composite formation[35,36] The higher conduction and lower activation energy observed in these quenched systems are mainly due to the presence of highly conducting α-phase stabilized at ambient temperature Interestingly, we could also stabilize the FCC Li_2SO_4 by addition of 2% $Fe_2(SO_4)_3$ to 'LSA

A comparison of the conductivities measured on a freshly prepared QL_{300} and on a QL_{300} stored for about three months revealed that σT of only the former but not the latter is higher than those of QL_{100} and QL_{200} reflecting that a maximum amount of cubic phase is stabilized in QL_{300} But such an optimal stabilization of cubic phase at ambient was found to be highly unstable and changes to a state of microcrystalline structure (having lower σT compared to that of freshly prepared QL_{300}) with the crystallite size too small to yield a diffraction pattern However, since no crystallization peak (T_x) was found during the thermal scanning by DSC, the structure is not truly amorphous either This microcrystalline sample with a structure intermediate between FCC and the non-crystalline, transforms into monoclinic structure in a non-reconstructive way through the endotherms at 350°C and 535°C without showing any T_x

Fig 4 9 shows the relation between log σT versus $10^3/T$ of QL_{300} The conductivity behaviour of this microcrystalline sample shows two Arrhenius region (activation energies being 1 13 and 0 05 eV respectively), the knee separating the two shifting to higher temperatures upon prolonged annealing The isothermal annealing was performed at a temperature slightly higher than the endotherm at 352°C for different periods of time As a result, the slope of the high-

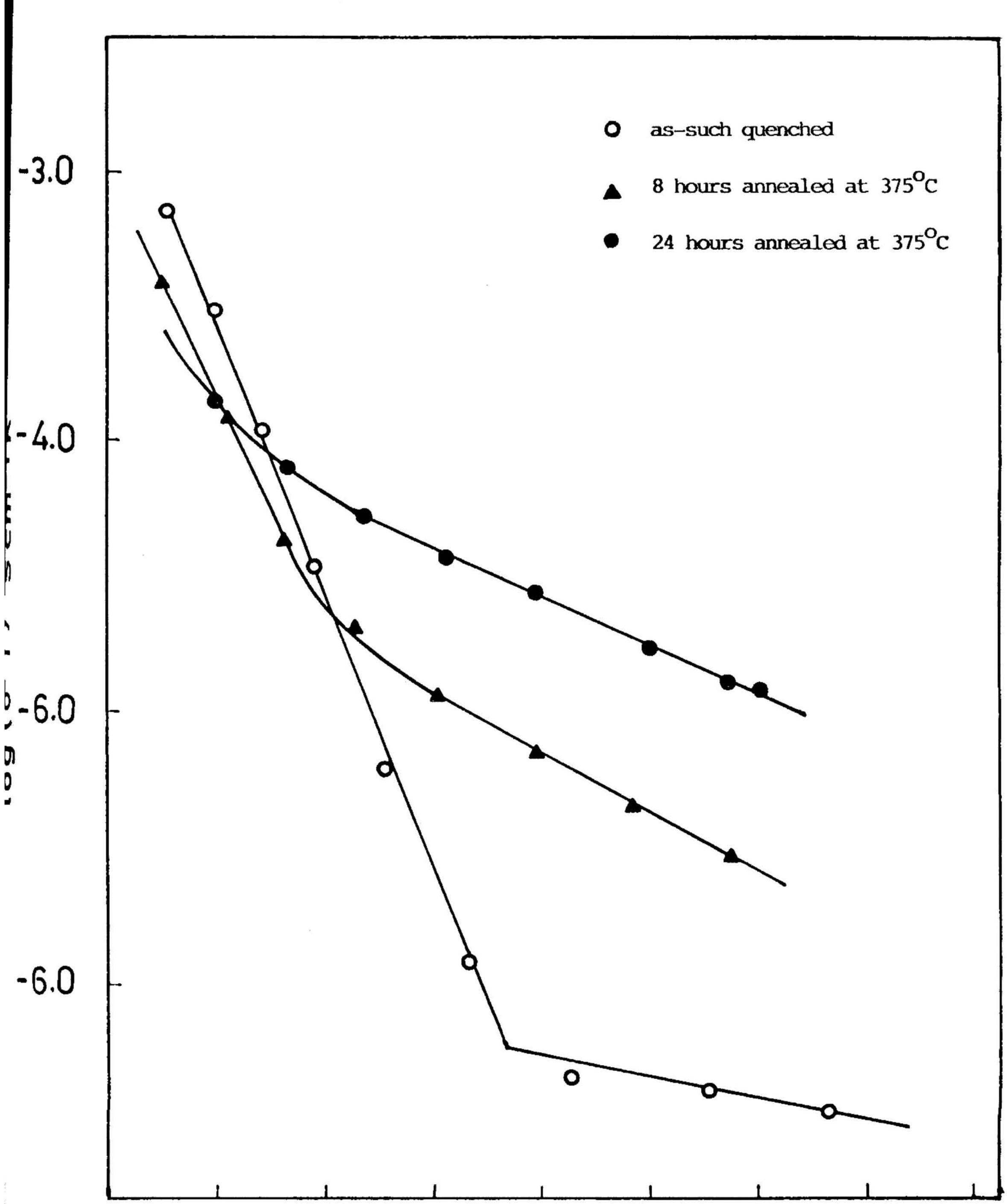

Fig. 4.10 Variation of conductivity with temperature of QL_{300} for different isothermal (375°C) annealing conditions

temperature region changes systematically from 1 13 eV to 0 18 eV, upon isothermal annealing for periods upto 24 hours

By quenching the melt of LSL, we freeze both the static and dynamical disorders of SO_4^{2-} sublattice at room temperature unlike the case in $Na_3In_2(PO_4)_3$ compound where only static disorder is frozen[24] upon quenching from solid state (XRD of these phosphate samples have shown the changes only in the unit cell volume as a result of this frozen-in static disorder) Annealing of QL_{300} relaxes this disorder to produce a configuration, which optimizes the conduction path for Li^+ ions This optimization upon annealing results in a lower activation energy without changing the magnitude of conductivity significantly at 300^oC i e , the number of Li^+ ions involved in the conduction process is nearly the same Thus the nature of the conduction process is unaltered, but the 'bottleneck' for facile Li^+ ion conduction, provided by orientationally disordered SO_4^{2-} ions, is removed upon annealing, leading to high conduction with low activation energy of 0 18 eV

4 3 4 Infrared Study of Molecular Disorder

Quenching from the melt freezes the local motions of SO_4^{2-} and the 'stabilizer" CO_3^{2-} ions and the extent of the resulting static and dynamic disorder[26,18] would be reflected in the IR spectra Present IR spectral features do indeed reveal interesting molecular disorder in CO_3^{2-} occurring as an accidental trace impurity and in the SO_4^{2-} sublattice of the FCC phase Fig 4 11 shows IR spectra of QL_{100} , QL_{200} and QL_{300} at RT which feature the internal motions (rotations and vibrations of SO_4^{2-} and CO_3^{2-} as well as the vibrations of H-OH and Li O

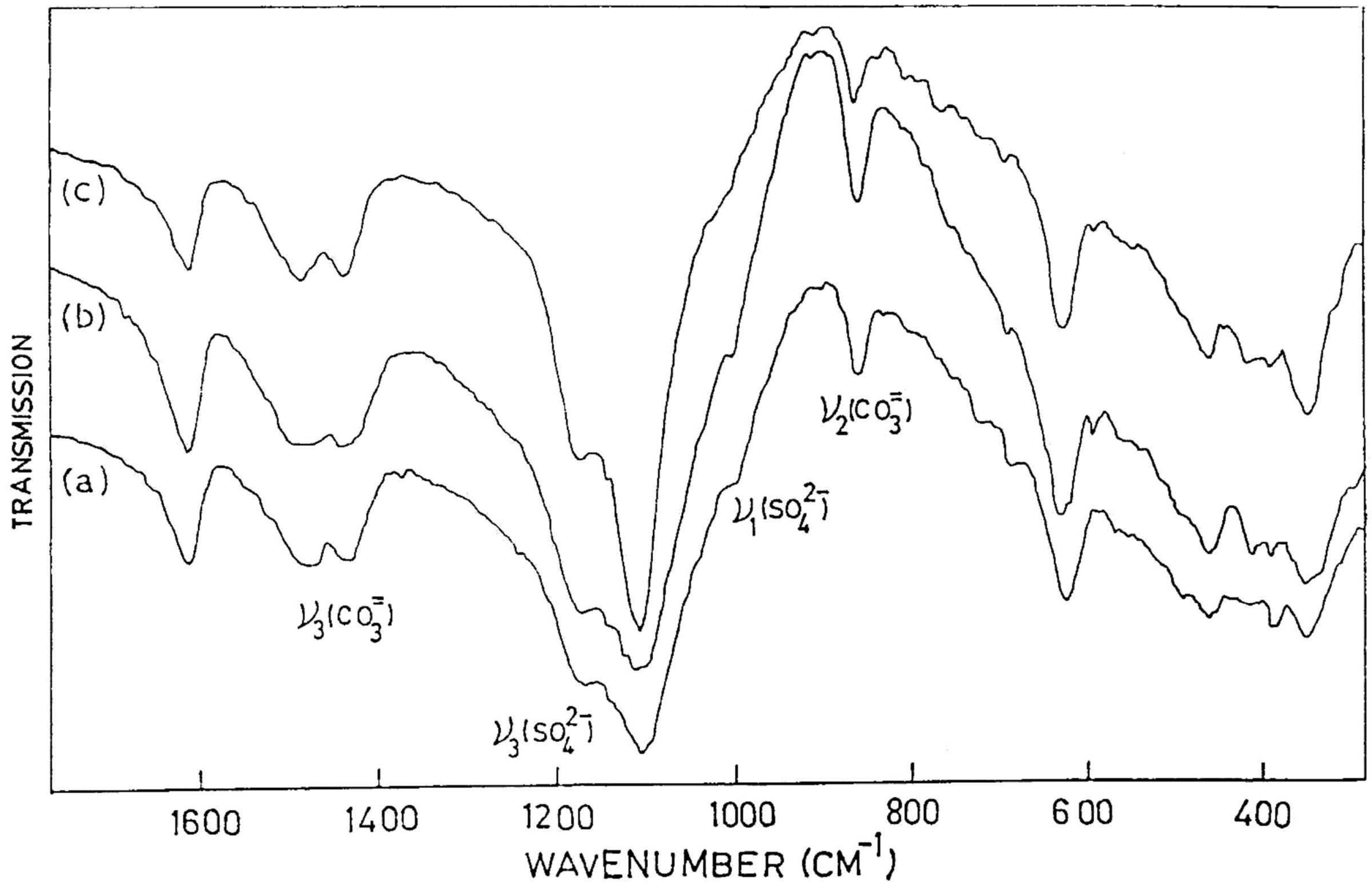

Fig. 4 11 IR spectra of melt-quenched Li_2SO_4 H_2O at RT (a) QL_{100}, (b) QL_{200} and (c) QL_{300} Note the sensitivity of ν_1 and ν_3 modes of SO_4^{2-}, and, ν_2 and ν_3 modes of CO_3^{2-} to quenching temperature and the resulting changes in environment Observe also the maximum broadening of ν_3 in sample QL_{200} indicating anion sublattice disordering in cubic Li_2SO_4 This sample quenched at 200°C has the highest conductivity

To discuss CO_3^{2-} first, of the four modes[37] (D_{3h} symmetry) only ν_2 and ν_3 are predominant (ν_1 and ν_4 being very weak). The ν_2 mode at 860 cm^{-1} (singlet) and the ν_3 mode - a doublet, are very sensitive to quenching conditions. ν_2 is sharper and stronger in QL_{200} than in QL_{100} and QL_{300}. The asymmetric stretching mode ν_3 is a doublet at 1440 and 1488 cm^{-1} in QL_{300} and at 1435 and 1480 cm^{-1} in QL_{100} and QL_{200}. The last feature is sensitive to T_q, its width increasing as $QL_{300} < QL_{100} < QL_{200}$. Dissolution of 'LSL' in distilled water resulted in a small insoluble fraction which upon analysis by XRD and IR spectroscopy turned out to be Li_2CO_3. The ν_3 band splitting of CO_3^{2-} in the case of quenched sample is quite complete (separation ~ 50 cm^{-1}) compared to that for Li_2CO_3 extracted from LSL, and thus ascribable to either site-splitting[38,39] or perturbation of CO_3^{2-} environment by Li_2SO_4 (cubic) structure, leading to its molecular disorder. No such disorder was noted in the Raman spectra[40] of Li_2CO_3 upto 692°C and thus the broadening of 1480 cm^{-1} component in QL_{100} and QL_{200} is a very strong evidence of perturbation of the CO_3^{2-} environment by an FCC structure stabilized with SO_4^{2-} molecular orientational disorder in Q_{100} and Q_{200}, compared to that in QL_{300} in which the cubic phase is unstable. On the other hand, while a rigidly trapped CO_3^{2-} would give rise to a sharp υ_3 doublet, the rotating CO_3^{2-} radical should exhibit broadness in the υ_3 degenerate stretching mode. The broadening of the 1480 cm^{-1} component of the υ_3 mode observed in QL_{100} and QL_{200} thus reflect the rotational motion of CO_3^{2-} ions.

A free sulphate ion (T_d symmetry) has four fundamentals[37] ν_1 (A1) at 981 cm^{-1}, ν_2 (E) at 451 cm^{-1}, ν_3 (T_2) at 1104 cm^{-1} and ν_4 (T_2) at 613 cm^{-1}. In 'LS' the symmetry is lowered by a slight perturbation of internal vibrations that remove the degeneracy of ν_2, ν_3 and ν_4. The

intensity of ν_1 of SO_4^{2-} increases as $QL_{300} << QL_{100} < QL_{200}$ This Raman active symmetry mode in FCC Li_2SO_4 - showed excess anisotropic broadening due to both vibrational and orientational relaxations[18] A comparison of band width, intensity and asymmetry of the band ν_3 in QL_{100} and QL_{200} with those in QL_{300} confirms the existence of disordered SO_4^{2-} sublattice in the former relative to the microcrystalline QL_{300} supporting our conductivity results that QL_{100} and QL_{200} are high-temperature plastic phases with an activation energy of ~ 0 4 eV for Li^+ conduction

It is well known that while the IR band positions are functions of atomic masses, the bandwidths are related to the charge density fluctuations inside the band region, here L-O and S-O bonds The increase in ν_3 band-widths of CO_3^{2-} and SO_4^{2-} molecular groups as a function of increased conductivity of QL_{100} and QL_{200} leads to the conclusion that the electronic charge density inside the bond region is being influenced by the mobility of the Li^+ cations surrounding them The higher conductivity of QL_{100} and QL_{200} and hence higher mobility would lead to more broadening of CO_3^{2-} and SO_4^{2-} bandwidths when compared to those for QL_{300}

4 3 5 Electron Spin Resonance

Electron spin resonance is a specific microscopic probe with which to examine molecular environments in crystalline and disordered systems Under favourable circumstances, it is possible to create and stabilize paramagnetic radicals which may reflect certain aspects of dynamics - which may be characteristic of the system itself Presently we describe our efforts to stabilize and identify molecular paramagnetic radicals in

melt-quenched LS, and discuss their formation with special reference to the cubic structure and Li^+ conduction in quenched 'LS' ESR of X-irradiated Li_2CO_3, Li_2SO_4 CO_3^{2-} (obtained by the reaction Li_2CO_3 + H_2SO_4 followed by crystal growth), 'LSA" + 0.5 % Li_2CO_3 denoted as QAC_{200} (0.5% Li_2CO_3),which is furnace cooled from melt have also been investigated for comparison

The ESR spectra of QL_{100} and QL_{200} (at RT and 130°C) are shown in Fig. 4.12. The ESR signals look similar in quenched samples, suggesting a common origin for the paramagnetic centre(s) involved. A closer look reveals that the most prominent symmetric signal with a g = 2.0094 is ≈ 6 G wide in QL_{100} while it is ≈ 7.7 G wide in QL_{200}. Microwave power saturation and thermal annealing experiments have shown that the intense signal in QL_{100} and QL_{200} (i) monotonically increases and (ii) thermally quite stable upto 200°C (compare Fig. 4.12 (b) and (c) for QL_{200}). These observations together with the absence of such a signal in X-irradiated unquenched Li_2SO_4 [41] allow us to infer that this signal arises from the cubic structure stabilized upon quenching.

Since Li_2CO_3 is present in LSL as a congenital impurity, CO_3^{2-} and SO_4^{2-} are the possible molecular ions that could undergo damage yielding, in principle, a variety of paramagnetic fragments CO_3^-, CO_3^{3-}, CO_2^-, SO_4^-, SO_3^-, SO_2^- and O_3^-. We now submit our arguments based on (i) comparison with ESR spectra of related compounds and (ii) probable formation pathways to identify the ESR spectra of QL_{100} and QL_{200}.

The ESR spectra of X-irradiated Li_2CO_3, Li_2SO_4 CO_3^{2-} and furnace cooled QAC_{200} (0.5% Li_2CO_3) are shown Fig. 4.13. A comparison of the

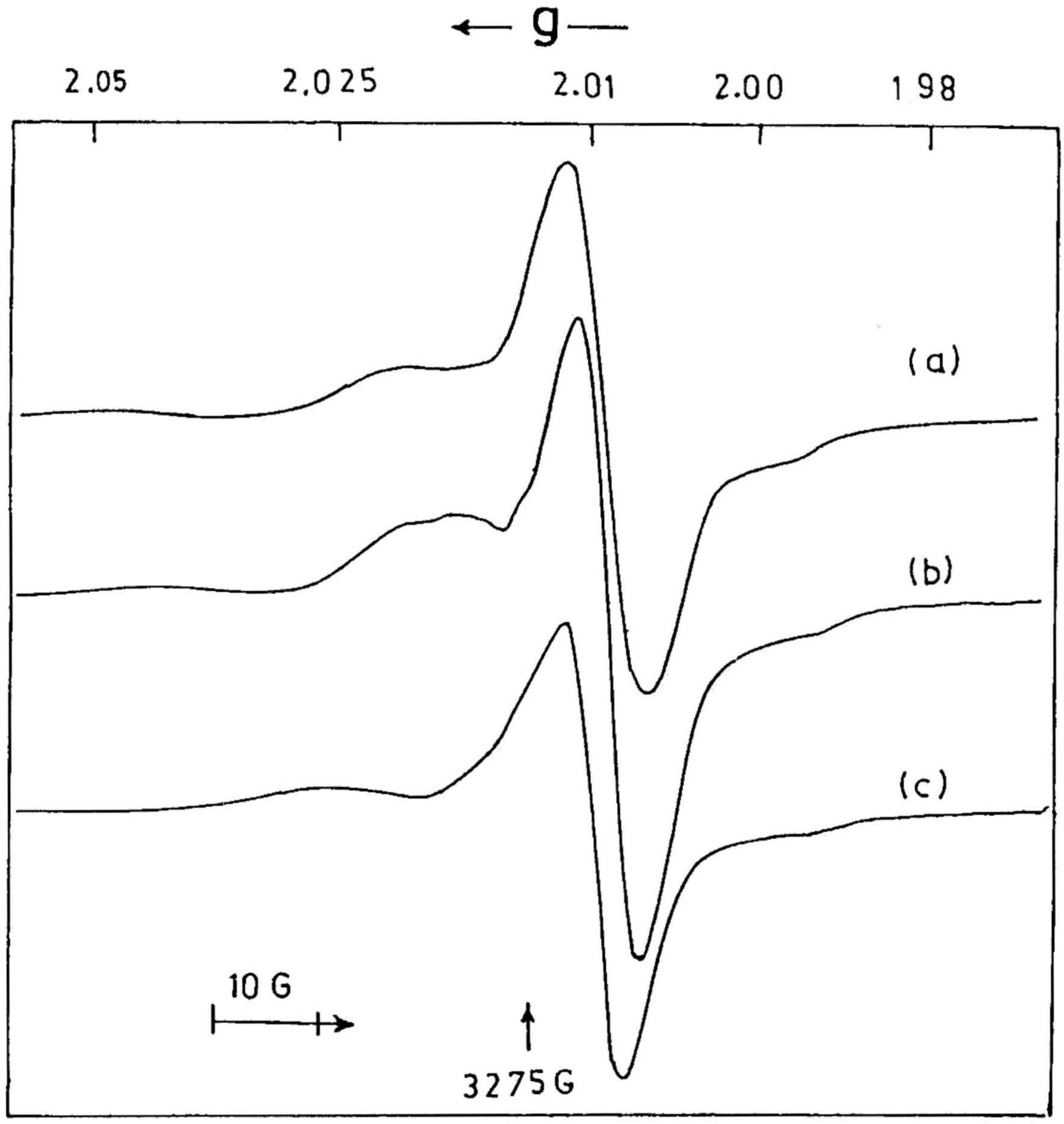

Fig. 4.12 ESR spectra of X-ray irradiated quenched Li_2SO_4 (a) QL_{100} at RT, (b) QL_{200} at RT and (c) QL_{200} at 130°C

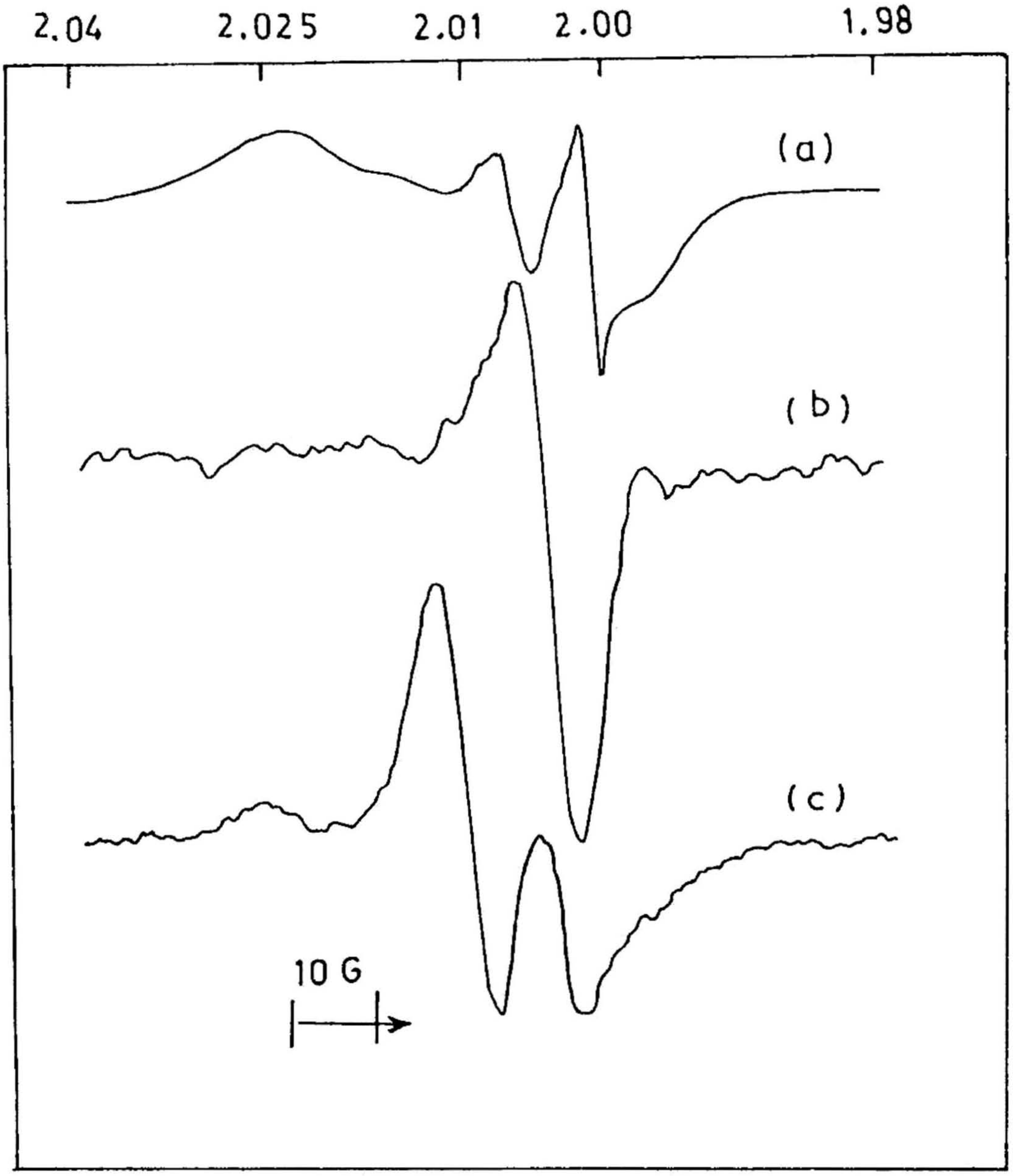

Fig. 4.13 Room temperature ESR spectra of X-irradiated (a) Li_2CO_3, (b) Li_2SO_4 CO_3^- and (c) QAC_{200} (Li_2SO_4 0 5% Li_2CO_3)

features in these three carbonate containing systems with those of QL_{100} and slow cooled QAC_{200}(0 5% Li_2CO_3) at once brings out the sensitivity of the paramagnetic radical(s) to the crystalline environment in which it (they) is (are) stabilized The occurrence of two signals - one sharp and another weak-in furnace-cooled sample could be taken as an indication of the stabilization of the cubic phase along with the monoclinic phase, with the ratio of their intensities suggesting their relative abundances The presence of a single species in Li_2SO_4 CO_3^{2-} and its resemblance to the less intense feature at 2 005 in QAC_{200}(0 5% Li_2CO_3) is to be noted It is to be observed that this feature is conspicuously absent in X-irradiated Li_2CO_3 More importantly, the intense symmetric feature ($\Delta H_{pp} \simeq 6$ G) at **g** = 2 010 compares rather well with the intense feature of Ql_{200} (Fig 4 10b) Note also that QL_{100}, QL_{200} and QAC_{200} (0 5% Li_2CO_3) share common features around **g** ≃ 2 02 This comprehensive comparison shows that CO_3^{2-} is predominantly involved in the radiation damage at the expense of SO_4^{2-} quite like NO_3^- at the expense of CO_3^{2-} in calcium carbonate[42] Thus one has to consider the possibility of stabilization of CO_3^{2-} based radicals under various static and dynamic conditions In view of the stabilization of the metastable cubic structure one has to consider the likelihood of the motions of paramagnetic fragment (e g tumbling of CO_3^{2-}) in accounting for the observed isotropic ESR spectra of QL_{100} and QL_{200}

Considering that carbonate ions are the most susceptible to X-ray damage in Li_2SO_4 containing CO_3^{2-} as minor/major impurity, the following mechanisms could operate

$$CO_3^{2-} \xrightarrow{h\nu_X} CO_3^- + e^-$$

$$CO_3^- \xrightarrow{h\nu_X} CO_2^- + 1/2\ O_2$$

$$CO_3^{2-} + e^- \longrightarrow CO_3^{3-}$$

where $h\nu_X$ is the X-ray photon energy

An alternative mechanism for CO_2^- formation could be decomposition of Li_2CO_3 to Li_2O and CO_2 and subsequent electron capture. Of the three species, CO_3^- happens to be the most probable to form because of a single rather easy step of electron ejection (compared to electron capture of CO_3^{3-} and, dissociation and electron capture for CO_2^-)

While a stationary CO_3^- would give[43] **g**-values 2.0058, 2.0084 and 2.0146, a dynamic (rotating/tumbling) one would tend to give an averaged **g**-value of 2.009, in close agreement with our observation. Furthermore, if CO_3^- is rotating in Li_2SO_4 matrix, then it is reasonable to expect CO_3^{2-} to behave similarly. The sharp ESR line of CO_3^- radical exhibits a broadening from 6 G to 8 G as the host Li_2SO_4 matrix is cooled from 300K to 77K, with anisotropic **g** component confirming the above interpretation of "dynamic' CO_3^{2-} [44a,44b]. Such a matrix isolated, freely rotating CO_3^- radical in KCl was observed[45] at 300K with a **g**-value of 2.0113 which upon cooling to 83K exhibit broadening from 3.7 G to 5.5 G and finally, at 77K split into three anisotropic components due to hindered rotations as the host matrix contracts upon cooling. That this radical is sensitive to quenching conditions is seen from the different line widths of QL_{100} and QL_{200}. It would be interesting to correlate the ESR results of X-irradiated QL_{100} and QL_{200} with the IR spectra of these mat rials.

The IR spectra give a well resolved doublet for the ν_3 mode of CO_3^{2-} (one of which is optimally broadened showing sensitive dependence on quenching temperatures) indicating considerable disorder due to CO_3^{2-} motion. It is observed that ESR spectra also reflect this aspect of CO_3^{2-} motion. The reasonable possibility of CO_3^{2-} stabilizing the high-temperature cubic structure of Li_2SO_4 at ambient with enhanced Li^+-conduction seems to have been strengthened by the present ESR results.

4.4 CONCLUSIONS

The high-temperature plastic phase (α-phase) of lithium sulphate with FCC structure has been stabilized at ambient by programmed quenching of the melt, aided by a few percent of lithium carbonate which arrests the cubic to monoclinic phase transformation. The metastable phase thus obtained has been characterized by X-ray diffraction (a = 6.98 Å), differential scanning calorimetry (endothermic humps at 351 and 542°C in QL_{200}), AC electrical conductivity, infrared and electron spin resonance spectroscopy. The nature of this stabilized metastable phase is quite sensitive to quenching temperatures (100, 200 and 300°C). DSC experiments provide unequivocal thermodynamic characterization of α-phase. Electrical conductivity of this phase is enhanced by ~ 6 orders relative to the insulating monoclinic phase, with an activation energy of 0.4 eV, characteristic of α-Li_2SO_4. The microcrystalline phase obtained by quenching at 300°C shows a two-slope Arrhenius plot (1.13 eV and 0.05 eV) with a knee separating them. The activation energy of the conductivity behaviour in the high-temperature region decreases systematically from 1.13 eV to 0.18 eV, upon prolonged isothermal annealing suggestive of molecular relaxation leading to the optimization of Li^+ conduction paths. The IR spectra reflect the quenched-in disorder

by way of broadening peaks characteristic of SO_4^{2-} and the stabilizer CO_3^{2-} ions. The ESR spectra of quenched Li_2SO_4, upon X-irradiation has given interesting microscopic evidence of a dynamically disordered CO_3^{2-} by way of an intense isotropic ($g \approx 2.009$) spectrum characteristic of the tumbling CO_3^- radical

REFERENCES

1 S Chandra, *Superionic Solids Principles and Applications* (North Holland, Amsterdam, 1981) P 31, K Schroeder Ph D Thesis 1975 Goteborg

2 A Kvist and A Lunden, Z *Naturforsch* **20A** (1965) 235

3 N Kimura and M Greenblatt, *Mat Res Bull* **19** (1984) 1653

4 B Jansson and C -A Sjoblom, Z *Naturforsch* **25 A** (1970) 1115

5 K Schroeder and C A Sjoblom, *High Temp High Pres* **12** (1980) 327

6 G Hatem, *Thermochim Acta* **88** (1985) 433

7 A R Ubbelohde, *The Molten State of Matter* (Interscience, New York, 1978)

8 C K Lee and A R West, *J Mater Chem* **1** (1991) 149

9 B Heed, A Lunden and K Schroeder, *Electrochim Acta* **22** (1977) 705

10 T Forland and J Krogh-Moe, *Acta Chem Scand* **11** (1957) 565

11 L Nilsson, J O Thomas and B C Tofield, *J Phys C Solid State Phys* **13** (1980) 6441

12 H Ohno and K Furukawa, *J C S Faraday Trans I* **74** (1978) 795

13 A Lunden, *Solid State Commun* **65** (1988) 1237

14 A Lunden, *Solid State Ionics* **28-30** (1988) 163

15 E A Secco, *Solid State Commun* **66** (1988) 921

16 E A Secco, *J Solid State Chem* **96** (1992) 366

17 R Aronsson and L M Torell, *Phys Rev* **B36** (1987) 4926

18 L Borjesson and L M Torell, *Phys Rev* **B32** (1985) 2471

19 R W Impey, M L Klein and I R McDonald, *J Chem Phys* **82** (1985) 4690

20 M A K L Dissanayake and B -E Mellander, *Solid State Ionics* **21** (1986) 279

21 C S Babu and B L Tembe, *Chem Phys Lett* (accepted)

22 M Tatsumisago, Y Shinkuma and T Minami, *Nature* **354** (1991) 217

23 A Hooper, P McGeehin, K T Harrison and B C Tofield, *J Solid State Chem* **24** (1978) 265

24 S E Sigaryov and A B Vasiliev, *J Phys Chem Solids* **52** (1991) 467

25 Ph Colomban, *J Molec Struct* **143** (1986) 191

26 M Barj, H Perthuis and Ph Colomban, *Solid State Ionics* **9 & 10** (1983) 845

27 C S Sunandana, *J Mat Sci Lett* **5** (1986) 650

28 R Aronsson, B Heed, B Jansson, A Lunden L Nilsson, K Schroeder, C -A Sjoblom J O Thomas and B C Tofield, in *Fast Ion Transport in Solids*, ed by T Vashishta J N Mundy and G K Shenoy (Elsevier, North Holland 1979) p 471

29 L M Di and H Bakker, *J Phys Condens Matter* 3 (1991) 9319

30a M Lasocka and H Matyja, *J Non-Cryst Solids* **14** (1974) 41

b B G Bagley, H S Chen and D Turnbull, *Mat Res Bull* 3 (1968) 159

31 A Lunden, A Bengtzelius, R Kaber, L Nilsson, K Schroeder and R Tarneberg, *Solid State Ionics* **9 & 10** (1983) 89

32 M A K L Dissanayake, M A Careen, P W S K Bandaranayake and C W Wijayasekera, *Solid State Ionics* **48** (1991) 277

33 K Singh and V K Deshpande, *Solid State Ionics* **7** (1982) 295

34 A Lunden, in *Materials for Solid State Batteries* ed by B V R Chowdari, and S Radhakrishna (World Scientific, Singapore, 1986) P 149

35 J Maier, in *Superionic Solids and Solid Electrolytes Recent Trends* ed by A L Laskar and S Chandra (Academic Press, New York, 1989) p 137

36 N J Dudney, *Ann Rev Mater Sci* **19** (1989) 103

37 G Herzberg, in *Infrared and Raman Spectra of Poly Atomic Molecules* (Van Norstrand, New York, 1945)

38 B G Oliver and A R Davis, *Can J Chem* **51** (1973) 698

39 D E Irish and A R Davis, *Can J Chem* **46** (1968) 943

40 J B Bates, M H Brooker, A S Quist and G L Boyd, *J Phys Chem* **76** (1972) 1565

41 N Hariharan and J Sobhanadri, *J Phys Chem Solids* 30 (1969) 778

42 P De Canniere, R Debuyst F Dejenet and D Apers, *Nucl Tracks Radiat Meas* **14** (1988) 267, and references cited therein

43 L G Glinskaya et al , *Sov Phys Cryst* **15** (1971) 1016

44a P W Atkins and M C R Symons, *The Structure of Inorganic Radicals* (Elsevier, Amsterdam, 1967)

b M C.R Symons, *Private Communication*

45 I C Hisatsune, T Adl, E C Beahm and R J Kempf, *J Phys Chem* **74** (1970) 3225

CHAPTER 5

ALKALI-TELLURITE GLASSES

5. ALKALI-TELLURITE GLASSES

A. CRYSTALLIZATION STUDIES

5.1 INTRODUCTION

There is much current interest in the study of TeO_2-based glasses, because of their low melting temperatures, high refractive indices, high dielectric constants, and absence of hygroscopic nature which limit the applications of phosphate and borate glasses.

TeO_2 by itself can be transformed to glassy state only by employing ultrafast quenching techniques, or by introducing a network modifier as a second component. Thus TeO_2 is known to be a conditional glass former. In the present investigation, a TeO_2-based glass is prepared with Li_2O as a network modifier.

There have been several recent reports on the synthesis and properties of binary and ternary TeO_2-glasses containing Li^+ ions from the point of view of ionic conduction[1-4]. Besides the ionic conductivity was found to exhibit non-linear variation with compositional changes in Li_2O-B_2O_3-TeO_2 glasses[1] due to the mixed former effect.

Furthermore TeO_2 readily forms glasses [5-7] with transition metal oxides (TMO) such as V_2O_5 and Fe_2O_3 in which TM ions exist in different valence states, and shows electrical conductivity several orders of magnitude higher than silicate, borate and phosphate glasses containing the same amount of TMOs. R. N. Hampton et al [8] have reported the dielectric constant of pure tellurite glass and compared with those of

binary glasses (33 WO_3-67 TeO_2 and 20 $ZnCl_2$-80 TeO_2) It was found that the dielectric constant of the binary glasses are close to that of the parent (TeO_2) glass indicating that the polarizablity of TeO_2 is largely responsible for the dielectric behavior of binary tellurite glasses

Kumar and Mansingh[9] have measured the optical and electrical properties of amorphous TeO_2 films The DC conductivity plot in the temperature range 77-500 K exhibits a non-linear behaviour at the low temperatures and an Arrhenius behaviour at high temperatures

In spite of such a large number of investigations on electrical properties, little attention has been devoted to the understanding of the crystallization phenomena in TeO_2-based glasses The knowledge of the crystallization process is important in the search for glasses with high resistance towards devitrification and for fabricating glass-ceramics through controlled crystallization Recently however, Kamatsu et al [10] have reported the crystallization behaviour of TeO_2-$LiNbO_3$ glasses by examining the phases using X-ray diffraction after different thermal treatments

Cachau-Herrilat et al [11] reported two varieties of Li_2O-$2TeO_2$ single crystals characterized by two different structures one monoclinic and the other orthorhombic At elevated temperatures, the metastable monoclinic crystals undergo irreversible transformation to the thermodynamically stable orthorhombic phase

In this chapter the results of our investigation on the eutectic glass composition 30 Li_2O-70 TeO_2 - a composition very close to that of

single crystals prepared by Cachau-Herrillat et al [11] are reported The objectives of the present work are (a) to determine the kinetics of crystallization using differential scanning calorimetry (DSC), (b) to characterize the crystalline phases formed in freshly prepared and stored glasses subjected to different thermal treatments, using powder X-ray diffraction, and (c) to measure the ionic conductivity of glassy and crystallized samples This investigation also focusses on related issues such as the ease of glass formation, thermal stability of glass and the effects of crystallization on electrical conductivity

5 2 EXPERIMENTAL

The pseudo-binary phase diagram of the Li_2O-TeO_2 system was investigated using differential thermal analysis (DTA) with a home-built stainless steel DTA apparatus α-Al_2O_3 powder was used as the reference material The temperature changes associated with thermal transitions were monitored by a differential, chromel/alumel thermocouple The apparatus was calibrated by measuring the phase transition temperature of $Li_2SO_4 H_2O$ (575^{o}C) The heating rate was controlled to 15^{o}C/min by proper adjustment of the power input to the vertical furnace and the precision of the temperature measurement was ± 3^{o}C

Li_2CO_3 (Alfa) and TeO_2 (BDH) were used as starting materials for the glass preparation The mixture was melted in an electrical furnace using a high pure alumina crucible Sufficient time was allowed for the melt to become visibly homogeneous and bubble-free The crucible containing the melt was constantly agitated to ensure homogeneous mixing The greenish transparent glass was obtained by quenching the melt between thick stainless steel plates

The thermal behaviour of the glass was investigated using Du Pont 9900 Differential Scanning Calorimeter (DSC) Measurements were performed in an argon atmosphere on glass powders of mass 20 mg, encapsulated between aluminum pans The kinetics of crystallization was investigated using DSC by recording the scans at heating rates of 2.5, 5, 10, 20, and 40^{o}C/min The temperature was calibrated and the cell constant of the instrument determined for each heating rate on the basis of onset temperature of the endothermal peak and the enthalpy recorded during melting of highly pure (5N) indium

The products of crystallization as reflected by DSC-were further characterized by X-ray diffraction after subjecting the glass samples to isothermal annealing for suitable periods at temperatures corresponding to the different stages of crystallization The X-ray diffractograms were recorded at room temperature with a Seifert X-ray powder diffractometer using Ni filtered Cu Kα radiation at 1.2^{o}/min in the range 5-80^{o} Data analysis was done using the "POWD" program

Two-terminal AC electrical conductivity measurements were performed both on polished bulk glass annealed at 200^{o}C for about 3 hours, and on the sintered glass-ceramics prepared by pelletizing the crystallized glass powder (p = 5 tons/cm^{2}) and heating at 400^{o}C for 10 hours The purpose of sintering was to increase the mechanical strength and to reduce the intergranular resistances Thick platinum foils spot-welded with platinum wires serving as blocking electrodes, were attached to opposite faces of samples using organo-gold paste which was decomposed and hardened by gradually heating to 200^{o}C

The bulk DC conductivities of these samples were derived from the complex admittance analysis at each of the several temperatures in the range 70-200^{o}C over the frequency range 100 Hz - 60 KHz using indigenously built AC conductivity meter (see Chapter 3)

5.3 RESULTS

5.3.1 Phase Diagram

The phase diagram of the pseudo binary system Li_2O-TeO_2 obtained from the DTA scans on selected composition is shown in Fig 5.1 One deep eutectic region was identified from the above diagram and the eutectic point corresponds to a composition 30 Li_2O-70 TeO_2 An earlier study[12] however, reported the eutectic point corresponds to the composition 25 Li_2O-75 TeO_2 This difference is probably due to the difference in the purity of the chemicals used The eutectic region observed in our phase diagram exactly coincides with that in the Ag_2O-TeO_2 system[13]

5.3.2 Thermal Behaviour by DSC

A typical DSC trace of 30 Li_2O-70 TeO_2 glass powders recorded at a heating rate of 10^{o}C/min is shown in Fig 5.2a Of the four thermal events observed, the first one appearing as an endothermic hump is the glass transition, araising from an abrupt increase in specific heat due to the liquid type long range diffusion The three remaining exothermic events correspond to crystallization processes The powdered glass heated beyond third exothermic peak got completely crystallized and did not show any crystallization peaks during subsequent heating scans

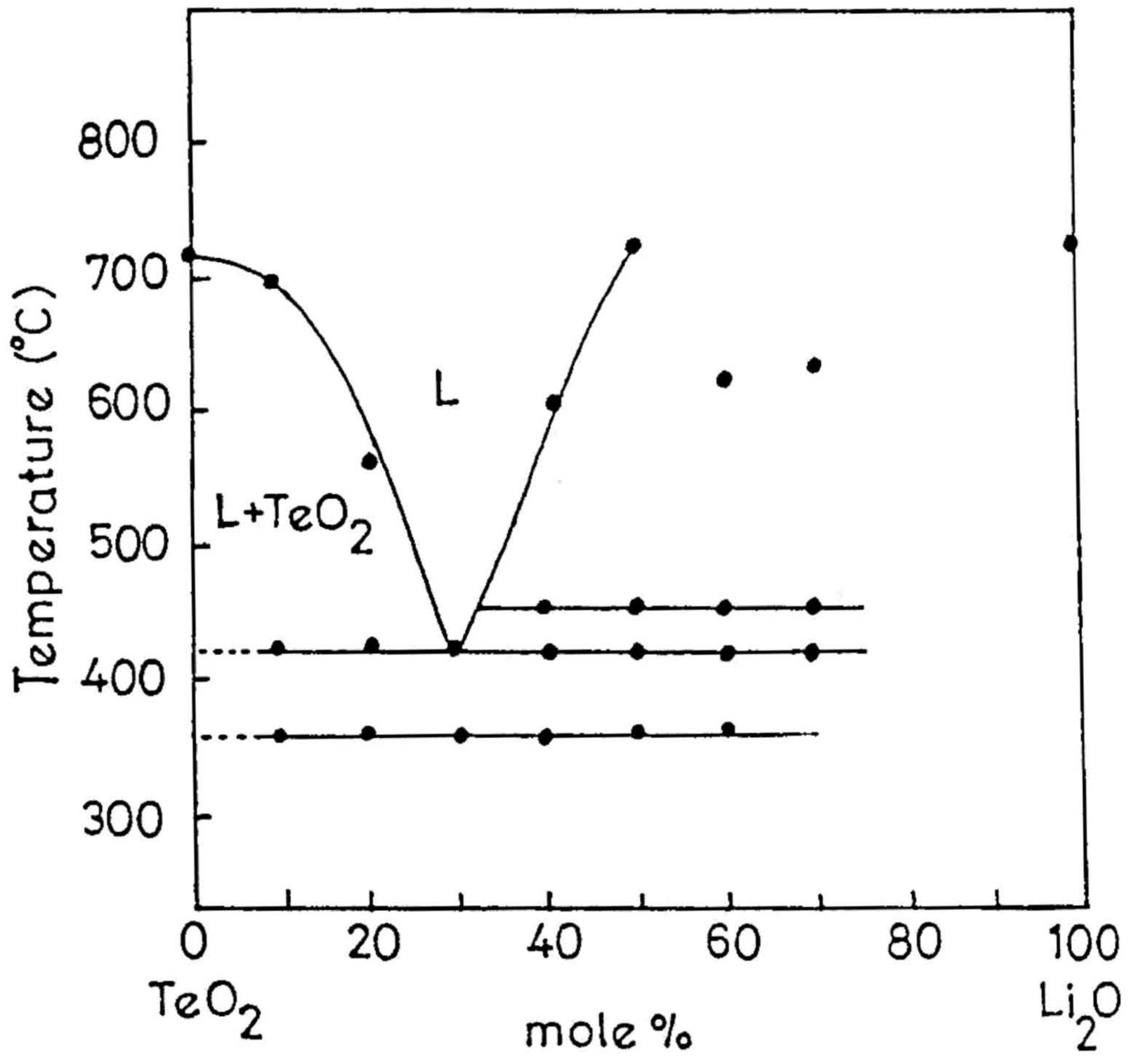

Fig 5.1 Partial phase diagram of the pseudo-binary system Li_2O-TeO_2 determined by DTA

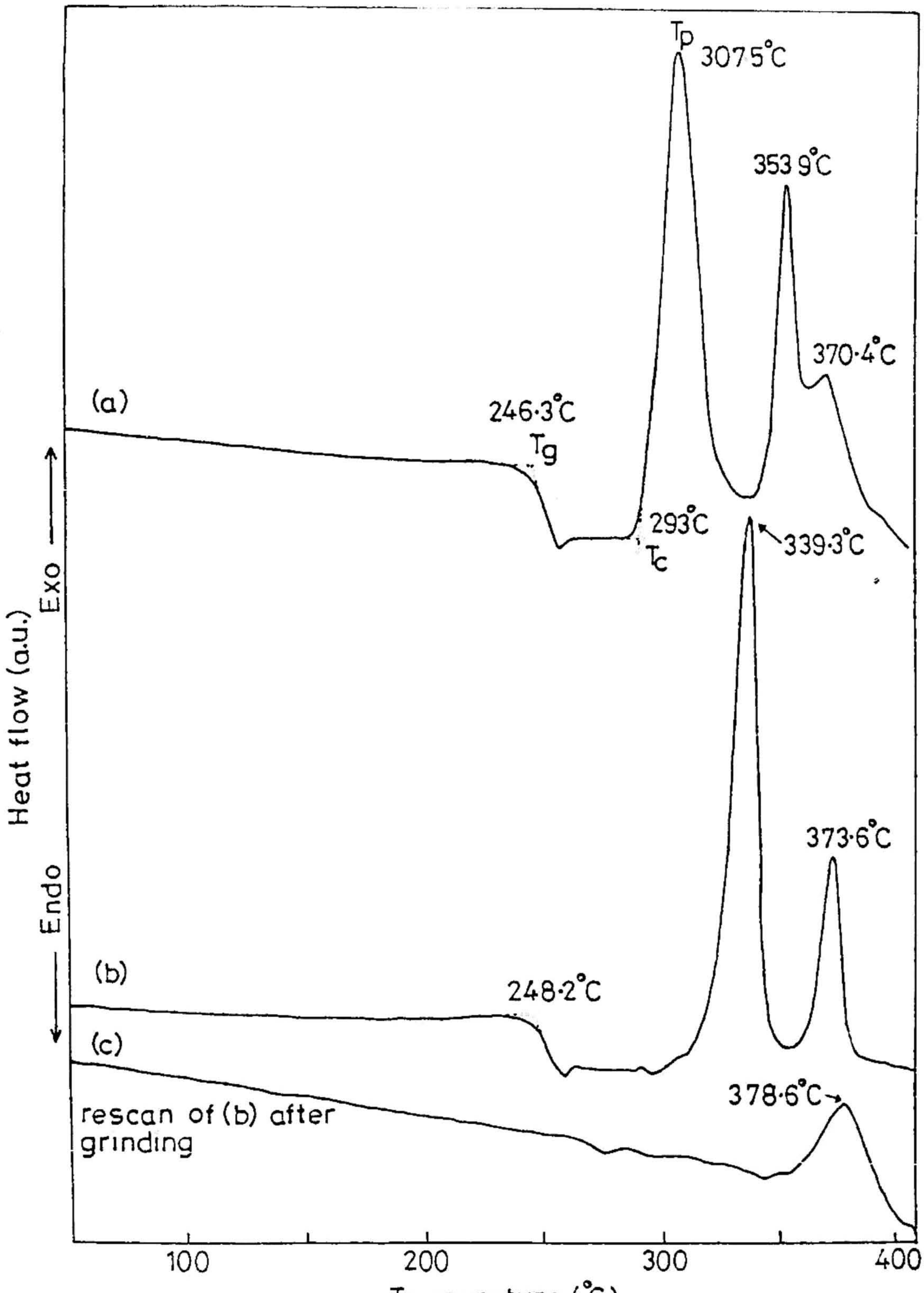

Fig 5.2 Typical DSC traces with a heating rate of 10°C/min showing the glass transition (T_g) and crystallization temperatures (T_x) for 30 Li_2O-70 TeO_2 glass, (a) in powder form (b) in bulk form and (c) bulk crystallized sample crushed into fine powder and rescanned

Fig 5.2b presents the DSC trace taken on a bulk glass It consists of an endothermic glass transition peak followed by two crystallization exotherms. The main difference between the two thermograms (Fig. 5.2a) is the disappearance of the third, weak, high temperature exotherm in the bulk glass. Also, the crystallization peaks have now shifted to higher temperatures. This crystallized bulk sample was crushed to fine powders of 150 mesh size and subjected to a second thermal scan upto 500°C. The DSC trace of this sample is shown in Fig. 5.2c to consist of only one exothermic peak. This exotherm appears again on rescanning the crystallized bulk sample after being ground to powder.

5.3.3 Crystallization Kinetics

Fig. 5.3 shows the evolution of DSC exotherms of the first stage crystallization upon increasing heating rates for the glass powder. It is seen that the crystallization temperature increases with increase in heating rate and the peak height increases by the same factor suggesting that the crystallization is an activated process. The activation energy of the crystallization kinetics of the first crystallization peak was evaluated using non-isothermal methods.

Many authors have used the Johnson-Mehl-Avrami (JMA) equation to examine the kinetics of non-isothermal crystallization process. As this equation was basically derived to analyze the isothermal crystallization data, several conditions will have to be satisfied[12] for the applicability of this equation to the analysis of the non-isothermal crystallization process. One of the conditions, that the volume fraction of the crystal x transformed at crystallization peak temperature T_p is around 0.60 to 0.63 can be used as a cursory check for the validity of

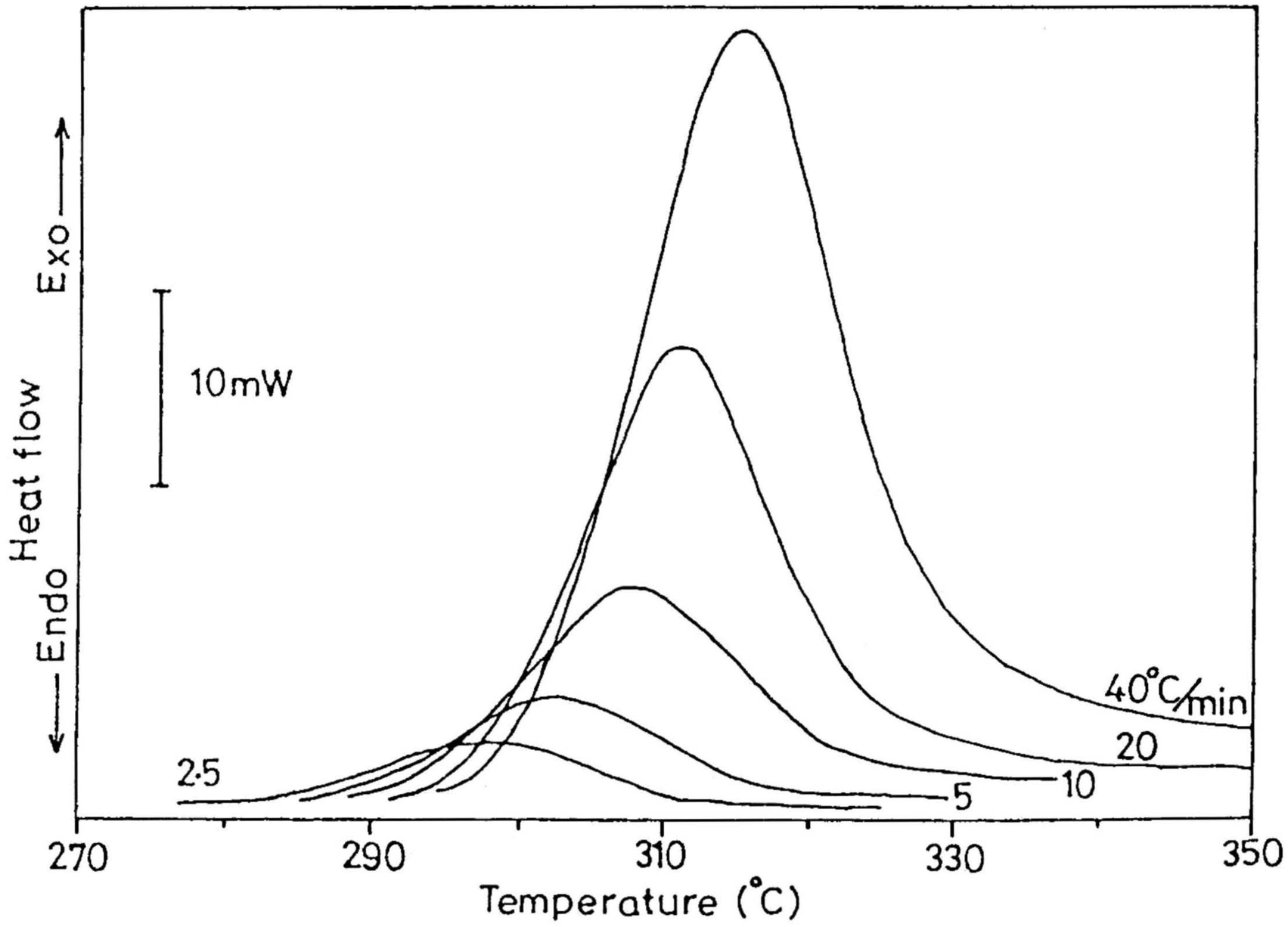

Fig 5 3 The exothermal curves of the first stage crystallization of powdered 30 Li_2O-70 TeO_2 glass for various heating rates

the interpretation of non-isothermal crystallization data in terms of the JMA equation. Since in this present investigation, the x_p at T_p for all heating rates had values outside the range 0.60 - 0.63, we decided to analyze our crystallization data based on the following equations[13,14]

$$\ln \alpha = 1.052 \frac{mE}{nRT} - \frac{1}{n} \ln [-\ln(1-x)] + \text{const} \qquad (1)$$

$$\ln \left(\frac{\alpha^n}{T_p^2} \right) = - 1.052 \frac{mE}{RT_p} + \text{const} \qquad (2)$$

where x, defined above, is obtained from the ratio of partial area to the total area. α is the heating rate, E is the activation energy for crystallization, R is the gas constant, T and T_p are the temperatures in Kelvin, and, m and n are the numerical factors depending on the crystallization mechanism. Expressions (1) and (2) are the so-called modified Ozawa and modified Kissinger equations respectively.

Since it is known that the x_p at T_p - in the DSC curves is almost independent of heating rate, equation (1) should apply for the peak temperature also. Hence the plot of ln α against $1/T_p$ should give a straight line with a slope of (m/n)E. Fig. 5.4 shows the plot of ln α versus $1/T_p$ from which (m/n)E is obtained as 434.7 kJ/mole. To extract E from this, the ratio (m/n) should be known.

Fig. 5.5 shows the relation between ln[-ln(1-x)] and ln α, for two different temperatures. According to equation (1), the slope of these lines give the parameter n. An average value of n - was found to be 1.3. This value together with the observation that powdered glass has a T_p lower than that of bulk glass for all heating rates employed, suggest

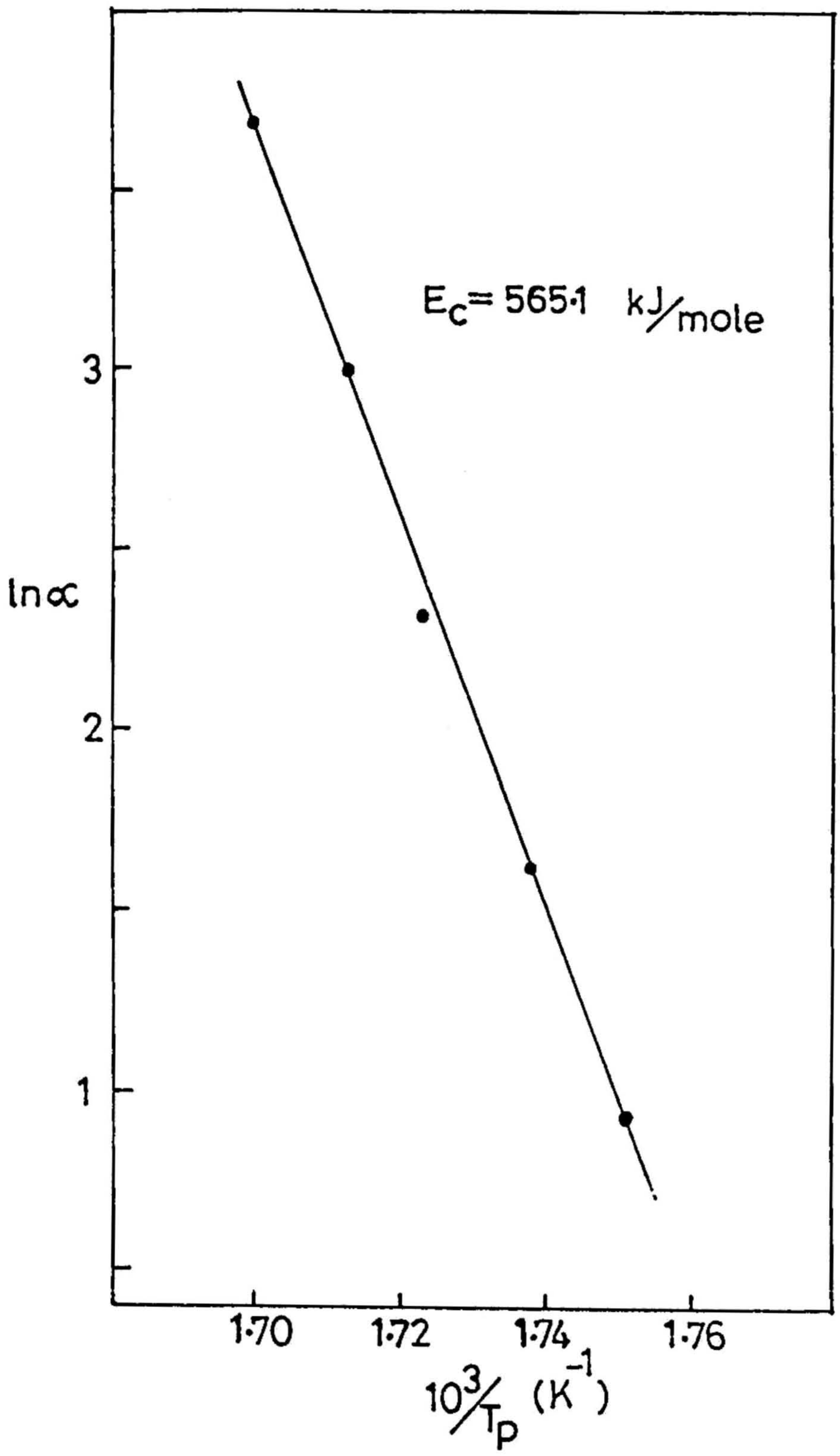

Fig 5.4 The plot of ln[heating rate] versus the reciprocal of crystallization peak temperature

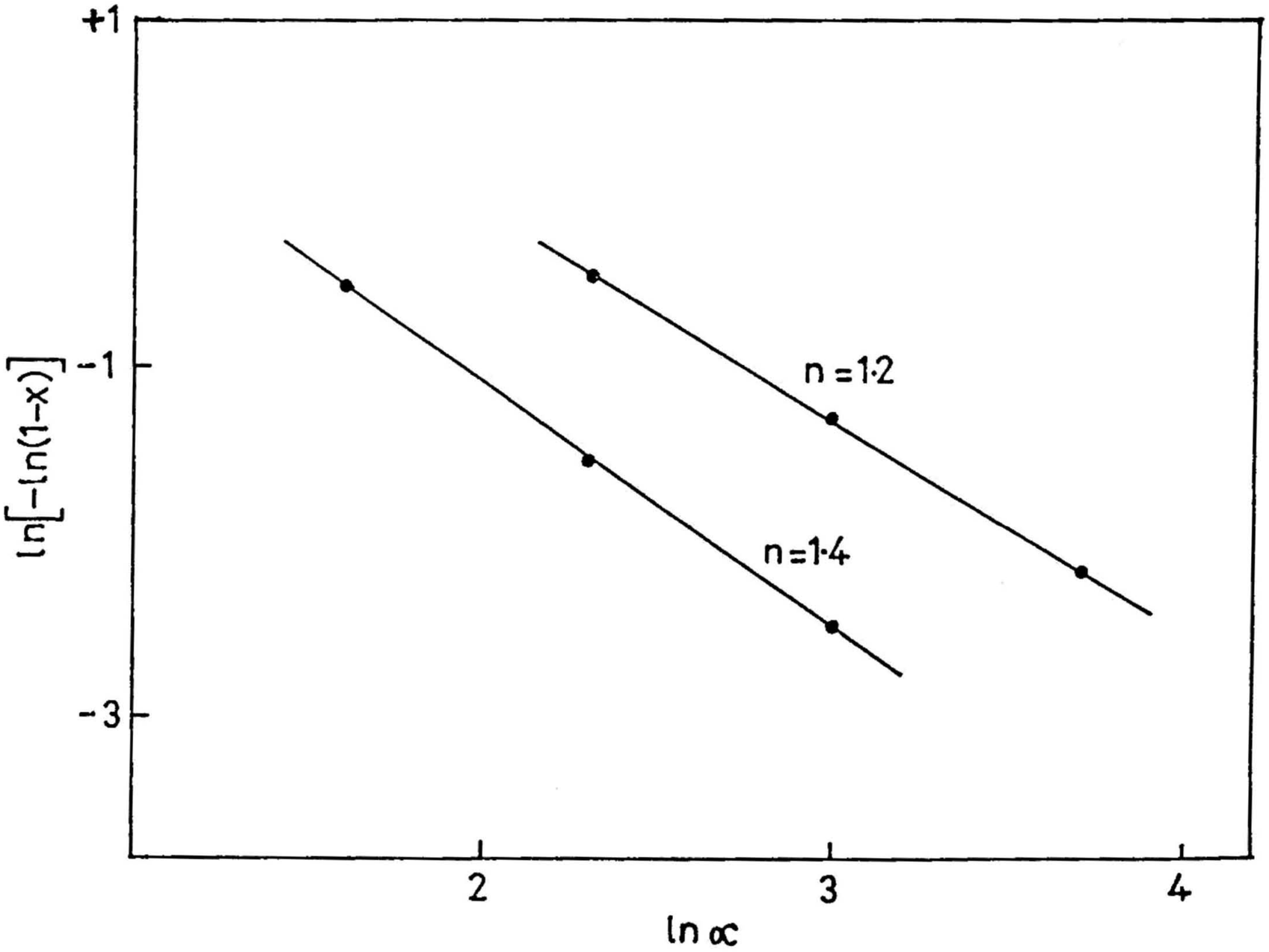

Fig 5 5 Variation of ln[-ln(1-x)] with ln(heating rate) at the temperatures 300°C and 310°C

the possible value of the parameter m to be 1,(from Table I) These results thus support a surface nucleation mechanism according to which the crystallization occurs mainly from the glass surface and crystal growth proceeds one-dimensionally into the bulk

Using these values of m and n along with the value of (m/n)E obtained from the plot of Fig 5.4, E was evaluated to be 565 kJ/mole

Fig 5.6 shows plots of ln[-ln(1-x)] against 1/T for various heating rates The plots are linear over a reasonably large range of temperatures with a slight change in slope at higher temperatures for all heating rates Such a non-linearity at high temperatures was also reported for chalcogenide glasses[17,18] Generally this break in slope is attributed to the saturation of nucleation sites in the final stages of crystallization[19] or to restricted crystal growth due to small size of the particles[20]

The slope mE was calculated from the linear region of the plot ln[-ln(1-x)] versus 1/T From the values of m and mE obtained by considering all heating rates, the average value of E was deduced as 556 kJ/mole

Fig 5.7 shows the modified Kissinger's plot in which $\ln(\alpha^n/T_p^2)$ is plotted against $1/T_p$ If the value of n is known, the slope of this plot should give the activation energy E The value of E thus determined from this plot is equal to 549 kJ/mole It is seen that the activation energies for crystallization kinetics estimated from the modified Ozawa

TABLE I

Values of n and m for various crystallization mechanisms[17]

Mechamism	n	m
Bulk nucleation		
three-dimensional growth	4	3
two-dimensional growth	3	2
one-dimensional growth	2	1
Surface nucleation	1	1

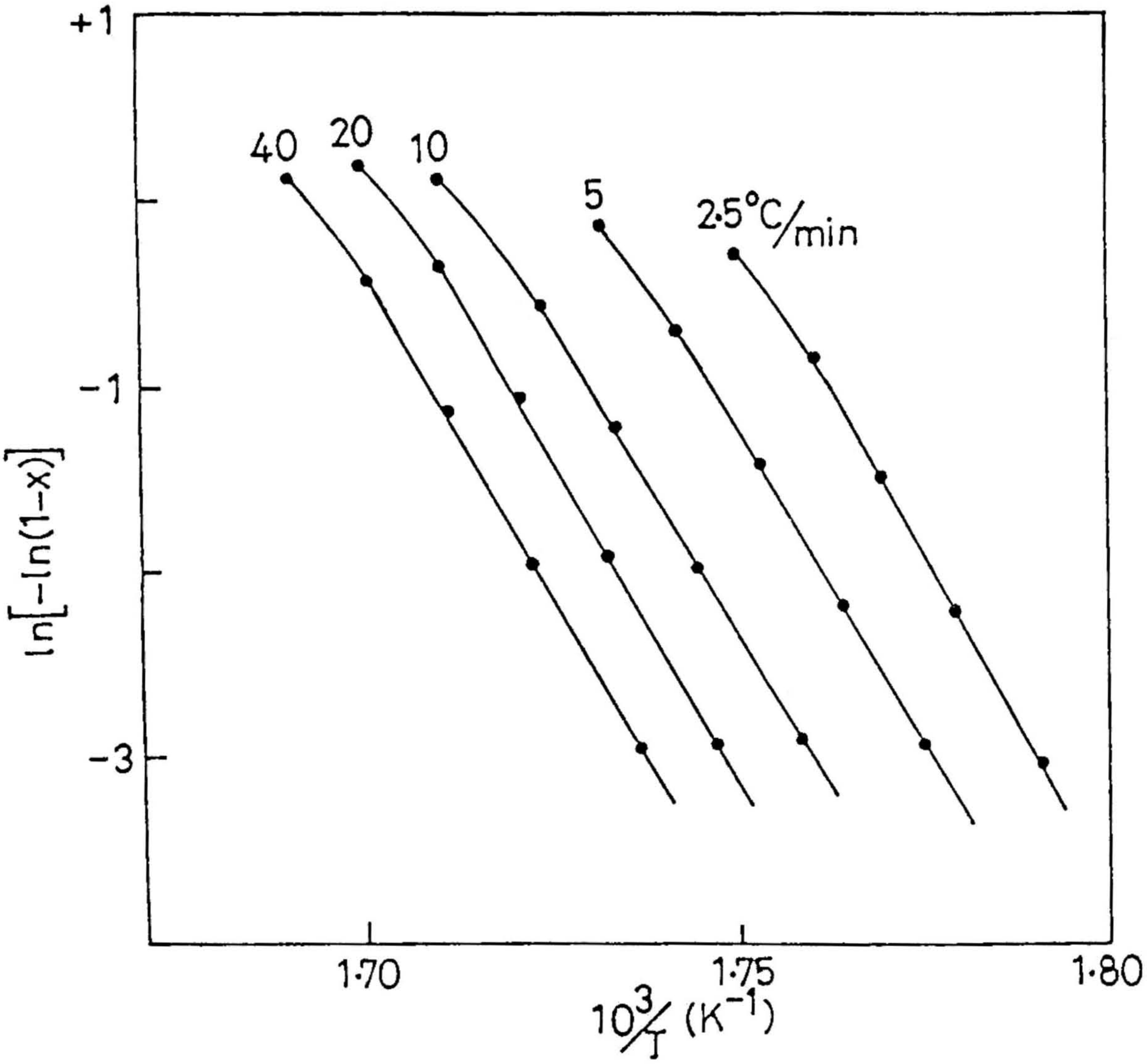

Fig 5 6 Variation of ln[-ln(1-x)] with reciprocal temperature for different heating rates

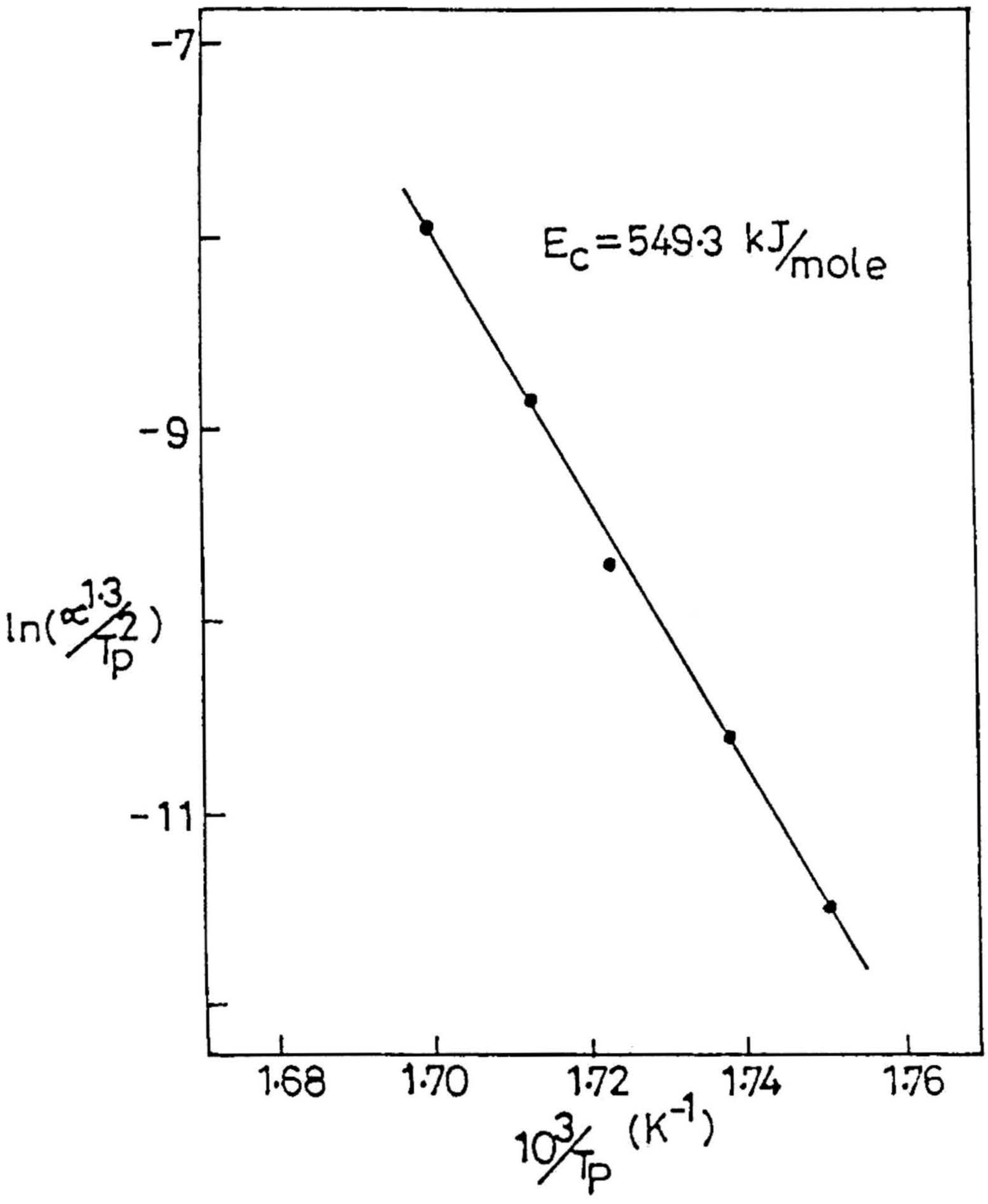

Fig. 5.7 The modified Kissinger's plot of the first-stage crystallization

and the modified-Kissinger methods are very close indeed (average of three independent determinations = 553 ± 6 kJ/mole)

5.3.4 Crystallization Studies by X-ray Diffraction

Fig 5.8 presents typical powder X-ray diffraction (XRD) patterns of as-quenched and heat treated glasses under different conditions. The XRD pattern of glass powder (Fig 5.8a) showed the absence of crystalline peaks, characteristic of amorphous phase, while that for glass in bulk or powder form when annealed isothermally at the first exothermal peak temperature for about 5 min (Fig 5.8b) revealed sharp diffraction lines. The intense peak (peak 'O') at 20.3° (2θ) belongs to the orthorhombic phase while the remaining lines (labeled 'X') are attributed to an unknown intermediate phase. Upon heat treatment of the bulk glass specimen after the second crystallization event of Fig 5.2b (annealed at 410°C) for about 10 hours (Fig 5.8c), all the diffraction lines X, have disappeared except the peak 'O', suggesting that the unidentified phase associated with the first exothermal peak has disappeared and a new phase has appeared without affecting the amount of orthorhombic phase. The diffraction peaks (labeled 'M') corresponding to this metastable phase could be indexed in terms of a monoclinic structure with the lattice parameters a = 10.291 Å, b = 4.710 Å, c = 10.832 Å, and $\beta = 109^{\circ}57'$. The indexing of the powder pattern of this phase is shown in Table II.

The XRD pattern (Fig 5.8b) of glass powder heat treated after third exothermic peak at 410°C for about one hour suggests that the metastable monoclinic phase might have transformed to the equilibrium orthorhombic phase. But the transformation was found to be incomplete. A

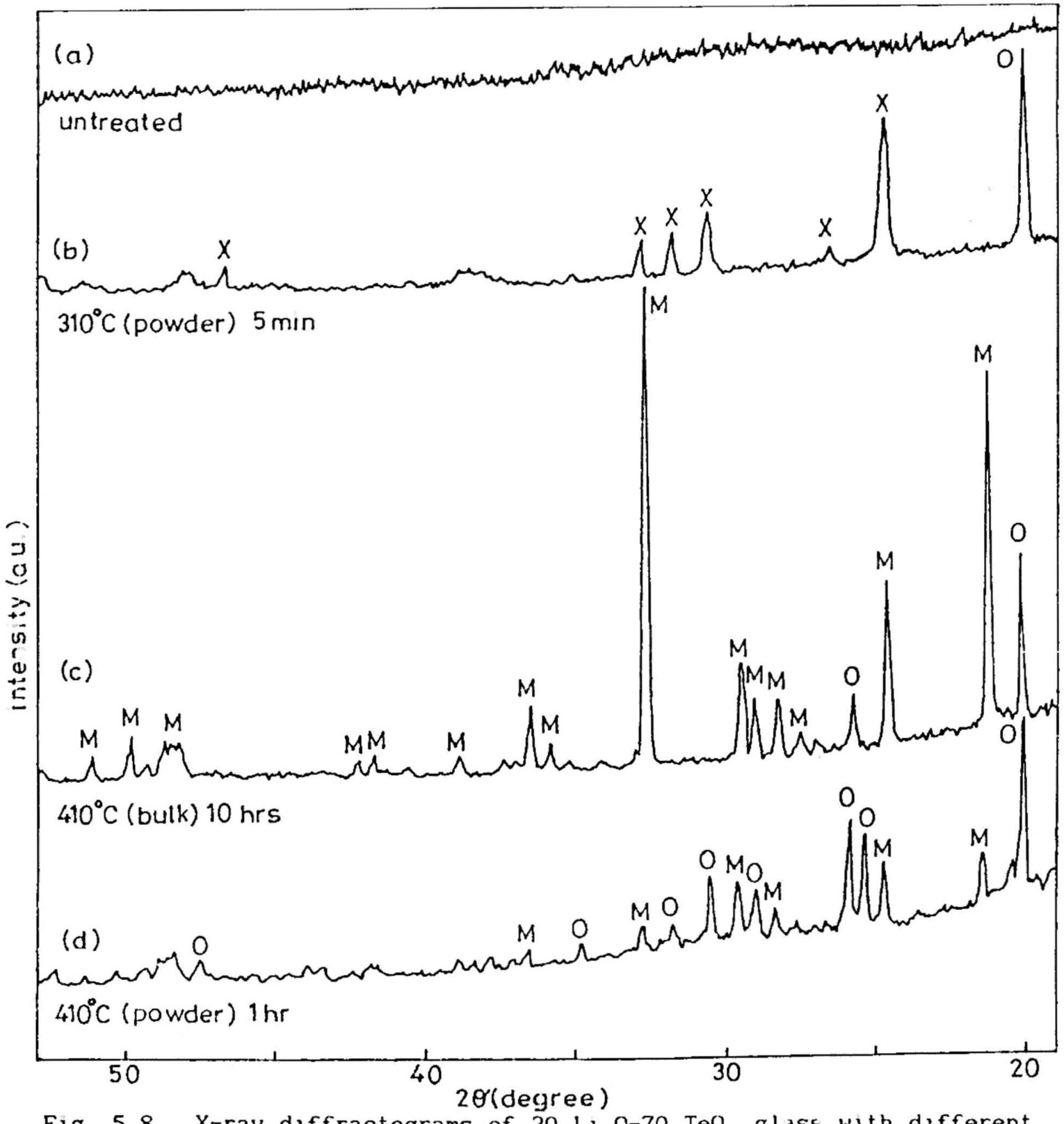

Fig 5.8 X-ray diffractograms of 30 Li_2O-70 TeO_2 glass with different heat treatments. O, M and X identify peaks due to

TABLE II

X-ray powder diffraction data for monoclinic phase

d_{obs} Å	d_{cal} Å	I/I_o	h	k	l
4.133	4.133	75	$\bar{1}$	1	1
3.597	3.610	36	$\bar{1}$	0	3
3.220	3.232	5	3	0	0
3.137	3.179	11	$\bar{2}$	1	2
3.048	3.048	11	1	1	2
3.013	3.005	20	2	1	1
2.730	2.738	100	$\bar{2}$	1	3
2.495	2.481	5	1	1	3
2.449	2.439	12	$\bar{3}$	0	4
2.309	2.312	4	$\bar{2}$	1	4
2.151	2.153	3	$\bar{1}$	2	2
2.132	2.133	2	3	1	2
1.870	1.873	6	0	1	5
1.824	1.821	8	$\bar{3}$	2	3
1.781	1.780	5	$\bar{1}$	0	6

prolonged heat treatment at 410°C, might assist complete phase modification This phase transformation is favoured only when the heat treatment was performed on powdered glass, but not on the bulk glass specimen The reason, for this phenomenon is not clear at present

In order to obtain some information on the stability of glass upon long-term storage at ambient, calorimetric and diffraction experiments were carried out on 30 Li_2O-70 TeO_2 glass stored for about 10 months at 30°C in a desiccator Fig 5 9 represents the DSC trace recorded with a heating rate 10°C/min and Fig 5 10a, the XRD pattern of this aged glass isothermally annealed for 5 min at the first crystallization peak temperature

Upon annealing this aged glass crushed into fine powder at 410°C, for about 10 hours the metastable to stable phase transformation was complete The XRD trace of this fully crystallized product is shown in Fig 5 10b All reflections can be indexed on the basis of an orthorhombic cell with lattice parameters a = 5 178 Å b = 8 142 Å and c = 23 939 Å Table III presents the indexing of the diffraction pattern of this orthorhombic phase

The lattice parameters obtained for the monoclinic and orthorhombic phases crystallized in tellurite glass agree well with those reported for Li_2O-2 TeO_2 single crystals[11]

5 3 5 Conductivity Measurement

Fig 5 11 presents the effects of crystallization on the electrical properties of the glass by comparing the temperature dependence of

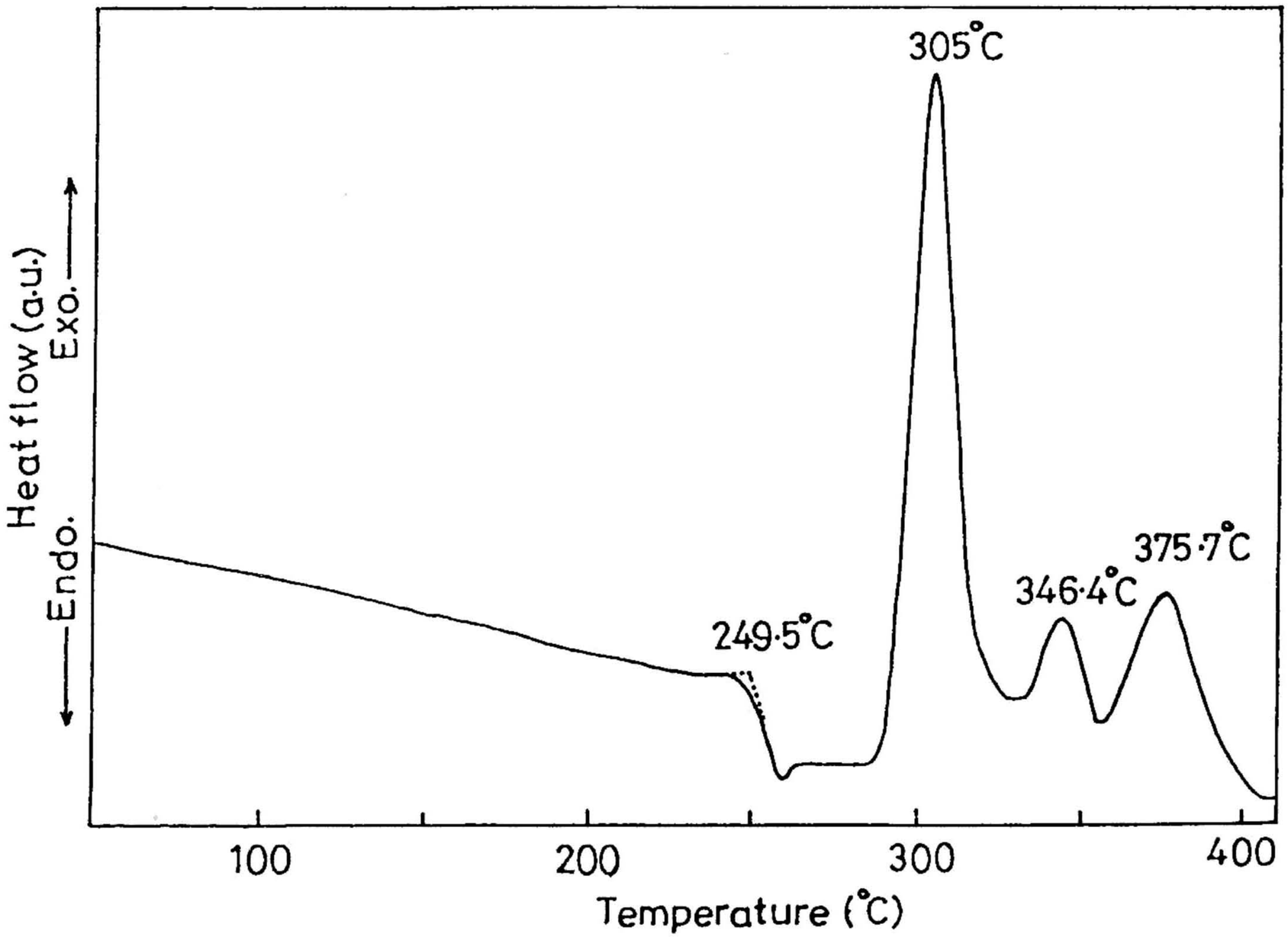

Fig. 5.9 DSC curve of 30 Li_2O-70 TeO_2 glass powder stored for about 10 months at ambient. Heating rate $10^{\circ}C$/min.

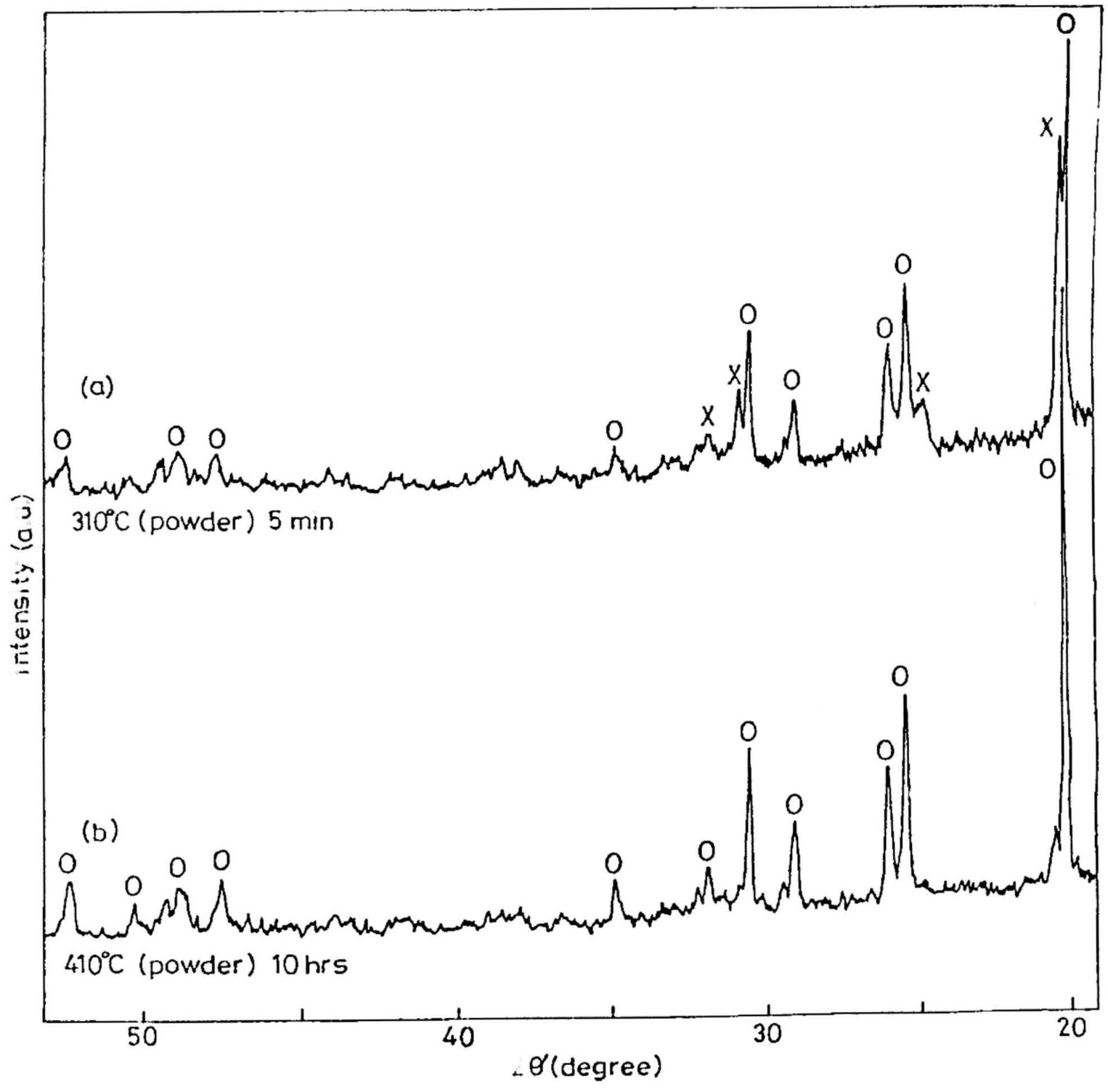

Fig. 5.10 X-ray diffractograms of stored glass heat treaated at different temperatures O,M and X are as defined in Fig 8

TABLE III

X-ray powder diffraction data for orthorhombic phase

d_{obs} Å	d_{cal} Å	I/I_o	h	k	l
4.375	4.369	100	1	1	0
3.486	3.515	34	1	0	5
3.414	3.420	22	0	0	7
3.069	3.092	14	1	2	2
2.921	2.946	27	1	1	6
2.811	2.809	5	0	1	8
2.571	2.569	8	0	3	3
1.914	1.917	8	1	2	$\underline{10}$
1.866	1.862	7	1	0	$\underline{12}$
1.814	1.815	5	1	1	$\underline{12}$
1.748	1.745	10	2	3	5

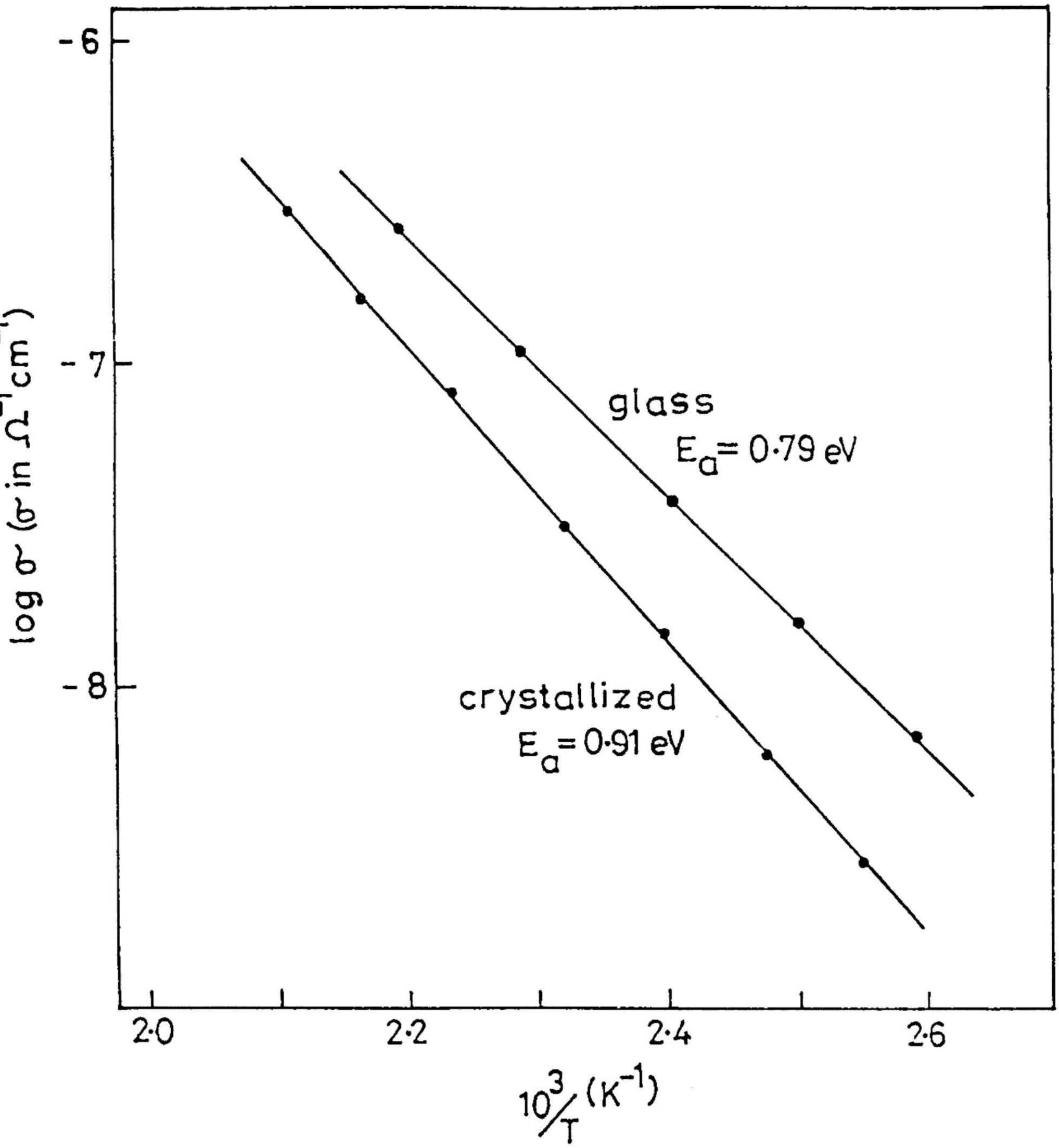

Fig 5 11 The temperature dependence of ionic conductivity of (a) 30 Li_2O-70 TeO_2 glass and (b) the crystallized sample

conductivities of glassy and crystallized samples. The crystallized specimen with orthorhombic structure used in the measurement was obtained by annealing the glass powder at 410°C for about 10 hours. the XRD pattern of which is shown in Fig. 5.10b.

5.4 DISCUSSION

The eutectic composition 30 Li_2O-70 TeO_2 determined from the phase diagram exhibits lower melting point,which possesses more resistance towards devitrification than other compositions, away from the eutectic. When the molten liquid is transformed to solid by quenching, the possibility of formation of glass, however,rests entirely with the process of crystallization. The precipitation of crystals involves nucleation and growth, as a result of rearrangement of particles (atoms or ions), requiring sufficient thermal energy to overcome the energy barrier which impede these rearrangements.

A quantitative measure of this thermodynamic barrier for crystallization is provided by the relation $\Delta S_m = \Delta U_m / T_m$ where ΔU_m is the enthalpy change ΔS_m the entropy change and T_m-the temperature of the melting[21], which implies a higher reconstructive entropy at T_m (lowest) for the eutectic composition. Hence a larger kinetic barrier exists to nucleation and crystal growth leading to a more favourable condition for the eutectic composition towards glass formation.

The thermal behaviour of the glass corresponding to the eutectic composition is revealed by DSC to have a three-step crystallization process for powdered glass (Fig. 5.2(a)), and a two-step crystallization process for bulk glass (Fig. 5.2(b)). When the crystallized bulk glass

is ground and rescanned the third high temperature exotherm (Fig 5.2(c)) appears again (see later).

The extensive analysis of the first stage non-isothermal crystallization kinetics by three different methods has yielded a value 556 ± 6 kJ/mole for the activation energy (E) for crystallization. This value of E is much larger than those reported for silicate glasses: 330 kJ/mole for $Li_2O\ SiO_2$ [22] and 249 ± 10 kJ/mole for $Li_2O\ 2SiO_2$ [23].

When a glass is heated beyond the glass transition temperature, it becomes kinetically capable of crystallizing through a nucleation-and-growth process. Usually the nucleation rate in glass reaches a maximum at a temperature somewhat higher than the glass transition temperature and then decreases rapidly with temperature. The rate of nucleation is observed to be maximum at a temperature well below the temperature at which the growth rate reaches maximum. In addition, due to the rapid rise in temperature and the large difference between the latent heats of nucleation and growth, it was suggested[24] that the crystallization exotherm in a non-isothermal measurement mainly characterizes the crystal growth. Thus the calculated E represents the value of activation energy for crystal growth. The rate of growth, however would be controlled by the rate at which the glass particles are being sorted out and aligned to form growing crystals.

The growth rate u can be expressed as[25a,25b]

$$u = \text{const} \cdot \exp(-E/RT)\,[1-\exp(\Delta G/RT)]$$

$$= u_o \exp(-E/RT)$$

where ΔG is the bulk free energy of crystallization and E is the

activation energy for crystal growth. If the crystal growth is controlled by diffusion at the temperature range studied, it will be influenced by the coefficient of viscosity η and its dependence on temperature. Hence the activation energy E for crystal growth should be related to that for viscous flow over a similar temperature range. The viscosity again depends upon the structure of glass network. As the temperature increases from T_g, the viscosity decreases in a different manner for different glass systems. Thus the higher activation energy for crystal growth in the 30 Li_2O-70 TeO_2 glass implies the high activation energy for viscosity around the crystallization temperature.

Unlike in borate and silicate glasses, the addition of the network modifier such as Li_2O to TeO_2 introduces non-bridging oxygens[26,27] (NBO's) leading to the disruption of the glass-forming network, thereby reducing the viscosity. From a structural point of view, therefore, the present higher activation energy for crystal growth than for silicate glasses, explains such a decrease in viscosity and thus the tellurite glass tends to be less stable, that is more prone to crystallization than silicate glasses, in line with the results obtained on ZBL (ZrF_4-BaF_2-LaF_3) and ZBLALi (ZrF_4-BaF_2-LaF_3-AlF_3-LiF) glasses,[28] where the modifiers (AlF_3 and LiF) reduced the activation energy of the parent ZBL glass leading to more stable ZBLALi glass. Introduction of another modifier such as Al_2O_3 into the 30 Li_2O-70 TeO_2 glass may increase the stability, by increasing the viscosity in the crystallization temperature range to some extent, because of ionic bonding of Al^{3+} to NBOs leading to a decrease in the number of NBOs.

The temperature gap $\Delta T=T_c-T_g$ observed as 47°C - a considerably lower value than for (100-x) TeO_2-x $LiNbO_3$ glasses[10] with x = 20 and 30, having T in the range 150-170°C also suggest a lower stability of the present glass system

The comprehensive X-ray diffraction studies (Fig 5 8(a,b,c,d)) on freshly prepared glasses subjected to various heat-treatment procedures, have established three distinct crystalline phases at different stages of crystallization Thus the first exotherm of DSC spectra represents the simultaneous growth of a minor orthorhombic phase, and a minor, unknown intermediate phase The second exotherm is associated with the disappearance of the unknown phase grown during the first stage of crystallization, and the appearance of the metastable monoclinic phase Finally, the third exothermic event refers to the irreversible phase transformation of the metastable monoclinic phase to an orthorhombic structure which is thermodynamically more stable

The DSC and X-ray diffraction results (Figs 5 9 and 5 10(a,b)) on glass samples aged at ambient and subsequently heat-treated under different conditions have thrown light on structural and thermal stabilities A comparison of the amount of orthorhombic phase crystallized due to first exothermic peak in Fig 5 10a and the ratio of the areas under the second and the first crystallization peaks in the DSC spectra of Fig 5 9 obtained for aged glass specimen to those presented for freshly prepared glass samples in Fig 5 8b and Fig 5 2b leads to the significant conclusion that prolonged storage of 30 Li_2O-70 TeO_2 glass specimen favours a structure, induced by relaxation, which can precipitate a major, stable orthorhombic phase along with a minor,

unknown intermediate phase, compared to freshly prepared 30 Li_2O-70 TeO_2

The bulk ionic conductivities deduced from the admittance measurements on both the glassy and the crystallized samples exhibited Arrhenius (log σ versus $10^3/T$) behaviour. The polycrystalline sample exhibits lower conductivity and higher activation energy compared to those of glassy sample. While the activation energy in glass can be attributed only to the migration Li^+ ions, in polycrystalline samples it includes the energy necessary for the migration of Li^+ ions as well as for the creation of defects in the orthorhombic crystalline phase.

5.5 CONCLUSIONS

The eutectic composition 30 Li_2O-70 TeO_2 in mole ratio identified from the phase diagram of the system Li_2O-TeO_2 is prepared as glass and its thermal and electrical behaviours are investigated in detail. The essential conclusions that may be drawn from this investigation are:

(a) The thermal behaviour of this glass studied through DSC reveals two and three stages of crystallization for the bulk and powdered glasses respectively,

(b) The study of non-isothermal crystallization kinetics suggests a surface nucleation mechanism for the devitrification process.

(c) The higher activation energy for crystal growth estimated for this glass compared to silicate glasses suggest that the former is less stable and more prone to crystallization,

(d) The main crystalline phases emerging out of the glass upon heat treatment as identified by X-ray diffraction studies are the intermediate unknown phase, the metastable monoclinic and the

stable orthorhombic phases. The final crystallized product was found to possess a monoclinic structure when the heat treated glass was in bulk form but an orthorhombic structure when the glass was crushed into fine powder,

(e) With reference to the freshly prepared glass the aged glass contains larger fractions of the orthorhombic phase precipitated during first stage crystallization giving some clues about the effect of prolonged storage on the stability of the glass structure and

(f) The crystallized product exhibits lower conductivity and higher activation energy compared to those of the uncrystallized glass

B MIXED-ALKALI EFFECT STUDIES

5 6 INTRODUCTION

Many physical properties of oxide glasses show non-linear behaviour as a function of alkali content, if one alkali type is gradually changed for another alkali ion type This behaviour is referred to as the mixed alkali effect It has also been called the 'neutralization effect' or "poly-alkali effect' This mixed alkali (MA) effect is found to be more pronounced for properties associated with alkali ion movement such as electrical conductivity, ionic diffusion, dielectric relaxation and internal friction[29,30] In marked contrast, other properties such as bulk density, molar volume and refractive index show such small deviations that their variation with composition can be considered "normal' For example Fig 5 12 shows the change in molar volume of $(1-x)K_2O-xLi_2O-2SiO_2$ glasses[30] to be nearly 'normal', but the departure from additivity for the electrical conductivity of these glasses, is nearly five orders of magnitude exhibiting a minimum at Li/(K+Li) ≈ 0 5 The activation energy and the pre-exponential factor (Fig not shown), both rise to maximum values corresponding to the minimum in the conductivity

This behaviour for properties related to alkali ion movement is essentially independent of the glass-forming oxide, being observed in silicate, borate, borosilicate phosphate and germanate glasses Further more the changes in properties typical of MA effect in glasses have also been observed in molten salts[31,32], porcelains[33] and crystalline materials containing mixtures of alkali ions[34] Thus the presence of dissimilar alkali ions appears to be more important than whether the structure is vitreous or crystalline However, no data are available on

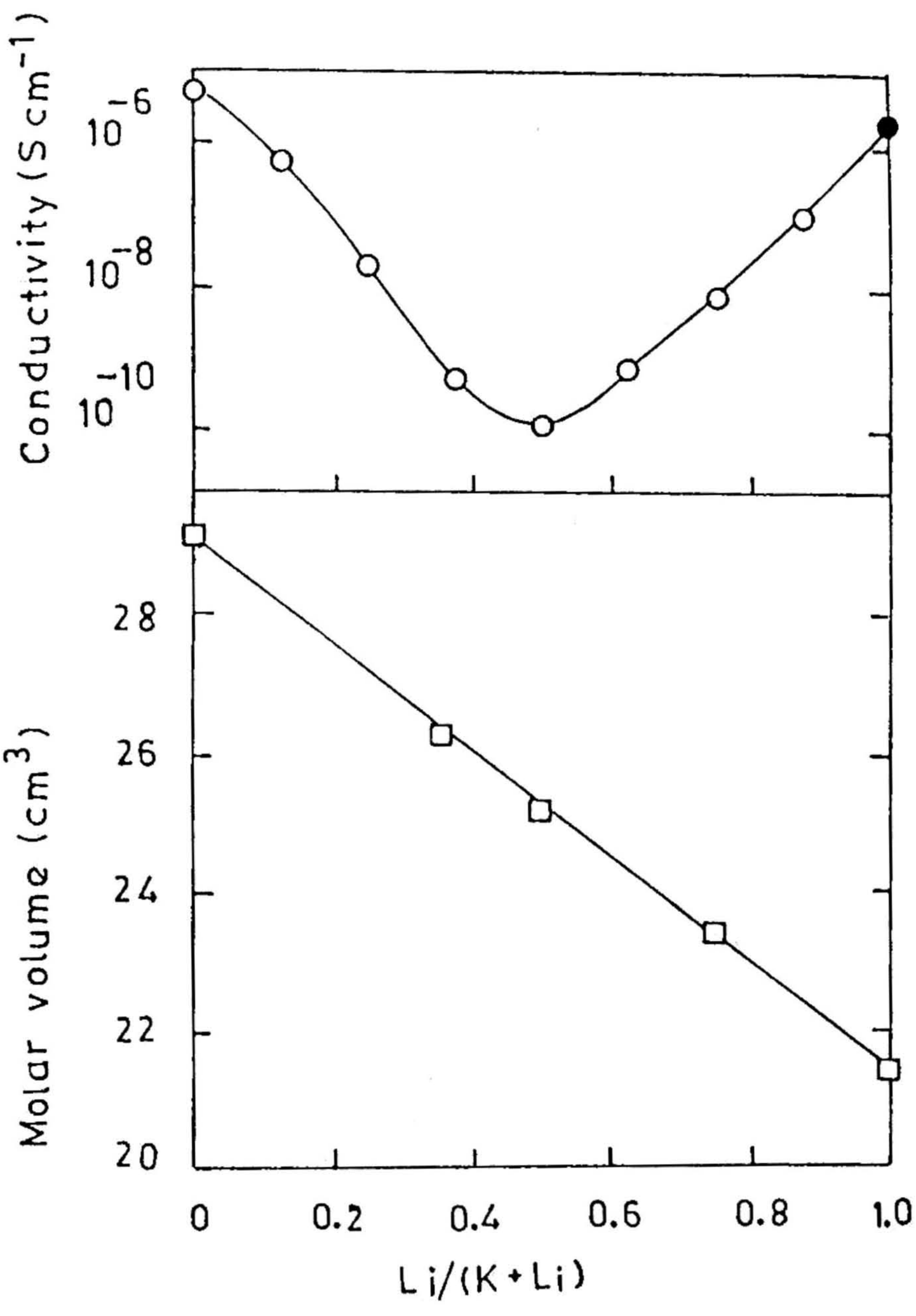

Fig 5.12 Electrical conductivity (at 150°C) and the molar volume (at 20°C of $[(1-x)\ K_2O\text{-}x\ Li_2O]\text{-}2\ SiO_2$ glasses[30]

single crystals containing a mixture of alkalis in solid solution It is also not unique to only mixed alkali systems Indeed it is observed in mixed glasses containing Ag^+ and Tl^+ cations[35] and also F^- and Cl^- anions[36]

The object of understanding the MA effect is to determine what relationship(s) - if any - exist between the observed anomalous physical changes and the glass structure

5.6.1 Ionic Diffusion

Since properties which show largest departure from additivity are directly related to alkali ion movement, it is more important to understand the alkali diffusion as a function of composition

The magnitude of the change in alkali ion mobility in mixed alkali glasses, varies directly with the second alkali One of the most significant features of MA effect is the "mobility cross- over" at some particular alkali ratio Typical diffusion data for $(1-x)Na_2O$-x Rb_2O-3 SiO_2 glasses[37] are shown in Fig 5 13 As a result of the cross-over the mobility of the more mobile ion passes through a minimum, whereas the mobility of the less mobile ion goes through a maximum While the individual alkali ion diffusion coefficients do not exhibit large departure from additivity, as shown by the dashed lines in Fig 5 13, the departure from additivity for the mobility of either the faster or slower moving ion is quite large

The alkali ratio corresponding to the cross-over point, where both alkali ions have the same mobility (diffusion coefficients) is usually

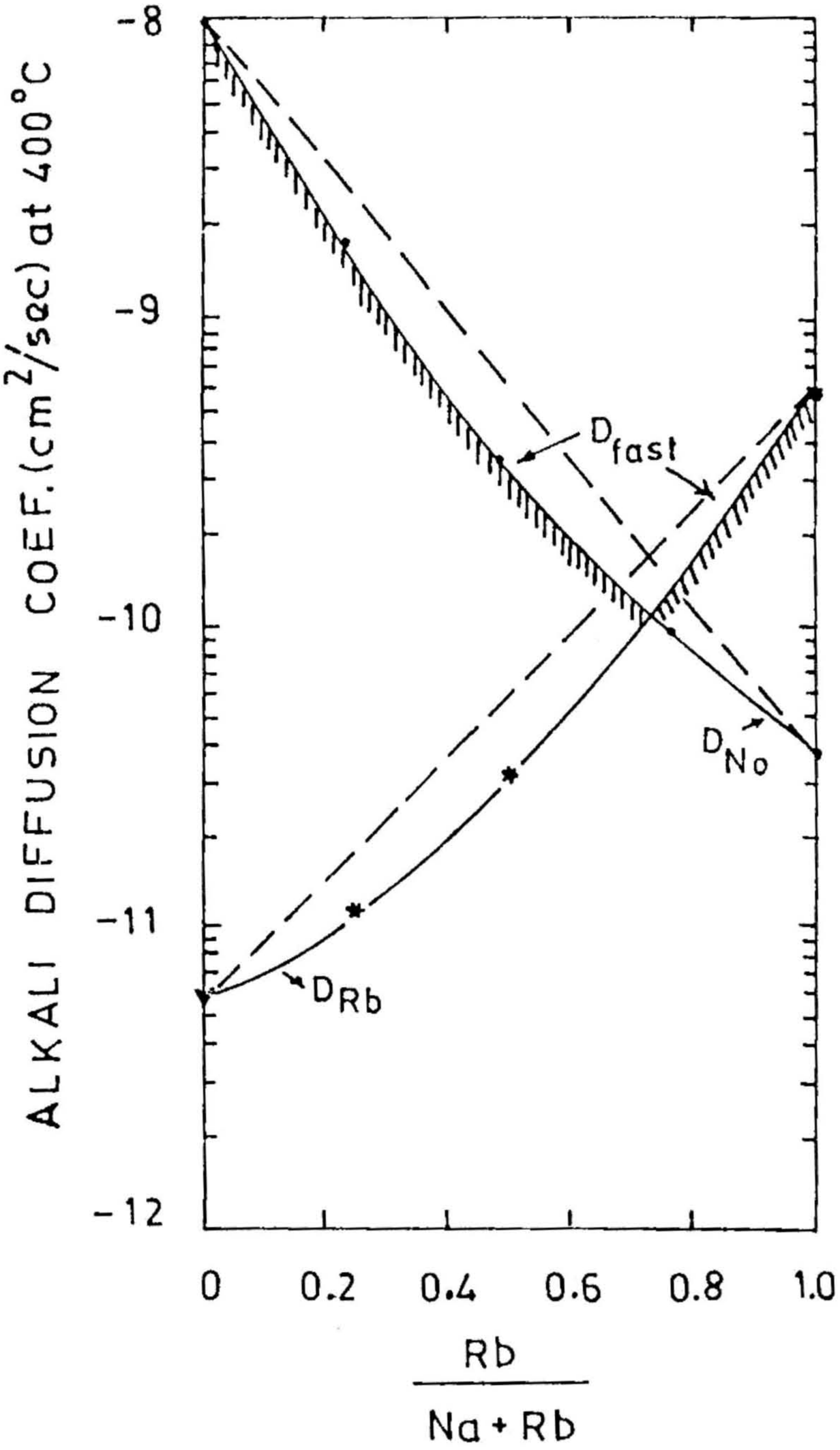

Fig 5.13 Composition dependence of tracer diffusion coefficients at 400°C in $[(1-x)\ Na_2O\text{-}x\ Rb_2O]\text{-}3\ SiO_2$ glasses. Cross-hatched curve denotes ion having larger diffusion coefficients[37]

not found at equal concentrations of the alkali ions but is a function of

(1) the type of alkali ions present,

(2) the total alkali concentrations,

(3) the glass former, and, in certain cases, and

(4) temperature

In $(Na_2O-K_2O)-3SiO_2$ glasses[38] the cross-over occurs at Rb/(Na+Rb) = 0.73.

5.6.2 Electrical Conductivity

The property which shows the largest MA effect is the electrical conductivity. Electrical conduction is of course due to alkali ion migration and is a measure of the alkali ion mobility. The minimum in conductivity and the maximum in activation energy for 30 $[(1-x)Li_2O-xNa_2O]-70B_2O_3$ glasses[39] are shown in Fig. 5.14. The conductivity minimum was observed at Na/(Na+Li) = 0.6 and the activation energy also exhibited its maximum at the same composition. A systematic study[40] of the electrical conductivity of $(15-x)\ Cs_2O-xR_2O-85\ SiO_2$ (R= Li, Na, K and Rb) glasses revealed the following typical features of the MA effect in electrical conductivity.

(1) the magnitude of the departure from additivity is a function of the alkalis present, increasing as the size difference increases, and

(2) the position of the maximum is usually not located at the composition containing equal concentrations of the two alkali ions, and is also a function of the size difference of the alkalis.

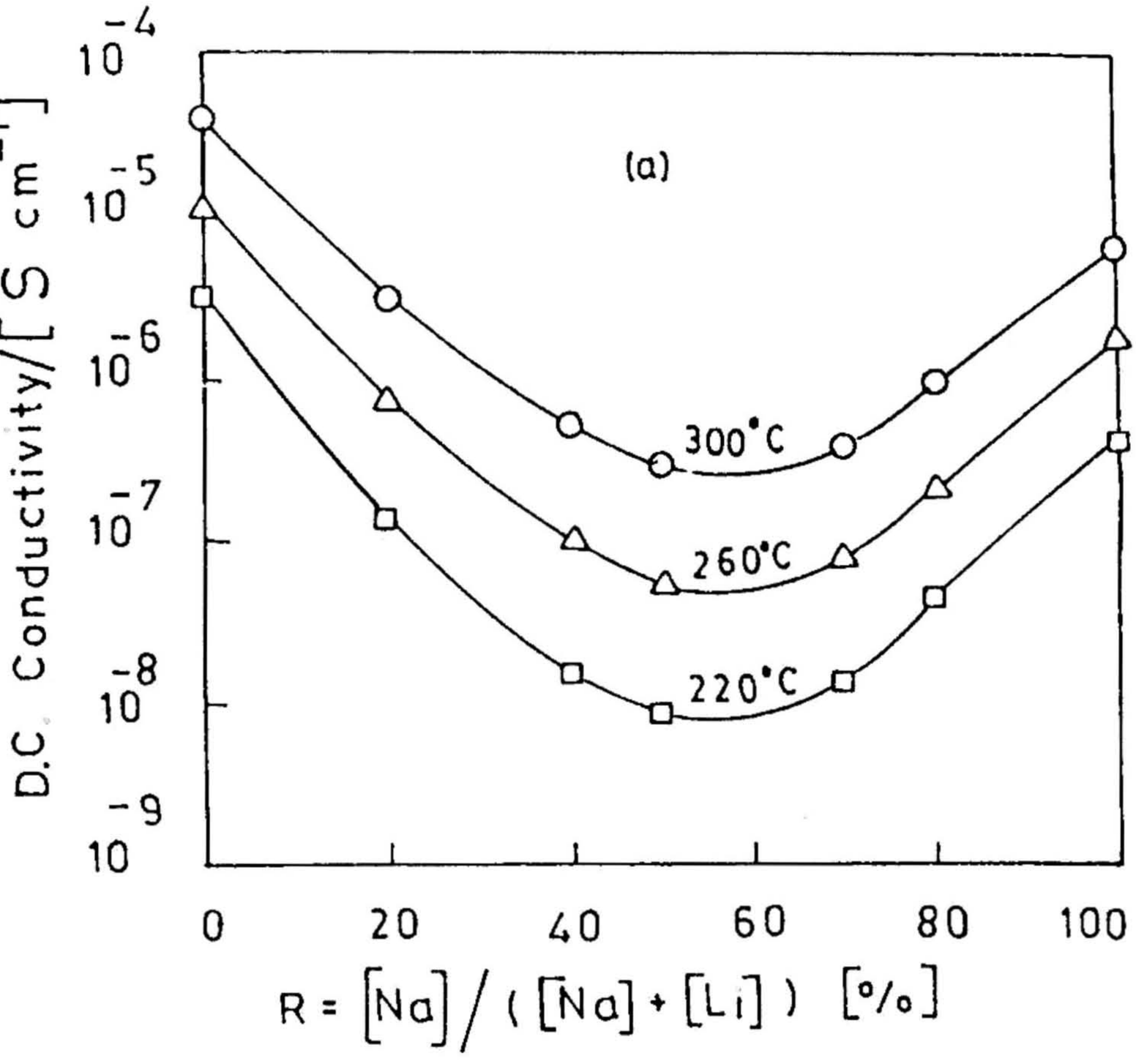

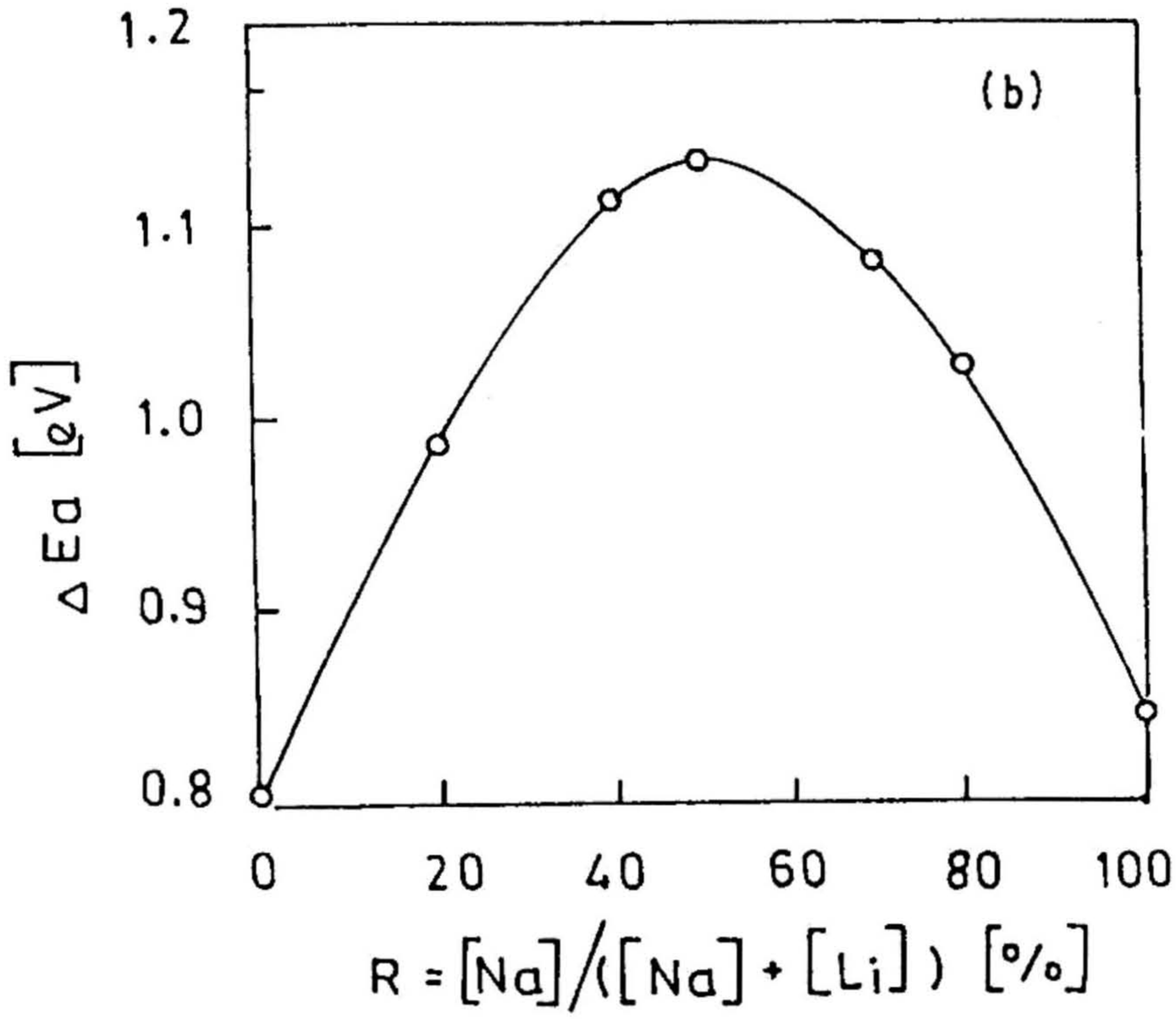

Fig. 5.14 The dependence of (a) DC conductivity and (b) activation energy on the molar fraction of sodium x in the glasses 30 [(1-x) Li_2O-x Na_2O]-70 B_2O_3 [39]

Qualitatively, the minimum in electrical conductivity follows the diffusion coefficient of the more mobile ion as shown by the cross-hatched curve in Fig 5 13 In the composition region near the cross-over point, both ions contribute to the conductivity but with a much lower mobility than in the end-member glasses Thus the dependence of the magnitude of the minimum in conductivity upon the second alkali can be accounted for by the compositional dependence of the alkali diffusion coefficients

5 6 3 Mechanical Relaxation

Evidence of ionic decoupling is graphically illustrated in the internal friction (delayed elasticity) effects Fig 5 15 shows data for Li/Na trisilicate glasses[41] Upon the addition of a second alkali to the first type, (1) the single alkali peak present originally becomes rapidly smaller and the peaks shift to higher temperatures, thereby increasing its activation energy This change as illustrated by the peak at $\approx 0^{o}C$ in Fig 5 15 is consistent with the reduction in alkali mobility and the increase in activation energy for alkali diffusion that occurs with the addition of a second alkali (2) A new mixed alkali peak appears for low concentrations of the second alkali which rapidly increased in magnitude (note the peak at $\approx 100^{o}C$ in Fig 5 15) Unlike the single alkali peak which correlates well with the mobility of the more mobile alkali ion, the mixed peak is primarily dependent upon the mobility of the less mobile ion

The single alkali peak seems to involve the motion of the host cations, whereas the mixed alkali peak have been attributed to the cooperative movement of dissimilar alkali ions[37,38,42]

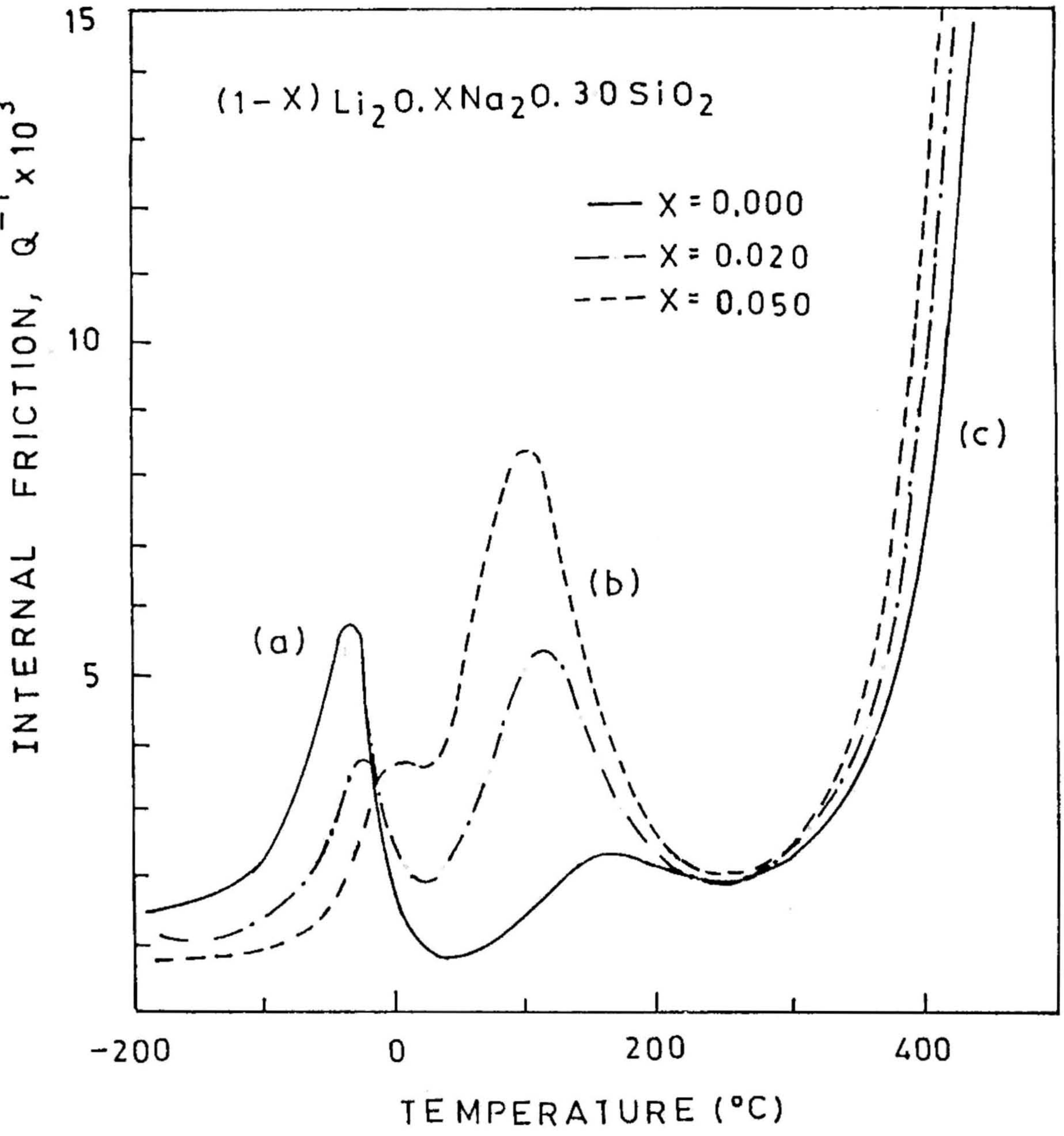

Fig. 5 15 Internal friction peaks in mixed (Li/Na) trisilicate glasses, showing (a) 'single alkali' peaks, (b) 'mixed alkali' peaks and (c) the onset of the glass transition[41].

5 7 THEORIES

Several theories have been proposed, but no single theory is universally accepted nor fully accounts for all features of the MA effect. Of the many theories of MA effect, those proposed by Weyl and Marboe [43], Sakrai and Oaka,[44] and Mazurin[45] are based on the consideration that the strengthening of the bond between oxygen and alkali ions play an important role in MA effect. Shelby and Day[41] also suggested a similar idea from their mechanical relaxation experiments on Li/Na silicate glasses. Weyl and Marboe's theory attributed the increase/ decrease in the bond-strength of alkali-oxygen to differences in atomic mass and their asymmetrical (anharmonic) thermal vibrations with no special structural differences between single and mixed alkali glasses and thus is not quantitative. Sakurai and Oaka's theory gives conductivity values which are considerably different from the observed ones. Mazurin explains the MA effect in terms of the polarizability of the non-bridging oxygen ions. The mobility of the smaller alkali ions is decreased by weakly polarized oxygens introduced by larger alkali ions. His explanation is applicable to the case when smaller ions are replaced by larger ions, but not to the reverse case.

Stevels[46] assumed that in the random network structure of glasses, such as SiO_4 units in silicate glass, the geometrical incorporation of different sized ions (mixed alkali) may be easier than that of ions which all have the same size (single alkali). Hence the binding and consequently the activation energies necessary for the ions to migrate are greater. In this theory the alkali ion binding energy varies from site to site and the conductivity is obviously determined by the less firmly held ions. In a single alkali glass the substitution of

some primitive (less held) ions by a different sized alkali causes a more stable geometrical configuration and a reduction of alkali conductivity (higher binding energy) This effect is more evident, the greater the ionic size difference Stevels' theory suggests a higher density for MA glasses due to a more efficient packing of the alkali ions of different size Depending upon the composition of the system, however, the density of MA glasses shows either positive or negative deviation from additivity, and the molar volume shows no evidence of higher atomic packing, being a nearly perfect function of composition and thus do not allow a comparison with the experimental data

The electrodynamic interaction model of Hendrickson and Bray[47a,47b] attributes the MA effect to the mass difference and the interaction between dissimilar alkali ions By treating the cations as harmonic oscillators vibrating in local oscillating electric fields, they show that an interaction energy develops between adjacent cations of unequal masses They account for the lower conductivities of mixed cation glasses, by including this additional interaction energy in the total activation energy

This theory attracted a much attention and enjoyed some experimental support[47a,47b,48] However, recent investigations of electrical conductivity[49] and NMR spectra[50], in Li^6/Li^7 borate glasses, with varying Li^6/Li^7 ratios do not show the expected mixed isotope effect Also, the size of conductivity anomalies in glasses containing Tl^+ (and also Ag^+ ions) seems to indicate that the magnitude of the conductivity anomaly is not controlled by a single ionic parameter such as mass or indeed ionic radius

The MA effect was explained by Dietzel[51] on the basis of difference between the cation field strengths $\Delta Z/a^2$ (or ΔF), where Z is the charge and a is the radius of the ion. The larger the value of ΔF

(1) the more the formation of $R_1 - \overset{Si}{\underset{|}{O}} - R_2$ is favoured in a MA silicate glass

(2) the stronger are the bonds within these groups,

(3) the more is the energy needed to remove a cation from the group,

(4) the nearer is the cross-over point of the diffusion coefficients to the side of the weaker cation, and,

(5) the more pronounced is the MAE, where ion mobility is concerned

This theory requires pairing of unlike alkali ions, about a non-bridging oxygen, i e , it predicts that no MA effect will occur, in the absence of NBOs

However, earlier studies on glass transformation temperature[52] and electrical conductivities[53] of glasses of the general formula $20(Na,K)_2O$-x Ga_2O-(80-x) SiO_2 demonstrated that the NBO content of the glasses have no significant role in the mechanism responsible for the MA effect

The present study is devoted to an examination of the MA effect in tellurite based alkali glasses While a large number of investigations have reported on MA effect in borate[39,54] and silicate[29,30,40] based alkali oxide glasses, no attempt was so far made to the best of our

knowledge, to look at the MA effect in tellurite glasses Compared with silicate and borate glasses, the structure of the tellurite glasses is somewhat extraordinary in the sense that the basic structural unit of the glasses is an asymmetrical TeO_4 trigonal bipyramid with a lone pair of electrons in an equatorial position and the coordination number of tellurium ion with respect to oxygen ions changes upon the incorporation of network modifying oxide such as Li_2O or Na_2O, eventually leading to a TeO_3 trigonal pyramid with the formation of NBOs Since the concentrations of NBOs in tellurite glasses can be systematically varied by controlling the alkali content these glasses also present an opportunity to test those theories which require NBOs for the occurrence of the MA effect

5 8 EXPERIMENTAL

30 $[(1-x)Li_2O - x\ Na_2O]$-70 TeO_2 glasses where x = 0, 0 2, 0 4, 0 6, 0 8 and 1 0 were prepared by melting in an electric furnace with appropriate quantities of Li_2CO_3 (Alfa) Na_2CO_3 and TeO_2 (BDH) - reagent grade, taken in a high pure alumina crucibles for 30 minutes between 500-600^{o}C depending on the composition and then quenching the homogenized, bubble-free melt by pouring on a stainless steel plate kept at ambient These quenched samples were immediately transferred to another furnace, and annealed for about 6 hours at 200^{o}C [~ 50^{o}C < T_g] to remove the residual stresses if any X-ray diffraction analysis was carried out in order to ascertain whether the samples were amorphous or not

The bulk DC electrical conductivity of these glasses are extracted from complex admittance measurements on the symmetrical cell

Pt/glass/pt, at selected temperatures in the range 70-200^{o}C using a home-built AC conductivity meter (see chapter 3) and lock-in amplifier (PAR model 5210) over a frequency range of 100 Hz - 120 KHz.

The infrared spectra were recorded at RT, by KBr pellet method on a Perkin Elmer double-beam spectrophotometer (Model 297) operating in the range 4000-200 cm^{-1}

DSC scans with heating rates of 10, 20 and 40^{o}C/min, were obtained from Du Pont DSC 9900, by heating ~ 15 mg of uniformly granulated glass powders hermetically sealed in an aluminum capsules with an identical empty aluminum capsule as the standard. The glass transition temperatures T_g, were measured using the intercept method and are reproducible to within ± 2^{o}C. The correction for each of the heating rates was applied by calibrating the temperature with the melting point of high pure Bismuth (271.3^{o}C) metal.

5.9 RESULTS AND DISCUSSION

Figs. 5.16 and 5.17 show the temperature dependence of the bulk electrical conductivity derived from the complex impedance plane analysis for the single alkali tellurite and mixed alkali tellurite glasses respectively. The conductivity (σ) of these glasses can be expressed using the Arrhenius relation $\sigma = \sigma_o \exp(-E_a/RT)$. Fig. 5.18 displays the conductivity isotherms i.e. $\log \sigma_T$ (at 150^{o} and 200^{o}C) and the activation energy E_a as a function Na/(Na+Li). The distinct feature of the MA effect is evident in this figure as a strong minimum in σ and a shallow maximum in E_a at Na/(Na+Li) = 0.6.

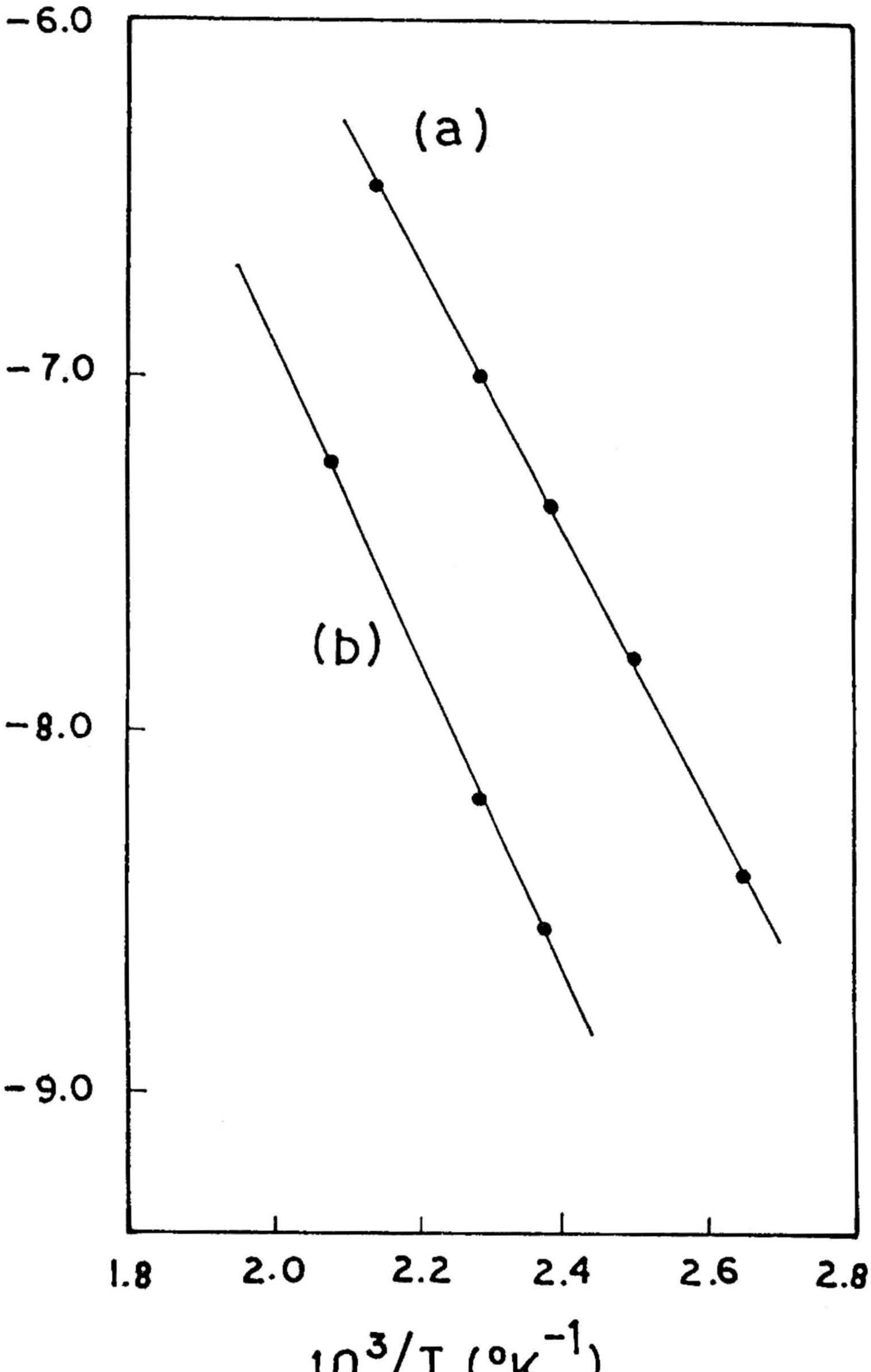

Fig 5.16 Temperature dependence of DC conductivity of (a) 30 Li_2O- 70 TeO_2 and (b) 30 Na_2O-70 TeO_2 glasses

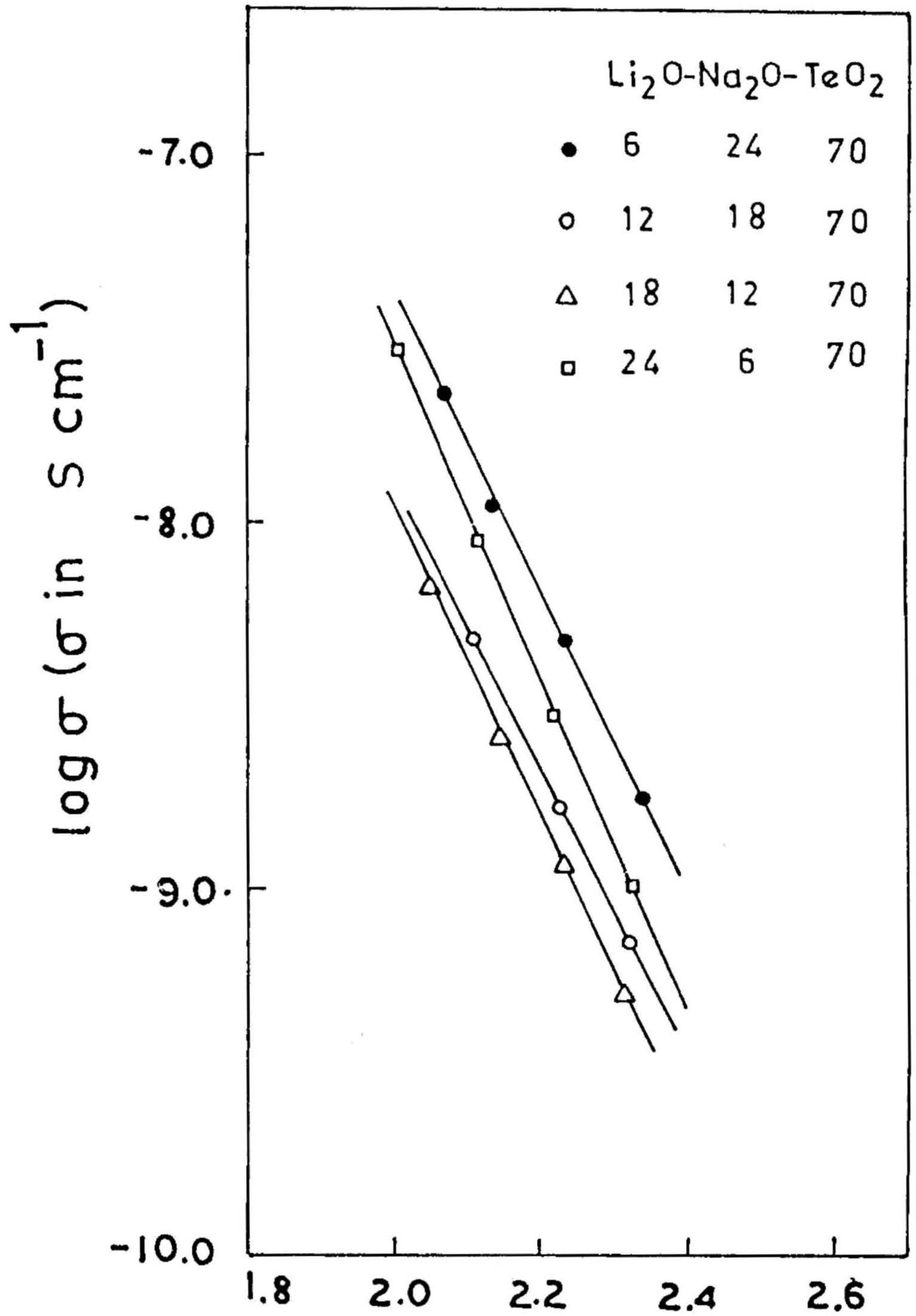

Fig. 5 17 Arrhenius plots of DC conductivity with temperature for the mixed alkali tellurite glasses

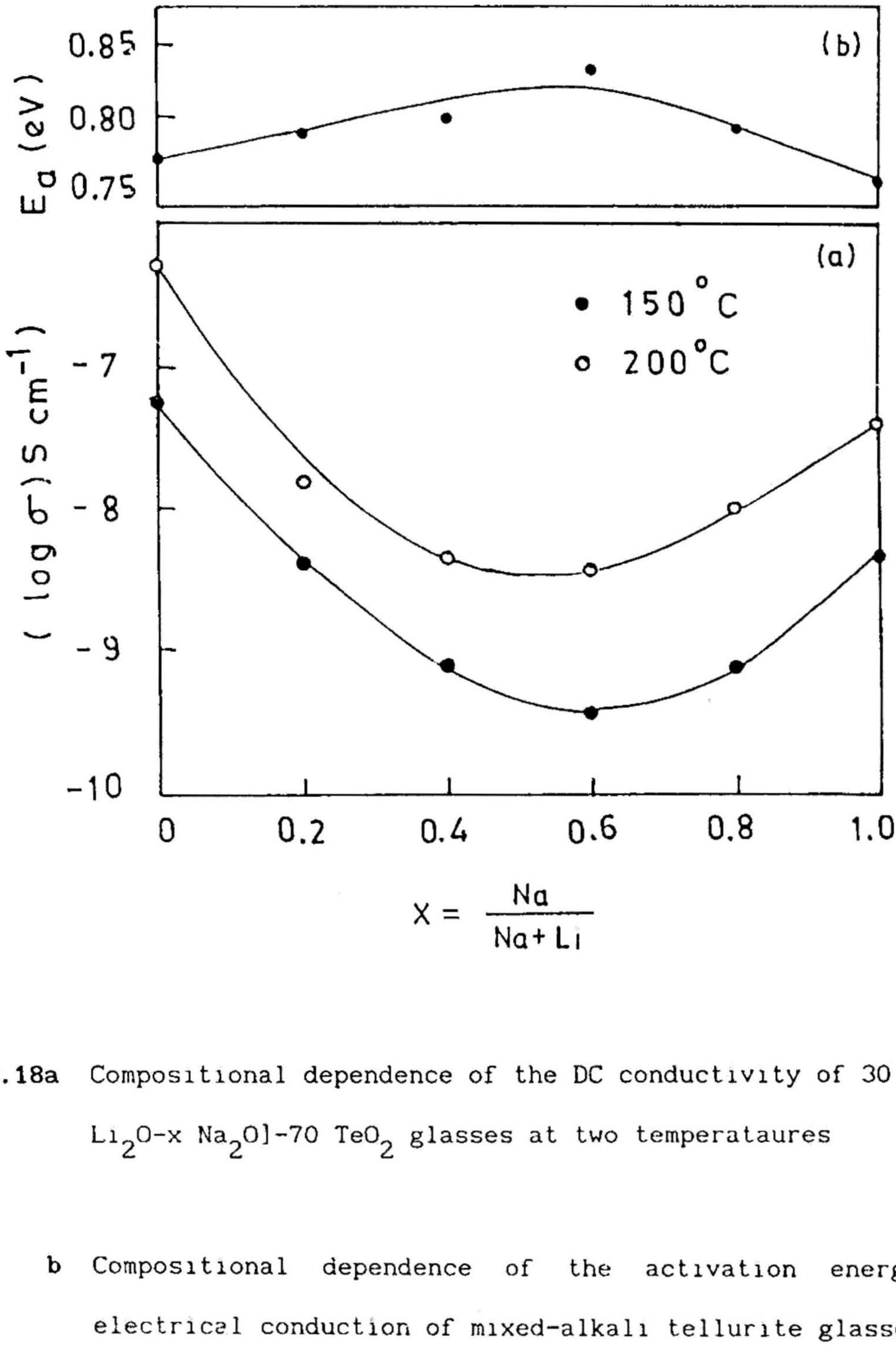

Fig. 5.18a Compositional dependence of the DC conductivity of 30 [(1-x) Li_2O-x Na_2O]-70 TeO_2 glasses at two temperataures

b Compositional dependence of the activation energy for electrical conduction of mixed-alkali tellurite glasses

These results mean that many alkali ions in MA glasses are being stopped, during their transport while their counterpart in single alkali glasses conduct without any excessive stoppage. It is important to note that (i) the magnitude of deviation in σ (2-3 orders) is nearly the same as that in borate glasses[39], (ii) while a deep minimum occurs in electrical conductivity at Na/(Na+Li) = 0.6, as in borate glasses, the positive deviation in E_a (with a maximum at Na/(Na+Li) = 0.6) is relatively shallow, in the present case. The comparison, particularly of the activation energy, suggests that the structural differences between tellurite and borate glasses might provide certain clues to understand the MA effect in the present system. Thus there is a need to carefully examine the structural aspects of the former and compare it to the latter especially with reference to (1) the reduced viscosity of the melt (visual observation) and the glass structure as a result of having more NBOs compared to borate glasses, and (2) the bond strengths in Te-O polyhedra compared to the B-O group.

It is considered[55] that the O^{2-} in Te-O_{eq} bond of TeO_4 network is fully ionized when they are formed as a result of the addition of either Li_2O or Na_2O to TeO_2. Because of its higher negative charge O^{2-} can donate many electrons to Te through the Te-O_{eq} bond. Since Te is originally rich in valence electrons, due to its lone pair of electrons, excess donation of electrons from the Te-O_{eq} bond causes much electron transfer from tellurium to oxygen, in the Te-O_{ax} bond, resulting in a weakening of Te-O_{ax} bond. It is thus expected that the Te-O_{ax} and Li-O-Na bonds undergo drastic changes (weakening/strengthening) depending upon the nature (e.g., size, mass) and the electronic

structure of the alkali ions involved in the diffusion process leading to a non-linear electrical behaviour

The main structural units making up the tellurite glasses are Te-O polyhedra As we discussed above, if the MA effect is related to the changes in the bond strength, of the Te-O structural network, of MA glasses, which in turn are related to the changes in the shape of the polyhedra, then it was thought appropriate to look for the variations in the stretching and bending frequencies of Te-O molecular groups Infra-red spectra of 30 $[x(Li_2O)-(1-x)Na_2O]$-70 TeO_2 glasses were found to exhibit one main peak around 615 cm^{-1} assigned to the assymmetrical vibration of $Te-O_{ax}$ bond of the trigonal bipyramidal, TeO_4 units[56] Interestingly, as shown in Fig 5 19, this vibrational mode of $Te-O_{ax}$, exhibits a significant deviation from linearity, with the minimum occurring at Na/(Na+Li) = 0 6 This is expected to be due to distortion of TeO_4 units by the substitution of a second alkali ion Na^+, leading to a slight decrease in the $Te-O_{ax}$ coupling constant A similar non-linear variation in the bending and stretching frequencies of the vibrational modes observed in MA borate glasses[57] was found to be relatively less

The glass transition temperature (T_g) is one of the fundamental properties related to the viscosity of the glass, - not directly dependent upon the alkali mobility Nevertheless T_g exhibits the MA effect Fig 5 20 shows the plot of glass transition temperature versus mole fraction Na/(Na+Li) for three different heating rates, namely, 10, 20 and 40°C/min The minimum in the non-linear variation of T_g occurs for all heating rates at Na/(Na+Li) = 0 6 The MA effect seems to be sensitive to heating rates, implying significant changes in structural

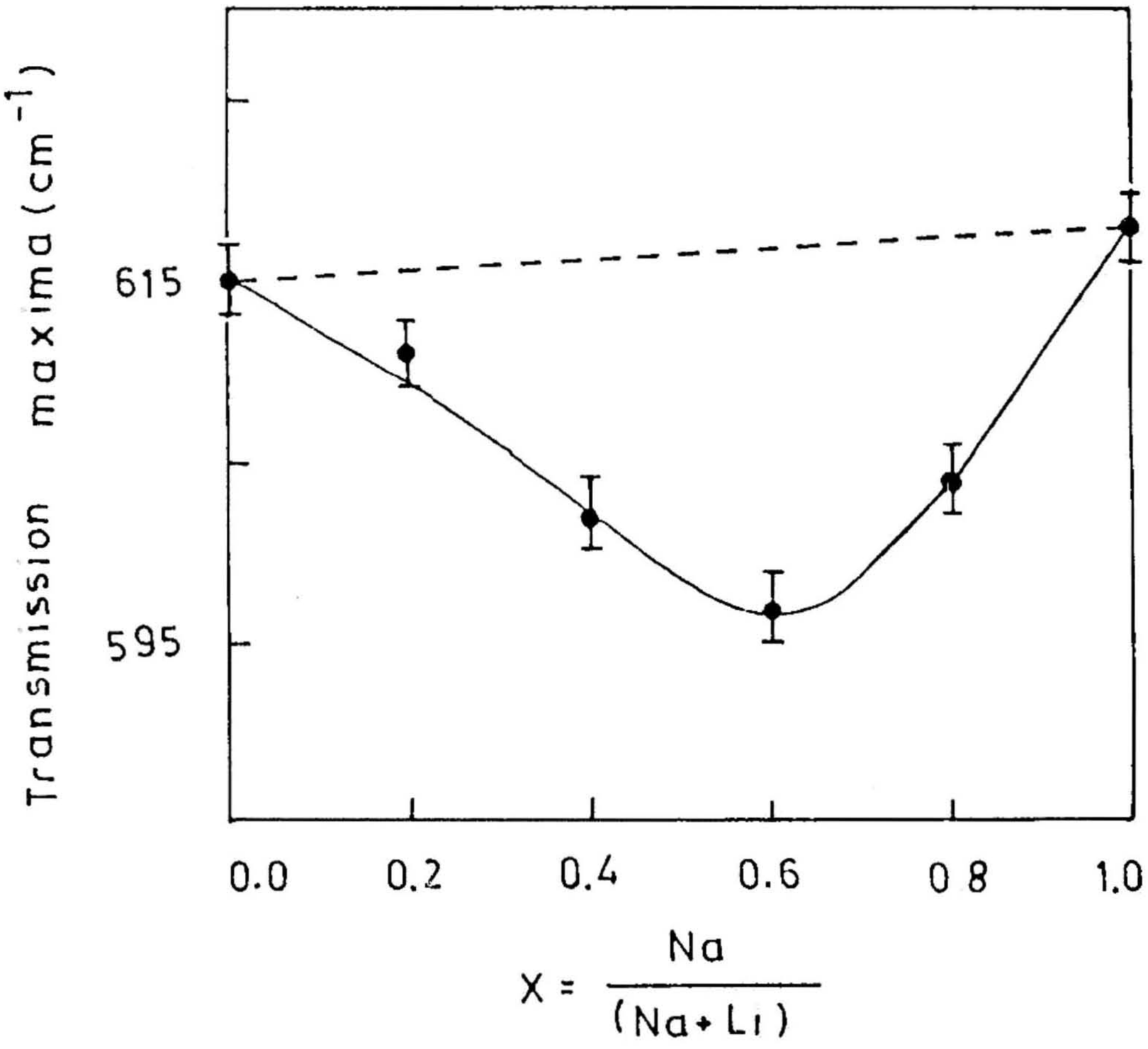

Fig 5.19 Variation of $Te\text{-}O_{ax}$ stretching frequency on the molar fraction of sodium x in the glasses 30 [(1-x) Li_2O-x Na_2C]-70 TeO_2

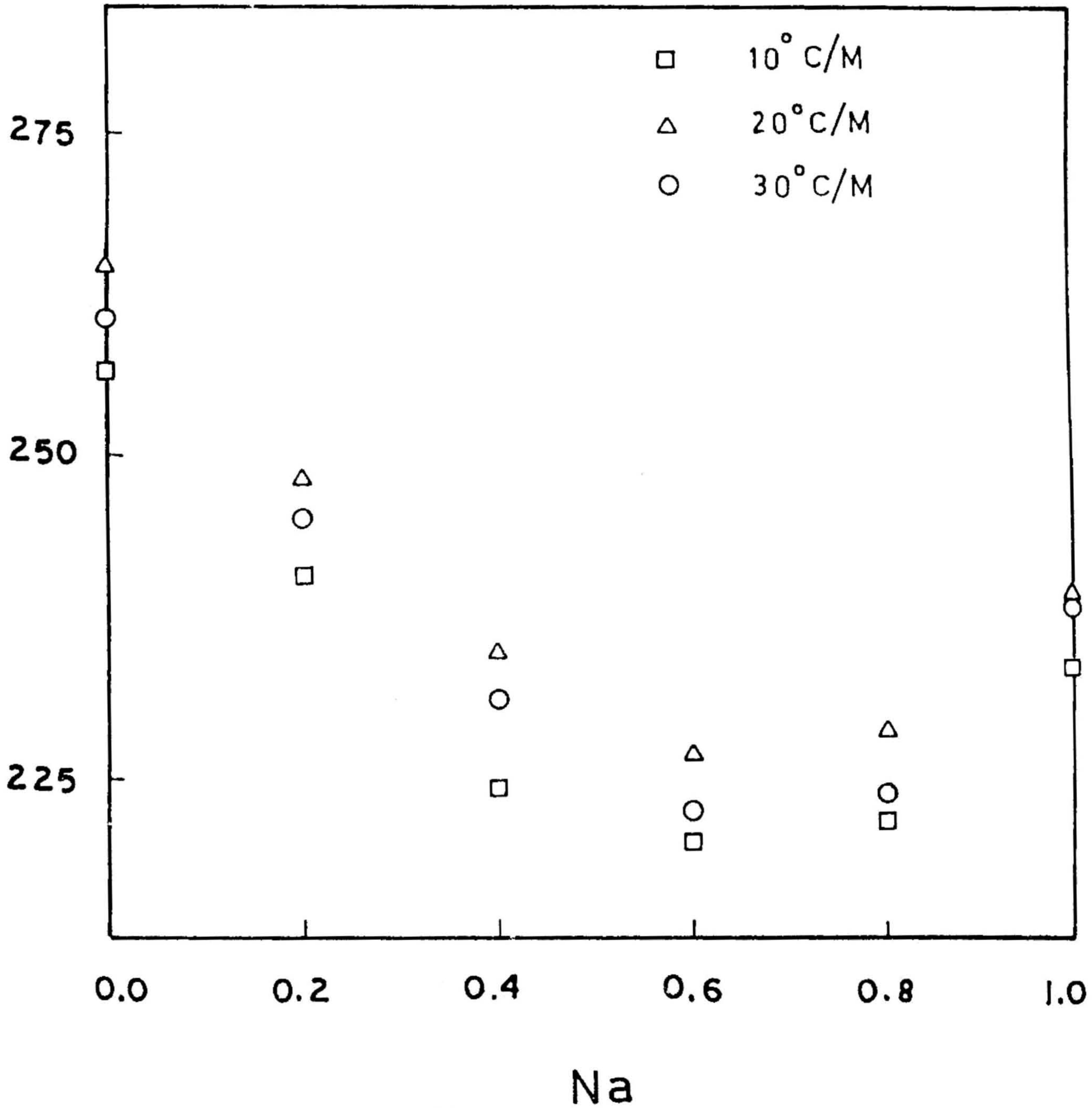

Fig 5.20 The dependence of the glass transition temperature (for three different scan rates) on the molar fraction of sodium x in the glasses 30 [(1-x) Li_2O-x Na_2O]-70 TeO_2

relaxation times quite akin to changes observed in electrical and mechanical relaxation[58,59] which also result in the MA effect

The observed negative deviation of the transformation temperature could mean that the MA glass with Na/(Na+Li) = 0 6 would attain a higher glass viscosity compared to single alkali glasses The viscosity could increase as a result of reduction in the concentration of NBOs Thus the addition of Na_2O to 30 Li_2O-70 TeO_2 brings about significant changes in the number of NBOs, leading to a non-linear variation of T_g with composition

The negative deviation of T_g with Li-Na tellurite glass compositions may be understood as follows The presence of two alkalis increases the entropy of mixing thereby depressing the melting temperature (T_m), which results in reduced T_g since generally $T_g \simeq 0.66$ T_m Thus one could also use the entropy model of the glass transition, to argue that the increase in configurational entropy of the mixed alkali melt has resulted in a decrease in T_g

5 10 CONCLUSIONS

Several theories for the MA effect have focused on an increase in binding energy of alkali ion to its site in the glass structure, when a second type of alkali ion is introduced Such theories have examined the strength of the bond between the alkali and NBO ions in the glass In the light of the present results on the MA effect in Li_2O-Na_2O-TeO_2 glass the scope of these theories must be increased to include the effects of different anion types,(such as TeO_4 and TeO_3) of structural networks in the alkali glasses

REFERENCES

1. A C Martins Rodrigues and M J Duclot, *Solid State Ionics* **28-30** (1988) 729.

2. K Tanaka, T Yoko, H Yamada and K Kamiya, *J Non-Cryst Solids* **103**, (1988) 250.

3. J M Rojo, J Sanz, J M Reau and B Tanguy, *J Non-Cryst. Solids* **116** (1990) 167.

4. K Tanaka, T Yoko, K Kamiya, H Yamada and S Sakka, *J Non-Cryst Solids* **135** (1991) 211.

5. V K Dhawan, A Mansingh and M Sayer, *J Non-Cryst solids* **51** (1982) 87.

6. C S Sunandana and A K Bhatnagar, *J Phys C Solid State Phys* **17** (1984) 467.

7. H Binczycka, O Gzowski, L Murawski and J Sawichi, *Phy status Solidi* (a) **70** (1982) 51.

8. R N Hampton, W Hong, G A Saunders and R A El-Mallawany, *Phys Chem Glasses* **29** (1988) 100.

9. S Kumar and A Mansingh, *Key Engineering Materials* **13-15** (1987) 821.

10. T Komatsu, H Tawarayama, H Mohri and K Matusita, *J Non-Cryst. Solids* **135** (1991) 105.

11. D Cachau-Herreillat, A Norkert, M Maurin and E Philippot, *J Solid State Chem* **37** (1981) 352.

12. A K Yakhind and G S Martishchenko, *Izv Acad Nauk USSR Neorg. Mat* **6** (1970) 1459.

13 S R Bharadwaj and G Chattopadhyay, *J Solid State Chem* **80** (1989) 256

14 K Matusita and S Sakka, *Bull Inst Chem Res* Kyoto Univ **20** (1981) 159

15 K Matusita, T Komatsu and R Yokota, *J Mat Sci* **19** (1984) 291

16 D W Henderson, *J Non-Cryst Solids* **30** (1970) 301

17 S Mahadevan, A Giridar and A K Singh, *J Non-Cryst Solids* 88 (1986) 11

18 N Afify, M A Abdel-Rahim, A S Abd El-Halim and M M Hafiz, *J Non-Cryst solids* **128** (1991) 269

19 P Duhaj, D Barancok and A Ondrejka, *J. Non-Cryst Solids* **21** (1976) 411

20 R F Speyer and S H Risbud, *Phys Chem Glasses* **24** (1983) 26

21 D Turnbull and M H Cohen, *J Chem. Phys* **34** (1961) 120

22 A Marotta, P Pernice, A Aronne and A Buri, *J Non-Cryst Solids* **127** (1991) 159

23 C S Ray and D E Ray, *J. Am. Ceram. Soc* **73** (1990) 439

24 E Illekova, *J Non-Cryst Solids* **68** (1984) 153

25 D Turnbull and M H Cohen, in *Modern Aspects of the Vitreous State* ed by J D Mackenzie (Butterworth, London, 1960) p-38

26 M Ueno and K Suzuki, *Kakuriken Kenkyu Hokoku*, Tohoku Univ **16** (1983) 49

27 S Neov, V Kozhukharov, I Gerasimova, K Krezhov and B Sidzhimov, *J Phys C Solid State Phys* **12** (1979) 2475

28 N P Bansal, A J Bruce, R H Dohemus and C T Moynihan, *J Non-Cryst Solids* **70** (1985) 379

29 J O Isard, *J Non-Cryst Solids* **1** (1969) 235

30 D E Day, *J Non-Cryst Solids* **21** (1976) 343

31 E R Van Artsdalen and I S Yoffe, *J Phys Chem* **59** (1955) 188

32 O J Kleppa and I S Hersh, *J Chem Phys* **34** (1961) 351

33 N F Astbury and W R Davis, *Trans Brit Ceram Soc* **63** (1964) 1

34 Y H Han N J Kreidl and D E Day, *J Non-Cryst Solids* **30** (1979)241

35 S Sakka, K Matusita and K Kamiya, *Phys Chem Glasses* **20** (1979) 25

36 R M Almeida and J D Mackenzie, *J Mat Sci* **17** (1982) 2533

37 G L McVay and D E Day, *J Am Ceram Soc* **53** (1970) 508

38 F W Fleming and D E Day, *J. Am Ceram Soc* **55** (1972) 186

39 J Kawamura, R Sato, S Mishina and M Shimoji, *Solid State Ionics* **25** (1987) 155

40 R M Hakim and D R Uhlmann, *Phys Chem Glasses* **8** (1967) 174

41 J E Shelby and D E Day, *J. Am Ceram. Soc* **52** (1969) 169

42 A Dietzel, *Glastech Ber* **56** (1983) 291

43 W A Weyl and E C Marboe, *The Constitution of Glasses*, Vol 2, Parts I & II (Interscience, New York, 1962)

44 J Sakurai and K Oaka, *Toshiba Rev* **23** (1968) 913

45 O V Mazurin, *Structure of Glass*, Vol 4 (Consultants Bureau, New York, 1965) p 5

46 J M Stevels, in *Handbuck der Physik*, Band 20, ed by S Flügge (Springer-Verlag, Berlin, 1957) p 350.

47a J R Hendrickson and P J Bray, *Phys Chem Glasses* **13** (1972) 3

b J R Hendrickson and P J Bray, *Phys. Chem Glasses* **13** (1972) 107

48 M Abou-el-leil, J Heasely and M H Owen, *Phys. Chem. Glasses* **19** (1978) 37

49 H L Downing, N L Peterson and H Jain, *J. Non-Cryst Solids* **50** (1982) 203

50 H Jain, G Blazer-Jollenbeck and O Kanert, *J Am Ceram Soc* **68** (1985) C 24

51 A H Dietzel, *Phys Chem. Glasses* **24** (1983) 172

52 J C Lapp and J E Shelby, *J Non-Cryst. Solids* **84** (1986) 463

53 J C Lapp and J E Shelby, *J. Non-Cryst. Solids* **86** (1986) 350

54 H Jain, H L Downing and N L Peterson, *J. Non-Cryst. Solids* **64** (1984) 335

55 K Tanaka, T Yoko, H Yamada and K Kamiya, *J Non-Cryst Solids* **103** (1988) 250

56 Y Dimitriev, M Arnaudov, V Dimitrov and Ch Petkov, in *Disordered Systems and New Materials* ed by M Borissov N Kirov and A Vavrek (World Scientific, Singapore, 1988) P 530

57 U Selvaraj and K J Rao, *Spectrochim Acta* **A 40** (1984) 1081

58 S. Mishina, J Kawamura and M Shimoji, *Solid State Ionics* 23 (1987) 323

59 A Klonkowski, *J. Non-Cryst. Solids*,57 (1983) 339

CHAPTER 6

SILVER-ION CONDUCTING GLASSES

6. SILVER-ION CONDUCTING GLASSES

6.1 INTRODUCTION

The first Ag^+ superionic glass was accidentally discovered by Kunze[1] in 1973 while trying to stabilize α-AgI at ambient by melting various mixtures of AgI with Ag_2SeO_4 i.e., by modifying the iodide ion matrix with an oxy-anion of similar size and shape, followed by rapid quenching of the melt

Since then many such glasses have been made and investigated, reviews for which have been given by Tuller[2a,2b], Minami[3a,3b], Angell[4] and Rao[5] These glasses include AgI mixed in various proportions with oxy-salts such as Ag_2MoO_4, Ag_2CrO_4 and Ag_3AsO_4 which are by themselves not glass formers AgI-based glasses have also been developed by combining AgI, Ag_2O and glass forming oxides such as B_2O_3, P_2O_5, Cr_2O_3, SiO_2, V_2O_5 etc

Among these AgI based glasses, $AgX-Ag_2O-B_2O_3$ (X = I,Cl, Br) is the most investigated Ag^+-ionic conductor due to its interesting electrical properties coupled with ease of preparation, high stability, and facile glass forming ability Indeed these AgI-based and other glasses may be considered as model systems for exploring the general question of structure-property relationships in glasses Furthermore, the high Ag^+ conductivity in these glasses appears to be related in a fundamental way with the coupling between Ag^+ translational degrees of freedom and the two level systems (TLS's), typical of glassy materials [6,7] Interestingly, the TLS's occur at as high as 100 K in these superionic glasses compared to < 10 K in insulating glasses In the silver borate

glass systems, the AgI addition results in an increase in conductivity of four order of magnitude (from ~ 10^{-6} to ~ 10^{-2}) at room temperature, accompanied by a reduction in activation energy (E_a) for ionic conduction.

These investigations - carried out mostly with samples containing AgI-indicate that the silver halide is mainly responsible for the high conduction even though the oxy-anions play a non-negligible role. Since glasses show the highest values of σ_{RT} at the maximum content of AgI and fast ionic conductivity was observed in α-AgI, it is argued that the enhanced conduction in AgI-based glassy electrolyte is due to the formation of α-AgI microdomains embedded in the host glass matrix. This approach is generally referred to as the cluster model. Some authors (especially Mangion & Johari[8] and Tachez et al[9]) have described a cluster-pathway model, where Ag^+ ions can percolate through the glass from one AgI microdomain to the next. Alternatively, Ingram[10] considered the cluster-bypass model with the microcrystalline particles concentrated in a "connective tissue" which provides preferential pathways for Ag^+ migration. Both these approaches can be regarded as extensions of theories of glass structure previously proposed by various workers including Rao & Rao[11] and Goodman[12], and which presume some sort of granular structure of glass.

Malugani and coworkers obtained experimental support for the cluster model from quasi-elastic and inelastic neutron scattering and Raman scattering experiments. The coefficient of self-diffusion of silver ion in $(AgI)_{0.5}$ $(AgPO_3)_{0.5}$ superionic glass, was calculated as a function of temperature from the quasi-elastic neutron scattering

experiment[13,14] The activation energy for this motion is very close to that obtained for α-AgI from electrical conductivity The Raman spectra of AgI-based borate[15,16] and phosphate[17] glasses revealed new bands, appearing in the low frequency region upon the addition of AgI whose band intensities evolve linearly with the AgX concentrations This mode observed in AgI-doped glasses is quite similar to those seen in α-AgI and $RbAg_4I_5$ compounds[18] reflecting that Ag^+ and I^- are tetra-coordinated Malugani et al suggested that the tetrahedrally coordinated AgX (X = I,Cl,Br) microdomains contribute predominantly and play a major role in the ionic conduction, and claimed that the structures of glasses containing AgBr - and AgCl - are different from their low conducting crystalline counterparts

Borjesson et al [19] observed that the velocity of the acoustic waves, calculated from the frequency shifts of the transverse and longitudinal components of the Brillouin spectra (hypersonic velocities) and certain mechanical properties such as elastic modulii for some AgI doped borate and phosphate glasses vary with the AgI concentration and extrapolate to the value corresponding to α-AgI

Another model contradicting the cluster model was proposed in which it was suggested that AgI is rather highly dispersed in the glassy matrix in positions controlled by the ionic groups, such as BO_3 and BO_4 in the borate glasses

Minami et al [20,21] based on conductivity and infrared results proposed that in AgI-based borate glasses, strong partial covalency exists between the Ag^+ ions and non-bridging oxygens of BO_3 groups which

gives rise to the immobile Ag^+ populations, while the Ag^+ ions interacting weakly with BO_4 groups and those surrounded by halide ions and BO_4 groups represent the mobile Ag^+ populations The observed halide concentration dependence of conductivity is explained in terms of the polarizability of the different halide ions The high pressure conductivity behaviour of these glasses observed by Senapati et al [22] is readily interpreted in terms of this model based on the existence of "mobile" and "immobile" Ag^+ cations According to Ingram et al [23] this model is a special case of the cluster-bypass model, with the AgI microcrystalline particles concentrated in the "tissue regions"

The radial distribution functions of $AgI-Ag_2O-B_2O_3$ and $AgI-Ag_2O-P_2O_5$ glasses[24-26], shown in Fig 6 1 are dominated by the large peak centered at the distance (2 80-2 85 Å) expected for Ag-I pairs The shoulder appearing on the left side, in the range 2 30-2 40 Å comes from the Ag-O distances which give a prominent peak in the $Ag_2O-B_2O_3$ radial curve (not shown) This seems to be a direct structural evidence against the hypothesis of α-AgI microcrystalline clusters

The structural details by the EXAFS studies on $AgI-Ag_2O-B_2O_3$ [27] and $AgI-Ag_2O-V_2O_5$ [28] glasses did not reveal any contributions from an ordered I-I second-shell coordination In crystalline AgI, each Ag-atom is surrounded by 12 silver atoms at 4 5 Å, and each I-atom is surrounded by 12 iodide atoms again at 4 5 Å For α-AgI clusters to exist in these glasses, large peaks due to Ag-Ag and I-I correlations should appear between 4 and 5 Å The absence of such peaks in the EXAFS results of these glasses exclude the presence of microcrystalline clusters of AgI in these glasses

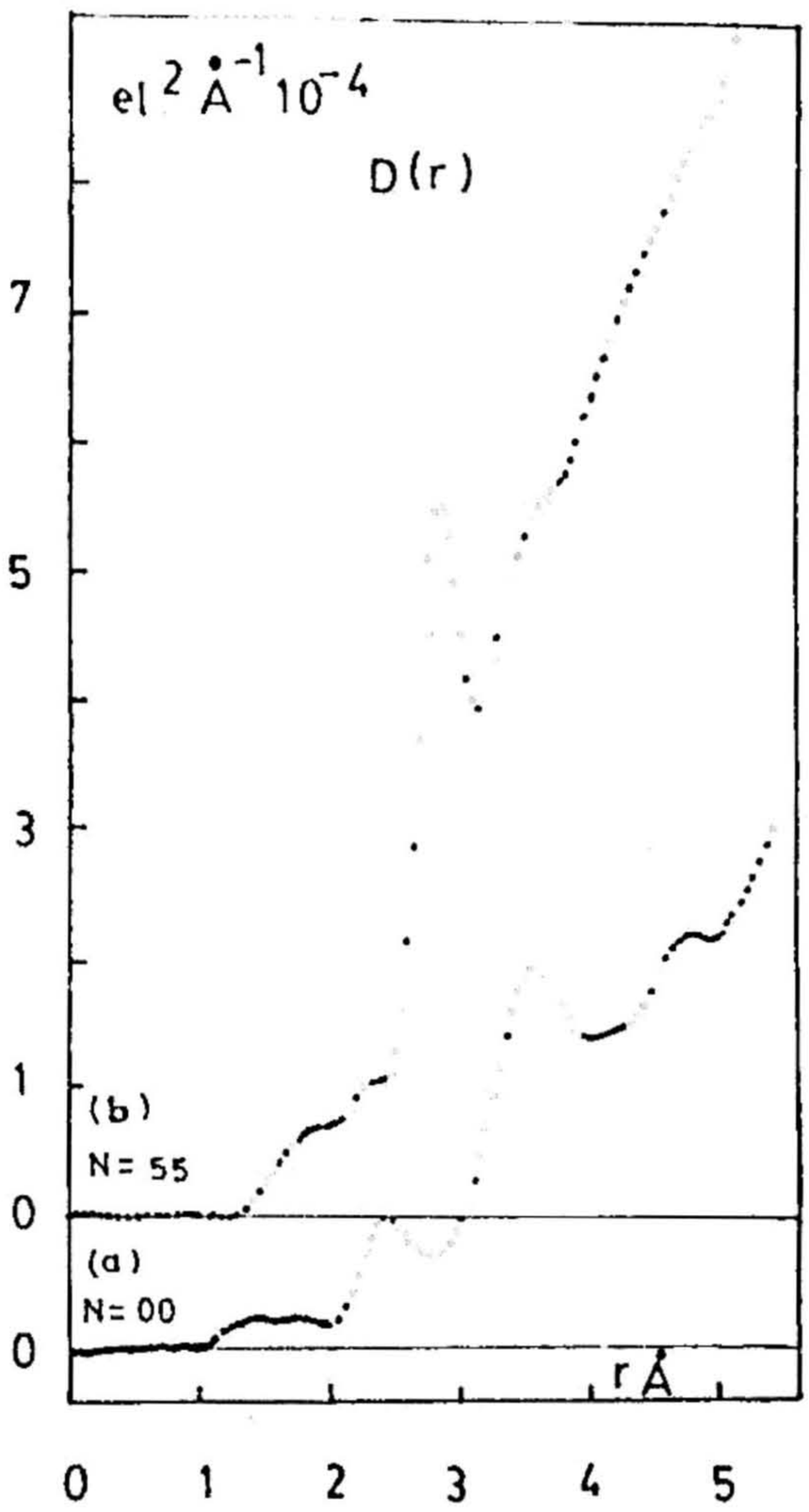

Fig 6.1 Experimental radial distribution functions of two vitreous samples [a] $(AgI)_{0.55}(AgPO_3)_{0.45}$ and [b] $(AgI)_{0.5}(AgBO_2)_{0.5}$

Despite many such concerted efforts, no general agreement has been reached on the nature of the Ag^+ ion conduction mechanism A definite choice between different proposed theories is prevented by the lack of sufficient microscopic information connecting the structural aspects with the ionic mobility In particular, a comprehensive knowledge of the local environment of the moving ions and their interaction with network former is highly desirable Nevertheless the high mobility of ions in these superionic glasses probably blurs the actual situation and asks for more refined experiments

Magnetic resonance experiments sample local motions of mobile ions and their coupling to network building units (NMR), as well as, the chemically distinct static environments around mobile ions (ESR) While NMR experiments[29a,29b] have established that the addition of metal halides has only a minor effect on the short range structure of the borate network, ESR active species stabilized accidentally/deliberately in superionic glasses may provide valuable clues to the local structures of the glass network and possibly assist in the elucidation of the conduction mechanism in these glasses

With the above ideas, we report, in this chapter on the conductivity and ESR studies of ternary silver borate and silver tellurite glasses, and discuss these results on the basis of structural models suggested by Minami[20] and Seshasayee and coworkers[28]

6.2 EXPERIMENTAL

6.2.1 Sample Preparation

The glass compositions chosen for the present investigations are

listed in Table I

Two separate procedures were adopted to prepare these glasses for the present study

The glass samples numbered 8, 9, 10 and 11 were prepared using high pure chemicals AgI ('Alfa'), Ag_2O ('Alfa') and B_2O_3 ('BDH'). B_2O_3 was dried under vacuum at 200°C for 3 hours. The mixture of the weighed raw materials, whose total weights were about 5 grams were taken in a silica tube (OD = 10 mm) with one end open, and melted at 500-800°C depending on the batch composition. The melt was kept at the appropriate temperature for about 2 hours and repeatedly stirred to ensure homogeneity of the melt. Finally the resultant melt was quenched by immersing the silica tube in an ice-cooled water bath upon cooling to room temperature, the tube was broken and the glass ingot retrieved.

All the remaining glasses were prepared using nominally pure chemicals AgI (BDH), Ag_2O ('Loba') and B_2O_3/TeO_2 ('BDH'). Nearly five gram batches of these were thoroughly mixed and then melted in an alumina/silica crucible at a temperature slightly higher than their corresponding melting points. The melts were then quenched by pouring between two polished stainless steel plates kept at ambient condition.

These quenched glasses were immediately transferred to an annealing furnace and annealed for about 4-5 hours at a temperature ~ 50°C less than their glass transition temperature predetermined by DSC.

6.2.2 Characterization by XRD, DSC and IR techniques

The X-ray diffraction measurements, using Cu-Kα radiation were made

Table I

Nominal Composition (in mole%) of the glasses prepared for the present study

A	<u>Borate Glasses</u>		
No	AgI	Ag_2O	B_2O_3
1	-	20	80
2	-	25	75
3	-	30	70
4	30	21	49
5	40	18	42
6	40	30	30
7	40	40	20
8	60	30	10
9	60	20	20
10	70	15	15
11	80	10	10
B	<u>Tellurite Glasses</u>		
12	-	20	80
13	-	25	75
14	-	30	70
15	20	24	56
16	30	21	49
17	40	18	42
18	50	15	35

on all the samples in order to ascertain whether any crystalline phase is included

The calorimetric experiments using DuPont 9900 differential scanning calorimeter, at selected heating rates (10, 40 and 60^{o}C/min) were used to determine (a) the glass transition temperature (b) the crystallization temperature and (c) the temperature ranges of any other endothermic or exothermic events

The infrared spectra were recorded at RT, by KBr pellet method on a Perkin-Elmer double beam spectrophotometer (model 297) operating in the range 4000-200 cm^{-1}

6 2 3 Electrical Properties

(a) Ionic Conductivity

The ionic conductivity measurements were performed on bulk glass specimens using complex admittance spectroscopy The design of the sample holder used for the measurement has been described in Chapter 2. Both the parallel faces of the disc shaped glass specimens were polished flat using silicon carbide (#200 #400 and #600) papers, and subsequently painted with gold paste, which served as electrodes and was baked at a temperature slightly less than their T_g values for 15 minutes in vacuum to remove organic ingredients

The complex admittance was measured over a frequency range 100 Hz-120 KHz by connecting the sample in series with the standard capacitor and measuring the voltage drop across the capacitor using the lock-in amplifier The AC conductivity meter described in Chapter 3 was

incorporated for current boosting in the circuit as shown in Fig 2.4. The DC conductivities were obtained from the analysis of complex admittance plots in the temperature range from 50°C to the one nearly 30°C below the glass transition temperature. The actual investigated frequency range was narrowed down in some cases depending on the conductance of the samples investigated.

(b) **Electronic Conductivity**

The electronic conductivity of a few selected glass compositions was measured by Wagner's polarization method[30] using the cell configuration

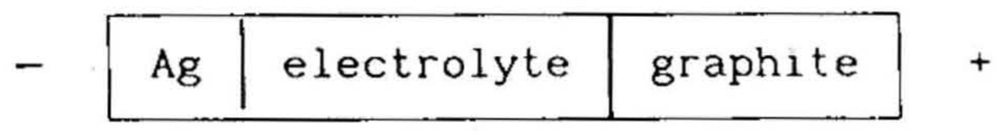

The electrodes were formed from fine grained silver and graphite powders. A constant DC voltage of ~ 350 mV is applied to this cell configuration and the current under steady-state condition is measured using a Keithley 195A DMM and/or a Keithley 642 electrometer.

When the DC voltage is applied, silver ions migrate initially from the graphite electrode (anode) towards the silver electrode (cathode), while electrons migrate in the opposite direction. Under the steady-state condition, the migration of silver ions due to the electric field gradient, is balanced by the diffusion due to the concentration gradient and the current is carried exclusively by excess electrons or electron holes. At each temperature it took nearly 60 minutes to carry out a measurement during which the temperature remained constant to ± 1°C.

6 2 4 Electron Spin Resonance

First derivative ESR spectra were recorded on a X-band (9 3 GHz) JEOL ESR spectrometer (Model FE-3X) at ambient temperature on both unirradiated and X-irradiated glasses To simplify the features observed at RT, the ESR spectra were also recorded at selected higher temperatures

6 3 RESULTS AND DISCUSSIONS

6 3 1 Borate Glasses

(a) Glass Formation and Characterization

The borate glass compositions prepared for the present study are identified in a ternary constitutional diagram AgI-Ag_2O-B_2O_3 (Fig 6 2) The boundary surrounded by a dotted line is the glass forming region Open circles represent glass forming compositions while triangles represent compositions that are only partially glassy under the metal plate quenching

The X-ray diffraction patterns of these quenched samples confirmed that they are amorphous materials Fig 6 3 presents a typical XRD pattern, at room temperature, of 60 AgI-30Ag_2O-10 B_2O_3 glass showing only diffuse structure typical of its glassy nature However, the diffraction pattern of 60 20 20 glass sample has shown a few weak lines, characteristic of β-AgI crystalline phase The intensity of these lines increased in the case of the 70 15 15 and 80 10 10 samples, i e , with increasing AgI content

(b) Glass Transition

The beginning of the glass softening process, or glass

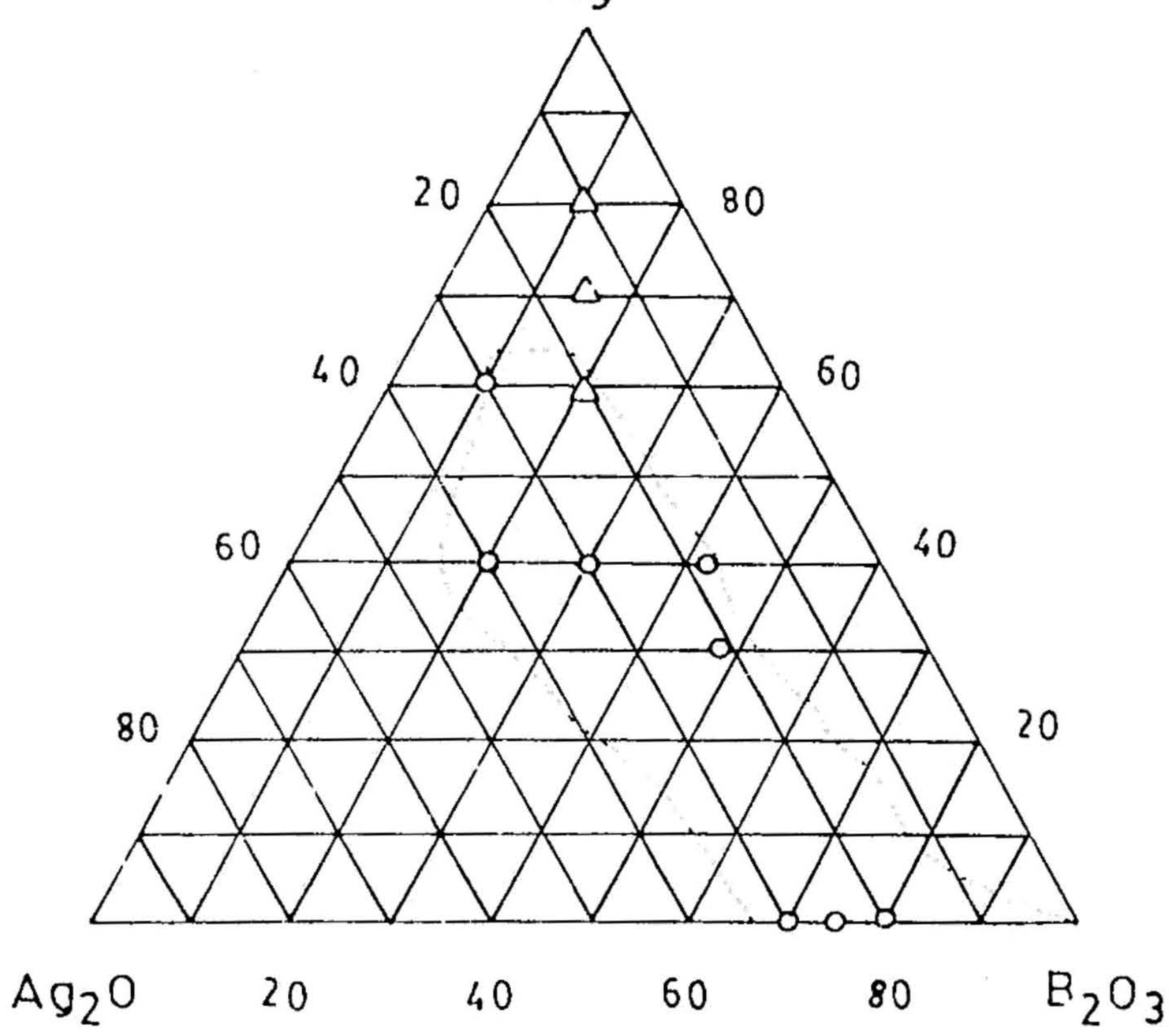

Fig 6.2 Composition (in mole%)of the borate glasses investigated (O) glass, (Δ) partially crystallized. The regions surrounded by dotted line is the glass forming region (from Minami et al.,[20])

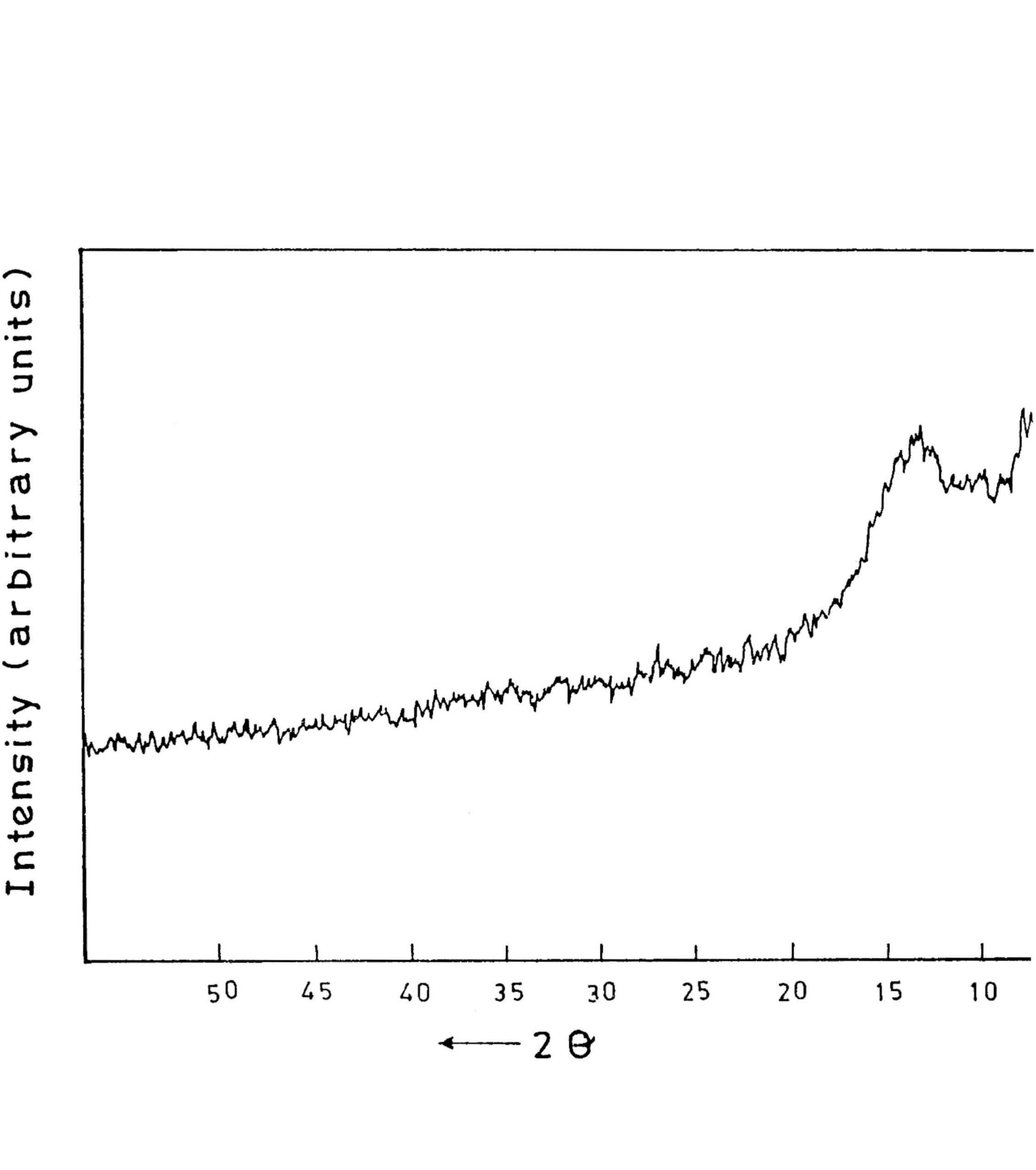

Fig 6 3 Powder X-ray diffraction pattern of 60 AgI-30 Ag_2O-10 B_2O_3 glass at room temperature

transition is associated in a DSC experiment with a shift of the baseline in the endothermic direction Table II presents the glass transition temperatures (T_g) of the borate glasses investigated While the T_g was well defined and reproducible for all ternary glass compositions, they could not be identified clearly in case of binary glasses and are thus not included in the table

The peak due to the well known β-α phase transition in AgI occurs at 151^{o}C only for 60 20 20, 70 15 15 and 80 10 10 glass compositions, whereas for the remaining compositions this signal was not detectable The intensity of this endothermic phase transition peak increases with increase of the amount of AgI as shown in Fig 6 4 in accordance with the XRD results

Fig 6 5a presents the variations of T_g against the molar ratio Ag_2O/B_2O_3 with a constant AgI content (= 40 mole%) Fig 6 5b shows the IR spectral features reported by Minami et al [20] where the composition dependence of relative intensities of absorption bands characteristic of BO_4 and BO_3 groups are plotted against Ag_2O/B_2O_3 ratio keeping AgI content at 40 mole% The IR spectral study and molecular dynamics calculations[31] have established that the non-bridging oxygens (NBOs) are present only in BO_3 group and not in BO_4 Increasing the ratio Ag_2O/B_2O_3 for a constant AgI content (40 mole%), reflect the essential role of Ag_2O in the formation of BO_4 group leading to a decrease in the number of BO_3 groups in the glass network

The T_g is known to be quite sensitive to the structural changes such as BO_4 to BO_3 conversion and vice versa, occurring as a result of compositional changes A comparison of Fig 6 5a with Fig 6 5b reveals

TABLE II

Glass transition T_g and the phase transition T_t (in case the sample is crystallized) temperature data of the ternary borate glasses studied

Composition			T_g °C	T_t °C (peak temp.)	
AgI	Ag_2O	B_2O_3			
30	21	49	365.0		
40	18	42	339.1		
40	30	30	269.6		
40	40	20	200.2		
60	30	10	110.3		
60	20	20	192.8	151.5	
70	15	15		150.1	
80	10	10		151.4	

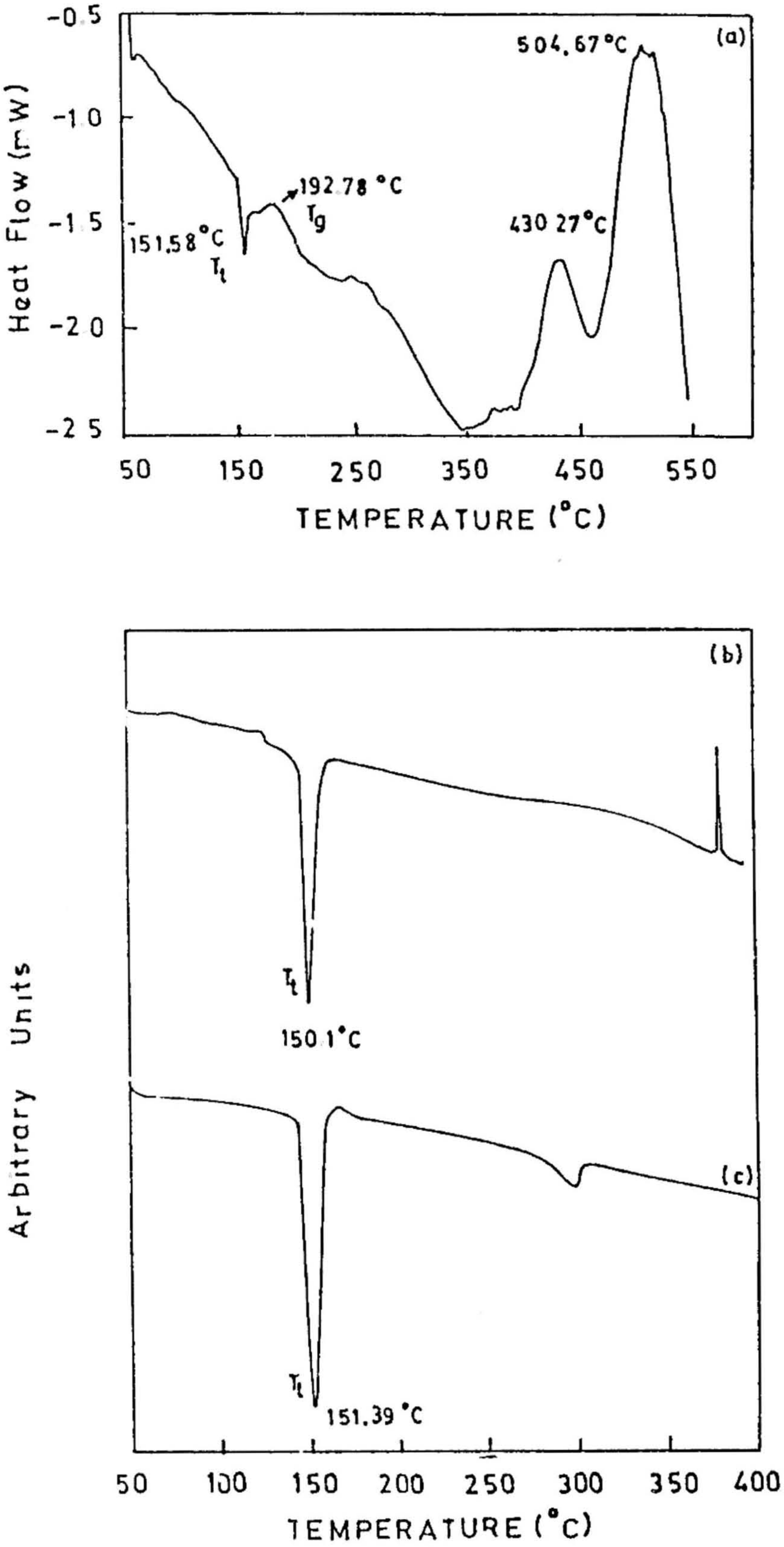

Fig. 6.4 DSC curve for the compositions (a) 60 20 20, (b) 75 15 15 and (c) 80 10 10 Note the disappearance of T_g & T_x in (b) and (c) and subsequently increase in $\beta \longrightarrow \alpha$-AgI phase transition peak with increase in AgI content

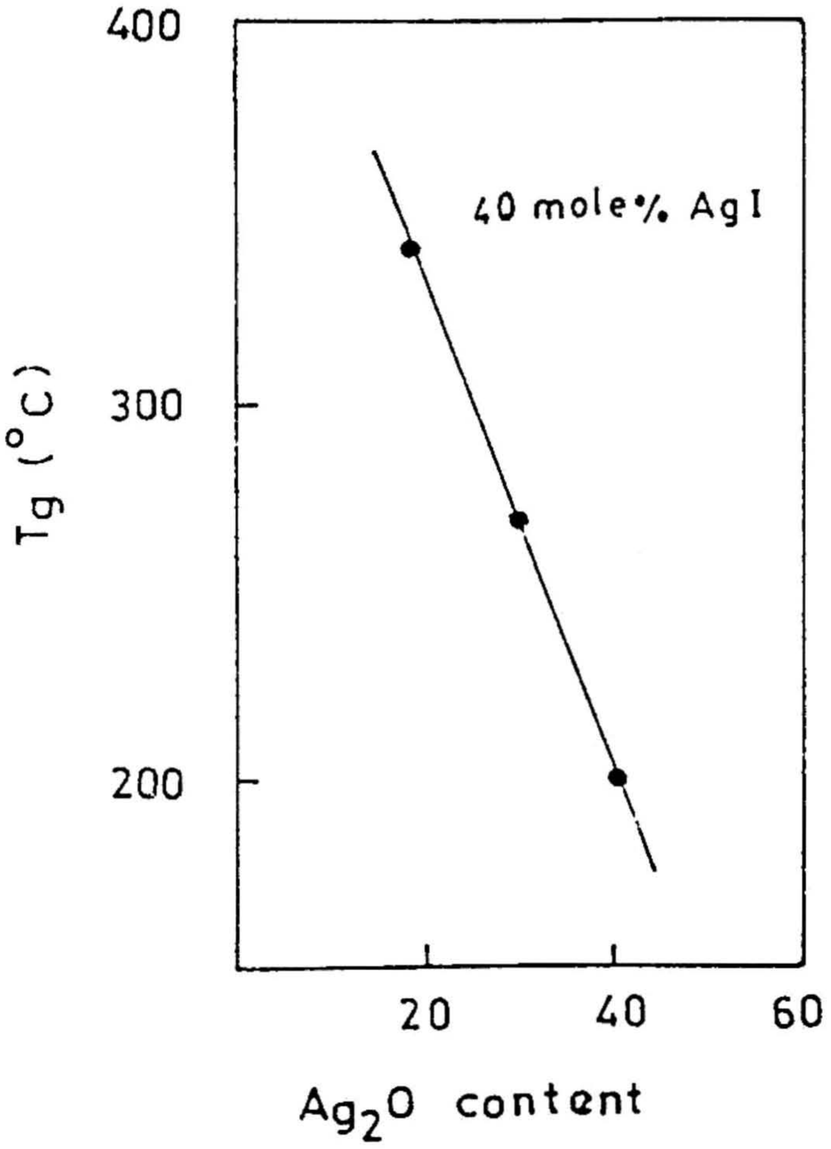

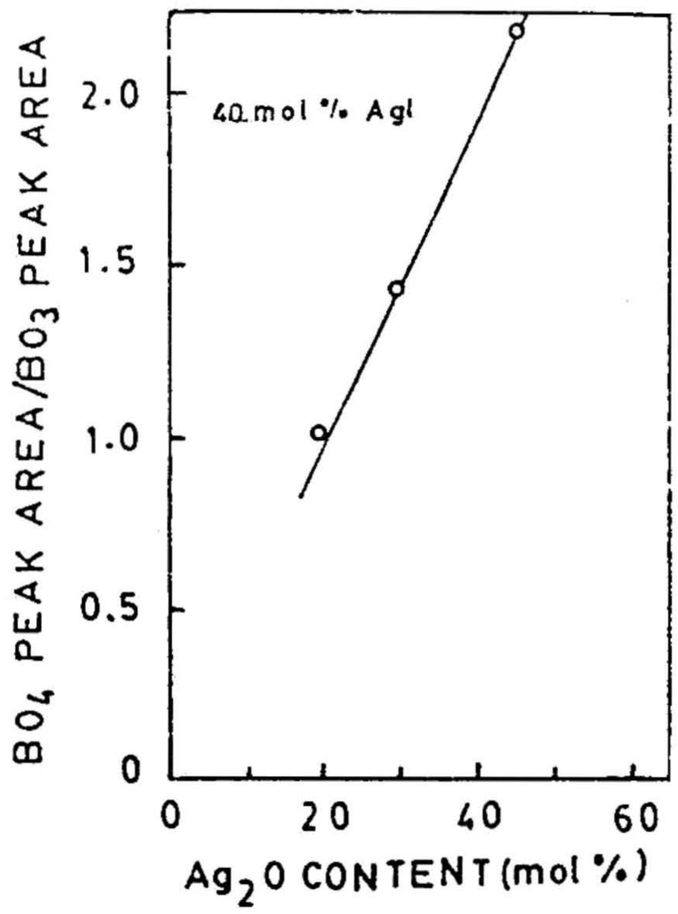

Fig. 6.5a The glass transition temperature against the molar ratio Ag_2O/B_2O_3 with 40 mole% of AgI content

Fig. 6.5b Relative intensity of absorption bands characteristic of BO_3 and BO_4 groups in $AgI-Ag_2O-B_2O_3$ glasses (Minami et al [20])

that the T_g decreases with increasing Ag_2O/B_2O_3 ratio, representing a decrease in the concentration of non-bridging oxygens. Thus the structural changes of these glass matrices are well reflected in the compositional dependence of T_g

(c) Electrical Properties

(i) Ionic Conductivity

The curves in Fig 6 6 represents the complex admittance plots (Y' versus Y'') for the binary glass 30 Ag_2O-70 B_2O_3 at various temperatures. Typical frequencies are indicated in kHz. It is seen that the data at low temperatures are nearly perfect semicircular arcs passing through the origin at low frequencies whereas a straight line fits data at high frequencies, as expected for an ideal Debye circuit[32]. The semicircular region corresponds to the interfacial (electrode-electrolyte) processes resulting from the completely blocking nature of the electrodes whereas the straight line region represents bulk relaxation due to the long range diffusion of Ag^+ ions in the glass sample. The corresponding equivalent circuit is also given in Fig 6.6 implying the presence of the bulk resistance R, the geometrical capacitance C and the interfacial double-layer capacitance C_{int}. The effective bulk conductivity could therefore be obtained from the intersection of this straight line on the real axis (Y').

The frequency at which Y'' is maximum shifts to higher frequencies upon increase of temperature, indicating a shift in the 'interfacial relaxation'. Slightly elongated, asymmetric semicircular plots are obtained at higher temperatures. The interfacial relaxation process is quite sensitive to the polishing of the glass surface prior to the

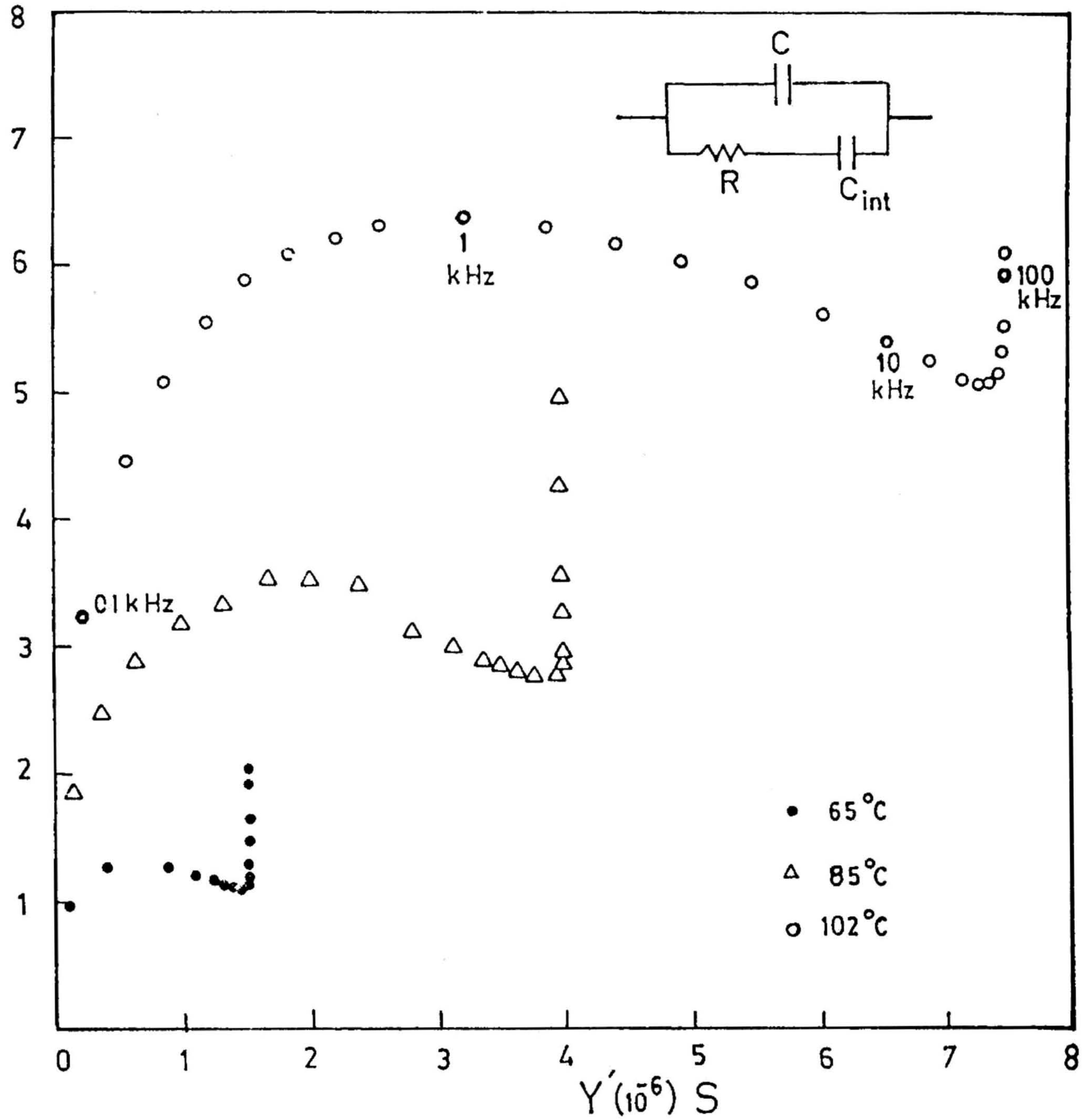

Fig. 6.6 The complex admittance plot at various temperatures for the binary glass 30 Ag_2O-70 B_2O_3

application of electrodes and so this non-circular behaviour which seems to be a common observation[33,34] could be attributed to the non-ideal Debye relaxational process[32] of the double-layer capacitance formed at the electrode/electrolyte interface

The temperature dependence of DC conductivity values extracted from the complex admittance plots are generally analyzed using the well known expression for the diffusion-controlled process

$$\sigma T = \sigma_o \exp(-E_a/kT) \quad (1)$$

where σ_o is the pre-exponential factor, and E_a is the activation energy for ion migration. From (1)

$$\log \sigma = \log \sigma_o - \log T - E_a/kT \quad (2)$$

Since log T does not vary much over a small temperature range, a simpler expression can be used

$$\log \sigma = \log \sigma_o - E_a/kT \quad (3)$$

The slope and intercept of the log σ against $1/T$ plot gives E_a and σ_o. Thus in the present analysis we have adopted the Arrhenius equation (3). Moreover just as in the present case, Eqn. (3) has been shown to give a better fit for the DC conductivity data of alkali silicate[35] and alkali phosphate [36] glasses.

Figs. 6.7 and 6.8 show some examples of the temperature dependence of DC conductivity for both binary and ternary glass systems. For samples with high conductance the complex admittance plot analysis introduced significant errors while deducing the bulk conductivity because of the poor resolution of the semicircular arc. The reason for this is not yet clearly understood. Hence the upper temperature limit of

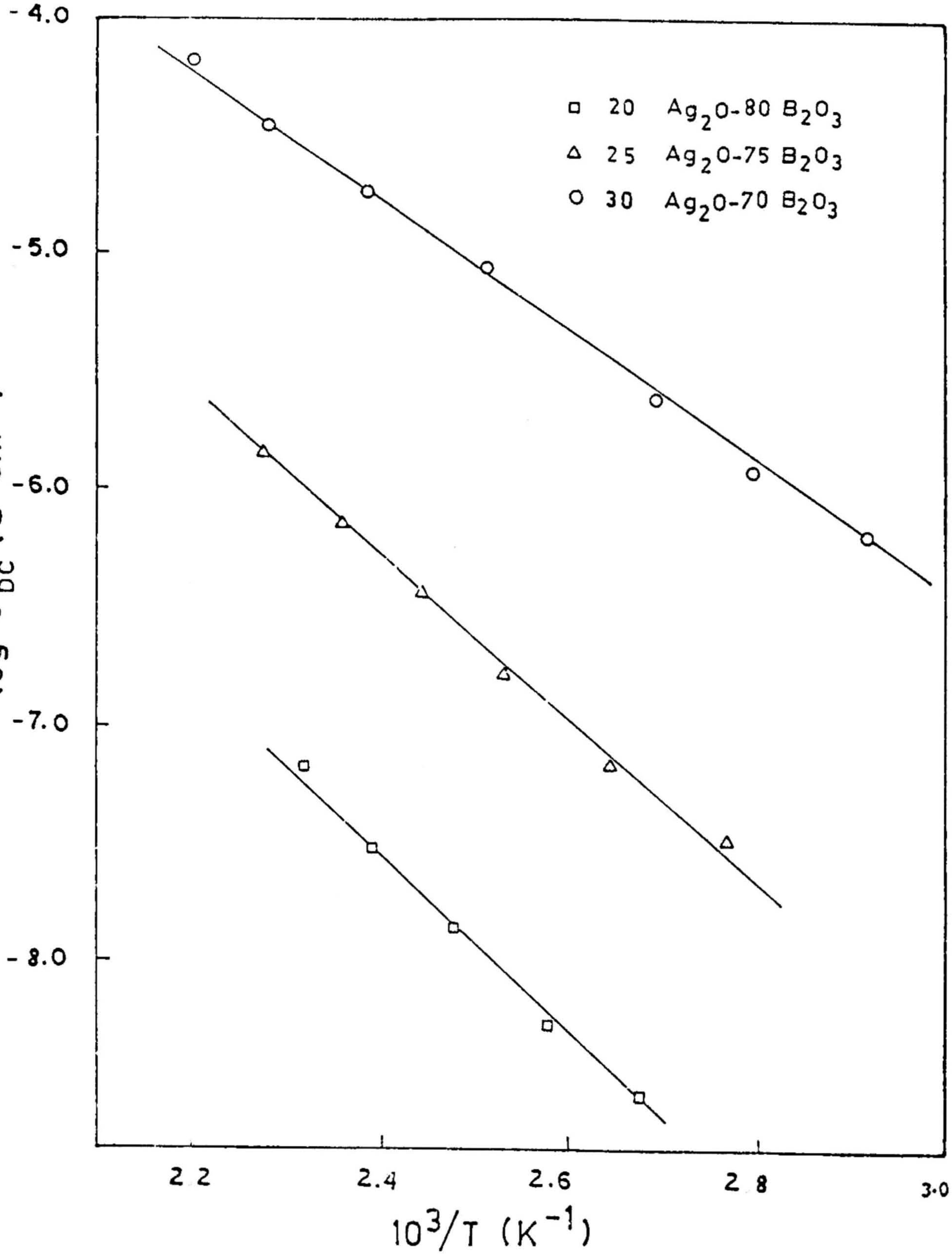

Fig. 6.7 Temperature dependence of DC conductivity of binary Ag_2O-B_2O_3 glasses

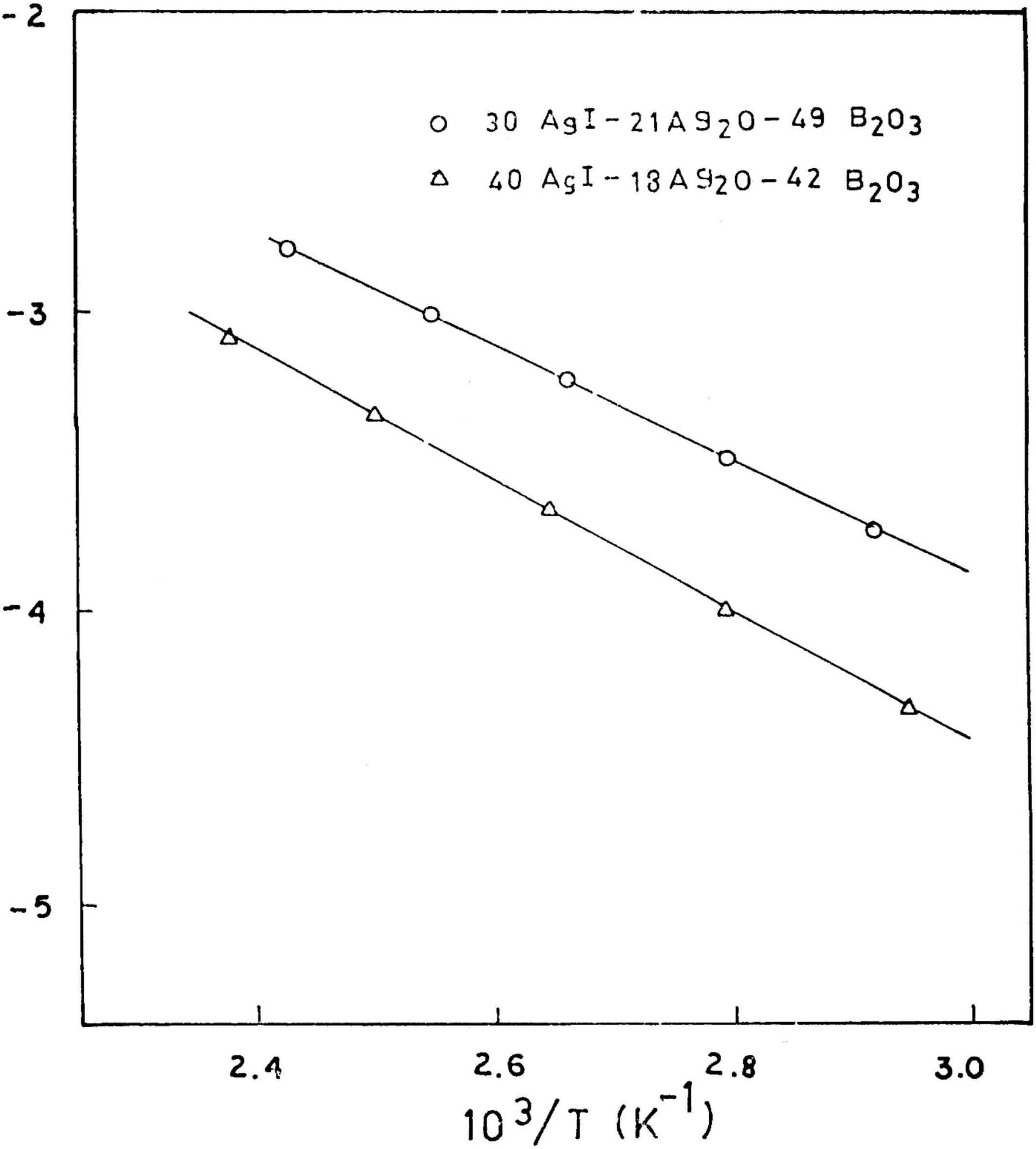

Fig. 6 8 Temperature dependence of DC conductivity of ternary $AgI-Ag_2O-B_2O_3$ glasses

the conductivity measurement on samples with high halide content was restricted to only 50°C.

Table III summarizes the bulk DC conductivity data at 50° and 100°C, along with the activation energy for ionic transport. Our data agrees well with those reported earlier[37a,37b] for silver iodo-borate glasses. It is clear from the table, that for a constant AgI content (= 40 mole%) the conductivity increases, as we increase the molar ratio, Ag_2O/B_2O_3. Also the glass composition with 60 mole% of AgI, attains a maximum value of conductivity.

(ii) Electronic Conductivity

The electronic conductivity of a few selected glass samples were obtained through polarization measurements carried out using the Wagner's method.

Assuming that σ_e (conduction due to electrons) dominates in the present glass system, compared to σ_n (conduction due to holes), the electronic conductivity of Wagner's polarization cell can be estimated using the relation

$$I = \sigma_e\left(\frac{RTA}{LF}\right)\left[1-\exp\ (-EF/RT)\right] \qquad (4)$$

Fig. 6.9 shows the plot of electronic conductivity versus temperature, for the 30 70 and 40 18 42 glass samples. The temperature dependence of σ_e looks linear for the binary glass and exponential for the ternary glass sample. The σ_e data at 50°C, of a few glasses are listed in table III. It is clear from this table that σ_e of 60 30 10 glass is nearly five orders of magnitude smaller than the total

TABLE III

Total conductivity and the electronic conductivity data of borate glasses at 50 and 100°C

Composition			σ_t (S cm^{-1})		E_a (eV)	σ_{elec} (S cm^{-1})
AgI Ag_2O B_2O_3			50°C	100°C	(± 03)	50°C
	20	80		2.51×10^{-9}	0.75	
	25	75		5.50×10^{-8}	0.69	
	30	70		2.82×10^{-6}	0.56	
30	21	49	2.29×10^{-5}	1.82×10^{-4}	0.44	
40	18	42	8.71×10^{-5}	5.50×10^{-4}	0.38	1.50×10^{-7}
40	30	30	2.70×10^{-4}			
40	40	20	6.20×10^{-4}			
60	30	10	6.10×10^{-3}			$<10^{-8}$

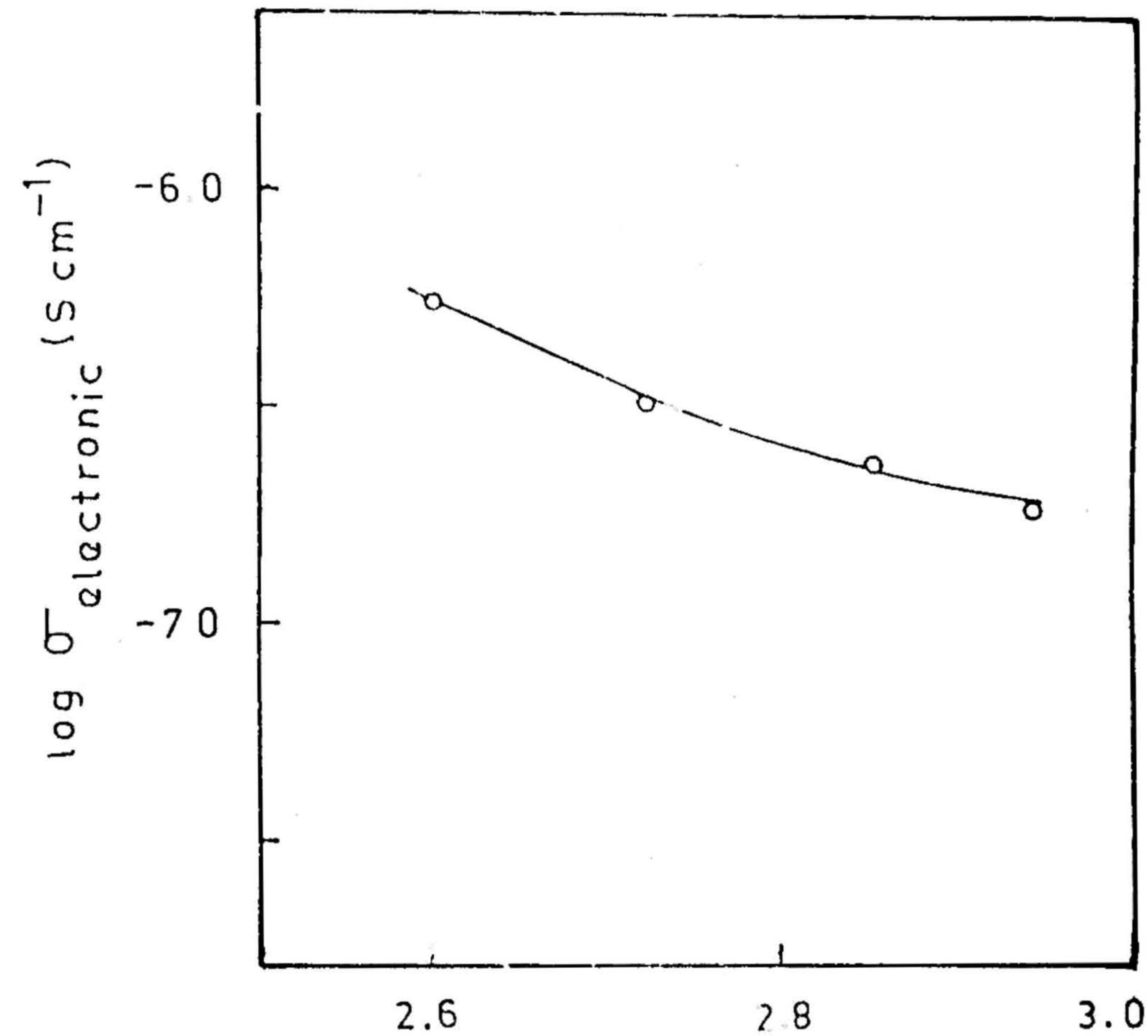

Fig. 6.9 Variation of electronic conductivity with temperature for the 40 AgI-18 Ag_2O-42 B_2O_3 glass

conductivity obtained by AC measurement However, the remaining glass samples prepared from nominally pure chemicals, exhibit electronic conductivities which are only one or two orders of magnitude lower compared to total conductivity and are attributed to larger concentration of impurities such as Fe_2O_3 present in these glass samples The electron hopping from Fe^{2+} to Fe^{3+} could also significantly contribute to σ_e Interestingly we have seen ESR signals attributable to Fe^{3+} in all these glasses, except in the 60 30 10 glass prepared from high pure chemicals

(d) **Electron Spin Resonance**

Fig 6 10 shows the ESR spectra of $60AgI\text{-}30Ag_2O\text{-}10B_2O_3$ glass recorded at RT and at 140°C Nearly identical axially symmetric patterns were obtained, both on unirradiated and X-irradiated glasses However, the spectra of latter are less intense The paramagnetic species in the glass are probably created and stabilized in the melt and/or during quenching There appears to be two hole-type centres "centre I and II' both of which are attributed on the basis of the ESR features and their temperature-dependence, to Ag^{2+} ($4d^9$, S = 1/2, I = 1) in two different chemical surroundings The observed spectra could be generally represented by the axially symmetric Spin Hamiltonian

$$H = g_{\parallel} \beta S_z H_z + A_{\parallel} I_z S_z + g_{\perp} \beta [S_x H_x + S_y H_y] + A_{\perp} [I_x S_x + I_y S_y]$$

where ($g_{\parallel}$, $g_{\perp}$) and ($A_{\parallel}$, $A_{\perp}$) are the principal-g values and principal nuclear hyperfine coupling constants, while S_x, S_y, S_z and I_x, I_y, I_z are the components of electron and nuclear spin vectors, and, H_x, H_y, H_z are the components of rf magnetic field However, $A_{\parallel}$ is not resolved in any of the spectra The g and A tensor parameters of these two centres I and II, at RT and at a few elevated temperatures are listed in table IV

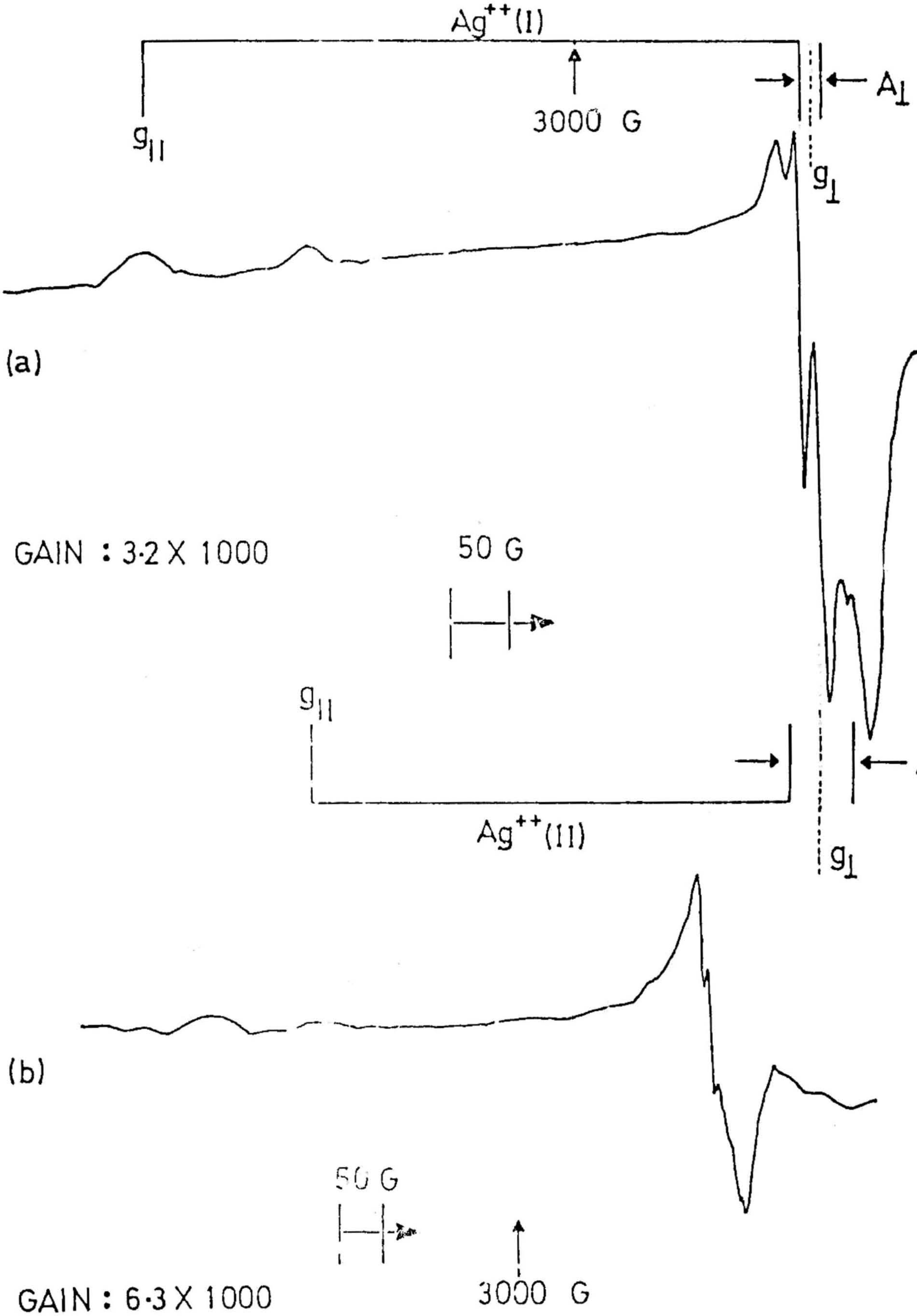

Fig 6.10 ESR spectra of Ag^{2+} in 60 AgI-30 Ag_2O-10 B_2O_3 at (a) 30°C and (b) 140°C

TABLE IV

Ag^{2+} ESR parameters in silver iodo-borate glasses and other systems

sample	g		A		ref
	$g_{\parallel}$	$g_{\perp}$	$A_{\parallel}$	$A_{\perp}$	
$60AgI-30Ag_2O-10B_2O_3$ (n)					
Centre I	2 495(2)	2 060(2)	not resolved	18(3)	Present work
Centre II	2 373(2)	2 054(2)	- do -	56(3)	
$30Ag_2O-70B_2O_3$(n)					
Centre I	2 503(2)	2 065(2)	- do -	20(3)	- do -
Centre II	2 388(2)	2 059(2)	- do -	65(3)	
$30Ag_2O-70TeO_2$(n)					
Centre I	2 493(2)	2 070	- do -	not resolved	- do -
Centre II	2 389(2)		- do -	- do -	
$Ag_2O-B_2O_3$(n) X-irradiated	2 310	2 040			38
Silver activated phosphate glass X-irrad at 300 K	2 350	2 050	not resolved	not resolved	39
β-Alumina X-irrad at 77 K					
Centre I	2 2730(5)	2 0230(2) 2 0678(15)			40
Centre II	2 2335(4)	2 0150(4) 2 0580(15)			
β-Alumina X-irrad at 77 K					
Centre I	2 240(3)	2 026(3) 2 083(3)			41
Centre II	2 240(3)	2 005(3) 2 068(3)			
AgCl Cu	2 135(3)	2 048(3)	31(5)	21(5)	42
KI Cu	2 193(3)	2 035(3)	38(2)	32(2)	43
Argentic di o-phenanthroline persulphate $(Ag(Prn)_2)S_2O_8$ at 290 K	2 180	2 040			44

to be compared with Ag^{2+} in X-irradiated Ag_2O-B_2O_3[38] and silver-activated phosphate glasses[39] and other related and relevant systems, where Ag^{+} is reported to trap an electron or a hole to form Ag^{o} and Ag^{2+} respectively. Significantly, in the present case, no other Ag-based centres such as Ag_2^{+} and Ag^{o} were formed as reported earlier by various workers[45-47] in silver and alkali borate glasses. Furthermore, in an earlier study on β-alumina by Barklie et al [40] Ag^{2+} were produced by X-irradiation at RT using a tungsten target. It is pertinent to point out here that Ag^{2+} centres were exclusively produced in X-irradiated (at 77K) β-alumina samples in which Na^{+} ions were completely replaced by Ag^{+}, whereas partial replacement by Ag^{+} yielded both Ag^{o} and Ag^{2+} centres.

Of the two Ag^{2+} centres, 'Centre I" is thermally more stable than 'Centre II'. The Ag (I = 1/2) hyperfine $g_{\perp}$ components are fully resolved in this glass composition. The origin of these 'centres I and II' are considered based on the structural model of these AgI-based borate glasses proposed by Minami and coworkers[20]. They pre-suppose the existence of three types of Ag^{+} ions in the ternary glass network. Type I ions are covalently bonded to the non-bridging oxygen of BO_3 groups and type II are interacting weakly with bridging oxygens of BO_4 groups while type III are surrounded by iodide ions only. In view of the unresolved $A_{\parallel}$ and rather small $A_{\perp}$ of "centre I" reflecting considerable covalency, we think that this arises from hole-trapping of type I Ag^{+} from the BO_3 groups with non-bridging oxygens. The good thermal stability of these type I centres suggests that they do not dissociate and get converted as Ag^{+} ions upon increasing the temperature and thus may not have a major role in ionic conduction.

On the other hand 'centre II" has a rather poor thermal stability. The relatively large $A_{\perp}$ value tends to make it more vulnerable to dissociation. These facts suggest that the 'centre II' could form by the hole-trapping of type II Ag^{+} ions from the BO_4 groups. When the temperature is increased beyond 120°C, the "centre II' starts decaying but the "centre I" persists even up to 180°C. The decay of "centre II" which leads to the conversion of the Ag^{2+} to Ag^{+} at higher temperatures may be involved more in ionic conduction compared to those originating from "centre I" Ag^{2+} paramagnetic ions.

Seshasayee and co-workers[28] in their structural investigation by EXAFS of $AgI-Ag_2O-V_2O_5$ glass observed two Ag-O distances at 1.93 and 2.30 Å indicating respectively strong and weak interactions and an Ag-I interaction at 2.86 Å. Based on these results, it is established that while some Ag^{+} ions remain bonded to the non-bridging oxygens of vanadyl groups, some interact weakly with vanadium polyhedra with bridging oxygens and some are surrounded by I^{-} ions. These Ag-O distances observed in vanadate glasses are close to the values reported for silver-borate glasses[27] and hence this structural model would apply to the case of $AgI-Ag_2O-B_2O_3$ glasses as well.

Correlating our observation of two Ag^{2+} centres, 'centre I and II', with the structural details of Minami (from conductivity measurements) and Seshasayee (EXAFS study) models, it is clear that only Ag^{+} ions of type III surrounded by I^{-} ions have a higher mobility than those of type I and II giving rise to superionic conduction in these glasses even at ambient. This interpretation agrees well with Minami's suggestion that Ag^{+} ions of type III have maximum mobility and contribute significantly

to ionic conduction, and also are in accord with the Auger studies on the silver iodo-phosphate glasses[48] where AgI appears to provide a highly polarizable environment for Ag, P and I , thus promoting high Ag^+ ion conductivity

The infrared spectra of 60 30 10 glass shown in Fig 6 11 reveals characteristic features (in the region 1310-940 cm^{-1}) corresponding to the ν_3 modes of BO_3 and BO_4 structural units The ratio of the areas of BO_4 and BO_3 peaks is found to be 1 8 implying that BO_3 groups with NBOs are relatively less in number compared to BO_4 groups in the 60 30 10 glass composition This lower number of BO_3 groups refers to the formation of less concentration of 'centre I' It is known that the total number of silver ions (calculated from chemical composition and molar volumes) remain constant for all the glass compositions[49,50] Thus the lower concentration of "centre I" reflects that more Ag^+ ions are derived for the ionic conduction from the silver ions of type III and type II (due to conversion of $Ag^{2+} \rightarrow Ag^+$ upon raising the temperature) Thus the observed higher (ionic) conduction of 40 40 20 glass compared to 40 18 42 glass may be explained as due to the fewer BO_3 groups formed in the former composition compared to the latter (see Fig 6 5b)

We also suggest <u>another</u> possibility for the origin of these two centres, based on the rather unusual DSC results and the temperature dependence of ESR **results** Fig 6 12 shows the DSC spectra of 60 30 10 glass recorded at **different** scan rates of 40 and 60°C/minute The observation of two glass transitions and two crystallization temperatures indicate the existence of two distinct glass networks Each network may inturn be considered to stabilize a centre arising from the

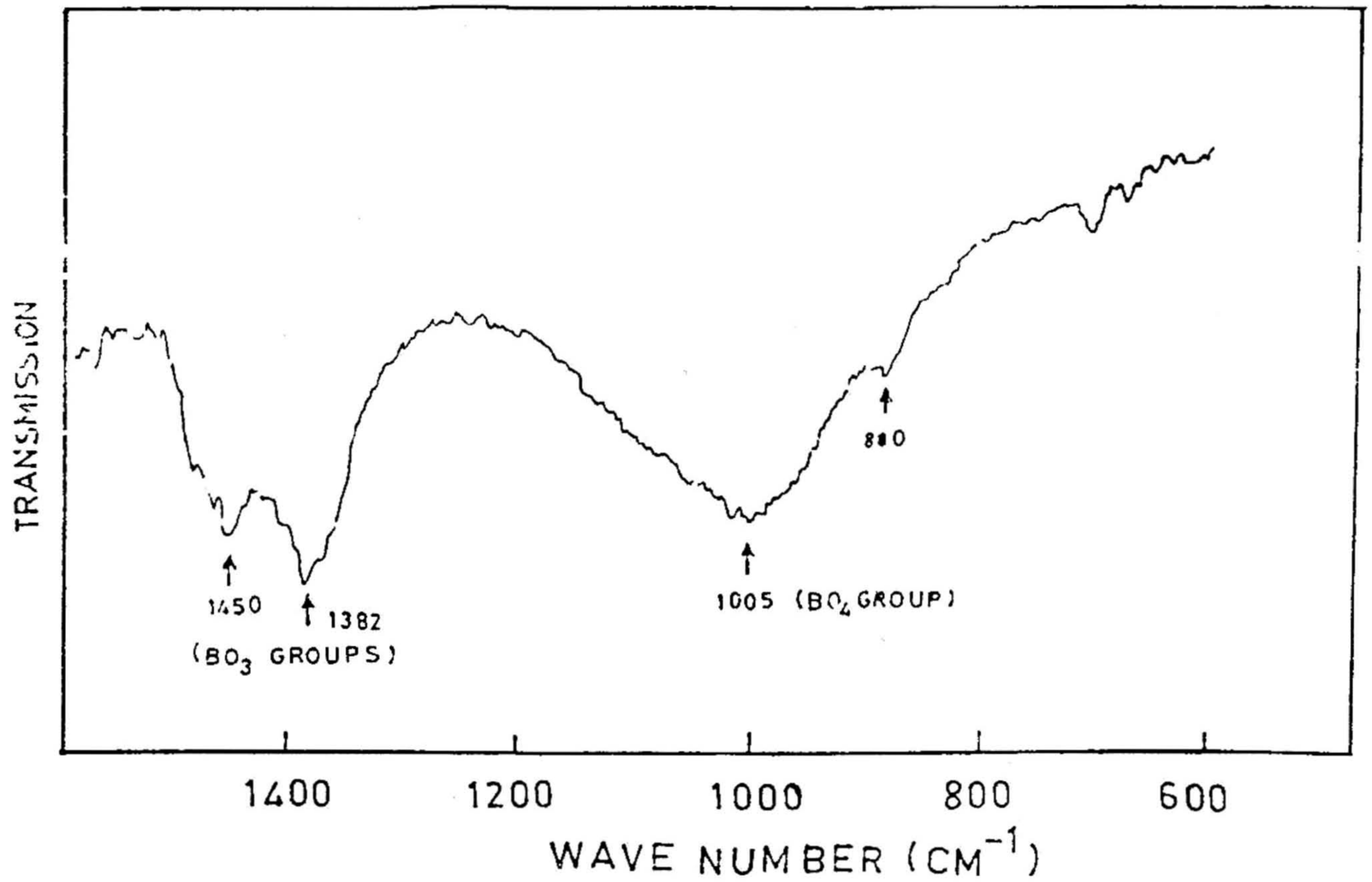

Fig. 6.11 Infrared spectra of 60 AgI-30 Ag_2O-10 B_2O_3 glass (BO_4 peak area/BO_3 peak area = 1 8)

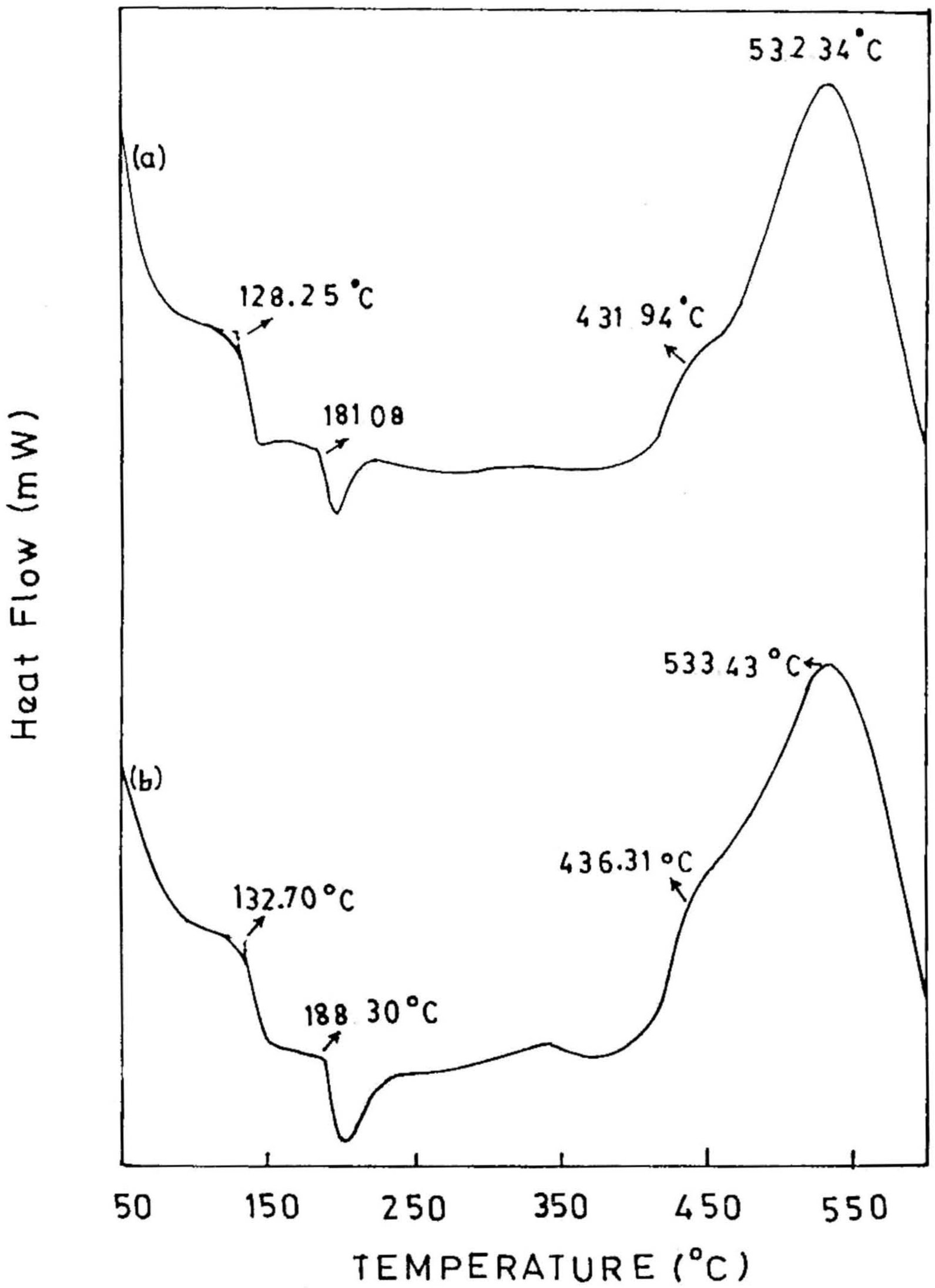

Fig 6.12 DSC Spectra of 60 AgI-30 Ag_2O-10 B_2O_3 glass recorded at different heating rates (a) 40°C/min and (b) 60°C/min

hole-trapping of type I Ag^{+} from the BO_3 molecular groups with NBOs Thus the present Ag^{2+} ESR results provide a direct experimental evidence for the co-existence of two distinct glass networks Very recently Chowdari et al [51] established that the glass composition 75 Li_2O-20 B_2O_3-5 As_2O_3 obtained by twin-roller rapid quenching exhibits maximum conductivity and exist as two glassy phases with the lower T_g being 210°C Thus the existence of two glass networks in a single homogeneous glass, appears to be a special feature of the superionic conducting glasses

It is noteworthy that the ESR spectra of 60 30 10 glass when prepared from nominally pure chemicals, have shown very weak signals unlike the one obtained for the glass prepared from high purity chemicals Relatively weak ESR signals are also obtained for the binary glass 30 Ag_2O-70 B_2O_3 (discussed later) However, the hyperfine features in the perpendicular components are better resolved in the ternary glass, implying a more covalent Ag-O bond in the binary glass network We expect that this could be because of the competition between Ag^{+} and Fe^{2+} ions (from Fe_2O_3 impurity) to trap the holes from BO_3 and BO_4 groups, thereby suppressing the Ag^{2+} formation and creating Fe^{3+} centres The Fe^{3+} centre is clearly seen as a axially symmetric signal, with an 'isotropic' g-value of 4 27 which may be attributed to $Fe^{III}O_6$ octahedra with a rhombic distortion

A further quantitative analysis of correlating Ag^{2+} concentration (obtainable from the area calculations of ESR and IR spectra) with the enhanced conduction due to Ag^{+} ions was not possible in the present case because of

(i) overlapping of $g_{\perp}$ signals due to 'centre I and II

(ii) observed g-anisotropy, and

(iii) weak signals obtained due to the presence of impurities

6.3.2 Tellurite Glasses

(a) Glass Formation and Glass Transition

The tellurite glass compositions studied are shown in Fig. 6.13. Open circles represent the glass forming compositions while the closed circles denote partially crystallized glass. XRD experiments have confirmed the amorphous nature of all compositions except the one with the composition 50 15 35 where a few faint lines were observed due to the β-AgI crystalline phase.

The thermal behaviour in the DSC experiment with a heating rate of 10°C/min was realized from the plot of the first derivative of heat flow versus temperature. For all the glass samples, a distinct glass transition at the temperature T_g was observed and the data is summarized in Table V. In the case of ternary glasses, T_g decreases upon increasing AgI content. The glass samples containing 50 mole% of AgI exhibit another endothermic maximum at 150°C, due to $\beta \longrightarrow \alpha$ phase transformation of the AgI constituent.

Upon increasing the silver iodide content, but keeping Ag_2O TeO_2 ratio fixed at 30 70, the T_g decreases. Such a decrease of T_g is similar to the trend observed previously in binary alkali oxide and sulphide glasses, upon halide incorporation. This implies a less rigid glass network structure as predicted earlier[52] to explain ionic conductivity enhancement upon dissolving halide in inorganic glasses. The

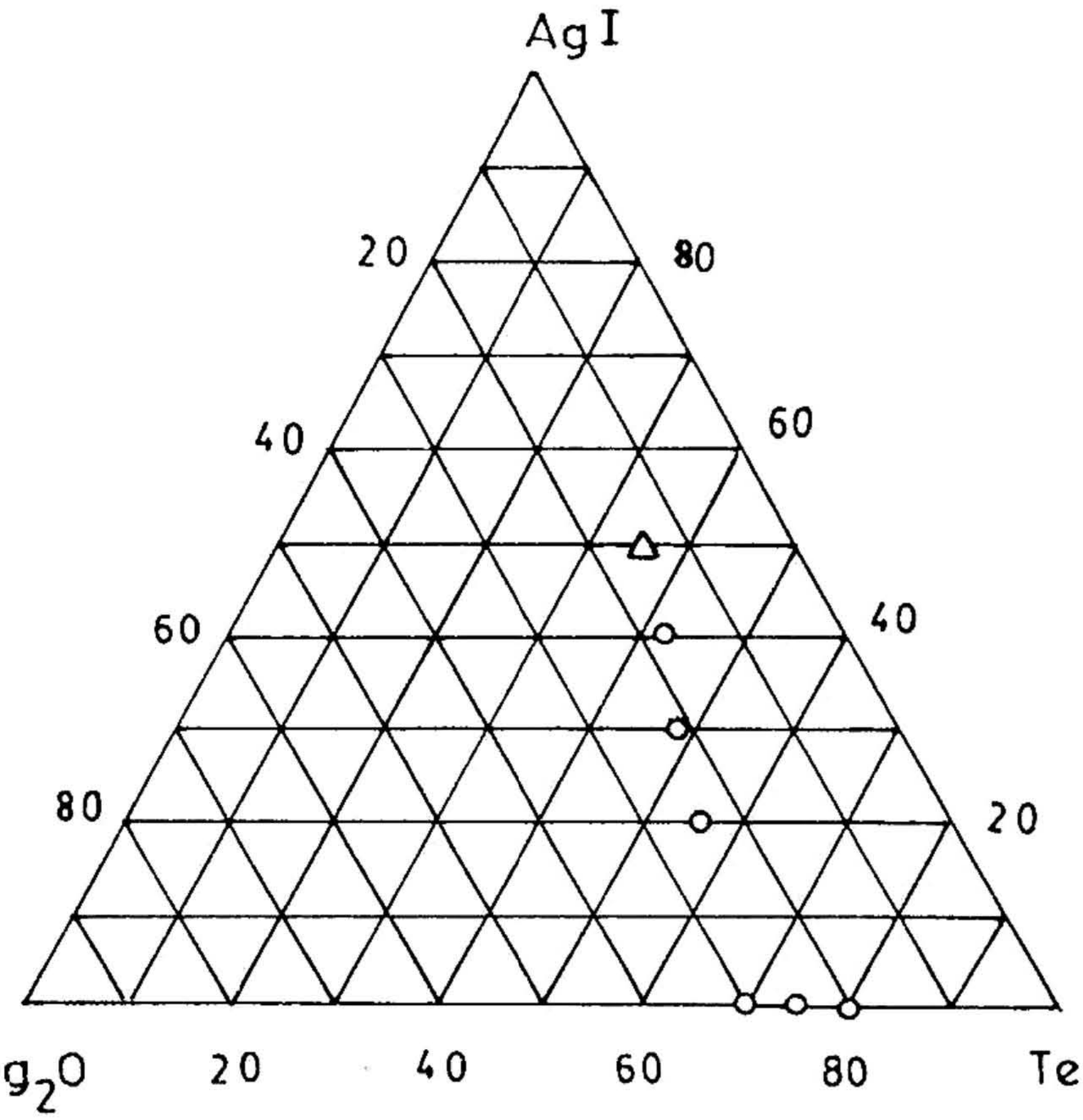

Fig. 6.13 Composition (in mole%) of the glasses investigated in tellurite system (**o**) denote glass samples while (Δ) partially crystalline sample

TABLE V

Glass transition temperature and the conductivity data of silver iodo-tellurite glasses

Glass Composition			T_g (°C)	log σ (S cm^{-1}) at		E_a (eV)
AgI	Ag_2O	TeO_2		50°C	100°C	
20	80		223		-7 84	0 73
25	75		206		-6 40	0 75
30	70		178		-5 48	0 59
20	24	56	143	-4 20		0 51
30	21	49	130	-3 82		0 46
40	18	42	116	-3 32		0 40
50	15	35	89			

compositional dependence of T_g thus highlights the thermal stability of these tellurite glasses

The correlation between structure and T_g has been established through Mossbauer studies[53] in tellurite glasses ^{57}Fe Mossbauer experiments on Fe_2O_3 doped K-, Mg- and Ba- tellurite glasses show interesting changes in the quadrupole splitting (Δ) parameter upon addition of the modifier oxide As Fe^{3+} substitute Te^{4+} these results reflect continuous changes in the matrix glass structure with the alkali-tellurite glass eventually assuming chain network structure and the alkaline earth tellurite glasses adopting a 3D network structure Furthermore a linear correlation between T_g and Δ, suggest that T_g is primarily determined by the magnitude of the distortion of TeO_2 trigonal bipyramids

(b) Electrical Conductivity

At any given temperature, the conductance G as well as the capacitance C, of these glass sample seems to be strongly frequency dependent To determine the bulk conductivity of these glasses, free from electrode interference the real (Y') and imaginary (Y'') parts of the complex admittance Y^* are plotted as Y' against Y'' at each temperature Typical plots for the glass 30 Ag_2O-70 TeO_2 glass are shown in Fig 6.14 Each plot consists of a low frequency semicircular arc and a high frequency straight line spike These low and high frequency responses are, due to electrode and bulk polarization processes respectively The bulk conductivity of these glasses are obtained as usual, from the intersection of high frequency spike on the real (Y') axis

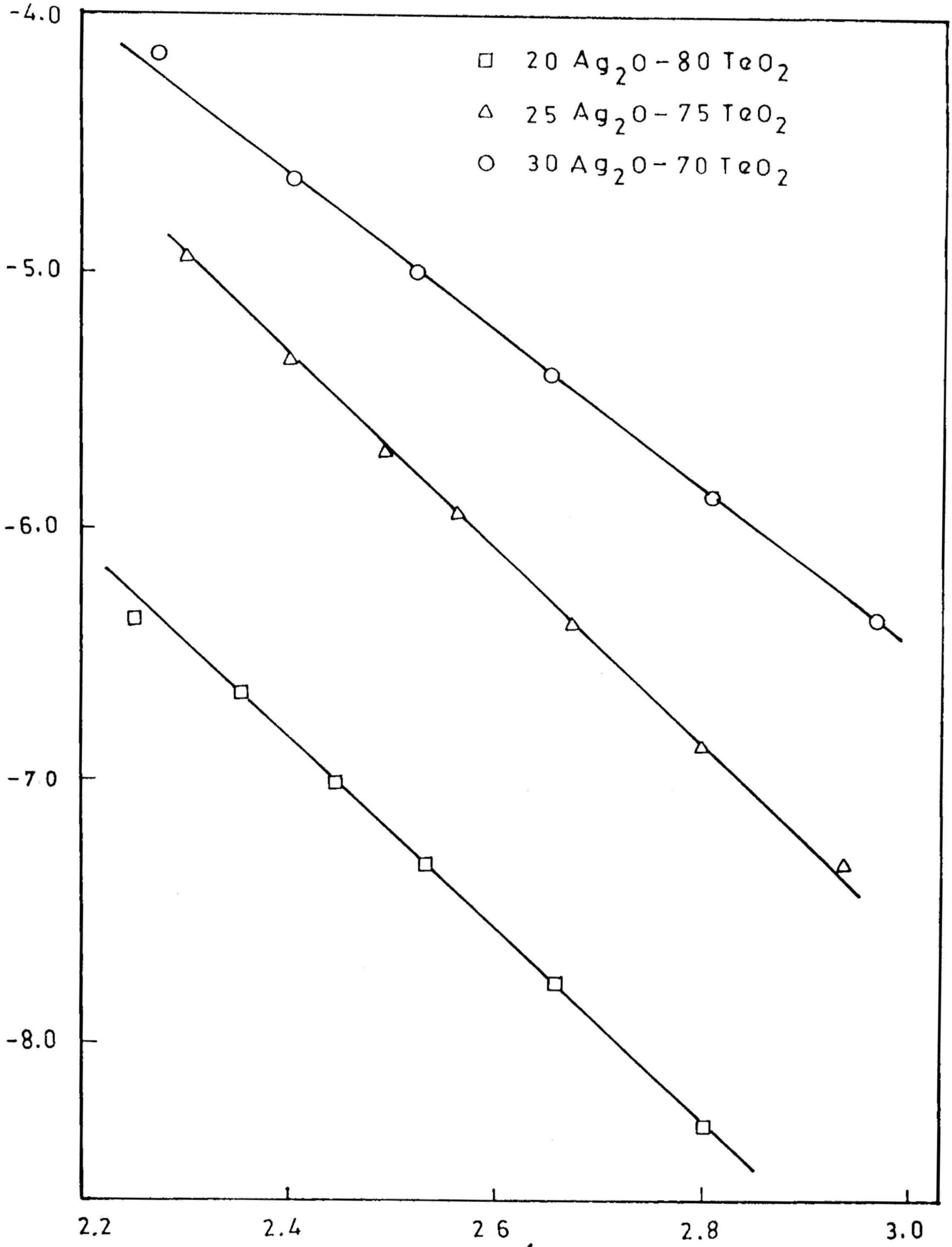

Fig 6 14 Arrhenius plot of the DC conductivity with temperature for the binary Ag_2O-TeO_2 glasses

The values of DC conductivity of these binary and ternary glasses were determined by the complex admittance technique As the 50 15 35 composition was partially crystallized we did not measure the electrical conductivity on this sample All the conductivity data can be approximated by

$$\log \sigma = \log \sigma_o - E_a/kT$$

Table V presents the conductivities and activation energies of the silver-tellurite and silver iodo-tellurite glasses An increase in conductivity was observed by increasing the AgI content from 0 mole% to 20, 30 and 40 mole%, with the Ag_2O TeO_2 ratio kept constant at 30 70 When the AgI content is increased, the Ag_2O content is decreased proportionately Therefore Ag^+ ion concentration due to AgI increases, whereas that from Ag_2O decreases The addition of 40 mole% AgI to 30 Ag_2O-70 TeO_2 glass has introduced a significant change in conductivity of nearly 3 orders of magnitude It is not clear whether the enhanced conductivity is due to increased concentration of Ag^+ ions or else due to enhanced mobility of Ag^+ ions, upon addition of AgI However, the tellurite glass structure is to be thoroughly understood, before a proper interpretation of these conductivity results is undertaken As a first attempt at getting an insight into the structures of these tellurite glasses, the ESR spectra of binary tellurite and borate glasses are compared and discussed in detail

6 3 3 ESR of Ag^{2+} in Borate and Tellurite Glasses· A Comparison

The ESR spectra of $AgI-Ag_2O-B_2O_3$, $Ag_2O-B_2O_3$ and Ag_2O-TeO_2 are all characteristic of the Ag^{2+} (I=1/2, S=1/2, 4 d^9) ion in an axially symmetric (such as distorted octahedral or tetragonal) environment

Following are the common features

1. The presence of one /two unresolved parallel component(s)
2. The existence of well resolved (ternary borate), partially resolved (binary borate) and unresolved (binary tellurite) perpendicular components
3. The absence of any other paramagnetic centres such as O^- and I_2^-, even upon X-irradiation

It is to be noted that unlike in most cases of Ag^{2+} EPR, the paramagnetic centres in the present case are

(a) created at the time of glass preparation (in the melt or during quenching), and,

(b) a native part of the glassy network and not a "guest ion' substituting some "host ion' of the network

Thus the spectra could provide a direct microscopic clue as to the nature of the short-range order in the glass

A comparison of ESR spectra of the common composition namely 30 Ag_2O-70 B_2O_3 and 30 Ag_2O-70 TeO_2 would be interesting from the points of view of glass structure and chemical bonding effects (Fig 6 15) On the basis of the temperature dependence and the saturation effects of the spectra, one could conclude that the two 'parallel" features represent two distinct $g_{\|}$ components corresponding to two chemically distinct Ag^{2+} centres in the glass network The non-resolution of the $A_{\|}$ resonances could be due to the rather small overlap of the d-wave function at the nucleus and the line broadening effects of ^{107}Ag and ^{109}Ag isotopes of Ag possessing nearly equal abundances (Ag^{107} = 51 84% , Ag^{109} = 48 11%) and the rather small nearly equal magnetic moments (-0 1135 μ_N, -0 1305

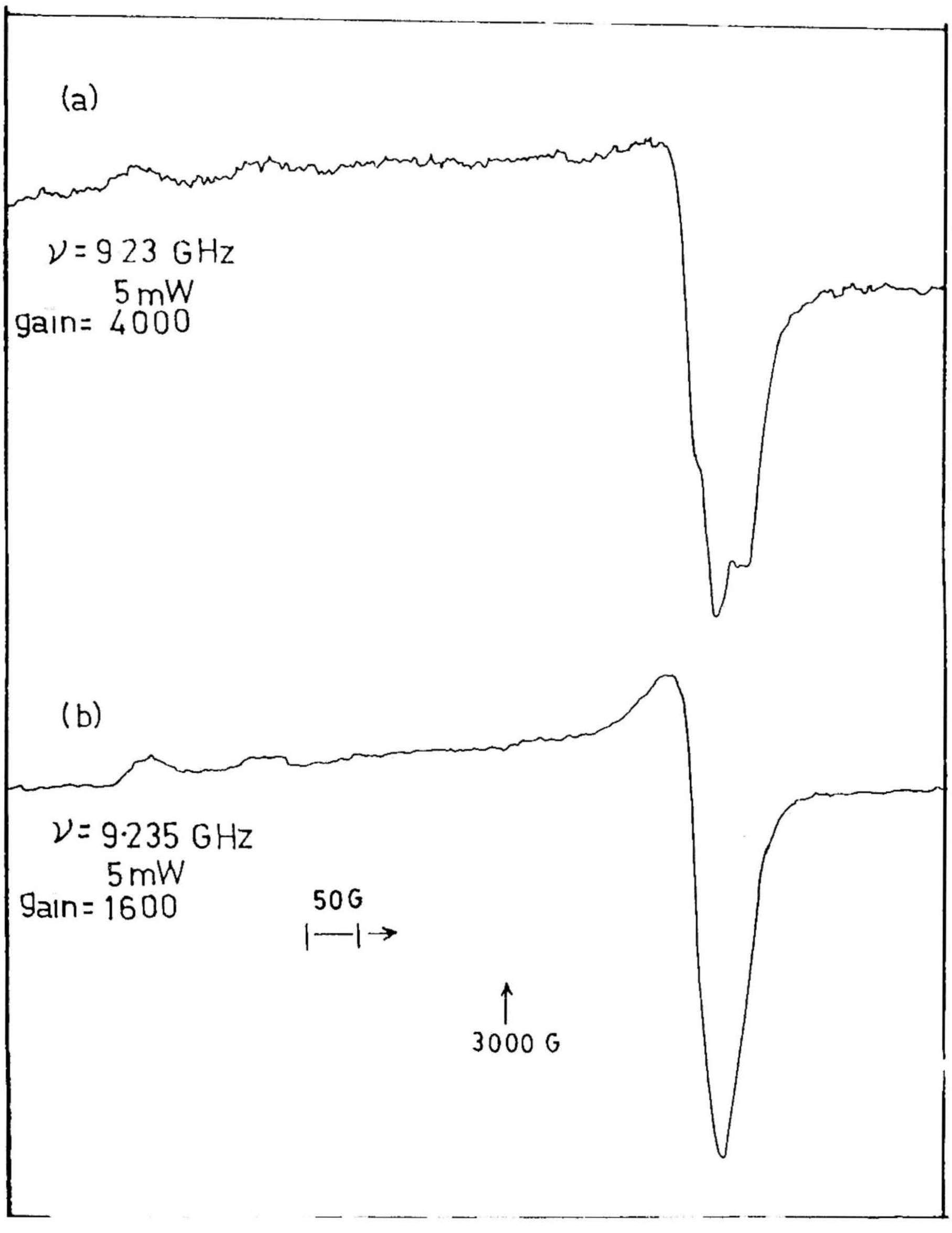

Fig 6 15 ESR spectra of (a) 30 Ag_2O-70 B_2O_3 and (b) 30 Ag_2O-70 TeO_2 glasses at room temperature

μ_N) However, this is not an uncommon feature of Ag^{2+} ESR spectra[44,54]

The perpendicular components are four in number for the borate glass while they are not at all resolved for the tellurite glasses even at 77K Two each of these four components must represent the two chemically distinct Ag^{2+} species, assuming that the isotopic resonances due to $^{107}Ag(I=1/2)$ and $^{109}Ag(I=1/2)$ are not resolved as in the parallel case Thus one could identify $\mathbf{A}_\perp$ and $\mathbf{g}_\perp$ corresponding to the two Ag^{2+} species, I and II A check on whether the perpendicular components do not indeed represent isotopic hyperfine components is provided by a comparison of the ratio of the separations between any <u>two</u> pairs of lines with the ratio of magnetic moments of the two isotopes

Therefore, the spectra of Ag^{2+} in the borate glass could be represented by the Spin Hamiltonian

$$H = \mathbf{g}_{\parallel}(I)\,\beta\,S_z\,H_z + \mathbf{g}_{\perp}(I)\,\beta\,[S_x\,H_x + S_y\,H_y] + A_{\perp}(I)[S_x\,I_x + S_y\,I_y]$$
$$+ \mathbf{g}_{\parallel}(II)\,\beta\,S_z\,H_z + \mathbf{g}_{\perp}(II)\,\beta\,[S_x\,H_x + S_y\,H_y] + A_{\perp}(II)[S_x\,I_x + S_y\,I_y]$$

The **g** and **A** - parameters are given in table IV

A distinctive feature of these spectra (for borate glasses) is the rather large deviation of $\mathbf{g}_{\parallel}$ from free spin value 2 0023 Indeed $\Delta g_{\parallel}$ = 0 500 for centre I and 0 386 for centre II to be compared with Ag^{2+} in phosphate glass and in crystalline superionic conducting matrices such as β-alumina 2 240-2 002 = 0 238 (for the two centres) Compared to the ESR spectra of crystalline halides, for example AgCl Cu where $\Delta g_{\parallel}$ = 0 133 or KCl Ag where $\Delta g_{\parallel}$ = 0 191 the $4d^9$ hole in the present case is strongly localized with considerable spin-orbit coupling

For the tellurite glass -by contrast- the $g_\perp$ feature is unresolved implying even further delocalization of the $4d^9$ hole and probably the same 'in-plane' oxygen coordination for the two centres

The questions that need to be asked and answered are :

1 What are the "environments" for the two Ag^{2+} centres I and II ?

2 What is the ground state of Ag^{2+} in these two glasses ?

3 How do the Ag^{2+} ions get stabilized, even without irradiation in these glasses ?

The general shape of EPR spectra and the magnitudes of Spin Hamiltonian parameters suggest a highly axial symmetry for the 'Ag^{2+} complex' which may be thought to consist of Ag^{2+} coordinated to oxygen atoms from the modified network building blocks BO_3/BO_4 and TeO_3/TeO_4

In the case of ternary glasses there is the additional possibility of I^- being one of the neighbours for Ag^{2+} especially in view of the large concentration of AgI in the 60-30-10 composition

While the exact identification and location of the neighbours of Ag^{2+} would require additional information - by way of additional hyperfine structure in EPR spectra due to magnetic ligands (non-existent in the present case) and/or structural data (average number of oxygens around Ag^{2+} in the glass and the approximate Ag-O distances), it could be inferred from the resolved (perpendicular) EPR spectra in borate glass that, since $A_\perp > A_\parallel$ (≈ 0), the unpaired $4d^9$ hole density is better localized in the equatorial plane In the case of tellurite glasses, however, <u>both</u> $A_\parallel$ and $A_\perp$ are nearly zero, which would imply near

complete delocalization of $4d^9$ hole density and also an identical equatorial plane neighbourhood for Ag^{2+}

As far as the Ag^{2+} centres in borate glasses are concerned one could conclude, from the thermal stability and saturation behaviour of Ag^{2+} centres, that the centre I has an axial oxygen derived from BO_3 while that of centre II originates from BO_4 As for the Ag^{2+} centres in tellurite glasses, both the centres have nearly the same thermal stability which could mean that both the Ag-O bonds in the tellurite glass are equally strong and that the TeO_3 and TeO_4 produce non-bridging oxygens of very similar chemical character[55] However, the differences in $g_{\|}$ values of the two centres once again point to the differences in the delocalization of $4d^9$ spin densities

In the absence of any ligand-hyperfine structure, and in view of the strongly axial character of the spectrum, the ground state of Ag^{2+} in these glasses is essentially free-ion like The ^2D ground state of Ag^{2+} ($4d^9$) is split into a lower doublet ($d_{x^2-y^2}$, $d_{3z^2-r^2}$) and an upper triplet (d_{xy} , d_{yz} , d_{zx}) by an average cubic/octahedral electrostatic field of the neighbors in the glass network Further distortion (e g , tetragonal compression) remove the degeneracy and make the ESR ground state non-degenerate This ground state could either be $d_{x^2-y^2}$ or $d_{3z^2-r^2}$ In view of the fact that $g_{\|} > g_{\perp}$, the coordination around the Ag^{2+} ion could be a prolate octahedron[40] i e , the symmetry would be tetragonal

Furthermore, $\Delta g_{\|} > \Delta g_{\perp} > 0$ for both the cases of borate and tellurite glasses and thus the ground state is $|x^2-y^2>$ A similar ground

state was derived for Ag^{2+} in β-alumina[40]

The question of formation of Ag^{2+} in the present glass is important because neither AgI nor Ag_2O has any native Ag^{2+} ions in them nor has any external means (e.g., X-irradiation) been employed by us, unlike all the previous investigators to produce the Ag^{2+} centres. In fact, X-irradiation has brought about a slight diminution of intensity of ESR spectra, indicating partial $Ag^{2+} \longrightarrow Ag^{+}$ conversion, and, more importantly, the inherent stability of the Ag^{2+} centres against electron capture. Unlike in cases (e.g., metaphosphate glass or β-alumina) where Ag^{0} is formed along with Ag^{2+}, there are no ESR active complementary electron-trapping centres in the present case. Furthermore, the purer the starting material, the more intense is the Ag^{2+} spectrum in our case.

The formation and the stabilization of Ag^{2+} in binary/ternary silver borate and silver tellurite glasses could take place in one or more of the following ways:

(a) Incomplete breaking of bonds. There are two types of bonds involving Ag: Ag-I and Ag-O. A complete breakage of bonds in the melt would give rise to "almost free" Ag^{+}, I^{-}, O^{2-} ions which could "momentarily" reorient themselves by forming into molecular groups such as AgI_4 or AgO_6 but then there are the glass-former bonds B-O, Te-O which would be forming and breaking. In view of the considerable viscosity of the melt, these bonds would not break completely. In case of incomplete dissociation, there is the possibility of hole transfer from BO_3 and BO_4 molecular groups to Ag^{+} and a sudden freezing of

Ag^{2+} upon quenching. This discussion - speculative and sketchy that it is - nevertheless underlines the need for a full-fledged experimental investigation on Ag^{2+} formation.

(b) Direct $Ag^{+} \longrightarrow Ag^{2+}$ conversion. As all our glasses are made in an oxidizing atmosphere, a direct $Ag^{+} \longrightarrow Ag^{2+}$ transformation in the melt cannot be ruled out. Such a conversion could initiate at the surface and gradually proceed to the bulk of the melt. Even in this case, quenching stabilizes the conversion.

Thus we believe that Ag^{2+} ions detected in the ESR spectra of borate and tellurite glasses are formed in the melt and stabilized during quenching.

6.4 CONCLUSIONS

Silver ion conducting glass systems Ag_2O-B_2O_3, Ag_2O-TeO_2, AgI-Ag_2O-B_2O_3 and AgI-Ag_2O-TeO_2 are investigated through AC admittance spectroscopy, DSC and X-band ESR spectroscopy from the points of view of (i) Ag^{+} conductivity (ii) thermal stability and (iii) mobile cation environment. The principal results are:

(a) the optimized glass composition 60 AgI-30 Ag_2O-10 B_2O_3 has high ionic conductivity (~ 10^{-3}-10^{-4} S cm^{-1}) at ambient with negligible electronic contribution.

(b) Decrease in T_g with increase of Ag_2O content, reflecting the compositional dependence of T_g.

(c) Two paramagnetic hole-type centres based on Ag^{2+} as detected by ESR. These centres formed during glass preparation are thermally more stable in tellurite glasses than those in borate glasses.

ESR of Ag^{2+} in 60 AgI-30 Ag_2O-10 B_2O_3 glass provides a strong microscopic support to Minami's model that there are three types of silver ions type I strongly interacting with BO_3 groups, type II weakly interacting with BO_4 groups and type III surrounded by I^- ions Our ESR results strengthen the suggestion that only II and III types of Ag^+ ions are responsible for ionic conduction, but not the I type

Temperature dependence of Ag^{2+} ESR spectra together with DSC results (which show two glass transition and two crystallization temperatures) that go with two Ag^{2+} centres, provide direct microscopic evidence for the co-existence of two distinct glass networks, which appears to be special feature of super ionic glasses

Ag^{2+} ESR spectra of 30 Ag_2O-70 B_2O_3 and 30 Ag_2O-70 TeO_2 binary glasses are compared in view of (a) the environment of this paramagnetic species and (b) the origin and ground state of Ag^{2+} in these glasses

REFERENCES

1 D Kunze, in *Fast Ion Transport in Solids*, ed by W Van Gool (North Holland, Amsterdam, 1973) p 405

2a H L Tuller, D P Button and D R Uhlmann, *J Non-Cryst Solids* **40**(1980) 93

b F A Fusco and H L Tuller, in *Superionic Solids and Solid Electrolytes Recent Trends*, ed by A L Laskar and S Chandra (Academic Press, London, 1989) p 43

3a T Minami, K Imazawa and M Tanaka, *J Non-Cryst Solids* **40** (1980) 469

b T Minami, *J Non-Cryst Solids* **73** (1985) 273

4 C A Angell, *Solid State Ionics* **18 & 19** (1986) 72

5 M C R Shastry and K J Rao, *Solid State Ionics* **37** (1989) 17

6 J L Black and B I Halperin, *Phys Rev.* **B 16** (1977) 2879

7 A Avogadro, F Tabak, M Corti and F Borsa, *Phys Rev* **B 41** (1990) 6137

8 M Mangion and G P Johari, *Phys Rev* **B 36** (1987) 8845

9 M Tachez, R Mercier, J P Malugani and A J Dianoux, *Solid State Ionics* **18 & 19** (1986) 372

10 M D Ingram, *Phil Mag* **60** (1989) 729

11 K J Rao and C N R Rao, *Mat. Res Bull* **17** (1982) 1337

12 C H L Goodman, *Phys. Chem glasses* **26** (1985) 1

13 M Tachez, R Mercier, J P Malugani and A J Dianoux, *Solid State Ionics* **20** (1986) 93

14 L Borjesson, L M Torell and W S Howells, *Phil Mag* **B 59** (1989) 105

15 A Fontana, G Mariotto, E Cazzanelli, G Carini, M Cutroni and M Federico, *Phys Lett* **93 A** (1983) 209

16 G Carini, M Cutroni, A Fontana, G Mariotto and F Rocca, *Phys Rev* **B29** (1984) 3567

17 J P Malugani and R Mercier, *Solid State Ionics* **13** (1984) 293

18 M J Delaney and S Ushioda, in *Physics of Superionic Conductors*, ed by M B Salamon, Top App Phys Vol 15 (Springer-Verlag, Berlin & New York, 1977) p 111

19 L Borjesson, S W Martin, L M Torell and C A Angell, *Solid State Ionics* **18 & 19** (1986) 431

20 T Minami, Y Ikeda and M Tanaka, *J Non-Cryst Solids* **52** (1982) 159

21 T Minami, *J Non-Cryst Solids* **56** (1983) 15

22 H Senapathi, G Parthasarathy, S T Lakshmikumar and K J Rao, *Phil Mag* **B 47** (1983) 291

23 M D Ingram, M A Mackenzie, W Muller and M Torge, *Solid State Ionics* **40 & 41** (1990) 671

24 G Licheri, A Musinu, G Paschina, G Piccaluga, G Pinna and A Magistris *J Chem Phys* **85** (1986) 500

25 A Musinu, G Paschina, G Piccaluga and M Villa, *J Chem Phys* **86** (1987) 5141

26 A Musinu, G Paschina, G Piccaluga and G Pinna, *Solid State Ionics* **34** (1989) 187

27 G Dalba, P Fornasini and F Rocca, *J Non-Cryst Solids* **123** (1990) 310

28 A Rajalakshmi, M Seshasayee, Y Yamaguchi, M Nomura and H Ohtaki, *J Non-Cryst Solids* **113** (1989) 260

29a G Chiodelli, A Magistris, M Villa and J L Bjorkstam, *J. Non-Cryst Solids* **51** (1982) 143

b G Chiodelli, A Magistris, M Villa and J L Bjorkstam, *Mat Res Bull* **17** (1982) 1

30 C Wagner, Z. *Elektrochem* **B60** (1956) 4

31 M C Abramo, G Carini and G Pizzimensi, *J Non-Cryst Solids* **21** (1988) 527

32 V V Daniel, *Dielectric Relaxation* (Academic Press, London & New York, 1967)

33 J Kawamura, R Sato S Mishina and M Shimoji, *Solid State Ionics* **25** (1987) 155

34 S R Elliott and A P Owen, *Phil Mag* **60** (1989) 777

35 C T Moynihan P L Gavin and R Syed, in *Proc* 5^{th} *Int Conf , J dePhys* C-9 (1982) 391

36 S W Martin and C A Angell *J. Non-Cryst Solids* **83** (1986) 185

37a A Magistris, G Chiodelli and A Schiraldi, *Electrochim Acta* **24** (1979) 203

b P Wesolowski, W Jakubowski and J L Nowinski, *Phys Stat Sol* **A 115** (1989) 81

38 A Asabghy, in *Recent Progress in Science and Technology of Matrials* ed by A Bishay, **1** (1971) 235

39 R Yokota and H Imagawa, *J Phys Soc Japan* **20** (1965) 1537

40 R C Barklie K O' Donnell and B Henderson, *J Phys C Solid State Phys* **11** (1978) 3881

41 A G Badalyan and R A Zhitnikov, *Sov. Phys Solid State* **27** (1985) 1774

42 R A Zhitnikov V D Lipatov and N G Romanov, *Sov Phys. Solid State* **15** (1973) 645

43 C J Delbecq, W Hayes, M C M O'Brien and P H Yuster, *Proc Roy Soc* **A 271** (1963) 243

44 K D Bowers, *Proc. Roy Soc* **A 66** (1953) 666

45 A Bishay, E Boulos, S Arafa, F Assabghy and N J Kreidl, in *Borate Glasses* ed by L D Pye, V D Frechette and N J Kreidl, Mat Sci Res vol 12 (Plenum, New York, 1978) P 11

46 D L Griscom, *J Non-Cryst. Solids* **40** (1980) 211

47 N I Meĺnikov, D P Peregood and R A Zhitnikov, *J Non-Cryst. Solids* **16** (1974) 195

48 B V R Chowdari, R Gopalakrishnan and K L Tan, *Solid State Ionics* **40 & 41** (1990) 709

49 T Minami and M Tanaka, *J. Solid State Chem* **32** (1980) 51

50 N Satyanarayana, G Govindaraj and A Karthikeyan, *J Non-Cryst. Solids* **136** (1991) 219

51 B V R Chowdari and S K Akhtar, *J Non-Cryst Solids* **116** (1990) 16

52 A Kone and J L Souquet, *Solid State Ionics* **18 & 19** (1986) 454

53 T Nishida, M Yamada, H Ide and Y Takashima *J Mat. Sci.* **25** (1990) 3546

54 J A McMillan and G C Munie, *J Chem. Phys* **56** (1972) 113

55 M Veno and K Suzuki, *Kakurikan Kenkyu Hokoku* (Tohoku Univ) **16** (1983) 49

CHAPTER 7

SUMMARY AND SUGGESTIONS FOR FURTHER WORK

7.1 SUMMARY

7.2 SUGGESTIONS FOR FUTURE WORK

7. SUMMARY AND SUGGESTIONS FOR FURTHER WORK

7.1 SUMMARY

A reasonably successful attempt has been made - as is probably evident from preceding chapters - to study thermal, electrical, structural and kinetic aspects of quenched-in disorder in alkali and silver-based superionic conductors. The major conclusions of this effort are as follows:

An electronic system based on quadrature oscillator, current-to-voltage converter and phase sensitivity detector (PSD) has been specially designed and constructed for the measurement of AC electrical conductivity and complex impedance/admittance on ionic and superionic conductors at several frequencies upto 60 KHz. The design incorporates a CMOS FET switch controlled by two anti-square reference signal for rectification and a differential amplifier for summation and impedance matching. The performance of the system has been demonstrated using test samples and the possibilities for complex permittivity measurement discussed. Our system obviates the need for an impedance transformer - usually employed to overcome mismatch problem in lock-in amplifier based circuit with highly resistive shunt loads. The definite advantages of this instrument such as effective noise rejection, simplicity and low cost facilitate development of the equipment even in a small research laboratory.

Quenched lithium sulphate (LS) have been investigated from the point of view of (a) long term, ambient stabilization of the plastic phase, and, (b) the mechanism of Li^+ conduction. Programmed quenching

from the melt was employed and XRD, DSC, IR and ESR spectroscopy were employed for characterizing the phase stabilized by quenched-in disorder The principal results are

(1) while pure LSA (Alfa) quenches from melt/high-temperature solid state to an extremely short-lived FCC phase, LSL (Loba) quenched to 200°C produces the hardened plastic phase which has a 5-6 order higher conductivity compared to the insulating monoclinic phase,

(2) XRD points to orientationally disordered cubic phase (a = 6 98 Å),

(3) The endothermic humps in DSC (~ 351 and 535-550°C) provides unequivocal thermodynamic characterization of the metastable phase,

(4) A strong, structure-sensitive microscopic evidence for the stabilization of cubic phase comes from the ESR of X-irradiated melt-quenched Li_2SO_4 containing Li_2CO_3, by way of a motionally averaged g-tensor characteristic of tumbling CO_3^- ions occupying the disordered lattice, and

(5) Direct IR spectroscopic evidence of orientational disorder involving SO_4^{2-} and CO_3^{2-} is provided by the considerably broadened ν_3 vibrational mode of the former, and, broadened ν_3 and intense & sharp ν_2 modes of the latter

The correlation between the structure of the metastable phase and ESR features on the one hand and between vibrational disorder and high Li^+ conductivity on the other, is discussed

The eutectic composition 30 Li_2O-70 TeO_2 (in mole %) identified by the phase diagram of the pseudo binary system Li_2O-TeO_2 is prepared as glass and its thermal and electrical behaviours are investigated in detail. The thermal behaviour of 30 Li_2O-70 TeO_2 glass studied through DSC reveals two and three stages of crystallization for the bulk and powdered glasses respectively. The non-isothermal kinetics of the first stage crystallization of powdered glass has been analyzed in terms of the modified Ozawa and the modified Kissinger methods and the crystallization products identified by XRD. Surface nucleation appears to be the dominant mechanism for crystallization with an activation energy barrier of 553 ± 6 kJ/mole, a value higher than for silicate glasses indicating the lower thermal stability of the tellurite glasses. Three products of crystallization - an intermediate unidentified phase, a metastable monoclinic phase and a stable, final orthorhombic phase - are revealed by XRD. The crystallized (orthorhombic) phase exhibits lower ionic conductivity and higher activation energy for conduction compared to the glass.

The mixed alkali effect is investigated in the tellurite glass system 30 [(1-x) Li_2O-x Na_2O]-70 TeO_2, (where x = 0, 0.2, 0.4, 0.6, 0.8 and 1.0), through (i) AC conductivity (ii) DSC and (iii) IR absorption.

The isothermal conductivity, activation energy for the conduction process (E_a), and Te-O_{ax} stretching frequency of molecular groups TeO_3/TeO_4 - all showed nonlinear behaviour upon gradual substitution of one alkali ion by another, with a minima (in σ and T_g) at Na/(Na+Li) ~ 0.6, as in borate glasses. A shallow positive deviation in E_a characterizes this system.

In the light of theories, based on the interaction between alkali ions and the glass structure, an examination of our results reveals that the effect and the nature of different structural networks (such as TeO_3 with NBOs and TeO_4) must be included to fully account for all features of mixed alkali effect.

Glass compositions are optimized in the systems $AgI-Ag_2O-B_2O_3$ and $AgI-Ag_2O-TeO_2$ with respect to Ag^+ conduction, so as to realize high ionic conductivity (~ 10^{-2} to 10^{-3} S cm^{-1}) at ambient with negligible electronic contribution. ESR of Ag^{2+} in 60 AgI-30 Ag_2O-10 B_2O_3 glass provides a strong microscopic support to Minami's model to the AgI-based borate glass structure and have strengthened the fact that the mobile Ag^+ ions responsible for superionic conduction in these glasses come from both AgI and Ag_2O constituents. The temperature dependence of Ag^{2+} ESR spectra together with DSC results also reveal the co-existence of two glass network in $AgI-Ag_2O-B_2O_3$ superionic glass. Ag^{2+} ESR spectra of 30 Ag_2O-70 B_2O_3 and 30 Ag_2O-70 TeO_2 glasses are compared in the light of short range order existing in the two networks.

7.2 Suggestions for Further Work

Based on the results of the present investigations, and the conclusions there of, the following suggestions could be made, for a better or deeper understanding of the systems and phenomena.

1 (a) The AC conductivity meter frequency range could be upgraded to 1 MHz.

(b) Digitization of output and interfacing the instrument with a computer.

2 (a) Neutron diffraction study on QL_{200} for the confirmation of structural model of α-Li_2SO_4, including carbonate ion positions for further interpretation of ESR results

(b) Estimation of frozen-in entropy in quenched Li_2SO_4 through specific heat measurements

(c) Identification of the unknown intermediate phase in quenched Li_2SO_4

(d) Microstructure of QL_{300} through transmission electron microscopy

(e) Stabilization of α-Li_2SO_4 in a glass matrix such as Li_2O-TeO_2

(f) Partial replacement of SO_4^{2-} by CrO_4^{2-} and ESR study of its quenched melt to probe dynamical disorder

(g) Role of $Fe_2(SO_4)_3$ in stabilization of α-Li_2SO_4 - a mixed conductor - and an electrode material to go with quenched Li_2SO_4

3 (a) Identification of the unknown crystallized product in 30 Li_2O-70 TeO_2 glass

(b) The influence of surface area upon crystallization (third stage)

(c) Viscosity measurement in the range $T_g \leq T \leq T_m$ and their correlation with crystallization kinetics

4 (a) Structural relaxation around T_g by DSC studies to probe the mixed alkali effect

(b) Mixed alkali effect in the system Li_2O-Ag_2O-TeO_2 using Ag^{2+} ESR as probe to investigate the role of non-bridging oxygens

5 (a) Optimization of Ag^+ conduction in AgI-Ag_2O-TeO_2 glass system for the use as a battery material and elucidation of conduction mechanism

(b) A dedicated study of the formation of Ag^{2+} paramagnetic species in $AgI-Ag_2O-B_2O_3/TeO_2$ glasses.

(c) A study of crystallization kinetics of optimized $AgI-Ag_2O-B_2O_3$ and $AgI-Ag_2O-TeO_2$ glasses to confirm the existence of micro-crystalline α-AgI.

(d) Optical studies (absorption and luminescence) of $AgI-Ag_2O-B_2O_3/TeO_2$ glasses, for a complete understanding of the Ag^{2+} environment and for a simulation of ESR spectra.

LIST OF PUBLICATIONS

1. "Calorimetric and electrical studies on quenched $Li_2SO_4.H_2O$",
   P. Balaya and C.S. Sunandana, Solid State Commun. 70 (1989) 581.

2. "A PSD-based electronic system for AC response studies of superionic conductors",
   P. Balaya and C.S. Sunandana, Pramana-J. Phys. 33 (1989) 627.

3. "ESR of Ag^{++} in 60 AgI-30 Ag_2O-10 B_2O_3 glass",
   P. Balaya and C.S. Sunandana, Solid State Ionics, 40/41 (1990) 770.

4. "ESR of X-irradiated melt-quenched Li_2SO_4",
   P. Balaya and C.S. Sunandana, Recent advances in fast ion conducting materials and devices, BVR chowdari, et al. (Eds.) World Scientific (1990) 535.

5. "Mixed-alkali effect in the Li_2O-Na_2O-TeO_2 glass system",
   P. Balaya and C.S. Sunandana, Recent advances in fast ion conducting materials and devices, BVR Chowdari, et al. (Eds.) World Scientific (1990) 539.

6. "Electrical and thermal studies on silver tellurite glasses",
   P. Balaya and C.S. Sunandana, "Recent advances in fast ion conducting materials and devices", BVR Chowdari, et al. (Eds.) World Scientific, (1990) 543.

7. "Metastable superionics",
   C.S. Sunandana and P. Balaya, accepted for presentation in 3rd Asian Conf. on Solid State Ionics, Varanasi-India, Nov. 1992.

8. "Spectroscopic, electrical and thermal studies on silver tellurite and silver-iodo tellurite glasses",
   P. Balaya and C.S. Sunandana, accepted for presentation in 3rd Asian Conf. on Solid State Ionics, Varanasi-India, Nov. 1992.

9. "Crystallization studies of 30 Li_2O-70 TeO_2 glass",
   P. Balaya and C.S. Sunandana, communicated to J.Non-Cryst. Solids.

10. "Quenched lithium sulphate",
    P. Balaya and C.S. Sunandana, communicated to J. Phys: Conden. Matter.